# Bainitic steel with 30 GPa% characteristics
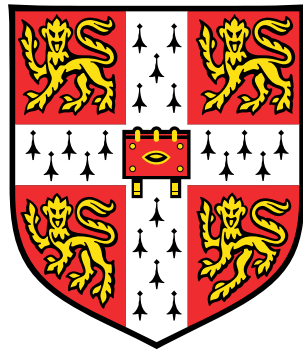
Shaumik Lenka

Materials Science and Metallurgy
University of Cambridge

A dissertation submitted for the degree of
Doctor of Philosophy

Churchill College   October 2019

Abstract

The ability of a steel to be formed is often measured as the product of the ultimate tensile strength and total elongation (GPa%). The aim of the work presented in this thesis was to produce a bainitic steel by continuous cooling transformation, with a ultimate tensile strength exceeding 1000 MPa and yet having a ductility of 30%. The challenge associated with the development is that the steel must be spot-weldable, which means that the carbon concentration needs to be kept low enough to avoid the formation of martensite in the heat-affected zones of resistance spot welds.

Fundamental phase transformation theory is used for alloy design, followed by alloy manufacture and validation using a variety of microstructural and mechanical characterization techniques. Progress is made in understanding the onset of plastic instability by critically examining the role of retained austenite in enhancing ductility. The literature on the transformation induced plasticity (TRIP) steels and factors affecting the strength and ductility in TRIP–assisted steels has been reviewed.

A model employing deformation induced martensitic transformation coupled with percolation theory has been revisited with fresh data collated from published work to estimate the elongation of TRIP-assisted steels. A novel quantitative estimation of the stability of austenite required for optimising ductility has been developed and demonstrated to explain the new data.

Two alloys emerged from the sequence of alloy and process design, which successfully broke the 30 GPa% barrier while maintaining the ability for mass production. Furthermore, tempering of the steel at a low temperature for few hours improved ductility by softening the small amount of martensite formed during cooling to ambient temperature.

"Premature" failure during mechanical testing is usually due to some sort of heterogeneity in the manufactured steel. Such behaviour can sometimes be mitigated by refining the microstructure. This was investigated to see whether the required combination of strength and ductility can be achieved by reducing the scale of the parent austenite grains to achieve greater structural uniformity. However, a detailed investigation showed that lowering the austenitization temperature led to a deterioration in the properties due to microstructural banding.

Mechanical stabilization during bainitic transformation from deformed austenite increased the volume fraction of martensite thus making the microstructure unfavourable for optimum mechanical properties. Therefore bainite should be generated from a strain–free recrystallised austenite grain structure.

The Habit plane, orientation relationship and associated shape strain were characterized simultaneously for the first time on individual bainite plates. The irrational habit plane of bainite measured by the two surface analysis was found to be close to $\{457\}_\gamma$, which is not far off the $\{557\}_\gamma$ lath martensite habit plane reported in the literature. Pole figure analysis of three plates of bainite showed consistent results. The shear strain associated with the bainite plate is consistent with the value estimated by the phenomenological theory of martensite.

Declaration

I hereby declare that this dissertation is the result of my own work and includes nothing which is the outcome of work done in collaboration except as specified in the text. It is not substantially the same as any that I have submitted, or, is being concurrently submitted for a degree or diploma or other qualification at the University of Cambridge or any other University or similar institution.

This dissertation contains fewer than 65,000 words including appendices, bibliography, footnotes, tables and equations and has fewer than 150 figures.

Shaumik Lenka
October 2019

Acknowledgements

I would like to express my most heartfelt gratitude to my supervisor Professor Sir Harshad Kumar Dharamshi Hansraj Bhadeshia, for his guidance, advice, support and enthusiasm during my research. One particular quotation he mentioned during my initial period at Cambridge that drives me towards the goal of creating new knowledge is "Progress and new insight come from challenging concepts".

I would like to thank Dr Saurabh Kundu and Mr Appa Rao Chintha for providing me with existing data and samples of 1000 MPa bainitic steel prepared at Tata Steel Limited. I am thankful to Dr Sanjay Chandra and Tata Steel Limited to provide me with an opportunity to pursue my Ph.D. at University of Cambridge by supporting me financially and funding my research. I would also like to thank the members of the Phase transformation group at the Department of Materials Science and Metallurgy, Cambridge, who have all been extremely kind and supportive. Dr Steve Ooi helped me in procuring the alloys used in my thesis and I am really appreciative for all his assistance during the tenure of my Ph.D.

I am really grateful to my wife, Snigdha and my son, Aarav for motivating me and helping me sail through the highs and lows. I really appreciate my mother, Sandhya and brother, Sai who selflessly pushed me to move to Cambridge to pursue my Ph.D.

...Dedicated to the fond memory of my father, Sarat Kumar Lenka...

Contents

Chapter 1

Introduction

Transformation induced plasticity (TRIP) steels possess a good combination of strength and ductility and have immense potential in automotive applications. This is due largely to legislative requirements for better passenger safety and environmental concerns regarding the minimisation of greenhouse gasses. More fuel efficient vehicles generally focus on weight reduction (Fig. 1.1) [1]. At the same time, enhanced safety, comfort and convenience features have added to the overall weight which surprisingly has increased continuously over the past 30 years, as shown in Fig. 1.2 [2]. Steels with a high strength to weight ratio can resist deformation during service, and yet enhance fuel efficiency and passenger safety. Properties such as ductility, crash resistance, formability and weldability are important in automotive applications.
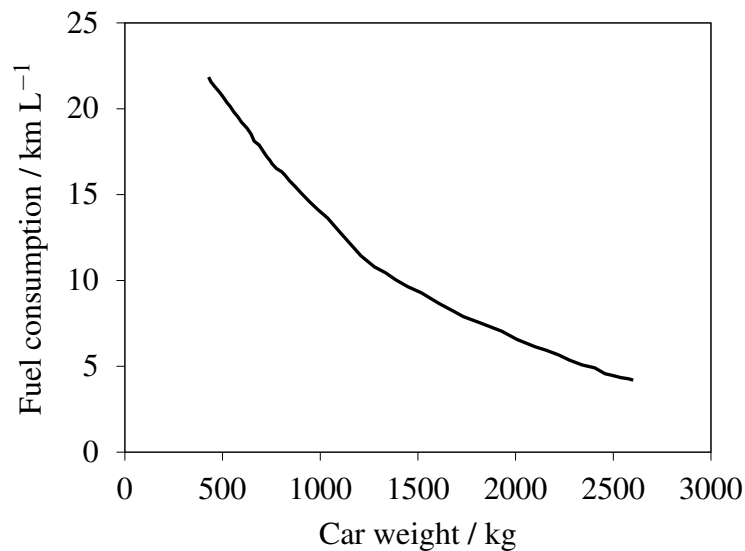
Figure 1.1 The relation between car weight and fuel consumption [1].
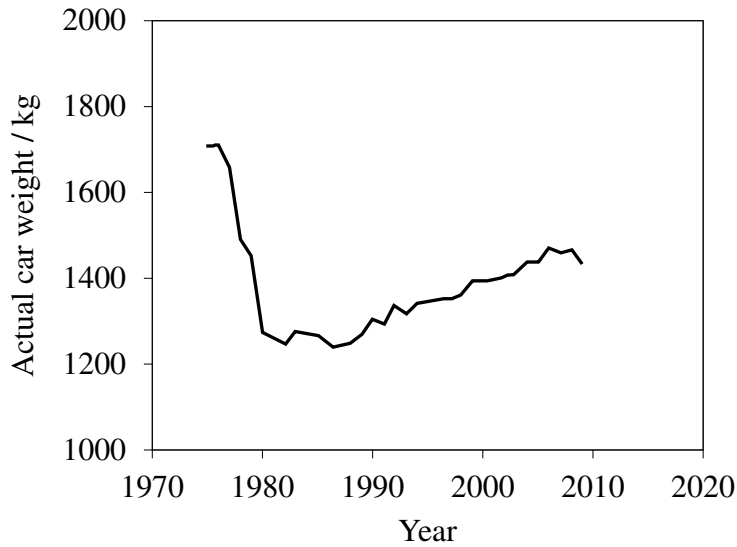
Figure 1.2 Actual average weight of cars in United States since 1975 [2].

1.1   Scope of the research

The aim was to develop a commercially viable steel with an ultimate tensile strength of 1000 MPa or more and having a ductility of $\approx 30\%$. This combination normally is expressed as a product 30 GPa%, and the steel must be capable of being produced by continuous cooling transformation. It must of course be spot weldable and hence have a low hardenability expressed in terms of an empirical carbon equivalent [3, 4]. The carbon content in general should be maintained below about 0.25 wt% so that any martensite that forms during welding is not too hard or brittle [5]. There exists a huge amount of published work on transformation induced plasticity steels and on twinning induced plasticity steels (TWIP) which apparently meet the 30 GPa% requirement (Figs. 1.3 and 1.4) [6–13]. However, they have not proved to be successful for a variety of reasons including poor weldability especially in the galvanised condition [14, 13]. TWIP steels contain large concentrations of manganese and hence increase the cost of the finished automotive components [1]. The high manganese content also makes it difficult to produce the steel using a continuous casting process because of the high vapour pressure of manganese in liquid steel [15]. TRIP–assisted steels are, by comparison, lean alloys having a bainitic and retained austenite microstructure. However, these steels are rich in carbon and can be problematic during welding [16, 17, 15]. It is evident that the development of the steel should be carried out bearing in mind a basket of properties.
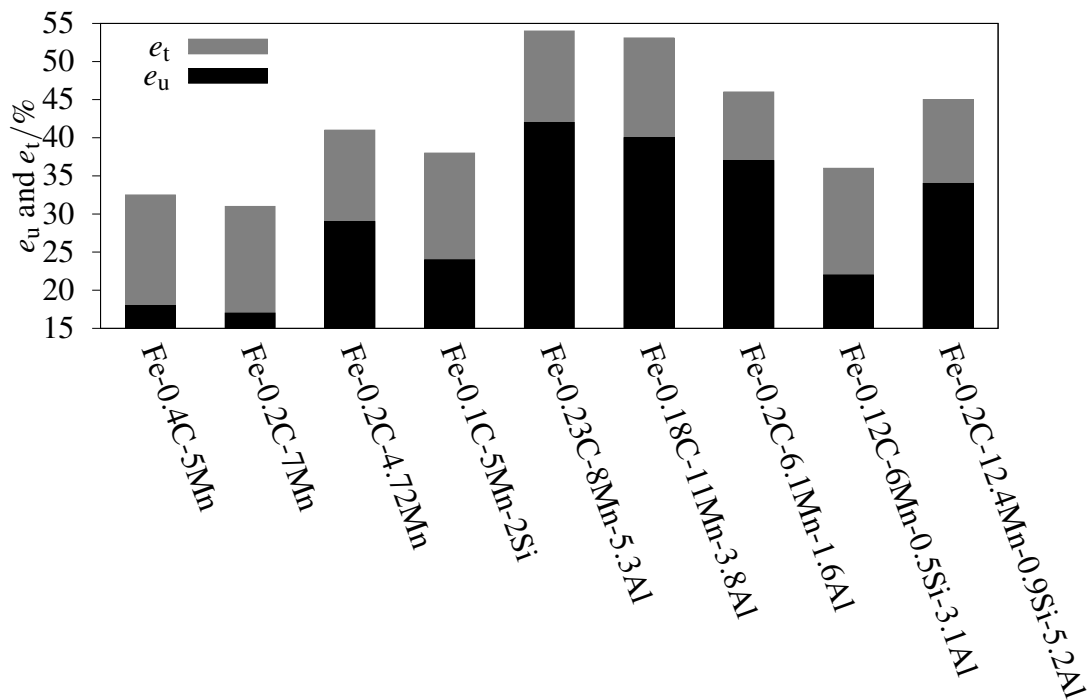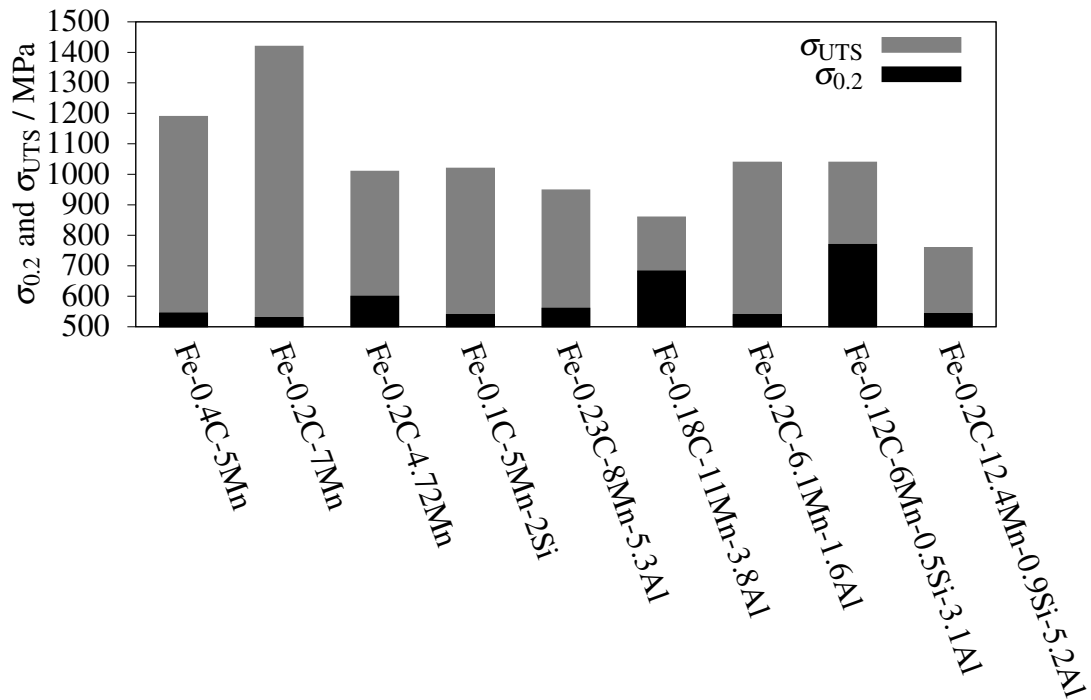
Figure 1.3 Mechanical properties of diverse TRIP steels tested at room temperature [6–10].
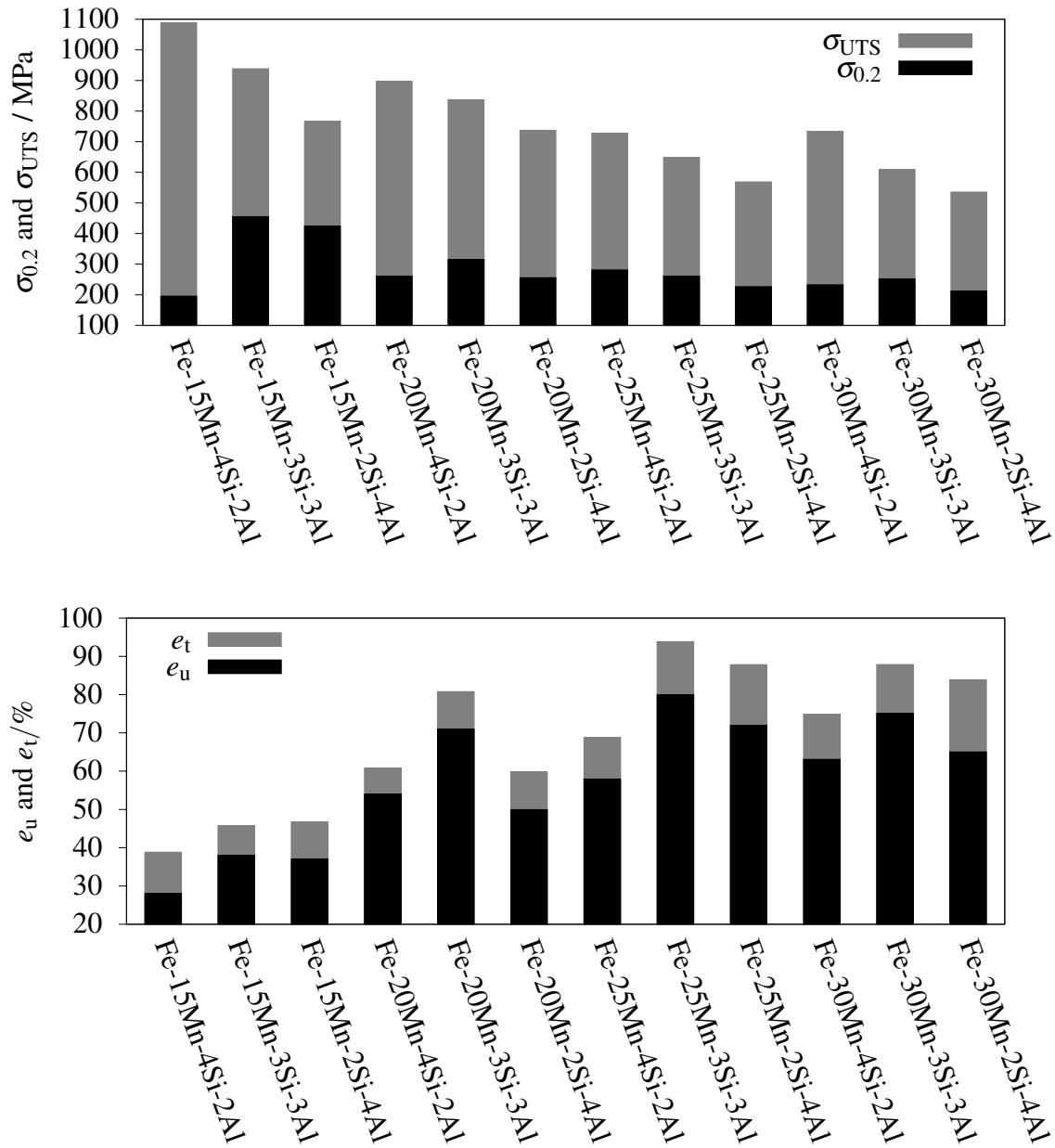
Figure 1.4 Mechanical properties of diverse TWIP steels with carbon concentration between 0.01–0.06 wt% tested at room temperature at a strain rate ($\dot{\varepsilon}$) of 10^{-4} s^{-1} [11].

Although there have been numerous studies on the mechanical properties of bainitic steels, they tend to be repetitious [18–25], so an understanding of the parameters controlling ductility in TRIP steel is not well established. Some of these parameters include the volume fractions of various phases (allotriomorphic ferrite, carbide–free bainite, retained austenite and martensite), the stability of retained austenite and other variables, detailed in subsequent

sections. Thus, what is believed to be the critical role of the volume fraction of retained austenite and its thermodynamic stability is assessed in the present work to create an optimum design procedure. In this context the proposed research will focus broadly on:

- development of a model to relate ductility to microstructural attributes especially the austenite content and it's stability.

- Formulation of a viable chemical composition and heat treatment strategy for achieving a bainitic steel with the 30 GPa% characteristics.

- Understanding the effect of austenite and its stress–induced transformation on the ductility of TRIP-assisted steels.

- Creation of finer austenite grains, with an examination of the consequences on austenite content, austenite stability and ductility.

- Study of the shape deformation, orientation relationship and indices of the habit plane of a bainite sub-unit.

The work commences with a description of available literature on various categories of automotive steels with extensive discussion of TRIP and TRIP–assisted steels. The alloy design philosophy is discussed with emphasis on optimising strength and ductility. The deformation–induced transformation of austenite to martensite yielding the characteristic elongation in TRIP–assisted steels is reviewed in the context of the phenomenological theory of martensite.

The estimation of elongation using the austenite percolation concept is used to design the alloys. A range of optimum stability of austenite expressed in terms of the free energy required for austenite to ferrite transformation, where the GPa% tends to maximise has been established. Improvement of properties by improvising process parameters made it possible to make the steel achieve the required targets in those cases where the properties were narrowly missed.

Chapter 2

Scientific background

2.1   Transformation–induced plasticity steels

Transformation induced plasticity steels rely on the principle of delaying the onset of plastic instability (necking) during tensile testing because of strain hardening caused by the formation of martensite. There are broadly two types of TRIP steels: (i) completely austenitic, (ii) those containing a limited fraction of retained austenite [26]. The former category is rich in solutes that stabilise austenite (Mn, Ni, and etc. [16]) to concentrations as large as 10 wt% to 15 wt%, making the alloys expensive.

TRIP–assisted steels in contrast contain combinations of allotriomorphic ferrite, carbide–free bainitic ferrite and retained austenite. By changing the proportions of different phases, it is possible to obtain a variety of strength and ductility combinations. The retained austenite is stabilised to ambient temperature by enriching it with carbon, that is partitioned into the residual austenite by allotriomorphic ferrite or bainitic ferrite [27]. Carbide–free bainite refers to that in which cementite is suppressed by the addition of silicon or aluminium. These elements are not soluble in the cementite lattice, so they retard or suppress it's precipitation when the cementite is forced to absorb them during paraequilibrium precipitation at low temperatures, Fig. 2.1 [28]. Paraequilibrium refers to the case in which phase transformation proceeds by the partitioning only of interstitial solutes with the substitutional solute to iron ratio remaining fixed everywhere [16, 17]. Jang *et al.* calculated the free energy of formation of cementite in the presence of silicon using density functional theory [29–31]. They showed that substitution of one iron atom in the unit cell of cementite by silicon (equivalent to 4.07 wt%), increased the free energy of formation of cementite from 86.05 to 123.22 kJ mol^{-1}. Phosphorous also achieves this but may cause embrittlement of steel if added in concentration excess of 0.05 wt% [32, 33].
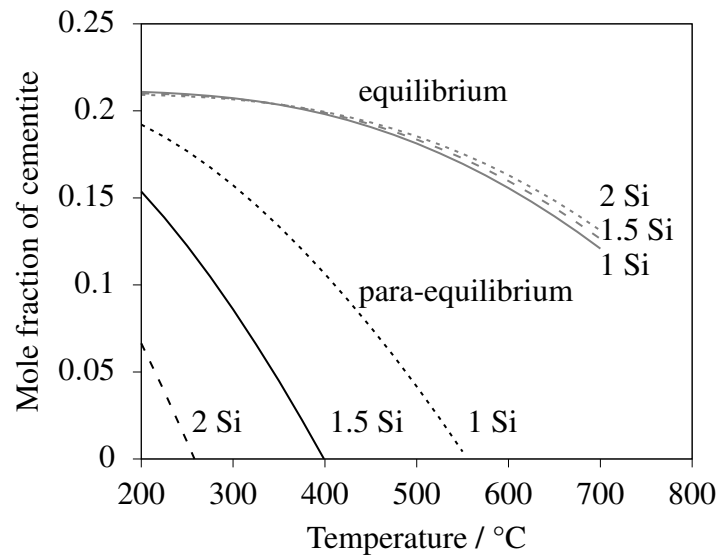
Figure 2.1 Calculated phase fraction of cementite in equilibrium and para–equilibrium with austenite in Fe–1.2C–1.5Mn (wt%) steel with varied Si levels in weight percent [28].

2.2   Microstructure mediated alloy design

Alloy design is envisaged keeping in mind the microstructure and mechanical properties to be achieved in the final product. Mechanical properties such as yield strength (σ_y), ultimate tensile strength (σ_{UTS}), uniform elongation (e_u), total elongation (e_t), strain hardening exponent (n) and plastic anisotropy ($\bar{r}$) are important to any product specification. The exponent n represents the ability of the material to work harden and may be a function of strain [34]. The Lankford coefficient $\bar{r}$ is a measure of deep–drawability given by the ratio of the in–plane strain to the through thickness strain averaged over three different directions of 0°, 45° and 90° within the plane of a sheet specimen [35]. However, these properties are not exhaustive. It may be necessary to weld and form the steel during fabrication. Formability is a complex combination of attributes such as deep drawability, stretch formability and stretch flangeability. All these properties are discussed in detail in Section 2.6.

Tables 2.1 and 2.2 show the different grades of steel used as structural components in automotive applications. Uses include ancillary parts, body structures, closures, fuel tanks, suspension/chassis and wheels. Each application demands a considered combination of microstructure and mechanical properties. Fig. 2.2 shows the usage of various automotive steels for structural components.

Table 2.1 Mechanical properties of various automotive steels, BH–bake hardening, IF–interstitial free, DP–dual phase, HSLA–high strength low alloy, TRIP–transformation induced plasticity, SF–stretch flangeable, CP–complex phase and Mart–martensitic [36].

Steel	σ_y / MPa	σ_{UTS} / MPa	e_t / %	n–value	$\bar{r}$
Mild	140	270	38-44	0.23	1.8
BH	210–260	340–370	29-39	0.13–0.18	1.6–1.8
IF	260–300	410–420	29-38	0.2	1.6–1.7
DP	280–700	600–1000	12-34	0.09–0.21	1
HSLA	350–490	450–600	21-27	0.13–0.22	1
TRIP	450	800	26-32	0.24	0.9
SF	570	640	20-24	0.08	1
CP	700	800	10-15	0.13	1
Mart	950–1250	1200–1520	4-7	0.07	0.9

Table 2.2 Chemical compositions of various automotive steels in wt% [36, 37].

| Steel	C	Si	Mn	Cr	Mo	Al	V	Nb	Ti
Mild	0.04–0.12	<0.1	0.25–0.60						<0.1
BH	<0.03	0.01–0.3	0.1–0.75			<0.05			<0.06
IF	0.003–0.007	<0.5	0.10–1.00			<0.03			<0.05
DP	0.06–0.15	0.01–0.30	1.20–2.40	0.1–0.6	<0.18	<0.04	<0.06		<0.01
HSLA	0.08–0.18	0.01–0.50	1.0–1.6	<0.2	<0.1	0.01-0.04	0.05–0.18		0.01–0.045
TRIP	0.06–0.22	1.00–1.75	1.2–2.0	0.1–1.0	<0.1	<0.04	<0.01	<0.05	<0.01
SF	<0.08	0.1–0.3	1.0–1.5				<0.06	<0.025	
CP	0.1–0.20	0.1–0.5	1.4–2.20	0.2–1.0	<0.2	0.04–0.12		<0.1	<0.06
Mart	0.15–0.20	0.01–0.5	1.00–1.60	<0.5		<0.04		<0.05	<0.05
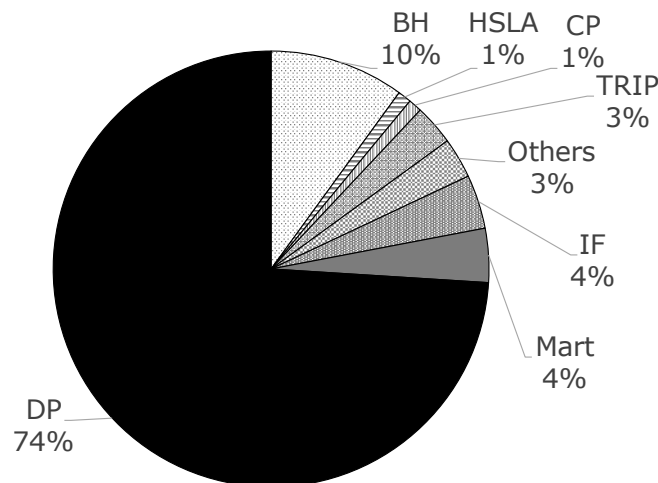
Figure 2.2 Usage of automotive steels in structural components. BH–bake hardening, IF–interstitial free, DP–dual phase, HSLA–high strength low alloy, TRIP–transformation induced plasticity, SF–stretch flangeable, CP–complex phase and Mart–martensitic [36].

Strength and ductility often vary inversely but TRIP and TWIP (twin induced plasticity) steels buck this trend. TRIP steels benefit from the deformation–induced transformation of austenite to martensite, that delays plastic instability during tensile loading [16]. TWIP steels rely, on the other hand, on mechanical twinning that divides the austenite grains into ever finer regions during deformation, leading to the work hardening that is responsible for resisting the early onset of plastic instability [16, 15].

TRIP–assisted steels can contain allotriomorphic ferrite, bainite, austenite and martensite, the proportions of which determine the mechanical properties of the steel. The austenite referred to in the TRIP–assisted steel is that which is retained at room temperature, usually occupying about 0.10 to 0.20 of the total microstructure. Martensite may also be present prior to deformation, and when associated with retained austenite, the mixture is commonly known as the MA (martensite–austenite) constituent. There are three combinations of microstructure in the TRIP–assisted steels. The first contains allotriomorphic ferrite, bainite and retained austenite (type I) in the approximate proportions of 50%, 30% and 20% respectively. These steels tend to have a relatively low strength ($\sigma_{UTS} \simeq 600\,\mathrm{MPa}$) and high elongation ($e_t \simeq 25\%$) [36, 13, 11]. Allotriomorphic ferrite and retained austenite contribute to the ductility and the bainite to strength. These steels are used already in the automotive industry, Tables 2.1 and 2.2. Type II contains only carbide–free bainitic ferrite and retained austenite in the approximate proportions of 80% and 20% respectively. As a result, these steels are stronger ($\sigma_{UTS} \simeq 1200$–$2500\,\mathrm{MPa}$) but still reasonably ductile ($e_t \simeq 10$–20%) [16], produced by isothermal transformation. They find applications in bainitic rails and armour applications [38–40]. The third kind consists of a mixture of martensite, preferably tempered martensite, and retained austenite (type III) and are known as quenched and partitioned steels [41, 42]. Quenched and partitioned steels have $\sigma_{UTS} \simeq 800$–$2500\,\mathrm{MPa}$ with $e_t \simeq 10$–25% [43, 44] and are used in armour, fasteners and landing gears of aircraft [45]. Type III alloys are not discussed further.

The processing routes are illustrated in Fig. 2.3. When fully austenitized, cooling introduces allotriomorphic ferrite which enriches the residual austenite with carbon. Some of the austenite is then transformed into bainitic ferrite at temperatures in the range 400–450 °C, leading to further enrichment of austenite, much of which is retained on cooling to room temperature. The intercritical annealing of cold–rolled steel (curve 2 in Fig. 2.3) forms a mixture of austenite and allotriomorphic ferrite, with the former then transformed partially into bainite at a lower temperature.
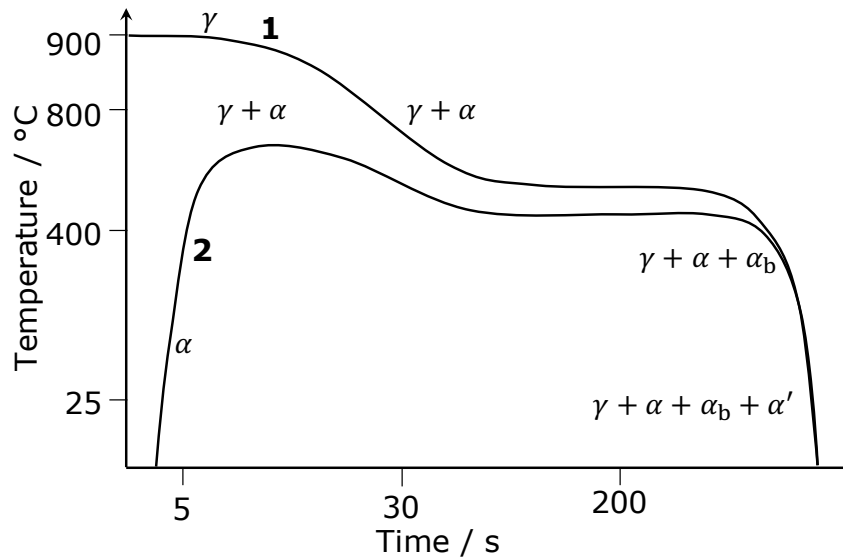
Figure 2.3 Schematic cooling profile of the two different process route to produce microstructure contributing to TRIP effect. Profile 1 is the transformation post austenitization after hot rolling route. Profile 2 represents intercritical annealing post cold rolling route. γ–austenite, α–allotriomorphic ferrite, α_b–bainitic ferrite and α'–martensite [17].

2.3 Martensite theory and the TRIP effect

2.3.1 Phenomenological theory

Martensite forms as a result of the diffusionless transformation of austenite. The transformation progresses by the migration of a sharp interface which can in principle move at speeds approaching that of sound in the steel. This change in structure occurs by a homogeneous deformation involving the cooperative movement of atoms [46]. The associated theory is quite well established [16, 17, 47, 48]. The face–centred cubic (FCC) structure of austenite converts to the body–centred cubic (BCC) structure of ferrite via the Bain strain [49]. For the transformation to progress without diffusion the interface between γ and α' should contain an invariant line along which lie just one set of interfacial dislocations. Such an interface is glissile. If there exist more than one set of dislocations at the interface, the interaction between them may lead to the formation of jogs which can be immobile, thereby rendering the interface sessile.

The Bain strain (**B**) can be explained by considering two adjacent FCC unit cells of austenite and then re–drawing an equivalent tetragonal unit cell of austenite with different basis vectors as shown in Fig. 2.4a. This tetragonal austenite undergoes deformation, as described in Figs. 2.4b and 2.4c [17, 16, 48, 47, 49]. The deformation of austenite to

(a)

(b)   (c)
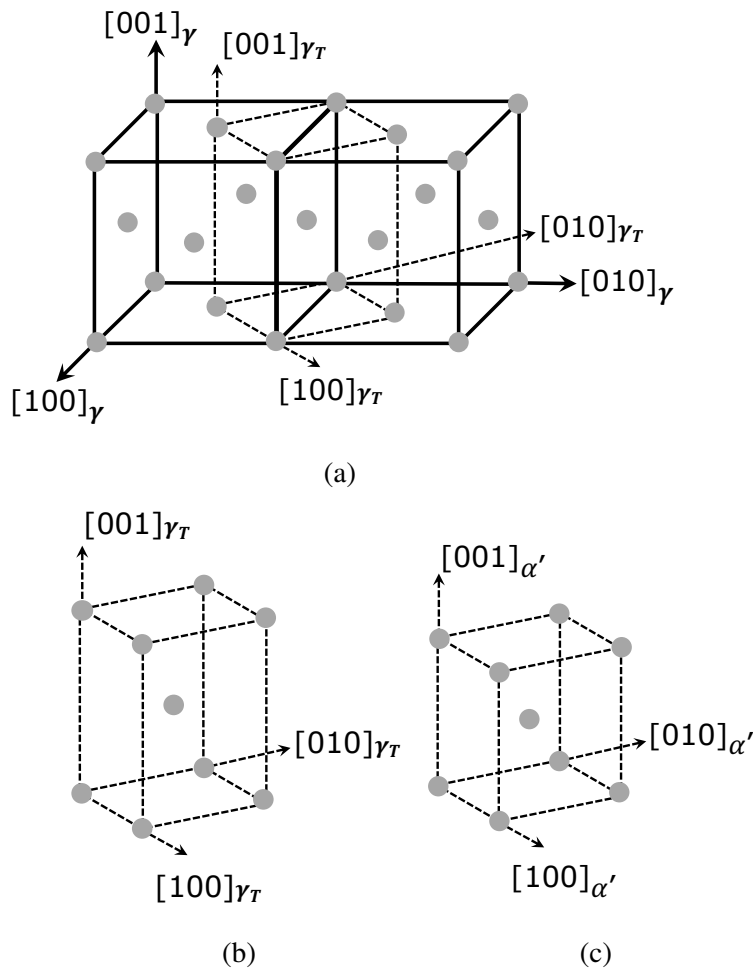
Figure 2.4 Lattice correspondence between austenite and martensite where (a) is the equivalent tetragonal unit cell of austenite defined by different basis vectors. Bain strain involving compression along c–axis of austenite and a uniform expansion in the horizontal plane (b) to martensite (c) with correct c/a ratio [50].

martensite can alternatively be described in the terms of a sphere being deformed under the influence of the Bain strain. The Bain strain would compress the [001] direction ($\mathbf{a}_{III}$) and expand uniformly the [100] and [010] directions ($\mathbf{a}_I$ and $\mathbf{a}_{II}$). In the $\mathbf{a}_{III}$ plane the γ is expanded to $\alpha^{'}$ as illustrated in Fig. 2.5a. Under the influence of the Bain strain the sphere changes into an ellipsoid of revolution about $\mathbf{a}_I$. There are no lines in $(001)_\gamma$ which are undistorted. However, there are lines such as xw and yz in Fig. 2.5b which are undistorted due to Bain strain but are rotated to $x^{'}w^{'}$ and $y^{'}z^{'}$. It can thus be concluded that Bain strain does not produce an invariant line as is necessary to ensure a glissile interface between austenite and martensite. A rigid body rotation ($\mathbf{R}$) following the Bain strain ($\mathbf{B}$), as illustrated in Fig. 2.5c, superimposes the line yz and $y^{'}z^{'}$. However, the angle between xw and $x^{'}w^{'}$

is doubled. The Bain strain coupled with a rigid body rotation (denoted by notation **RB**) therefore generates an invariant line strain (ILS).
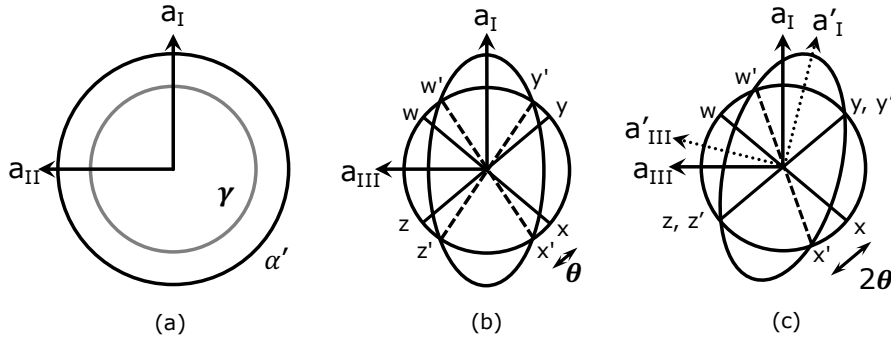
Figure 2.5 Spherical representation of austenite and application of Bain strain followed by a rigid body rotation. (a) Bain strain deformation of austenite to martensite along the c–axis showing expansion in $\mathbf{a_I}$ and $\mathbf{a_{II}}$ directions. (b) Bain strain deformation along the c–axis showing formation of ellipsoid of revolution about $\mathbf{a_I}$. (c) Rigid body rotation coupled Bain strain showing the formation of invariant line strain (ILS) [46, 17, 16].

Under the influence of **RB**, austenite in Fig. 2.6 converts into martensite having the correct crystal structure but wrong macroscopic shape. There exist two ways to correct the macroscopic shape of martensite without changing the structure, twinning or slip. This phenomenological theory of γ to $\alpha^{'}$ transformation has been proved through the measurement of orientation relationship between the two phases and the precise determination of habit plane and shape deformation of martensite. It is found that the orientation relationship is not exactly Kurdjumov–Sachs (KS) [51] or Nishiyama–Wasserman (NW) [52] but in practice are irrational. This is explained by the rigid body rotation coupled with Bain strain to generate an invariant line strain (ILS) which brings about the irrationality. Also, the precise habit plane of martensite measured is irrational, because of the slipped or twinned martensite which gives rise to an average habit plane [47, 48].

2.3.2   Deformation–induced martensitic transformation

Martensitic transformation is athermal in nature and in general the extent of transformation in normal steels does not depend upon time but on the undercooling below the M_S temperature. The relation between the volume fraction of martensite and the undercooling below M_S is given by the Koistinen and Marburger equation [53]:

$$1 - V_{\alpha'} = \exp\{-0.011(M_S - T)\} \tag{2.1}$$
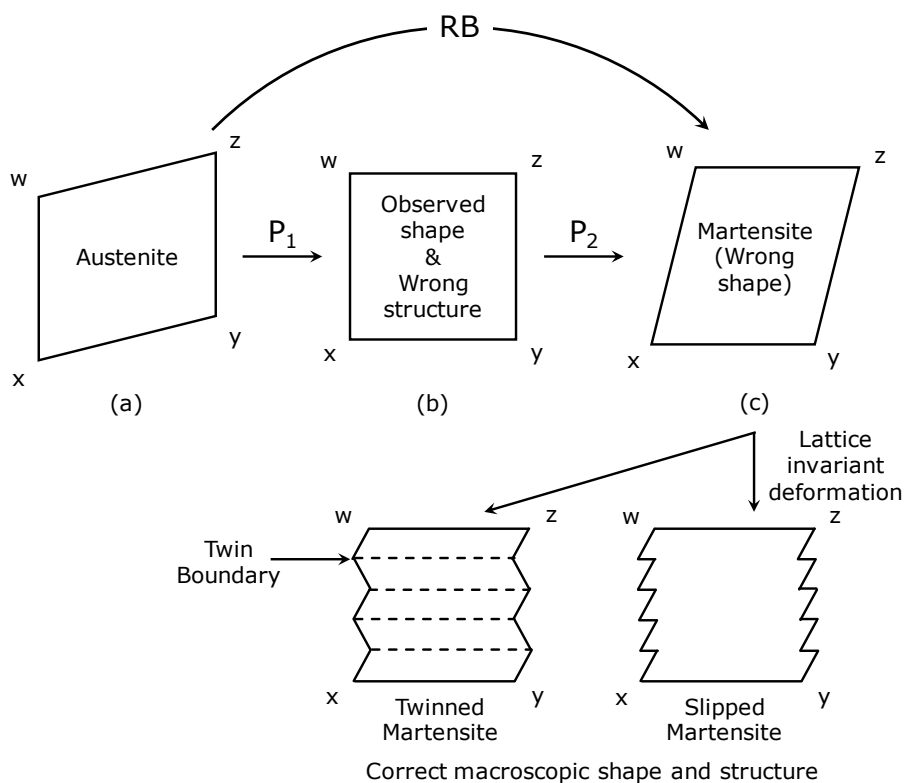
Figure 2.6 Phenomenological theory of martensite showing the formation of martensite by virtue of twinning or slip to ensure correct crystal structure and macroscopic shape during transformation under the influence of Bain strain and rigid body rotation [46, 17, 16].

where, $V_{\alpha'}$ is the fraction of martensite and T is the temperature below M_S. During martensitic transformation, α' inherits the composition of γ, the free energy change is illustrated in Fig. 2.7a. Transformation is possible at compositions where there is a reduction in free energy, i.e. when $\bar{x} < x_{T_0}$. x_{T_0} is the carbon concentration at which austenite and ferrite of identical chemical composition have the same Gibbs free energy. Alternatively, it is the concentration at which $G^\alpha - G^\gamma = \Delta G^{\gamma\alpha} = 0$ for same composition of austenite and ferrite. Fig. 2.7a is at a constant temperature, similar curves can be generated at other temperatures using thermodynamic data and commercially available software such as MTDATA or ThermoCalc [54–56]. The temperature at which $\Delta G^{\gamma\alpha}$ is sufficient for the nucleation of α' is known as the martensite–start temperature and the corresponding free energy is the critical chemical driving force ($\Delta G_{M_S}^{\gamma\alpha}$) for α' formation. Fig. 2.7b illustrates the M_S temperature and corresponding chemical driving force for martensite formation ($\Delta G_{M_S}^{\gamma\alpha}$).

At any temperature between M_S and T_0, γ to α' transformation is not possible. However, by an application of an appropriate external stress to austenite the transformation can be
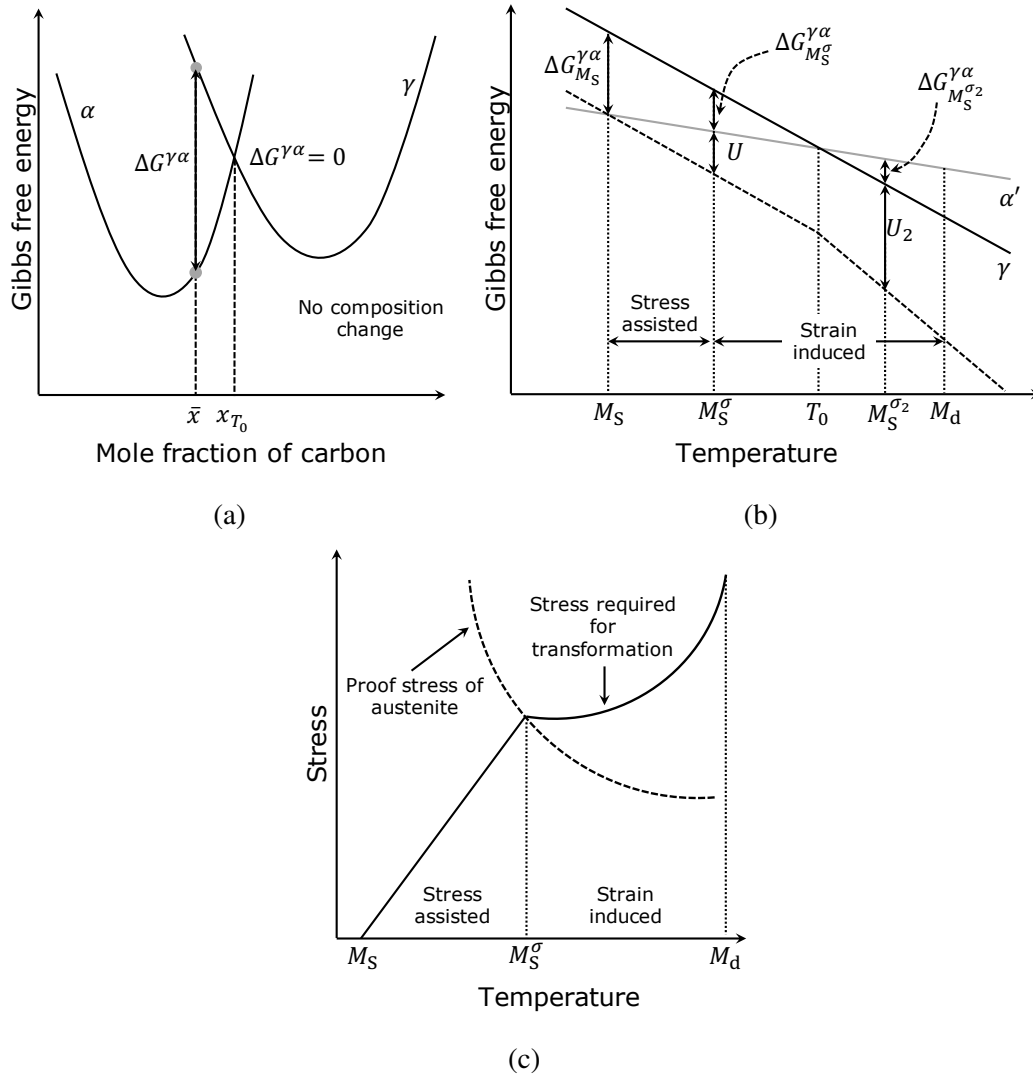
Figure 2.7 (a) Chemical free energy change associated with martensitic transformation from austenite without composition change. (b) and (c) showing variation of chemical free energy change and deformation mode for γ to α' transformation with respect to temperature. M_S^σ and M_S are martensite start temperature with and without external stress respectively. $\Delta G_{M_S^\sigma}^{\gamma\alpha}$ and $\Delta G_{M_S}^{\gamma\alpha}$ are the chemical driving force with and without external stress respectively. U is the mechanical free energy change. M_d is the temperature above which deformation induced transformation of γ to α' is not possible [17, 16, 57]. $M_S^{\sigma_2}$ is equivalent to M_S^σ but corresponds to different chemical ($\Delta G_{M_S^{\sigma_2}}^{\gamma\alpha}$) and mechanical ($U_2$) free energies.

initiated at a lower chemical driving force. In Fig. 2.7b, at the temperature M_S^σ, the smaller chemical driving force ($\Delta G_{M_S^\sigma}^{\gamma\alpha}$) can be compensated for by the mechanical driving force (U) arising from the external stress [58, 59] provided that the sign of U assists throughout. The free energy required to nucleate martensite at M_S^σ then given by:

$$\Delta G_{M_S}^{\gamma\alpha} = \Delta G_{M_S^\sigma}^{\gamma\alpha} + U \tag{2.2}$$

where for tensile testing, all these terms have negative magnitudes. Similar equality holds for temperature $M_S^{\sigma_2}$ (above the T_0 temperature). The mechanical free energy required to nucleate martensite increases with temperature above M_S, because of the corresponding reduction in $|\Delta G^{\gamma\alpha}|$. This increased mechanical free energy is achieved by increasing the external stress. As the temperature increases the strength of austenite decreases. At the temperature M_S^σ, Fig.2.7b, the applied external stress surpasses the elastic limit of austenite, causing plastic deformation. The region between M_S and M_S^σ is where the external stress is below the yield strength of austenite, so any martensite must nucleate on pre–existing defects, the transformation is said to be stress assisted. However, between M_S^σ and M_d the external stress causes plastic deformation that creates new defects such as dislocations, shear bands and faults, which are potent nuclei that stimulate strain–induced transformation. M_d is the maximum temperature at which the deformation–induced martensitic transformation is possible because the mechanical driving force cannot provide a significant stimulus.

2.3.3 Role of martensite in TRIP steel

The contribution of stress–induced transformation induced plasticity to the total elongation of TRIP–assisted steels is in fact meagre [60]. The γ to α' transformation generates a shape deformation which is characterised as an invariant–plane strain with a dilatation (δ) of 0.03 and large shear component (s) of 0.26, as illustrated in Fig. 2.8a [17]. The maximum interaction due to a tensile force can occur if the tensile axis acting along **u** with a magnitude σ, martensite habit plane normal ($\mathbf{Z}_3$) and shear direction ($\mathbf{Z}_1$) as shown in Fig. 2.8b lie in the same plane [58]. Note that Z_i form a orthonormal set. The mechanical driving force when the stress is uniaxial tension, can be calculated as follows:

$$U = \sigma_N \delta + \tau s \tag{2.3}$$

$$U = \sigma \sin(\theta)s + \sigma \cos(\theta)\delta \tag{2.4}$$

The angle between the tensile axis **u** with magnitude σ and martensite habit plane normal which generates the maximum mechanical driving force can be calculated by differentiating Equation 2.4 with respect to θ and equating it to zero. The θ computed comes out to be $41.7°$ [58]. The deformation matrix in the basis Z, is then given by [17, 61, 62]:

$$(Z\,P\,Z) = \begin{pmatrix} 1 & 0 & s \\ 0 & 1 & 0 \\ 0 & 0 & 1+\delta \end{pmatrix}$$

(a)   (b)
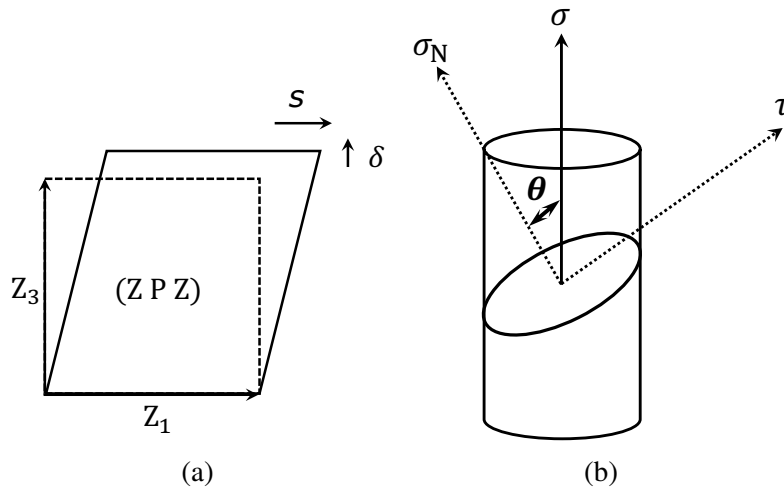
Figure 2.8 (a) Invariant plain strain with shear strain s and dilatation δ described in the orthonormal coordinate system with axes $\mathbf{Z}_1$, $\mathbf{Z}_2$ and $\mathbf{Z}_3$. $\mathbf{Z}_3$ is the normal to the habit plane made by $\mathbf{Z}_1$ and $\mathbf{Z}_2$. $\mathbf{Z}_1$ parallel to the shear direction. $\mathbf{Z}_2$ is perpendicular to $\mathbf{Z}_1$ and $\mathbf{Z}_3$ and is directed out of the plane of paper. (Z P Z) is the deformation matrix. (b) Schematic showing the tensile axis of magnitude of stress σ, habit plane normal and shear direction lying in the same plane. θ is the angle between tensile axis and habit plane normal [60].

The direction of the tensile axis in basis Z is written [Z;**u**], interacts with the deformation matrix (Z P Z) giving rise to a rotated and distorted vector [Z;**v**]. This interaction is computed by the matrix multiplication [17]. The vector [Z;**u**] can be determined by resolving the stress σ in the normal and shear directions. Thus the vectors [Z;**u**] and [Z;**v**] are given as follows:

$$[Z;\mathbf{u}] = [\ \sin\theta\ \ 0\ \ \cos\theta\ ]$$

$$[Z;\mathbf{v}] = \begin{pmatrix} 1 & 0 & s \\ 0 & 1 & 0 \\ 0 & 0 & 1+\delta \end{pmatrix} \begin{pmatrix} \sin\theta \\ 0 \\ \cos\theta \end{pmatrix}$$

$$[Z;\mathbf{v}] = [\ (\sin\theta + s\cos\theta)\ \ 0\ \ (1+\delta)\cos\theta\ ]$$

The total strain is computed to be 0.15 as follows:

$$1 - \frac{|\mathbf{v}|}{|\mathbf{u}|} = 0.15$$

A fully austenitic steel on transformation to martensite with the favoured orientation can therefore generate a maximum strain of 0.15. TRIP–assisted steels only contain 10–20% retained austenite [60], so the strain contribution is just 0.015–0.03. However, the elongation of TRIP–assisted steels is much higher [63–65]. This is because the hard, stress–induced martensite increases the work hardening rate, thus delaying failure through plastic instabilities.

2.4 Importance of retained austenite

The stability of austenite is important to ensure it transforms gradually into martensite so that a work hardening capacity is available over a large strain range. Conversely, too high a stability means that it becomes ineffective in contributing to strain hardening. The stability of austenite can be altered by changing (i) the chemical composition, (ii) microstructural attributes and (iii) deformation conditions.

2.4.1 Effect of alloying

Alloying elements such as C, Mn, Ni that stabilize austenite by expanding the γ–field are typically added to TRIP–assisted steels to retain austenite at room temperature by suppressing the martensite–start temperature. The empirical equation correlating the M_S temperature with the alloying element concentration is given by [66]:

$$M_S(^\circ\mathrm{C}) = 539.0 - 423.0\mathrm{C} - 30.39\mathrm{Mn} - 12.14\mathrm{Cr} - 17.69\mathrm{Ni} - 7.46\mathrm{Mo} \ (\mathrm{wt\%}). \qquad (2.5)$$

Carbon clearly is the most effective in suppressing M_S. Alloying also influences the stacking fault energy and the difference between the M_d and M_S temperatures [67]. It is said [67] that M_d and M_S should bound room temperature to optimise elongation [68, 69]. Tamura *et al.* pointed out that for Fe–29Ni–0.26C (wt%) TRIP steel, the elongation goes through a maximum as a function of test temperature, Fig. 2.9 [70]. Ideally, the maximum should therefore lie in the vicinity of room temperature for the best elongation [17]. Cooman [71] pointed out that TRIP–assisted steels with composition wherein room temperature lies between M_S^σ and M_{d30} best exploits the TRIP effect from the point of view of uniform elongation. M_{d30} refers to the temperature at which 50% austenite is transformed

into martensite at 30% strain. M_{d30} is generally used in practice owing to the ease with which it can be experimentally determined than M_d [71]. 30% strain in M_{d30} is adopted for reasons of passenger safety [71].
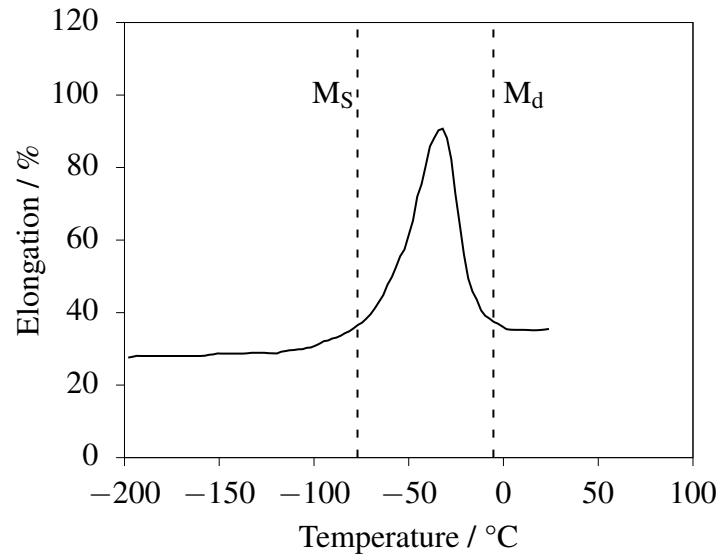
Figure 2.9 Effect of test temperature on the elongation behaviour Fe–29Ni–0.26C (wt%) TRIP steel [70].

Sugimoto *et al.* [72] did a similar study as in Fig. 2.9, to correlate the peak elongation with respect to tensile test temperature for various TRIP–assisted steels with composition range tabulated in Table 2.3. These all are Type I TRIP-assisted steels with a strength–ductility product range of 20–40 GPa%. They derived an equation (Equation 2.6) to predict the temperature at which peak elongation occurs with respect to the M_S temperature of the retained austenite. This equation can further be used to estimate the M_S of the retained austenite required for the maximum elongation to occur at room temperature. Thus helping to narrow down the carbon content of the retained austenite necessary to achieve highest possible elongation at room temperature.

Table 2.3 Chemical composition of seven different alloys used by Sugimoto *et al.* for developing Equation 2.6 [72]. All alloying elements are in wt%.

Reference	C	Si	Mn	S	P	Al	N
[72]	0.19–0.21	1.00–2.48	1.00-2.51	0.013	0.015	0.038–0.041	0.0011–0.0017

$$T_p \, / \, °C = 3.04 \times M_S + 187 \ [72] \tag{2.6}$$

Alloying elements also increase the strength of austenite through solid solution strengthening. The martensite plate thickness depends on that strength, driving force for γ to α' transformation and temperature of transformation [17, 16]. Fewer plates form in stronger austenite, which results in gradual decomposition of austenite and increased stability. Aluminium and phosphorous increase the stacking fault energy which enhances austenite stability [67, 57, 71, 73].

Data pertaining to various TRIP-assisted steels from literature have been collated to correlate different parameters to the strength–ductility product [74, 75, 64, 76, 77, 65, 78–80, 18, 23, 81–83]. Fig. 2.10 shows the inverse relationship between tensile strength and ductility. 80% of the data points in Fig. 2.10 belong to ≤ 30 GPa% domain, the remainder 20% achieved a strength–ductility product of 30 GPa% and higher.
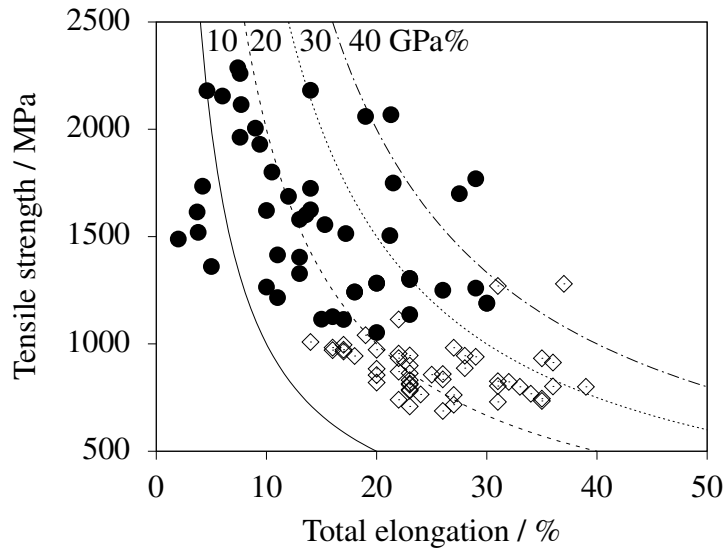
Figure 2.10 Strength and elongation of TRIP–assisted steels showing inverse relationship with different iso–GPa% lines. Diamond shaped points denote microstructure containing substantial amount of allotriomorphic ferrite with combinations of bainite, retained austenite and martensite (Type I). The solid dots represent data from TRIP–assisted steels having bainite, retained austenite and martensite in the microstructure (Type II).

Plotting bulk carbon content (c_{bulk}) against strength–ductility product showed no correlation (Fig. 2.11). Similarly, no correlation between the carbon equivalent (CE, defined later in this chapter) expressed as Equation 2.12 and GPa% is found (Fig. 2.12). These plots (Figs. 2.11 and 2.12) are however, independent of the type of heat treatment used. The microstructures under consideration can be any combination of ferrite, bainite, retained austenite and may contain some martensite upon cooling to room temperature. Some data

points clearly show that it is possible to obtain 30 GPa% at $c_{bulk} \leq 0.25$ wt% or CE ≤ 0.6 wt%. The cut off of carbon content and carbon equivalent is suggestive of good weldability.
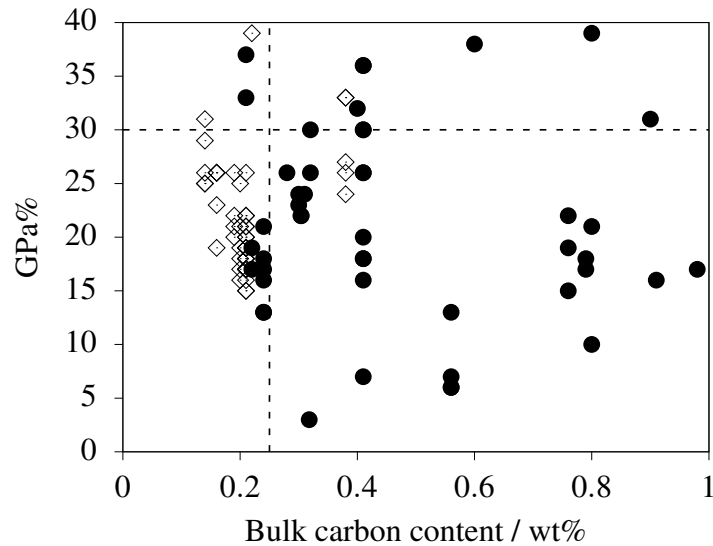
Figure 2.11 Effect of bulk carbon content on the product of strength and ductility expressed as GPa% in TRIP–assisted steels. Diamond shaped and solid points denote Type I and Type II steels respectively.
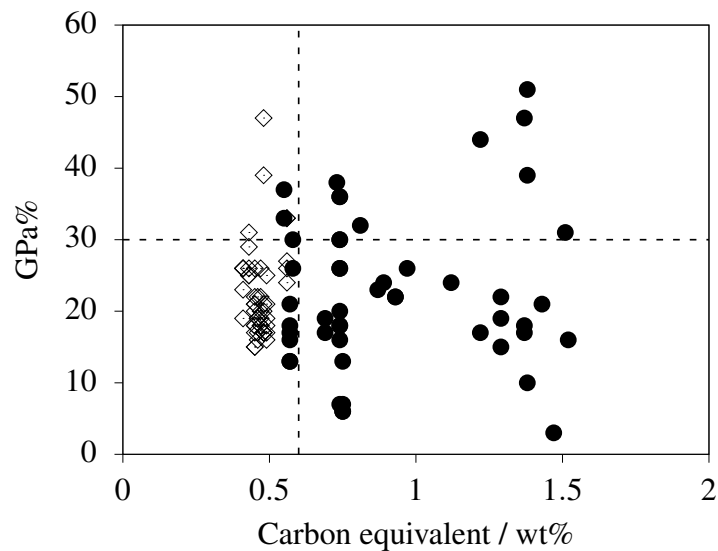
Figure 2.12 Plot of carbon equivalent and the product of strength and ductility expressed as GPa% in TRIP–assisted steels. Diamond shaped and solid points denote Type I and Type II steels respectively.

Same data of GPa% when plotted against the retained austenite content in the microstructure and carbon content in retained austenite, begin to show some correlation, Figs. 2.13 and 2.14 respectively. It is evident that an increase in retained austenite content a higher strength–ductility product is achievable. The measured carbon content in the retained austenite (c_γ^e) shows a lot of scatter when plotted against GPa% (Fig. 2.14), there is a trend of increasing GPa% against c_γ^e. This is explained by the increase in stability of retained austenite which is dependent on c_γ^e. The free energy of transformation of retained austenite to ferrite calculated from the composition of retained austenite with enriched carbon (c_γ^e) and similar substitutional alloying composition as the bulk gives the trend with GPa% as shown in Fig. 2.15. Clearly, the higher is the absolute value of the driving force the less stable is the austenite and thus exhausting transformation at low strain. Thus, a value of $|\Delta G^{\gamma\alpha}| \leq 2500\,\text{J}\,\text{mol}^{-1}$ may be optimum to achieve 30 GPa%.
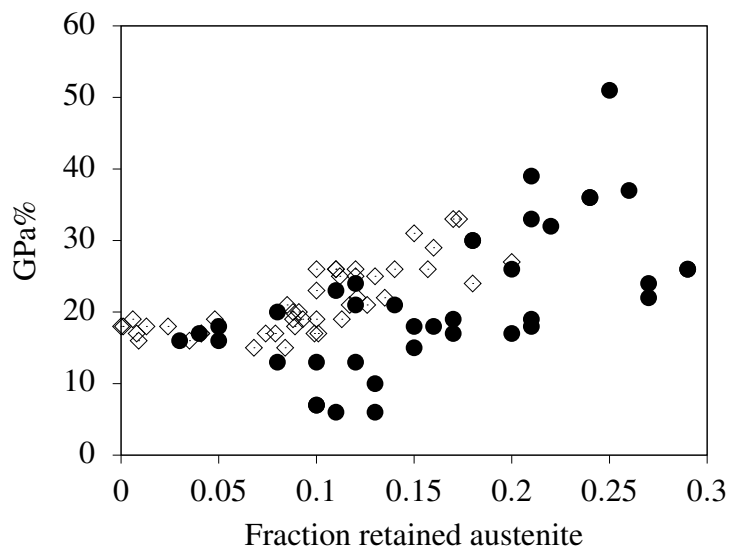
Figure 2.13 Correlation between retained austenite content and the product of strength and ductility expressed as GPa% in TRIP–assisted steels. Diamond shaped and solid points denote Type I and Type II steels respectively.
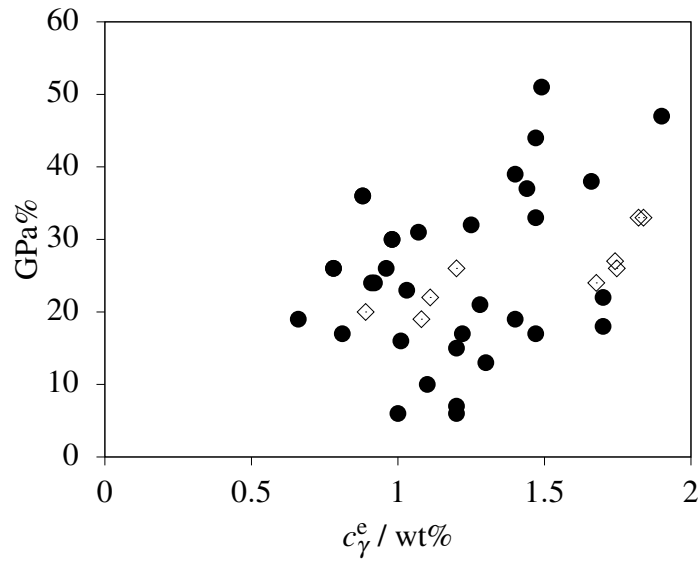
Figure 2.14 Correlation between carbon content of retained austenite (c_γ^e) and the product of strength and ductility expressed as GPa% in TRIP–assisted steels. Diamond shaped and solid points denote Type I and Type II steels respectively.
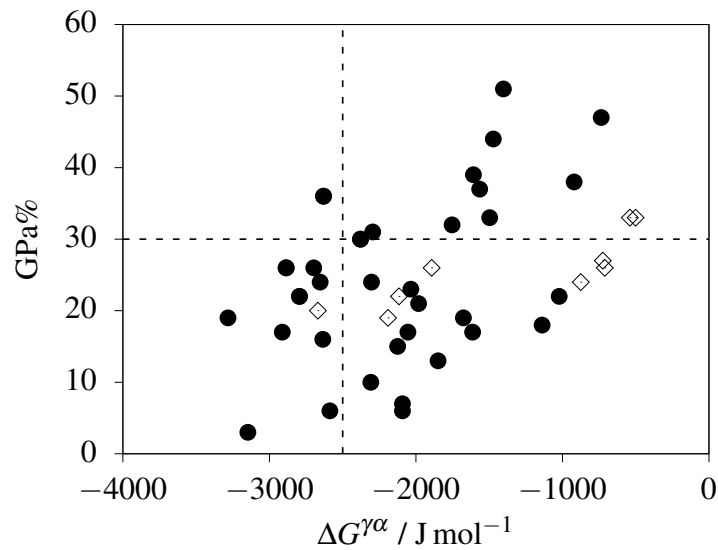
Figure 2.15 Correlation of Gibbs energy of transformation of retained austenite to ferrite and product of strength and ductility expressed as GPa% in TRIP–assisted steels. Diamond shaped and solid points denote Type I and Type II steels respectively. Note that $600\,\mathrm{J\,mol^{-1}}$ of strain energy is not deducted from data [84].

Effect of alloying elements in context to achieving 30GPa%

Carbon is key in achieving a high strength–ductility product [75, 74, 85]. Fig. 2.16 clearly shows that 30 GPa% is easily achievable in 0.6 wt% C composition than in 0.1 wt% C.

Duong *et al.* used steels with two different carbon contents (0.24 and 0.41 wt%) and showed that the strength–ductility product of the higher carbon variant can be above 30 GPa% (Fig. 2.17). The authors also conducted single (one step) and double (two step) isothermal heat treatments and concluded that higher carbon always performed better. However, a high carbon content is not conducive to weldability.
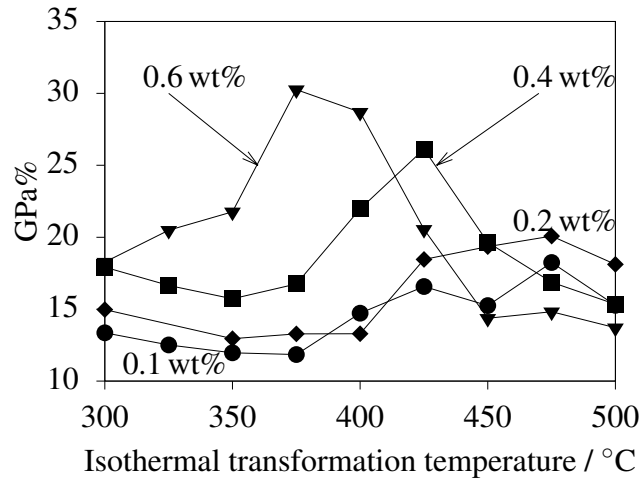
Figure 2.16 Carbon increment from 0.1 to 0.6 wt% enhancing GPa in a Fe–1.5Mn–1.5Si Type II TRIP–assisted steel for different isothermal bainitic transformation temperature [85].
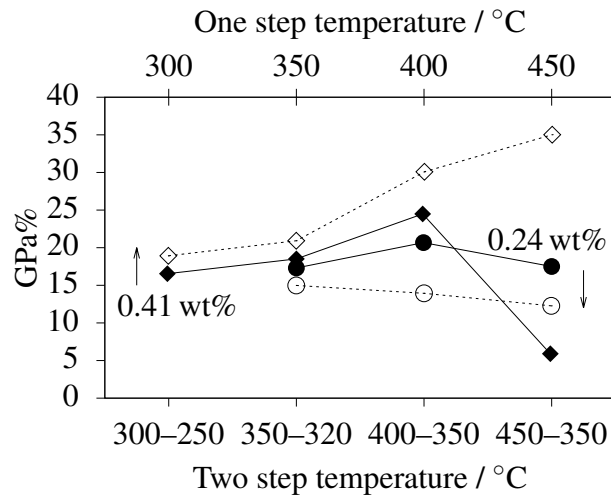
Figure 2.17 GPa% improvement for medium carbon TRIP-assisted steel with two step heat treatment. Low carbon variant showing deterioration in properties. Solid and open points denote single step and two step heat treatments respectively. The circle and diamond points represent low carbon (0.24 wt%) and medium carbon (0.41 wt%) compositions respectively [74]. The lower and upper X–axis represents the temperature of double and single isothermal heat treatments respectively.

Sakura *et al.* used a 0.2 wt% carbon steel with varying Mn and Si content [22], with both solutes increasing the strength–ductility product at 400 °C and 425 °C respectively as shown in Figs. 2.18a and 2.18b. Mn enhanced the austenite volume fraction which is the primary reason for the improved GPa%, although c_γ^e is limited by the effect of Mn on the T_0 curve[1] (Fig. 2.19). Si on the contrary affected the GPa% by increasing the stability of retained austenite by suppressing carbide precipitation and improving c_γ^e.
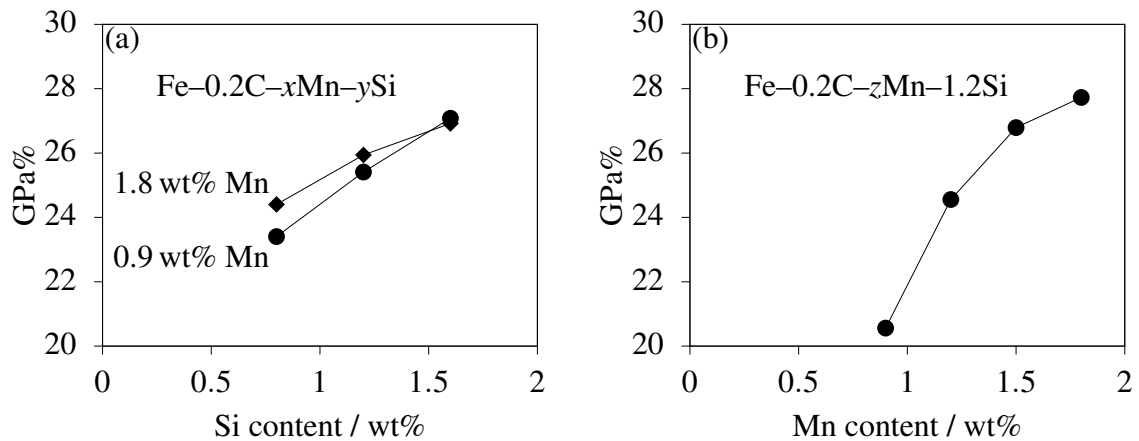
Figure 2.18 Si and Mn showing increasing trend in GPa% with increase in alloy content at 400 °C and 425 °C respectively [22].
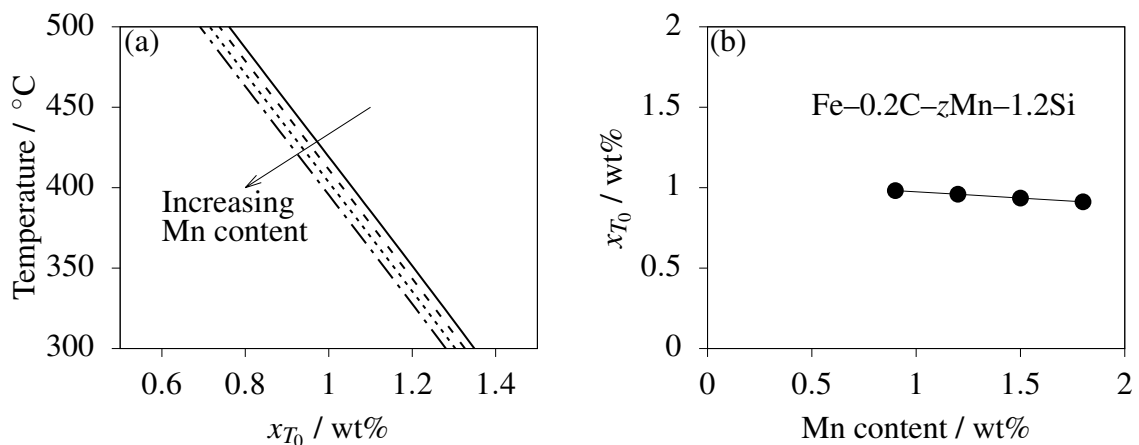
Figure 2.19 (a) T_0 curve for Fe–0.2C–1.2Si TRIP-assisted steel with varying Mn content and (b) x_{T_0} variation with respect to Mn content at 425 °C.

---

[1]T_0 curve is the locus of all carbon concentrations at which γ and α of identical chemical composition have the same Gibbs energy.

Phosphorus like silicon and aluminium inhibits cementite and is used in variety of TRIP–assisted steels to increase the strength of ferrite [86, 87]. Just 0.1 wt% of phosphorous increases the strength by 75 MPa [88]. Phosphorous is found to increase both GPa% and V_γ and it's effect is magnified manifolds as shown in Fig. 2.20 in the presence of Si [89, 90]. However, addition of P is restricted owing to the reduction in toughness and weldability due to grain boundary segregation.
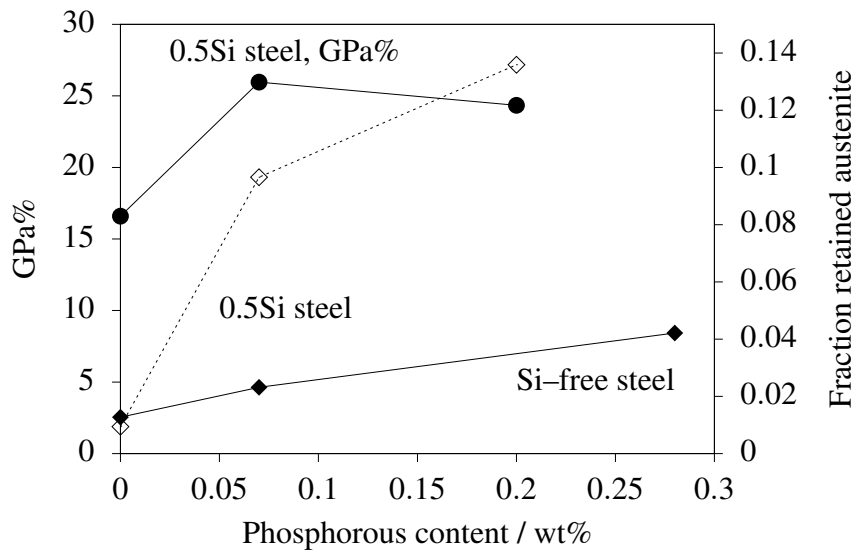
Figure 2.20 Increment in the austenite content for both Si–free and 0.5Si, low carbon TRIP–assisted steels by the addition of Phosphorous. GPa% showing an increasing trend with increase in P content. Solid circular dots represent the GPa% curve. Solid and open diamond shaped points denote fraction of retained austenite for Si–free and 0.5Si steel respectively [87].

Carbide forming microalloying elements (Ti, V and Nb) tend to reduce the stability of the carbon–depleted retained austenite and hence a reduction in GPa%. For example, Ti was found to deteriorate elongation from 29% to 22% due to the aforementioned reason in Fe–0.23C–1.65Mn–0.4Si–1.14Si (wt%) steels [91]. Many authors have tried to deduce the effect of Nb and the gist of improvement of GPa% has been plotted in Fig. 2.21 [92, 93].

Other alloying elements like nickel and copper have been known to positively impact ductility and increase GPa% [94–99] in TRIP–assisted steels. Kim and co–workers showed tramp quantities of Cu and Ni of 0.5 wt% and 0.4 wt% respectively (found in steels produced through electric arc furnace route) was enough to break the 30GPa% barrier in a Fe–0.15C–1.5Mn–1.5Si (wt%) steel [97, 94, 95]. On the contrary there exists contradicting results about impact of elements like chromium and molybdenum on improving ductility and GPa% [95, 98].
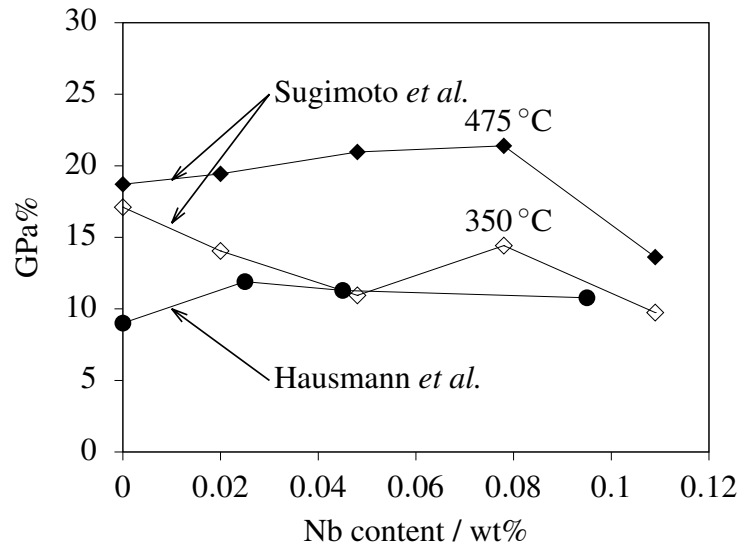
Figure 2.21 Nb content marginally improving the strength–ductility product for TRIP–assisted steels. Solid circular dots are due to Hausmann *et al.* [92] on Fe–0.17C–0.79Si–2.6(Mn,Cr,Mo) Type II alloys. Diamond shaped points are for the compositions of steels used by Sugimoto *et al.* [93]. The two temperatures correspond to the isothermal bainitic transformation temperatures.

2.4.2   Effect of microstructural attributes

Role of grain size

A finer austenite grain size suppresses the M_S temperature, an effect attributed to the sensitivity of the experiments, Fig. 2.22 [100]. Retained austenite size before and after tensile testing changes from $2\,\mu m$ to less than $0.7\,\mu m$ respectively, Fig. 2.23 [57], is consistent with this trend.

In the case of a fully austenitic steel, the strength increases with grain refinement consistent with the Hall–Petch relationship. However, a declining trend in elongation was observed with increasing austenitic grain size which further translated into deterioration of GPa%, Fig. 2.24 [101]. The observed peak in Fig. 2.25, where elongation of TRIP steels goes through a maximum when plotted against tensile test temperature, shifts to lower temperatures with decreasing grain size. The width of this peak also broadens suggesting improved ductility at finer austenite grain size. Others have tried to correlate grain size and ductility for TRIP steels but its effect has not been studied extensively [102, 103].
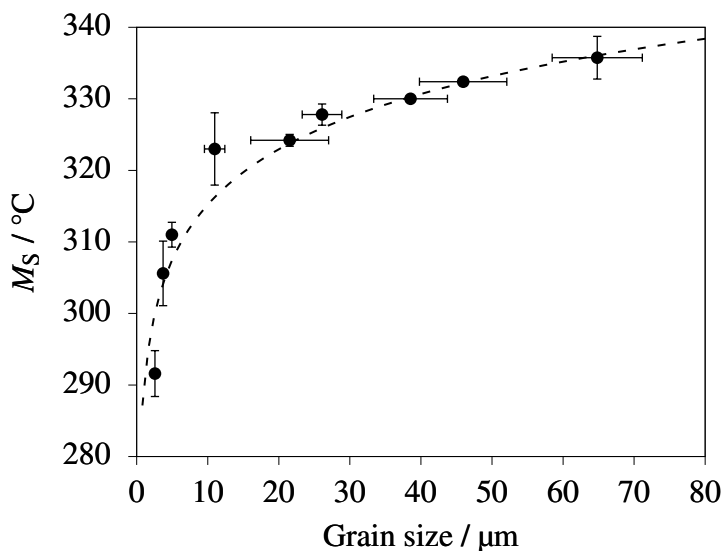
Figure 2.22 Measured variation of martensite–start temperature with respect to austenite grain size for Fe–0.13C–5Ni–2.27Mn (wt%) steel. The dashed line represents a fitting through a predictive model described by Yang *et al.* [100].
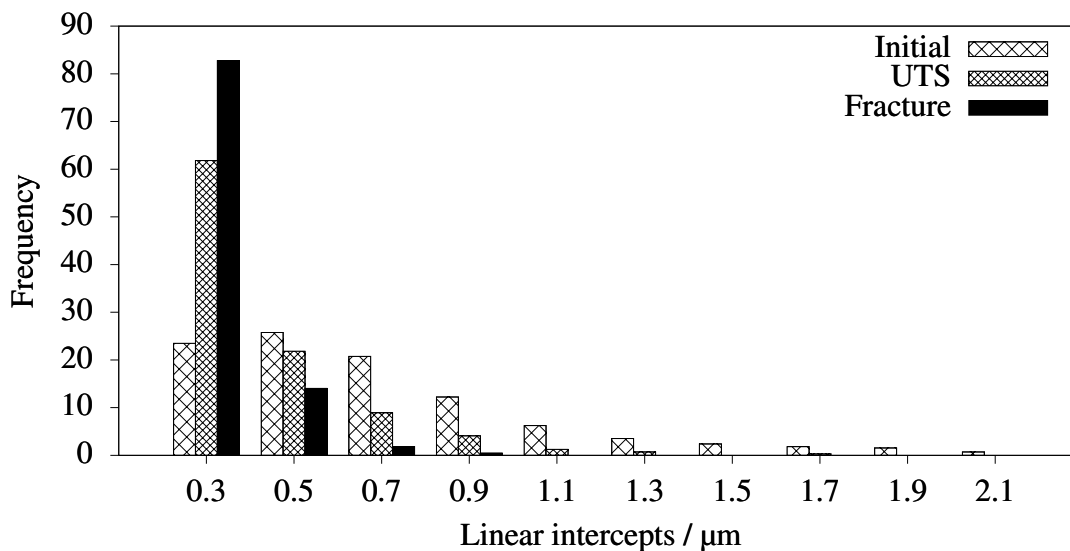
Figure 2.23 Linear intercepts (L_γ) of retained austenite measured using electron back–scattered diffraction at various stages of tensile test [57].
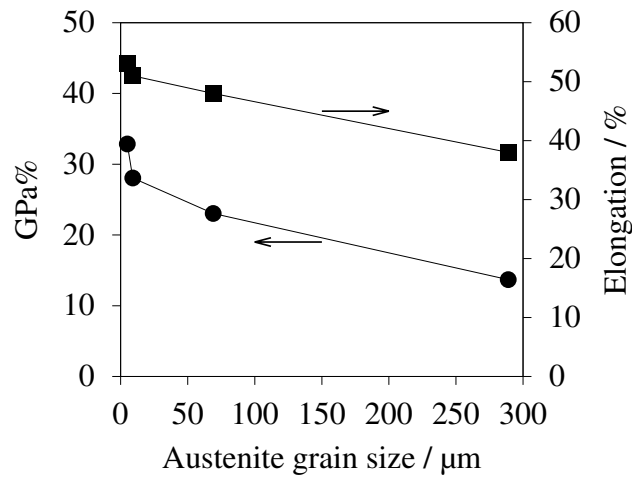
Figure 2.24 Effect of grain size on elongation and GPa% of Fe–30Ni–0.23C (wt%) TRIP steel, tensile tested at room temperature at a strain rate of 5.5×10^{-1} s^{-1} [101]. Square points represent the data for elongation and circle points denote the data for the strength–ductility product.
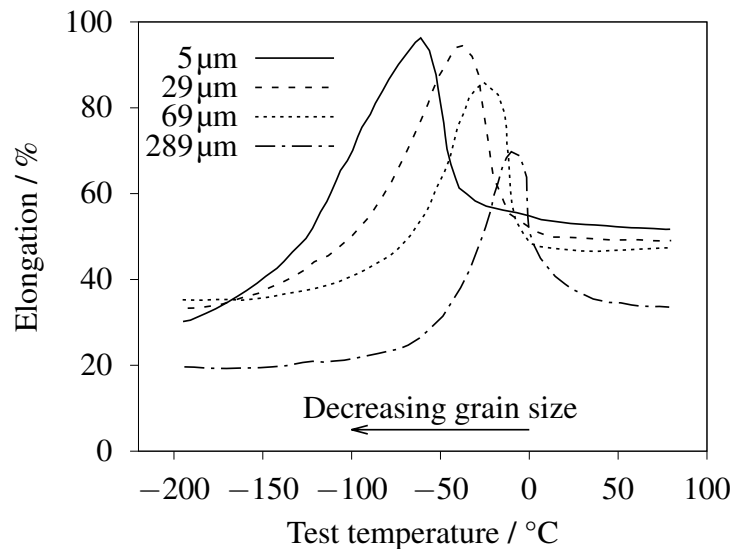
Figure 2.25 Effect of grain size on peak elongation observed for Fe–30Ni–0.23C (wt%) alloy at various tensile test temperatures at a $\dot{\varepsilon}= 5.5\times10^{-1}$ s^{-1} [101].

Role of morphology of austenite

Retained austenite in TRIP–assisted steels is generally present as, (i) blocks (γ_B) and (ii) films (γ_F) [104, 105]. The former refers to the austenite island between sheaves of bainite, Fig. 2.26a. The films are between the subunits within a sheaf of bainite, Fig. 2.26b [104].

The mechanical stability of blocky austenite is less than that of film austenite, partly because of its relatively low carbon concentration in γ_B [106–109]. Blocky austenite therefore tends to transform into martensite during the early stages of deformation. In some cases film austenite remains untransformed even at fracture, exemplifying its stability [57, 104, 105]. Carbon may be heterogeneously distributed in the austenite (Fig. 2.27), causing localised martensitic transformation within a single austenite grain [110]. Such inhomogeneity can also arise due to inadequate time available for the long–range diffusion of carbon, so that there will be a spectrum of M_S temperatures [111–114]. This has been demonstrated by deformation where the high carbon film austenite remains stable by applying 2% strain on Fe–0.22C–1.8Mn–1.4Si (wt%) quenched and partitioned steel, Fig. 2.28 [115].

(a)   (b)
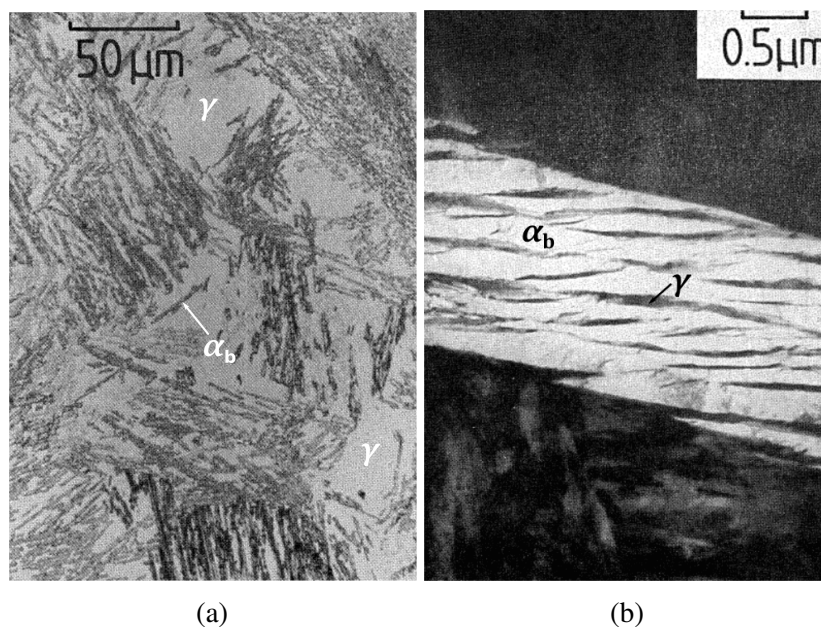
Figure 2.26 Isothermal transformation of Fe–0.43C–2.02Si–3Mn (wt%) at 360°C for 115 mins, (a) Optical micrograph showing presence of blocky austenite (b) Electron micrograph showing sheaf of bainite with lightly etched regions of bainitic subunits and darkly etched film austenite [104]. α_b–bainitic ferrite plates and γ refers to blocky or film austenite in (a) and (b) respectively.
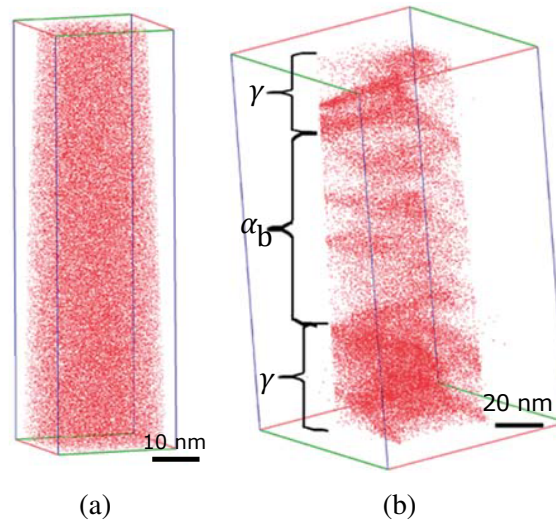
Figure 2.27 Atom probe tomography maps showing the carbon distribution in (a) blocky austenite and (b) film austenite (γ). Blocky austenite showing homogeneous distribution of carbon atoms and film austenite showing carbon enriched and depleted zones. [57]
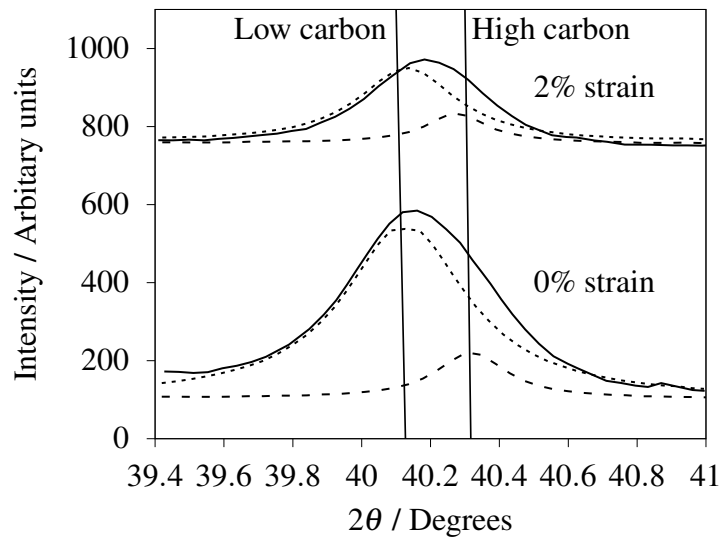
Figure 2.28 Deconvoluted (200) austenite peak into high and low carbon austenite peaks. Solid, dotted and dashed lines denote $(200)_\gamma$ peak, deconvoluted low and high carbon peaks respectively [115].

Tsuchida *et al.* evaluated the effect of austenite morphology (γ_B and γ_F) on the strength and ductility of Fe–0.3C–2Mn–1.5Si (wt%) TRIP-assisted steels [116]. Two different heat treatments were adopted to produce microstructures having similar austenite content but dissimilar austenite morphologies. γ_B and γ_F achieved significantly different strength–

ductility product at slow strain rate tensile tests as shown in Fig. 2.29. However, the difference diminished at strain rates greater than $10^{-2}\,\mathrm{s}^{-1}$. The c_γ^e reported for blocky and film morphologies are 1.11 and 1.19 wt% respectively, explaining the variation in GPa%. The caveat being that the microstructure containing blocky austenite has a ferrite–bainite matrix whereas, other microstructure is constituted of film austenite and bainite/martensite. Though the two microstructures are very different yet the UTS ($\sim$1000 MPa) obtained are similar.
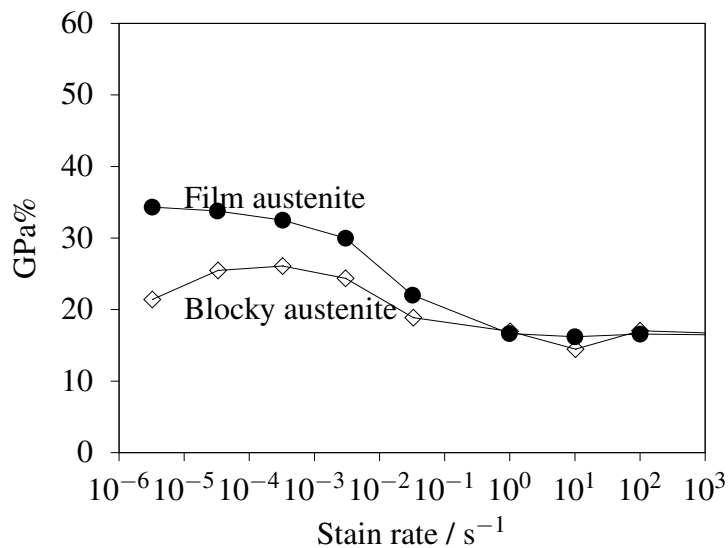
Figure 2.29 Blocky and film morphologies of austenite showing significantly different GPa% at slow strain rate tensile test as compared to higher strain rate for Fe–0.3C–2Mn–1.5Si (wt%) TRIP-assisted steels [116].

Role of neighbouring phases

Films of austenite that are surrounded by strong bainitic ferrite or martensite experience pressure, which opposes transformation [117, 118]. On the other hand, if strong phases are incapable of accommodating external stress, the direct transfer of load onto retained austenite increases the tendency for deformation induced transformation [119]. Tomita *et al.* concluded that stress localisation can cause high–carbon relatively stable film austenite to transform faster as compared to low–carbon blocky austenite [108].

2.4.3   Effect of deformation conditions

A glissile interface can be arrested in its motion by obstacles in the surrounding austenite. These obstacles effectively mechanically stabilise the transformation. Deformed austenite

containing a sufficiently large density of defects (dislocations and shear bands) becomes mechanically stabilised [57]. Although defects increase the nucleation site density and hence accelerate allotriomorphic ferrite formation, they can retard displacive transformations. It is said [57, 106] that the extent of deformation in the austenitic region, alters the bainitic ferrite structure and volume fraction of retained austenite, Fig 2.30. Deformation of austenite increases the possibility of the strain induced precipitation of alloy carbides in microalloyed TRIP–assisted steels, which strengthens the austenite with possible stabilization towards martensitic transformation, although the magnitude of this effect is not known. The precipitation of carbides naturally reduces the chemical stability of retained austenite.

(a) $\varepsilon_1 = 0.25$ and $\varepsilon_2 = 0.47$, $V_\gamma \approx 0\,\%$ (b) $\varepsilon_1 = 0.50$ and $\varepsilon_2 = 0.47$, $V_\gamma \approx 2\,\%$

(c) $\varepsilon_1 = 0.25$ and $\varepsilon_2 = 1.2$, $V_\gamma \approx 4\,\%$
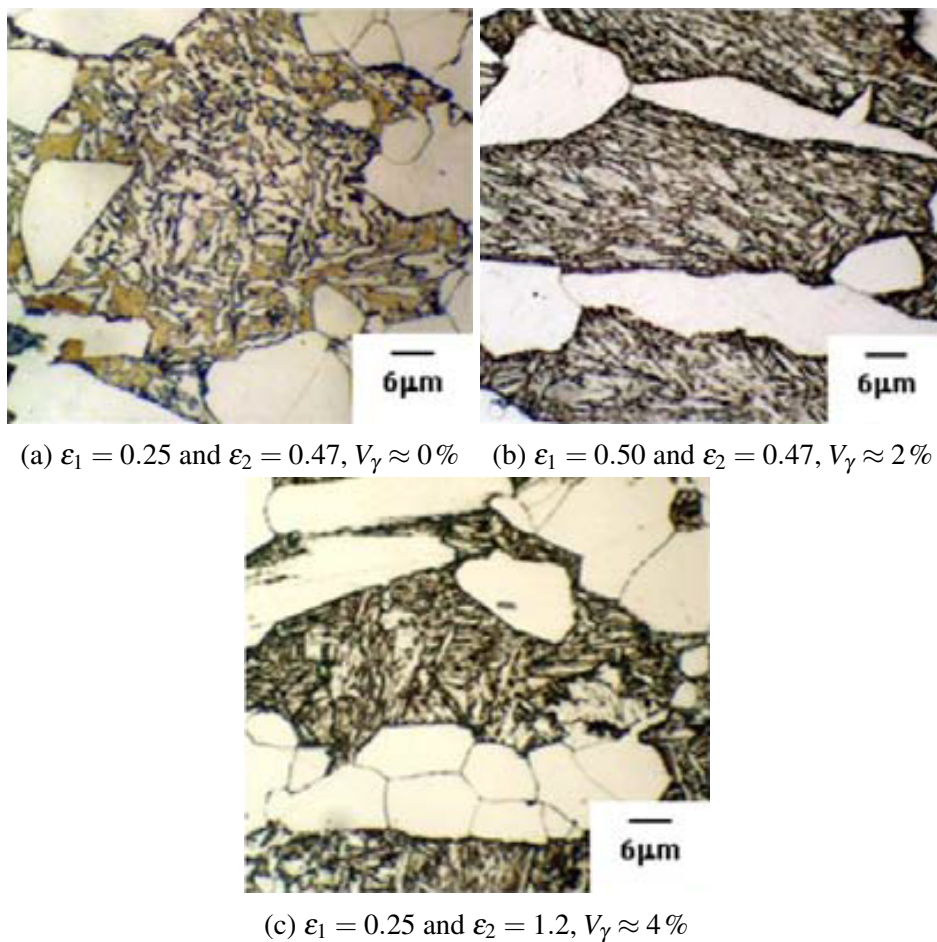
Figure 2.30 Microstructural variations due to different extent of deformations with strains of ε_1 and ε_2 for Fe–0.2C–1.7Mn–1.5Si (wt%) steel [57, 106]. ε_1 and ε_2 are the deformation strains given during finish rolling where the steel is fully austenitic in the recrystallized and non recrystallized regions respectively. Light etched regions of allotriomorphic ferrite and dark etched regions of bainitic ferrite and retained austenite. V_γ is the volume percent of the retained austenite in the microstructure measured at room temperature.

2.5 Mechanism of strengthening by bainite

Bainite is similar to martensite, but forms at a higher temperature where, the diffusion of carbon occurs subsequent to growth. Thus, bainite is observed in two different morphologies depending upon the location of carbon in the form of carbides. If the cementite precipitates between the ferrite plates the resultant microstructure is labelled upper bainite. However, if cementite also precipitates within the ferrite plates the structure is designated lower bainite, Fig. 2.31. There are two school of thoughts explaining the mechanism of bainite formation: (i) diffusional describing the growth of bainite by the propagation of ledges [120–122] and (ii) displacive or diffusionless mechanism [123, 124, 122].
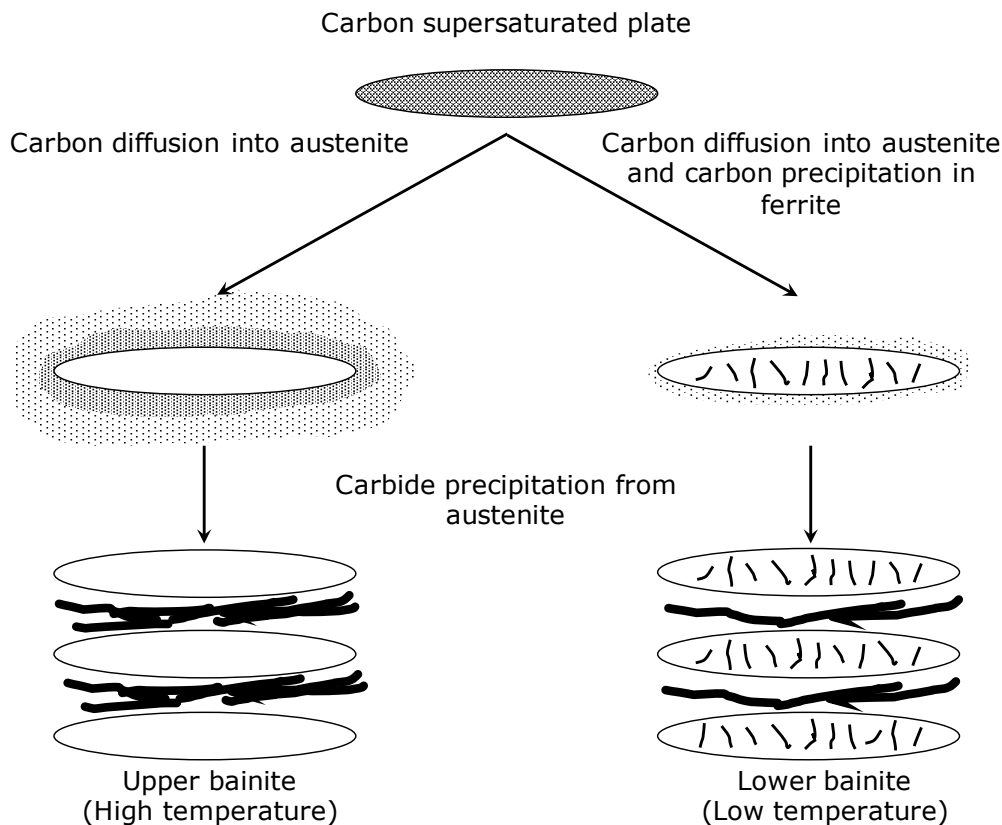
Figure 2.31 Schematic of upper bainite and lower bainite reaction mechanism [17].

There is a shape deformation when bainite forms and the formation of α_b stops when the carbon content of the residual γ reaches the T_0 (strictly $T_0^{'}$) limit. T_0 and $T_0^{'}$ compositions are the points at which ferrite and austenite of identical composition have the same chemical free energies, without and with a stored energy of $400\,J\,mol^{-1}$ respectively, Fig. 2.32. Diffusionless transformation cannot be sustained above T_0. The transition between upper and

lower bainite occurs over a narrow range of temperature and can be explained by the Matas and Hehemann model [17, 125]. This model proposes that the formation of upper bainite or lower bainite or both is driven by the competition between the rate of carbide precipitation in ferrite and speed of carbon partitioning from supersaturated ferrite to austenite [125]. If t_d is the time required to decarburise ferrite and t_θ is the time required for detectable cementite precipitation, then $t_d < t_\theta$ is the condition for formation of upper bainite and vice versa [125].
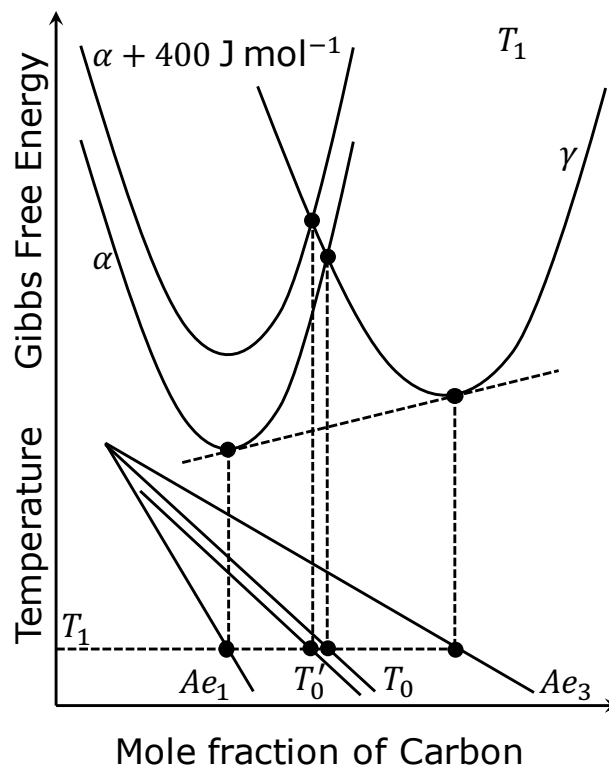
Figure 2.32 Schematic of T_0 and T_0' construction on Fe–C phase diagram [17]. Ae_1 is the temperature separating the $\alpha + \gamma$ and α phase fields for an alloy. Ae_3 is the temperature separating the $\alpha + \gamma$ and γ phase fields for an alloy.

The bainite–start temperature is that at which the phase can nucleate and then grow without a change in composition. The nucleus of bainite and Widmanstätten ferrite is the same but its evolution into either of the two phases is dependent upon the conditions for growth. T_h is the temperature marked by the characteristic flat top in the lower C–curve of a TTT diagram as shown in Fig. 2.33. Thus, if diffusionless growth cannot be sustained below T_h, then the nucleus grows into Widmanstätten ferrite and corresponding T_h temperature is known as the Widmanstätten ferrite start temperature (W_S). However, at a larger undercooling where driving force is sufficient to sustain diffusionless growth below T_h bainite forms with

$T_{\mathrm{h}} = B_{\mathrm{S}}$. The conditions below the T_0' temperature for bainite to form are:

$$\Delta G^{\gamma\alpha} < -G_{\mathrm{SB}} \tag{2.7}$$

$$\Delta G_{\mathrm{m}} < G_{\mathrm{N}} \tag{2.8}$$

where, G_{SB} is the stored energy of bainite of 400 J mol^{-1} and G_{N} is the universal nucleation function, defining the minimum driving force necessary for perceivable nucleation rate of Widmanstätten ferrite or bainite given by [126–128]:

$$G_{\mathrm{N}} = 3.637 \pm 0.2 \times (T - 273.18) - 2540 \pm 120 \qquad \mathrm{J/mol} \tag{2.9}$$
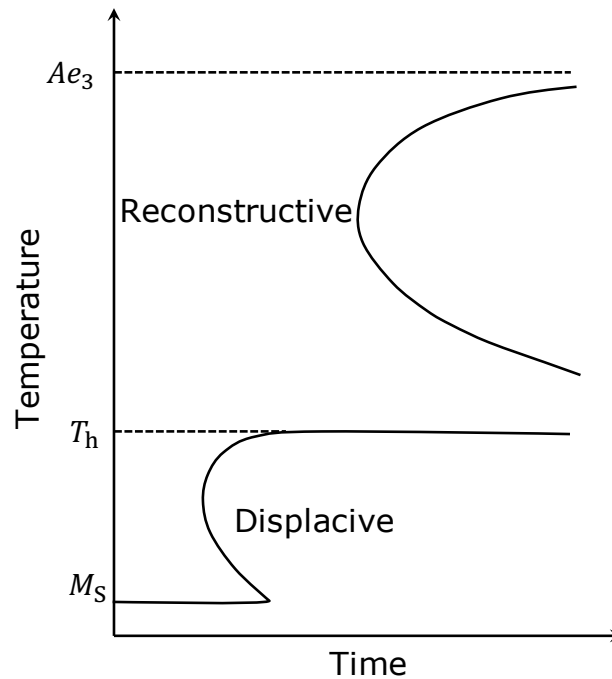
Figure 2.33 Schematic of TTT diagram depicting the separate C–curves for reconstructive and displacive transformation and the T_{h} temperature [17].

2.5.1 Mechanical properties of bainitic microstructures

Strength of bainite

The strength can be factorised into contributions from substitutional solid solution strengthening, interstitial strengthening due to carbon, dislocation strengthening, strengthening from

carbide particles and plate size effects. The empirical relationship for determining the strength of bainite taking these factors into consideration is [129, 17]:

$$\sigma = \sigma_{Fe} + \sum_i \sigma_{SS}^i + \sigma_C + k_\varepsilon (\overline{L}_3)^{-1} + k_P \Delta^{-1} + C_{10} \rho_d^{0.5} \qquad (2.10)$$

where, σ_{Fe} is the intrinsic strength of pure annealed iron, σ_{SS}^i is the solid solution strengthening due to substitutional element i, $\sigma_C = 1722.5 c_\alpha^{e\,1/2}$ is the strengthening due to carbon in bainitic ferrite denoted by c_α^e (wt%) [130, 131], $k_\varepsilon = 115$ MPa m, $\overline{L}_3$ is the measure of ferrite plate size in µm, $k_P = 0.52 V_\theta$ MPa m and depends upon the volume fraction of cementite V_θ, Δ is the inter–particle spacing of cementite, $C_{10} = 0.38 \mu b$ where μ is the shear modulus and b is the magnitude of the Burgers vector, ρ_d is the dislocation density in m^{-2}. The dislocation density at temperature T, can further be estimated empirically [125, 17],

$$\log(\rho_d) = 9.2840 + \frac{6880.73}{T} + \frac{1780360}{T^2} \qquad (2.11)$$

It is evident from Equation 2.10 that the carbon content and the plate size of bainitic ferrite have a profound effect on the strength of bainite. The carbon concentration in bainitic ferrite is assumed to $\simeq 0.03$ wt% after complete decarburisation, except when the plates form at a very low temperature. Hulme–Smith *et al.*, through synchrotron X–ray analysis of nanostructured bainite concluded that the carbon concentration retained in α_b can be as high as 0.16 wt% [132, 133]. This value is evaluated from the c/a ratio of a tetragonal unit cell and is much greater than the concentration expected from equilibrium. The results are consistent with the atom probe experiments showing excess carbon concentrations in low temperature bainitic ferrite [111, 134, 79], which enhances strength. The effective grain size of a bainitic plate is twice the thickness [135], and hence contributes significantly to the strength [136]. Other sources of strengthening include dislocations and precipitates [129].

Ductility of bainite

Low–carbon bainitic steels exhibit higher elongation than the high–carbon variants, when compared at similar strength levels [137]. This is because carbides initiate voids, so few and widely spaced particles are conducive to greater ductility [104, 105]. In carbide–free TRIP–assisted steels the voids initiate at the martensitic region induced by deformation [138]. Ductility will be discussed in greater depth later in this chapter.

2.6 Other aspects

2.6.1 Weldability

Techniques such as resistance spot welding, laser welding and arc welding are essential in engineering applications. However, the localised heat input creates a heat–affected zone with compromised properties and gradients of structure. Weldability is quantified by the "carbon equivalent" which is a measure of the hardenability of the steel. The hardness of the welded joints in the case of TRIP–assisted steels tend to increase at the fusion zone. However, the unmelted heat–affected zone which is intercritically annealed, softens [139]. A variation in grain size and microstructure is also observed between the fusion and the heat affected zone. The resulting differences induce residual stresses and generate heterogeneity during deformation at the welded joint, thus limiting the ductility. For example, nanostructured bainite [140, 141] which has 1 wt% carbon forms coarse untempered martensite during welding, thus cracks spontaneously [17]. The carbon equivalent is defined empirically as: where $w_c > 0.18$ wt% [142, 17],

$$CE = w_C + \frac{w_{Mn} + w_{Si}}{6} + \frac{w_{Ni} + w_{Cu}}{15} + \frac{w_{Cr} + w_{Mo} + w_V}{5} \qquad (2.12)$$

where $w_c \leq 0.18$ wt% [142, 17],

$$CE = w_C + \frac{w_{Si}}{30} + \frac{w_{Mn} + w_{Cu} + w_{Cr}}{20} + \frac{w_{Ni}}{60} + \frac{w_{Mo}}{15} + \frac{w_V}{10} + 5w_B \qquad (2.13)$$

Shi and Westgate improved the spot weldability of Fe–0.31C–1.54Mn–0.29Si–1.01Al (wt%) Type I TRIP–assisted steel by post–welding heat treatment cycles to reduce the hardness of the weld from 500 HV_1 to 400 HV_1 [143]. The base metal hardness being 240 HV_1 and the CE = 0.57 wt%. With 25 cycles of tempering heat treatments at 4.9 kA current the weld showed full plug failure[2] without any cracks as shown in Fig. 2.34. The plug diameter also increased and approached closer to the weld diameter with an increase in number of cycles of tempering heat treatment. Similar optimization of spot weld parameters with pre and post heat treatment cycle carried out by Tosal–Martinez *et al.* on Fe–0.3C–1.5Mn–0.3Si–1.2Al (wt%) TRIP–assisted steel resulted in sound welds without any cracks. Fig. 2.35b shows no crack formation after the optimised spot welding due to a reduction in hardness of the weld achieved because of the pre and post heat treatment. Also the fracture

---

[2]A failure occurring in spot welded sheets where, metal pulled from one sheet remaining attached to the surface of the other after testing.

surface showed significant improvement due to a change in failure mode from brittle to
ductile as shown in Fig. 2.36.
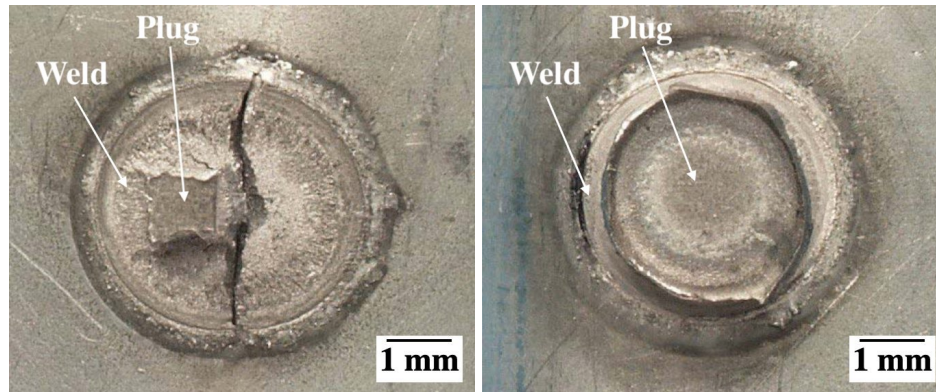
(a) Without heat treatment.   (b) 25 cycles of heat treatment.

Figure 2.34 Spot weld (a) without (b) with tempering heat treatment showing the plug
diameter. Cracking is observed in the spot weld without tempering heat treatment after shear
strength test [143].
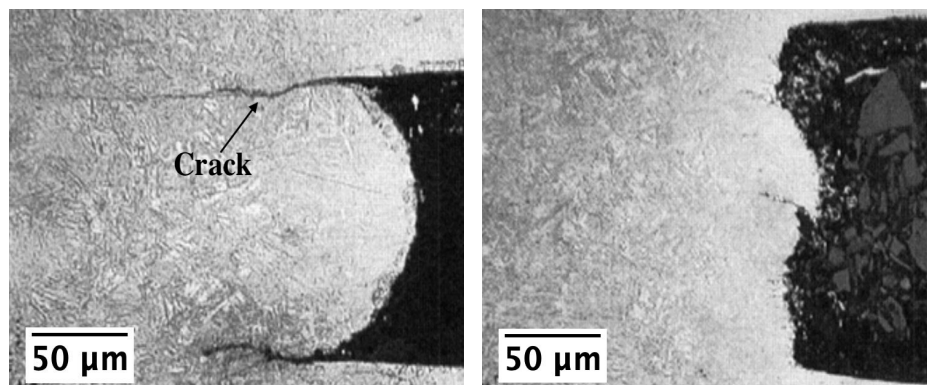
(a) Standard spot welding   (b) Optimised spot welding.

Figure 2.35 No cracks observed in optimised spot welding used to join Fe–0.3C–1.5Mn–
0.3Si–1.2Al (wt%) Type I TRIP–assisted steel [144, 145].
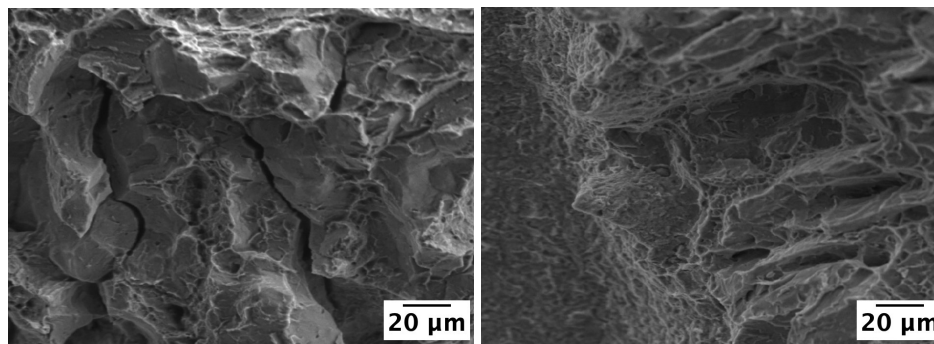
(a) Cleavage or brittle fracture.   (b) Dimples showing ductile failure.

Figure 2.36 Fracture surface after cross tension test of weld joints showing brittle and ductile failure in standard and optimised spot welding respectively. [144, 145]

2.6.2   Formability

There are various parameters that define formability, including:

1. Stretch formability is determined by deforming a rigidly fastened sheet to failure using a hemispherical dome [146–148]. The maximum load at fracture and the maximum stretch height at the peak load are measured and used to construct a forming limit diagram [149]. Fig. 2.37 shows the steel sheet after the limiting dome height test [150]. Since the formability is closely linked to the elongation of the steel, thus the parameters affecting ductility or GPa% affects the maximum stretch height. Lee *et al.* evaluated the formability of Fe–0.15C–1.5Mn–1.5Si–0.5Cu–(Ni,Cr) (wt%) Type I TRIP–assisted steel and found a strong correlation between GPa% and the maximum stretch height of the dome (Fig. 2.38) [151]. The forming limit diagram[3] of the same set of steels showed an identical trend with GPa% i.e. with increasing GPa% the major strain in the forming limit diagram increased.

2. Stretch flangeability is assessed by expanding a 10 mm diameter hole at the centre of a 100 mm square steel [152, 153]. A conical punch expands the hole until a crack develops on the surface. The initial diameter (D_0) and the final diameter (D_h) are measured, with ($D_h - D_0$)/D_0 being the hole expansion ratio. Single phase microstructures give a better hole expansion ratio because strain incompatibles are avoided. Sugimoto *et al.* showed a strong correlation between strength–stretch flangeability product and c_γ^e as shown in Fig. 2.40, however no correlation was found between the former and

---

[3]A graphical description of major and minor strains obtained from the measurements of the deformed circular grids showing material failure, such as a dome test.
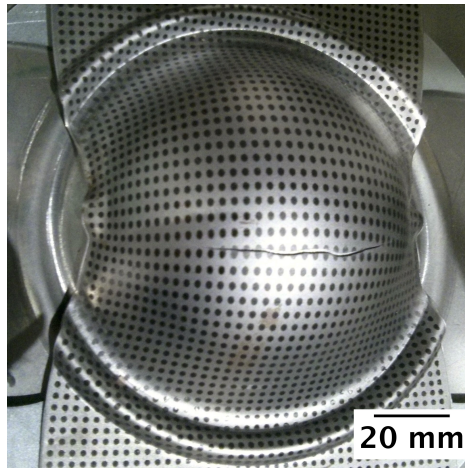
Figure 2.37 The deformed steel sheet following the limiting dome height test [150].
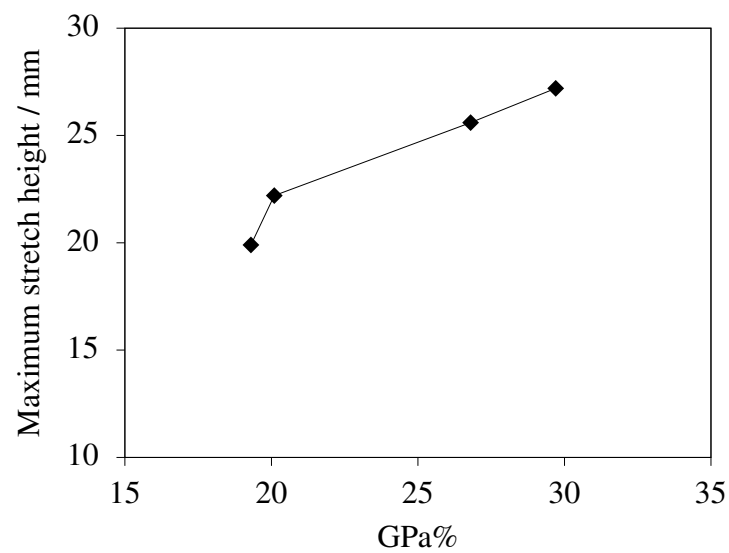
Figure 2.38 Maximum stretch height during a stretch formability test increases with increasing strength–ductility product in TRIP–assisted steels [151].

austenite content. They also showed that uniform bainitic plates and presence of a large amount of film austenite in Fe–0.2C–1.51Mn–1.51Si (wt%) Type II TRIP–assisted steel ensured a superior hole expansion ratio [154]. This also restricted the surface damage and allowed severe plastic flow during the hole punching operation.
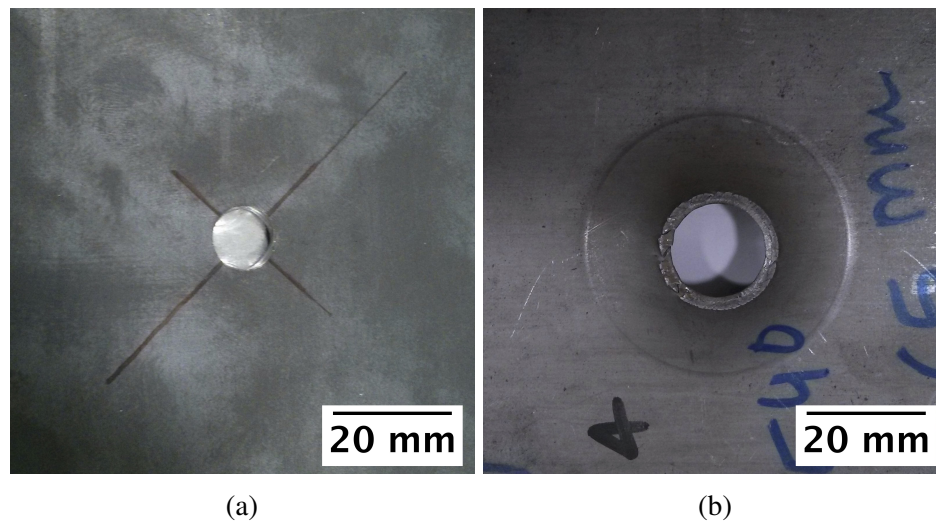
Figure 2.39 Steel sheets showing the (a) initial and (b) final condition before and after the hole expansion test [155, 156].
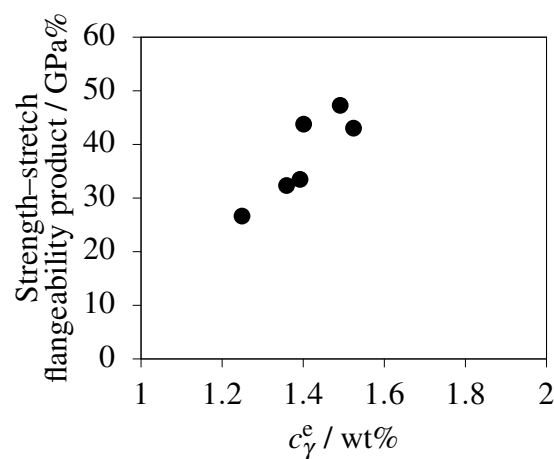
Figure 2.40 Stretch flangeability (hole expansion ratio) and tensile strength product expressed as GPa% plotted against carbon in retained austenite showing strong correlation [154].

2.7   Summary

The important findings of this review are:

1. There exists an optimum carbon content in retained austenite for maximising the elongation at room temperature and enhancing GPa%.

2. The strength–ductility product can be enhanced by increasing the volume fraction of austenite, with stability expressed as the free energy of transformation to martensite ($|\Delta G^{\gamma\alpha}|$) being less than $2500\,\mathrm{J\,mol^{-1}}$.

3. A small prior austenite grain size is important to obtain better elongation and GPa%, thus thermo–mechanical deformation along with microalloying seems a possible route to produce fine grained austenite. The loss of stability and reduction in volume fraction of austenite due to loss of carbon caused by carbide precipitation by certain microalloying elements is an important aspect to consider during alloy design. Bulk carbon content and carbon equivalent should be restricted to $0.25\,\mathrm{wt\%}$ and $0.6\,\mathrm{wt\%}$ respectively.

4. Eliminating blocky austenite or reducing its volume fraction improves ductility by ensuring prolonged strain hardening and results in higher strength-ductility product.

5. Spot welding parameters incorporating pre– and post–heat treatment schedules improves the soundness of the welds in $0.3\,\mathrm{wt\%}$ carbon TRIP–assisted steels. Thus achieving good weldability while keeping the bulk carbon content and CE below $0.25\,\mathrm{wt\%}$ and $0.6\,\mathrm{wt\%}$ seems plausible.

6. Increasing the GPa% enhances the stretch formability of the steel which can lead to achieving overall superior properties. To improve the stretch flangeability of the steel, the carbon content of the retained austenite should be increased and uniform bainitic structure with higher volume fraction of film austenite should be achieved.

Chapter 3

Experimental Procedure

3.1   Alloys

A commercially available steel from Tata Steel formed the basis of development of four different alloys, which were manufactured at OCAS, Belgium. The chemical compositions of the all the steels were determined using spark optical emission spectroscopy for metallic elements and combustion analysis for (C, N and O). The commercial alloy was a 25 kg cast, made using vacuum induction melting, yielding an ingot of size 120 mm×100 mm×250 mm. The ingot was then heated to 1250 °C and forged in to blocks of thickness about 25 mm. A part of each block was used to prepare cylindrical dilatometer samples 4 mm diameter and 10 mm long. The remainder was hot rolled after soaking at 1250 °C for an hour. The finish–rolling temperature was maintained in the range 850–930 °C. The rolled plate was subsequently air cooled and isothermally transformed at 400 °C in a salt bath for 1 h, followed by air cooling to room temperature. All of this processing was done at Tata Steel.

The remaining four steel melts were manufactured using a vacuum induction furnace at OCAS, Belgium. Each 100 kg ingot was reduced to about 50 kg after removal of porous regions. The cast was then cut into 4 blocks of 125 mm×125 mm×95 mm and each block hot rolled to 30 mm thick plate. Similar cylidrical samples were cut for dilatometric assessment. The chemical compositions of the commercial steel from Tata Steel and the four designed alloys are given in Table. 3.1.

Table 3.1 Chemical compositions of commercial steel from Tata Steel and the four designed alloys A, B, C and D.

Steel	Chemical composition / wt%											
	C	Si	Mn	Cr	Ni	Mo	Nb	Al	P	S	N	Cu
Tata Steel	0.22	1.01	1.48	0.95	–	0.10	0.035	0.143	0.024	0.020	0.0119	–
Alloy A	0.21	1.91	1.97	0.54	–	0.52	0.025	0.04	0.0023	0.0007	0.0049	–
Alloy B	0.23	1.39	1.35	0.29	1.65	0.45	0.003	0.03	0.0100	0.0100	0.0066	0.15
Alloy C	0.22	1.95	1.97	0.54	–	0.47	–	0.04	0.0026	0.001	0.0050	–
Alloy D	0.41	1.96	1.52	1.01	–	0.36	0.023	0.03	0.0037	0.0026	0.0040	–

3.2 Microstructural characterization

3.2.1 Sample preparation

Cross–sectional and longitudinal cuts were made on samples using an ATM Brilliant 220 cutting machine. Samples were hot-mounted in conductive Bakelite and prepared for metal-lographic study by grinding using silicon carbide emery papers (800–grade to 4000–grade), followed by polishing with 6–0.25 μm paste on a polishing cloth. Samples which were sensitive to heat and where hot mounting was not feasible, were mounted using Tri–Hard cold mount. Samples were etched with 2% nital (2% nitric acid, 98% methanol by volume) to reveal the microstructure. Coloured etching was achieved after etching a pre-etched sample with sodium metabisulphite solution (8 g per 100 ml water).

Unmounted samples were prepared in a similar fashion and final–polished with 0.25 μm colloidal silica on a polishing cloth, before ultrasonically cleaning with VLSI grade ace-tone/ethanol and then used for electron back-scattered diffraction study. Samples sensitive to mechanical polishing owing to the stresses induced during preparation, were electrolytically polished.

Electropolishing

Electrolyte (5% perchloric acid, 25% glycerol and 70% ethanol solution by volume) was maintained at a temperature less than 10 °C, achieved in an ice bath. A closed circuit potential of 10 V was used for 2 min to obtain a shiny surface, free from any scratches. A voltage–current (V–I) curve was obtained to determine the range of voltages over which polishing occurs for the two alloys presented in this work. The voltage was increased from 0 to 30 V in 0.5 V increments and the current was recorded, Fig 3.1. At each voltage step, the current was allowed to stabilise.
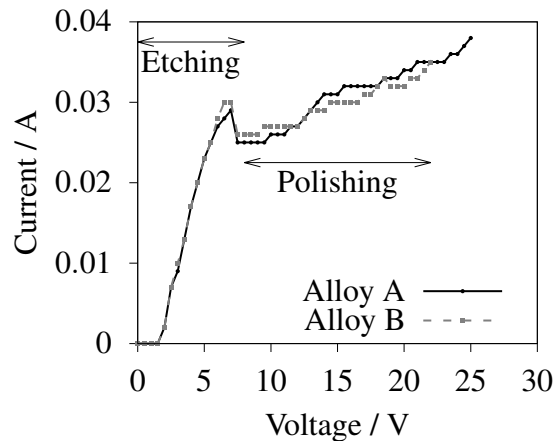
Figure 3.1 V–I calibration curve indicating the regions where etching and polishing occurs for the two alloys A and B presented in this thesis. The microstructure were predominantly bainite and retained austenite.

3.2.2 Optical microscopy

Optical microscopy was done at magnifications in the range 50–500×, using Olympus BH and Leica Microsystems DM2500M upright light microscopes. Image recording was done using a DFC295 camera attached to both the microscopes. Leica Application Suite (version 8.1) software and Fiji–ImageJ were used for digital improvements (like cropping, scale bar addition, brightness and contrast adjustments) and quantitative analysis (grain size measurements and blocky retained austenite size determination).

3.2.3 Scanning electron microscopy

Scanning electron microscopy (SEM) was carried out using Nova NanoSEM 450 (Fei Instruments) and Gemini 300 (Zeiss) field-emission gun (FEG) scanning electron microscopes. The microscopes were operated in the back scattered and secondary electron modes to image the specimen. The voltage of operation varied from 5–20 kV depending upon the requirements. The aperture size (spot size) and the working distance were adjusted appropriately to achieve the best resolution images. The Nova NanoSEM is equipped with an Oxford Instruments solid state detector for energy dispersive X–ray spectroscopy (EDS), to characterise the inclusions/precipitates on the fracture surface of the tensile tested samples.

3.2.4   Electron back scattered diffraction (EBSD)

The samples were tilted at 70° to the electron beam which was accelerated at 20 kV in the Gemini 300 scanning electron microscope by Zeiss. The aperture size was fixed at 120 μm and was operated at high current mode. The working distance was maintained between 15–20 mm. The symmetry EBSD detector by Oxford instruments was used at an insertion distance of 150 mm to capture the Kikuchi patterns, which were later indexed though the Aztec software. Post processing of the EBSD data was done using Channel 5 software by Oxford Instruments or MATLAB–MTEX software.

3.2.5   Atomic force microscopy (AFM)

A Dimension Icon atomic force microscope by Brüker was used in tapping mode to recreate a 3–dimensional computerised image of the surface topology. Tapping mode uses a silicon etched nanometre scale tip, vibrating at a frequency of 300 kHz with a spring constant of 40 N m^{-1} (RTESPA–300 tip). The measurement was done at a scan rate of 50 Hz with a image size of 512 pixels. For higher resolution scans, the image size can be increased greater than 512 pixels, but it significantly increases the acquisition time.

3.2.6   X–ray diffraction

X–ray diffraction measurements were done in a Brüker Davinci D8 diffractometer. Samples for X–ray diffraction were prepared metallographically with repeated etching/polishing cycles to obtain a strain–free surface. In some cases, where sample dimensions were small, electropolishing was used. The samples were mounted on silicon wafers of known crystal orientation, which were in–turn affixed to the sample holder of the X–ray diffractometer. Measurements were done for 2θ from 35° to 120° using a divergent beam with constant irradiated/exposure length[3] on the specimen to maximise signal to noise ratio. Cu K_α radiation at 40 kV voltage and 40 mA current was used. The step size and dwell time were 0.01° and 5 s, respectively. K_β radiation was absorbed using a 0.012 mm thick nickel–filter. The samples were rotated (30 rotations per minute) to minimize texture effects. A Lynxeye XE position sensitive detector was used to acquire the diffraction data which possesses good energy resolution, and eliminates fluorescence. Raw data were then analysed using HighScore+ or MAUD software [157, 158]. The Rietveld refinement was used to estimate

---

[3]The illumination length on the sample is kept constant by increasing the opening of the slits with increasing 2θ.

the phase fraction by the integrated intensity method and the lattice parameters were obtained from the peak positions [159]. In cases where samples were textured, the method proposed by Dickson [160] was to use to determine the phase fraction.

Analysis of X–ray diffraction data

Determination of the volume fraction of austenite and ferrite in an untextured sample was quite straight forward and was done by Rietveld refinement. However, usage of Rietveld refinement on textured samples was trickier owing to the strong favoured orientation. Thus the method adopted by Dickson [160] was used in such cases, which dealt with the direct comparison method extended to correct for preferred orientation effects.

The integrated intensities of 4 reflections from ferrite and austenite were considered for the determination of the volume fraction. These reflections were $(111)_\gamma$, $(200)_\gamma$, $(220)_\gamma$ and $(311)_\gamma$ for austenite and $(110)_\alpha$, $(200)_\alpha$, $(211)_\alpha$ and $(310)_\alpha$ for ferrite. Dickson proposed that the volume fraction of austenite and ferrite can be given by:

$$\frac{V_\gamma}{V_\alpha} = \frac{\frac{1}{n_\gamma} \sum_0^{n_\gamma} \left(\frac{I_\gamma}{R_\gamma} \right)}{\frac{1}{n_\alpha} \sum_0^{n_\alpha} \left(\frac{I_\alpha}{R_\alpha} \right)} \tag{3.1}$$

where, V_γ is the volume fraction of austenite, V_α is the volume fraction of ferrite, $n_\gamma = n_\alpha = 4$ (number of reflections of austenite and ferrite taken into consideration), I_α and I_γ are the integrated intensities of each reflections of austenite and ferrite, R is the factor that is dependent on θ.

Also, it is known that the summation of all the phases in the microstructure is unity:

$$V_\gamma + V_\alpha = 1 \tag{3.2}$$

The integrated intensity was computed from the X–ray diffraction data using the HighScore+ software and profile fitting. Further I_{hkl} and R_{hkl} for the four reflections of austenite and ferrite were computed and then using Equations 3.1 and 3.2 the volume phase fraction was determined.

The nature of the peaks were assumed to be Pseudo–Voigt profile. In some cases it was found that the peaks of austenite were not symmetrical, which could be attributed to a range of lattice parameters expected in the retained austenite due to the presence of blocky and film austenite. Thus to increase the goodness of fit of such asymmetrical peaks the austenite peaks were deconvoluted as shown in Fig. 3.2.
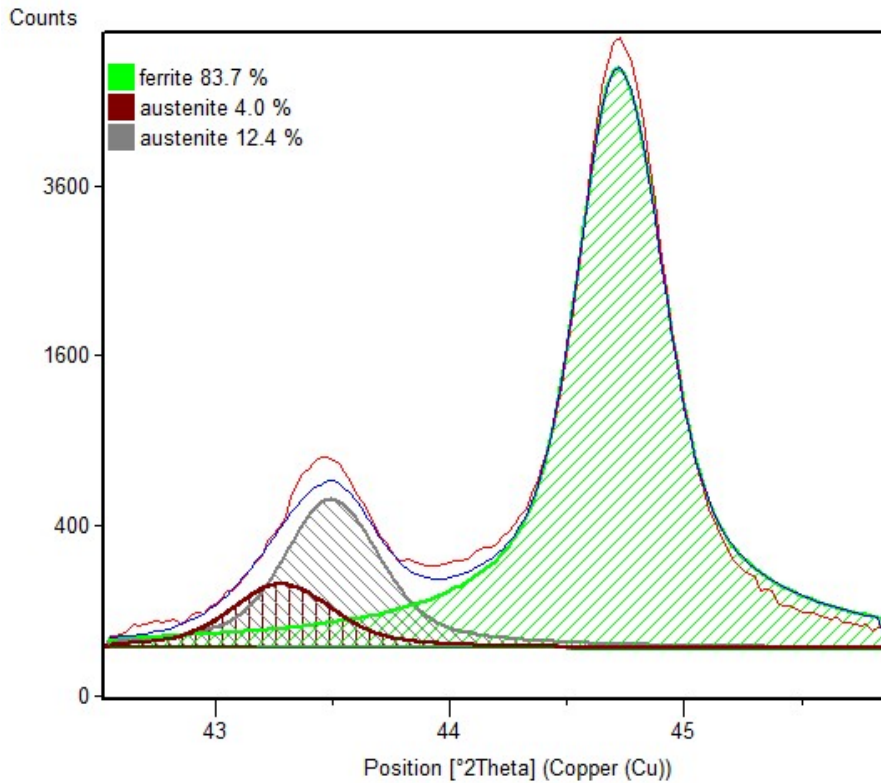
Figure 3.2 Snapshot of $(111)_\gamma$ and $(011)_\alpha$ peaks from HighScore+ software. The austenite peak is deconvoluted into two austenite peaks of high and low carbon content along with one single ferrite peak. The red curve is the raw data and the blue curve is the fitted profile.

3.3   Dilatometry

A Bähr dilatometer DIL805A/D was used for dilatometry experiments. Cylindrical samples of 10 mm long and two different diameters of 4 mm and 5 mm were used for quenching and deformation modes, respectively. These samples were prepared by electric discharge machining. R-type thermocouples were spot welded onto the sample, which was inductively heated in vacuum. The dimensional change in the transverse direction (diameter) of the sample during heating and cooling was measured by a laser with a precision of $\pm 1\,\mu m$. However, the length (longitudinal) strain was measured using the linear variable differential transducer connected to silica push rods. Continuous cooling experiments were performed using argon as the coolant, in order to determine the transition temperatures and continuous cooling diagrams. The quenching gas used for thermal grooving experiments for grain size

determination and surface relief experiments was helium, due to low contaminants present in the gas, thus helping in achieving a good surface finish. Deformation setup had a hydraulic attachment for the application of stress or strain imparted to the samples using a Si_3N_4 die. The load cell measures the applied load on the sample during axisymmetric compression.

3.4 Mechanical tests

3.4.1 Tensile Test

Dumbbell shaped tensile specimens in accordance to ASTM E8M standard with diameter of 6 mm and gauge length of 24 mm ($4\times$diameter) were made, Fig 3.3 [161]. The tests were carried out in a Instron 100 kN machine at a cross head speed of 0.24 mm/min, instrumented with a clip type extensometer. Tensile tests at 100 °C were carried out in the same tensile tester equipped with a movable split furnace and a k–type thermocouple.
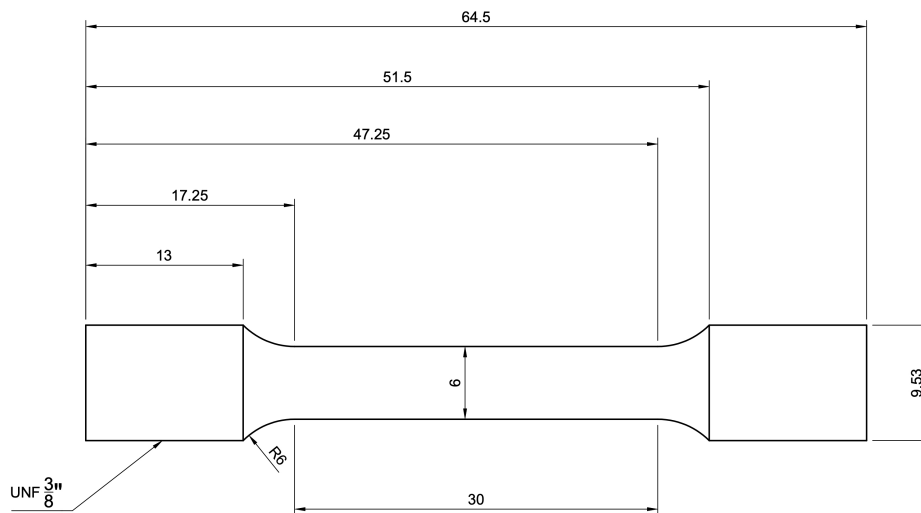
Figure 3.3 Engineering drawing of the tensile specimen according to the standard [161]. All dimensions are in mm and R6 denotes the fillet radius to be 6 mm. UNF 3/8" refers to threads at the grip to be of the unified national fine standard and diameter of 9.52 mm.

3.4.2 Hardness

Sample preparation for hardness measurements was similar to that of optical or SEM sample preparation. Bulk hardness was measured using a Qness Q60 Vickers hardness tester by applying 10 kg dead load. The dwell time for application of the load for a single indent was

10 s. The average of the two diagonal lengths made by the pyramidal indenter was measured optically and the hardness was estimated using equation:

$$\text{HV}_\text{L} = \frac{0.1891F}{d^2} \tag{3.3}$$

where, F is the applied load in newtons and d is the measured diagonal length of the indentation in mm. The subscript "L" denotes the load at which the measurement is done in kg. A gap equal to at least $2.5 \times d$ between two nearest indentations were maintained in order to avoid the increase in hardness due to the work-hardening of the deformed structure due to indentation. Microhardness was done using 300 g load on etched samples to correlate with the microstructural features.

Chapter 4

Predictive calculations

4.1 Estimation of ductility of TRIP steels

The kinetics of the deformation–induced transformation of austenite into martensite, coupled with percolation theory, are used to estimate the elongation of carbide–free bainitic steels that have a mixed microstructure of bainitic ferrite and carbon–enriched retained austenite. Experimental data from the literature have been collated and assessed to test the model. Data pertaining to an $\alpha_b + \alpha'$ microstructure were chosen for the analyses. The data where matching is found to be poor have been analysed further in order to understand any discrepancies.

4.1.1 Kinetics of deformation–induced transformation

The deformation–induced transformation of austenite can be expressed as a function of plastic strain (ε), with empirical constants obtained using experimental data [162–165, 75, 68, 166, 167]. Some of these empirical relationships have been derived for fully austenitic stainless steels [162–164] whereas others [165, 75, 68, 166, 167] are for TRIP–assisted steels, dependent on the initial volume fraction of austenite. Table 4.1 collates the variety of empirical relationships used to represent the decomposition of austenite under the influence of a combination of plastic strain and stress (the role of stress needed to deform the material is often ignored in the analysis of deformation–induced transformation).

The equation for decomposition of γ to α' derived by Sherif *et al.* [166] is more generic as it takes into account the chemical stability of retained austenite in the form of a chemical free energy change $\Delta G^{\alpha\gamma}$ and contains just one empirical constant that applies to all steels, as compared with those listed in Table 4.1. This is a modification of the model suggested by

Table 4.1 List of models for kinetics of deformation induced transformation of austenite into martensite. $V_{\alpha'}$ is the volume fraction of martensite. ε is the plastic strain due to deformation. V_{γ}^0 and V_{γ} are the fractions of retained austenite at zero and finite plastic strain respectively. M_d is the maximum temperature till which deformation–induced martensitic transformation of austenite is possible. σ_{YS} and σ_{flow} are the yield strength and the instantaneous plastic flow stress respectively.

Equation and Reference	Comments on the fitting constants
$V_{\alpha'} = 1 - \exp[-\beta\{1 - \exp(-\alpha\varepsilon)\}^n]$ [162]	α depends upon the stacking fault energy (SFE) β is the probability of shear band interaction generating α' embryo $n = 4.5$
$V_{\alpha'} = 1 - \exp[-k\varepsilon^Z]$ [163]	$k = 28$ $Z = 3.7$
$V_{\alpha'} = m\varepsilon^{\frac{1}{2}}$ [164]	$m \simeq \frac{M_d}{160}[\frac{M_d - T}{M_d}]\frac{M_d}{160}$
$V_{\alpha'} = A_1 \varepsilon^B V_{\gamma}^0$ [165]	A_1 is a constant $B = 3$ for stainless steel
$\frac{1}{V_{\gamma}} - \frac{1}{V_{\gamma}^0} = \frac{k_p}{p}\varepsilon^p$ [75]	$p = 3$ for austenitic stainless steel $p = 2$ for duplex stainless steel $p = 1$ for dual phase steel
$\ln(V_{\gamma}^0) - \ln(V_{\gamma}) = k\varepsilon$ [68]	k needs to be calculated for each steel
$\ln(V_{\gamma}^0) - \ln(V_{\gamma}) = k_1 \Delta G^{\alpha\gamma}\varepsilon$ [166]	$k_1 = 0.002017$ J^{-1} mol $\Delta G^{\alpha\gamma}$ is the driving force for γ to α' transformation
$\frac{V_{\gamma}}{V_{\gamma}^0} = \delta\exp(-\lambda(\frac{\sigma_{flow} - \sigma_{YS}}{\sigma_{YS}}))$ [167]	$\delta = 0.9 \pm 0.03$ $\lambda = 1.85 \pm 0.08$

Sugimoto *et al.* [68]. The chemical free energy change of austenite to ferrite transformation ($\Delta G^{\alpha\gamma}$) at the same composition without incorporating stored energy due to the shape deformation is calculated by the difference of G^γ and G^α. The model proposed by Sherif *et al.* [166] is given by:

$$\ln(V_\gamma^0) - \ln(V_\gamma) = k_1 \Delta G^{\alpha\gamma} \varepsilon \tag{4.1}$$

where, V_γ^o is the initial volume fraction of retained austenite in TRIP–assisted steels, V_γ is the volume fraction of austenite retained in the microstructure after a plastic strain of ε, $\Delta G^{\alpha\gamma}$ is the chemical driving force for the austenite to ferrite transformation of identical composition without incorporating the stored energy for shape deformation, and k_1 over a wide range of steels is the empirical constant. The value of k_1 is computed from experimental data [168, 69, 169–171, 75, 172]. There are three different values of k_1 used by Sherif *et al.* [166], as listed in Table 4.2, depending upon the data set used for the fitting.

Table 4.2 Fitting parameters proposed by Sherif *et al.* [166] to determine the kinetics of deformation induced–transformation of austenite to martensite.

k_1 / mol J^{-1}	Remarks on fitting parameter
0.002017	Derived from the entire data set
0.00446	Derived from individual data set and then averaged
0.008478–2.42×10$^{-6}\Delta G^{\alpha\gamma}$	Accounts for the plate volume which is dependent on $\Delta G^{\alpha\gamma}$

The decomposition of austenite into martensite due to plastic deformation during a tensile test can be used to estimate the total elongation of steel by the percolation concept [173]. The model suggests that failure during a tensile test occurs when the retained austenite in the microstructure loses continuity due to progressive transformation during deformation. This percolation threshold is about 0.1 (10%), below which continuity in austenite is lost and failure is initiated. This model is potentially a powerful tool to estimate the elongation of steel containing a mixture of bainitic ferrite and austenite. One objective in the current work was to evaluate the elongation using the percolation model for steels having bainite, retained austenite and/or martensite microstructure and compare against experimental tensile data available in the literature.

4.1.2 Calculation of deformation–induced transformation

The chemical compositions of the steels studied are presented in Table 4.3 from published data, including processing details along with any details of phase fractions. Data pertaining

to volume fraction of austenite (V_γ^0 and V_γ) and wherever available, the measured carbon contents of the austenite estimated from the X–ray diffraction parameters are reported in Table 4.4. Similarly, the volume fraction of retained austenite in the form of films between the plates of bainite or blocks within sheaves of bainite are listed where reported. The volume fractions and lattice parameters of austenite for the steels studied, were obtained by the analysis of X–ray diffraction data. The measured carbon in austenite by c_γ^e is then computed using empirical relationships between the lattice parameter and composition [174, 175]. The corresponding value calculated using mass balance is denoted c_γ, assuming all but 0.03 wt% is retained in the bainitic ferrite.

The free energy, $\Delta G^{\alpha\gamma}$ was computed using MTDATA with the NPL–plus database for steels. The T_0 and $T_0^{'}$ compositions, at which ferrite and austenite of identical composition have the same chemical free energies without and with a stored energy contribution of $400 \, \mathrm{J\,mol^{-1}}$ respectively, were computed similarly [54]. The reason for selecting the NPL–plus database for the calculation of $\Delta G^{\alpha\gamma}$ is that Sherif *et al.* [166] used it in deriving k_1 values. The yield strength, tensile strength, uniform elongation and total elongation of the steels are tabulated in Table 4.5.

The elongation was predicted using Equation 4.1 with the three different values of k_1, as listed in Table 4.2. Fig. 4.1 correlates the predicted elongation (e_t^p) with the measured uniform elongation and shows that there is little correspondence between the two. However, a better correlation is observed between the predicted elongation and measured total elongation, as illustrated in Fig. 4.2. This conclusion is drawn on the basis of the percentage of number of cases explained by the model. Thus, all discussions henceforth are based on the measured total elongation.

(a)

(b)

(c)
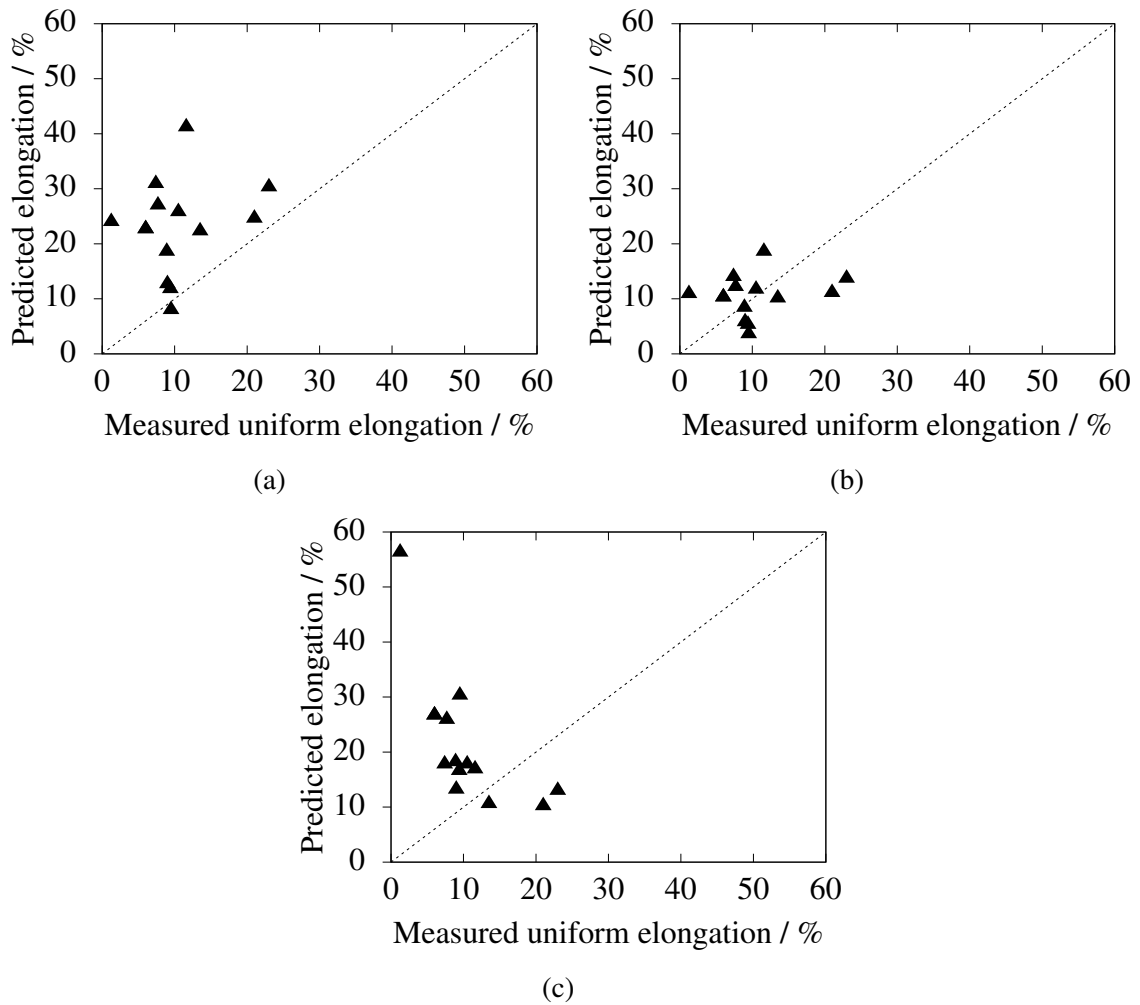
Figure 4.1 e_t^p using model proposed by Sherif *et al.* versus measured uniform elonga-tion with fitting parameter k_1 of (a) $0.002017\,\mathrm{mol\,J^{-1}}$ (b) $0.00446\,\mathrm{mol\,J^{-1}}$ (c) 0.008478–$2.42{\times}10^{-6}\Delta G^{\alpha\gamma}\,\mathrm{mol\,J^{-1}}$. The data plotted are for the steels studied with the uniform and predicted elongation tabulated in Table 4.5.

(a)

(b)

(c)
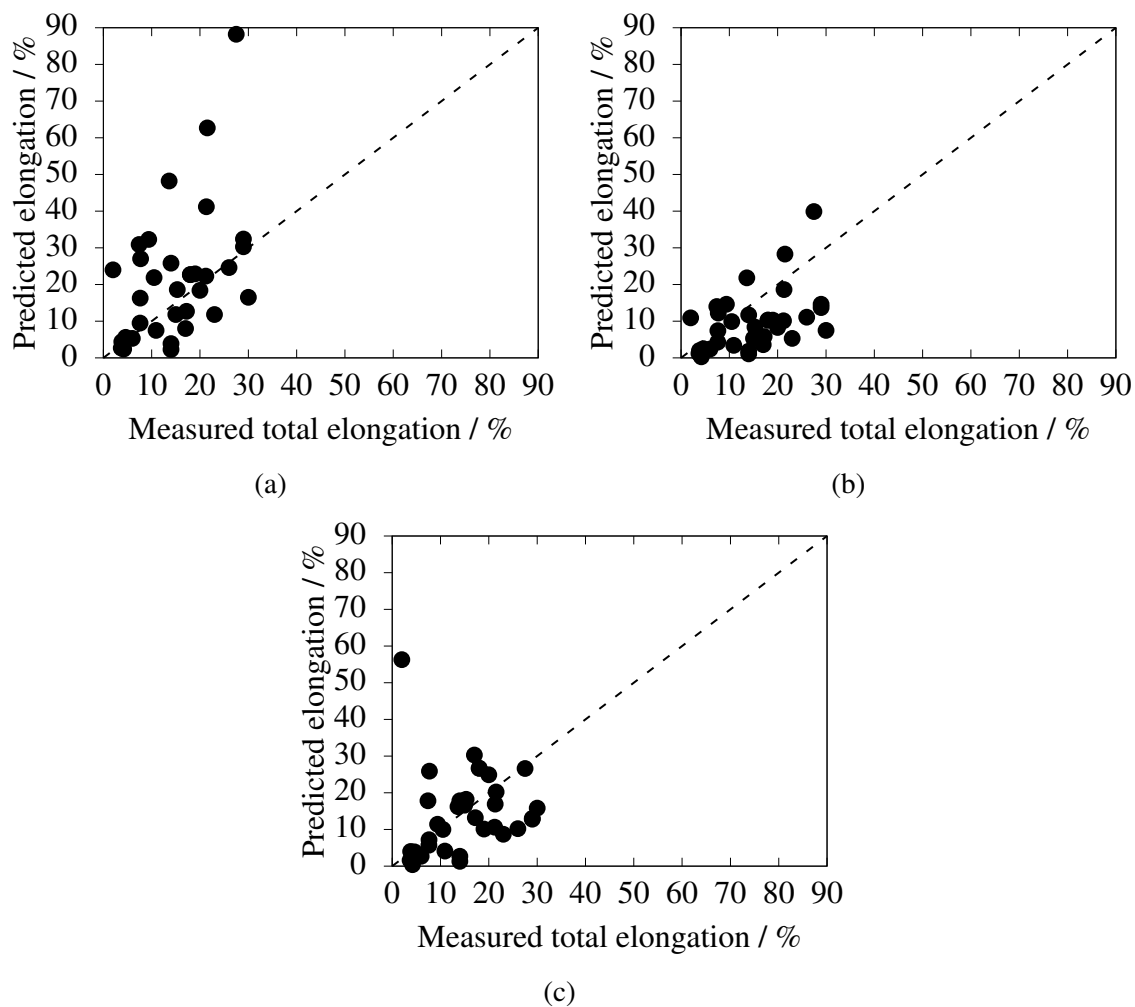
Figure 4.2 e_t^p using model proposed by Sherif *et al.* versus measured total elongation with fitting parameter k_1 of (a) $0.002017\,\mathrm{mol\,J^{-1}}$ (b) $0.00446\,\mathrm{mol\,J^{-1}}$ (c) $0.008478-2.42\times10^{-6}\Delta G^{\alpha\gamma}\,\mathrm{mol\,J^{-1}}$. The data plotted are for the steels studied with the total and predicted elongation tabulated in Table 4.5.

Table 4.3 Chemical composition (weight percent) of steels transformed isothermally to produce a microstructure of bainite, retained austenite and/or martensite. IBT stands for isothermal bainitic transformation.

Reference	Heat treatment	C	Si	Mn	Cr	Ni	Mo	Al	Co	Cu	V	Nb	S	P
1. Garcia et al. [64]	IBT 200 °C	0.80	1.59	2.01	1.0		0.24		1.51				0.002	0.002
2. Garcia et al. [64]	IBT 250 °C	0.80	1.59	2.01	1.0		0.24		1.51				0.002	0.002
3. Garcia et al. [64]	IBT 300 °C	0.80	1.59	2.01	1.0		0.24		1.51					
4. Garcia et al. [64]	IBT 200 °C	0.79	1.56	1.98	1.01		0.24	1.01	1.51					
5. Garcia et al. [64]	IBT 250 °C	0.79	1.56	1.98	1.01		0.24	1.01	1.51					
6. Garcia et al. [64]	IBT 300 °C	0.79	1.56	1.98	1.01		0.24	1.01	1.51					
7. Panov et al. [65]	IBT 375 °C, 20 min	0.21	1.06	0.87	0.92	0.06	0.006	0.026		0.16				
8. Panov et al. [65]	IBT 375 °C, 40 min	0.21	1.06	0.87	0.92	0.06	0.006	0.026		0.16				
9. Simonov et al. [78]	IBT 300 °C	0.318	1.57	2.38	2.87	0.378	0.626				0.159			
10. Simonov et al. [78]	IBT 325 °C(1)	0.304	1.61	0.268	1.25	3.14	0.501				0.128			
11. Simonov et al. [78]	IBT 325 °C(2)	0.304	1.61	0.268	1.25	3.14	0.501				0.128			
12. Caballero et al. [76]	IBT 500 °C	0.28	1.50	2.04	1.50		0.24		1.48					
13. Caballero et al. [76]	IBT 350 °C	0.30	1.44	2.06	1.60	1.70	0.24	1.01	1.43					
14. Garcia et al. [77]	IBT 220 °C	0.98	2.90	0.77	0.45	0.16				0.21			0.014	
15. Garcia et al. [77]	IBT 250 °C	0.98	2.90	0.77	0.45	0.16				0.21			0.014	0.016
16. Gao et al. [176]	IBT 360 °C, 120 min	0.4	1.7	2.0	0.4									0.016
17. Duong et al. [74]	IBT 400 °C	0.41	1.5	2.0				0.03					0.01	
18. Duong et al. [74]	IBT 400 °C+ IBT 350 °C	0.41	1.5	2.0				0.03					0.01	
19. Duong et al. [74]	IBT 450 °C+ IBT 350 °C	0.41	1.5	2.0				0.03					0.01	
20. Tomita et al. [169]	IBT 400 °C, 600 s + Tempering	0.60	1.52	0.80										
21. Bainite 1000 TSL	IBT 400 °C(1)	0.22	1.0	1.5	1.0		0.1	0.12				0.035	0.004	0.02
22. Bainite 1000 TSL	IBT 400 °C(2)	0.22	1.0	1.5	1.0		0.1	0.12				0.035	0.004	0.02
23. da Cruz et al. [25]	IBT 200 °C, 2 hours	0.56	1.43	0.58	0.47									
24. da Cruz et al. [25]	IBT 270 °C, 30 min	0.56	1.43	0.58	0.47									
25. da Cruz et al. [25]	IBT 270 °C, 2 hours	0.56	1.43	0.58	0.47									
26. da Cruz et al. [25]	IBT 270 °C, 24 hours	0.56	1.43	0.58	0.47									
27. Caballero et al. [177]	Air cooling	0.31	1.51	0.01	1.44	3.52	0.25			0.1				
28. Caballero et al. [177]	Air cooling	0.30	1.51	0.01	1.42	3.53	0.25			0.005				
29. Yoozbashi et al. [81]	IBT 300 °C	0.80	1.84	2.18	1.04		0.30	0.85	1.31					
30. Shendy et al. [82]	IBT 300 °C	0.76	1.96	1.4	1.24		0.24	0.7	0.14					
31. Shendy et al. [82]	IBT 250 °C	0.76	1.96	1.4	1.24		0.24	0.7	0.14					
32. Shendy et al. [82]	IBT 200 °C	0.76	1.96	1.4	1.24		0.24	0.7	0.14					

Table 4.3 – *Continued from previous page*

Reference	Heat treatment	C	Si	Mn	Cr	Ni	Mo	Al	Co	Cu	V	Nb	S	P
33. Avishan *et al.* [83]	IBT 200 °C	0.91	1.58	1.98	1.12	0.06	0.25	0.53	1.37					
34. Avishan *et al.* [83]	IBT 200 °C	0.90	1.51	0.94	1.14	2.61	0.25	0.59	1.37	0.09				

Table 4.4 Table collating the microstructural attributes of the various composition of steels under consideration. Volume fraction of bainite (V_{α_b}), retained austenite (V_γ) and martensite ($V_{\alpha'}$) are tabulated. The measured (c_γ^e) and calculated (c_γ) carbon in austenite are collated. $\Delta G^{\gamma\alpha} = -\Delta G^{\alpha\gamma}$, T_0 and T_0' compositions are calculated using MTDATA and NPL–plus database for steels. * marked $\Delta G^{\gamma\alpha}$ are those which are computed using calculated carbon (c_γ) in austenite using mass balance.

Reference	Heat treatment	V_{α_b}	V_γ (film+blocky)	$V_{\alpha'}$	c_γ^e wt%	c_γ wt%	T_0 wt%	T_0' wt%	$\Delta G^{\gamma\alpha}$ J mol^{-1}
1. Garcia et al. [64]	IBT 200 °C	0.87	0.13 (0.13+0)	0	1.10	5.95	1.66	1.46	-2308
2. Garcia et al. [64]	IBT 250 °C	0.79	0.21 (0.12+0.09)	0	1.40	3.70	1.52	1.31	-1608
3. Garcia et al. [64]	IBT 300 °C	0.73	0.25 (0.11+0.14)	0	1.49	3.07	1.36	1.15	-1403
4. Garcia et al. [64]	IBT 200 °C	0.83	0.17 (0.13+0.04)	0	1.47	4.50	1.77	1.56	-1613
5. Garcia et al. [64]	IBT 250 °C	0.79	0.21 (0.12+0.09)	0	1.70	3.65	1.62	1.40	-1139
6. Garcia et al. [64]	IBT 300 °C	0.63	0.37 (0.09+0.28)	0	1.90	2.08	1.47	1.24	-736
7. Panov et al. [65]	IBT 375 °C, 20 min	0.74	0.26	0	1.44	0.72	1.14	0.93	-1565
8. Panov et al. [65]	IBT 375 °C, 40 min	0.79	0.21	0	1.47	0.88	1.14	0.93	-1497
9. Simonov et al. [78]	IBT 300 °C	0.54	0.46 (0.25+0.21)	0		0.66	1.31	1.08	-3147*
10. Simonov et al. [78]	IBT 325 °C(1)	0.64	0.36 (0.32+0.04)	0		0.66	1.13	0.92	-2795*
11. Simonov et al. [78]	IBT 325 °C(2)	0.64	0.36 (0.33+0.03)	0		0.79	1.13	0.92	-2795*
12. Caballero et al. [76]	IBT 500 °C	0.77	0.20 (0.12+0.08)	0.03	0.96±0.3	1.28	0.75	0.51	-2697
13. Caballero et al. [76]	IBT 350 °C	0.70	0.27 (0.11+0.16)	0.03	0.91±0.3	1.03	1.15	0.91	-2654
14. Garcia et al. [77]	IBT 220 °C	0.64	0.36	0	1.22	2.58	1.61	1.42	-2055
15. Garcia et al. [77]	IBT 250 °C	0.66	0.34	0	1.47	2.79	1.49	1.29	-1472
16. Gao et al. [176]	IBT 360 °C, 120 min	0.57	0.22 (0.13+0.09)	0	1.25	1.71	1.08	0.87	-1753
17. Duong et al. [74]	IBT 400 °C	>0.65		<0.05	0.78	1.33	0.97	0.76	-2886
18. Duong et al. [74]	IBT 400 °C+IBT 350 °C	>0.65		<0.05	0.98	2.19	1.11	0.92	-2378
19. Duong et al. [74]	IBT 450 °C+IBT 350 °C	>0.65		<0.05	0.88	1.61	1.11	0.92	-2630
20. Tomita et al. [169]	IBT 400 °C, 600 s + Tempering	0.68		0	1.66	1.81	1.06	0.85	-920
21. Bainite 1000 TSL	IBT 400 °C(1)	0.80	0.20	0	0.81	0.98	1.03	0.81	-2912
22. Bainite 1000 TSL	IBT 400 °C(2)	0.83	0.17	0	0.66	1.15	1.03	0.81	-3283
23. da Cruz et al. [25]	IBT 200 °C, 2 hours	>0.80	0.12	<0.10	1.3	4.37	1.66	1.47	-1849
24. da Cruz et al. [25]	IBT 270 °C, 30 min	>0.80	0.10	<0.10	1.2	5.18	1.47	1.27	-2092
25. da Cruz et al. [25]	IBT 270 °C, 2 hours	>0.80	0.11	<0.10	1.2	4.76	1.47	1.27	-2092
26. da Cruz et al. [25]	IBT 270 °C, 24 hours	>0.80	0.13	<0.10	1.0	4.24	1.47	1.27	-2587
27. Caballero et al. [177]	Air cooling	0.62	0.12	0.26	0.92	2.36			-2303
28. Caballero et al. [177]	Air cooling	0.81	0.11	0.08	1.03	2.48			-2035

Table 4.4 – *Continued from previous page*

Reference	Heat treatment	V_{α_b}	V_γ (film+blocky)	$V_{\alpha'}$	c_γ^ε wt%	c_γ wt%	T_0 wt%	T_0' wt%	$\Delta G^{\gamma\alpha}$ J mol^{-1}
29. Yoozbashi et al. [81]	IBT 300 °C	0.86	0.14	0	1.28	5.73	1.43	1.20	−1982
30. Shendy et al. [82]	IBT 300 °C	0.73	0.27	0	1.7	2.73	1.42	1.20	−1022
31. Shendy et al. [82]	IBT 250 °C	0.79	0.21	0	1.4	3.51	1.58	1.36	−1676
32. Shendy et al. [82]	IBT 200 °C	0.85	0.15	0	1.2	4.90	1.72	1.51	−2125
33. Avishan et al. [83]	IBT 200 °C	0.58	0.42 (0.09+0.33)	0	1.01	0.91	1.71	1.50	−2635
34. Avishan et al. [83]	IBT 200 °C	0.67	0.33 (0.10+0.23)	0	1.07	1.15	1.58	1.37	−2295

Table 4.5 Table collating the mechanical properties of the various composition of steels under consideration. Yield strength, tensile strength, measured uniform elongation, total elongation and corresponding predicted elongation for the three different fitting parameters suggested by Sherif *et al.* [166] are tabulated. The elongation is expressed in %. † indicates cases where matching between predicted and measured total elongation is poor with $k_1 = 0.002017 \, \text{mol J}^{-1}$.

Reference	Heat treatment	σ_y MPa	σ_{UTS} MPa	e_u %	e_t %	e_t^p (Using k_1 / mol J^{-1})		
						0.002017	0.00446	0.008478-2.42×10$^{-6}\Delta G^{\alpha\gamma}$
1. Garcia *et al.* [64]	IBT 200 °C	1410	2180		4.6	5.6	2.5	3.9
2. Garcia *et al.* [64]	IBT 250 °C	1480	2060		19	22.9	10.3	10.1
3. Garcia *et al.* [64]	IBT 300 °C	1240	1770		29	32.4	14.6	12.8
4. Garcia *et al.* [64]†	IBT 200 °C	1414	2260		7.6	16.3	7.4	7.2
5. Garcia *et al.* [64]†	IBT 250 °C	1400	1930		9.4	32.3	14.6	11.4
6. Garcia *et al.* [64]†	IBT 300 °C	1250	1700		27.5	88.2	39.9	26.6
7. Panov *et al.* [65]	IBT 375 °C, 20 min	1080	1260	23	29	30.3	13.7	13.0
8. Panov *et al.* [65]	IBT 375 °C, 40 min	1070	1250	21	26	24.6	11.1	10.2
9. Simonov *et al.* [78]†	IBT 300 °C	1332	1489	1.25	2	24.0	10.9	56.3
10. Simonov *et al.* [78]	IBT 325 °C(1)	1063	1242	6	18	22.7	10.3	26.7
11. Simonov *et al.* [78]	IBT 325 °C(2)	1063	1242	6	18	22.7	10.3	26.7
12. Caballero *et al.* [76]	IBT 500 °C	904	1514	9	17.2	12.7	5.8	13.2
13. Caballero *et al.* [76]	IBT 350 °C	975	1556	8.9	15.3	18.6	8.4	18.2
14. Garcia *et al.* [77]†	IBT 220 °C	1704	2287	7.4	7.4	30.9	14.0	17.8
15. Garcia *et al.* [77]†	IBT 250 °C	1698	2068	11.6	21.3	41.2	18.6	16.9
16. Gao *et al.* [176]	IBT 360 °C, 120 min	1218	1505	13.5	21.2	22.3	10.1	10.6
17. Duong *et al.* [74]	IBT 400 °C		1283		20	18.4	8.3	24.9
18. Duong *et al.* [74]†	IBT 400 °C+ IBT 350 °C		1305		23	11.8	5.3	8.7
19. Duong *et al.* [74]†	IBT 450 °C+ IBT 350 °C		1190		30	16.5	7.5	15.8
20. Tomita *et al.* [169]†	IBT 400 °C, 600 s + Tempering		1750		21.5	62.7	28.3	20.2
21. Bainite 1000 TSL	IBT 400 °C(1)	618	1115	9.4	15	11.8	5.3	16.6
22. Bainite 1000 TSL†	IBT 400 °C(2)	625	1114	9.5	17	8.0	3.6	30.3
23. da Cruz *et al.* [25]	IBT 200 °C, 2 hours	980	2155		6	5.3	2.4	2.7
24. da Cruz *et al.* [25]	IBT 270 °C, 30 min	1275	1735		4.2	2.4	0.3	0.4
25. da Cruz *et al.* [25]	IBT 270 °C, 2 hours	1365	1615		3.7	2.7	1.2	1.6
26. da Cruz *et al.* [25]	IBT 270 °C, 24 hours	1355	1520		3.8	4.4	2.0	4.0
27. Caballero *et al.* [177]†	Air cooling	1150	1725		14	3.9	1.8	2.7
28. Caballero *et al.* [177]†	Air cooling	1100	1625		14	2.3	1.1	1.3
29. Yoozbashi *et al.* [81]	IBT 300 °C	1230–1580			8.7–13	7.5	3.4	4.1

Table 4.5 – *Continued from previous page*

Reference	Heat treatment	σ_y	σ_{UTS}	e_u	e_t	e_t^p (Using k_1 mol J^{-1})		
		MPa	MPa	%	%	0.002017	0.00446	0.008478-2.42×10^{-6}$\Delta G^{\alpha\gamma}$
30. Shendy *et al.* [82]†	IBT 300 °C	961	1602		13.6	48.2	21.8	16.2
31. Shendy *et al.* [82]†	IBT 250 °C	1138	1801		10.5	21.9	9.9	10.0
32. Shendy *et al.* [82]	IBT 200 °C	1288	1963		7.6	9.5	4.3	5.7
33. Avishan *et al.* [83]†	IBT 200 °C	1405	2115	7.7	7.7	27.0	12.2	25.9
34. Avishan *et al.* [83]†	IBT 200 °C	1730	2182	10.5	14	25.8	11.7	17.8

4.1.3 Discussion on predictive calculations

A high value of k_1 implies a lower austenite mechanical stability, as does a large magnitude of free energy change $|\Delta G^{\alpha\gamma}|$. All the fitting parameters used to correlate calculated and measured elongation have some degree of matching (Fig. 4.2). However, use of one fitting parameter to predict the entire spectrum of data gives a generic model that can used in design. Notably, k_1 of $0.002017\,\mathrm{mol\,J^{-1}}$ predicts well, except for the cases marked by † in Table 4.5.

The compositions studied in cases 4, 5 and 6 by Garcia *et al.* are those of nanostructured bainite [17], silicon and aluminium–rich high–carbon steel transformed isothermally at 200, 250 and 300 °C. Cobalt was also added to accelerate bainite transformation kinetics. As the temperature is reduced, the retained austenite fraction decreases due to the greater fraction of bainite. This ensures a greater enrichment of austenite with carbon. However, the measured carbon content of austenite (c_γ^{e}) shows an opposite trend with respect to that calculated (c_γ) or the T_0 and T_0' conditions, as shown in Table 4.4. This is perhaps due to the increased trapping of carbon at dislocations in bainitic ferrite and retained in solid solution in α_{b}, as proven by atom probe tomography [79]. Fig. 4.3 shows that with the increase in isothermal transformation temperature the carbon content of bainitic ferrite (c_α^{e}) decreases, thus supporting the argument that high temperature retained austenite is more enriched as compared to the low temperature counterparts. Therefore, high austenite volume fraction and low driving force $\Delta G^{\alpha\gamma}$ lead to an overestimation of elongation. A similar explanation applies to the other cases marked in Table 4.5.
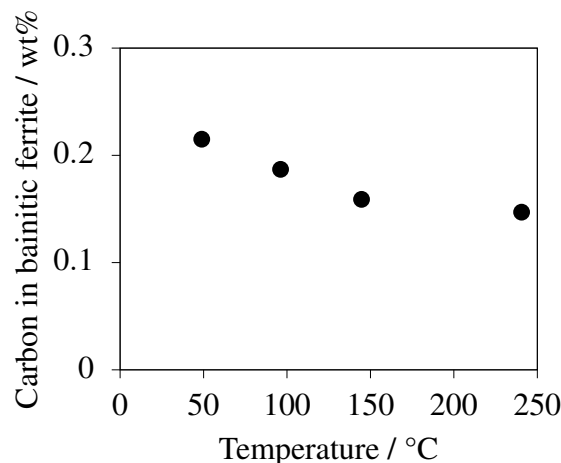

Figure 4.3 Atom probe data for carbon in solid solution in bainitic ferrite in contact with austenite determined by Caballero *et al.* [80] using atom probe tomography, which has its limitation in terms of the number of atoms analysed.

The experimental data by Simonov *et al.* [78], case 9 gave a predicted elongation (e_t^p) of 24% against a measured total elongation of just 2%. This is because of the large macro defects and inclusions resulting from poor casting (D. O. Panov, private communication, July 4, 2016).

Duong *et al.* [74] used a two step isothermal bainitic transformation to maximise the volume fraction of bainite and stabilise the retained austenite. The retained austenite in cases 18 and 19 is not greatly enriched ($c_\gamma^e < 1\,\mathrm{wt\%}$) making it less stable. This may be attributed to the higher isothermal transformation temperature ($> 350\,°\mathrm{C}$) to form bainite. The value of c_γ^e is low when compared with the high–carbon carbide–free bainitic steels, so there is an underestimation of elongation. Cases 21 and 22 are similar in this respect, where c_γ^e is just $0.66\,\mathrm{wt\%}$. Prediction for cases 27 and 28 of Caballero *et al.* in Table 4.5 is not satisfactory due to the low retained austenite content obtained during continuous cooling or normalizing heat treatment. In air cooled samples data, V_{α_b} is low, affecting the enrichment of residual γ which is then prone to formation of α' ($V_{\alpha'} = 0.26$ and 0.08, respectively) whilst cooling to room temperature. A meagre 11–12% austenite remained at room temperature leading to underestimation of e_t^p.

The elongation is predicted reasonably well using $k_1 = 0.008478\text{–}2.42 \times 10^{-6} \Delta G^{\alpha\gamma}$ but the original derivation [178] was limited to $\Delta G^{\alpha\gamma} \le 2500\,\mathrm{J\,mol^{-1}}$. Fig. 4.4 shows the elongation estimates for all the three approaches to k_1. Each graph in Fig. 4.4a to Fig. 4.4ah corresponds to the cases mentioned in Table 4.5. Each graph comprises of a solid, dashed and dotted curve representing decomposition of austenite to martensite following Sherif's model with k_1 of 0.002017, 0.00446 and $0.008478\text{–}2.42 \times 10^{-6} \Delta G^{\alpha\gamma}$ respectively. The Sherif kinetics model coupled with the percolation theory is valid for a bainitic ferrite and retained austenite microstructure.

It is evident that the usage of single value of k_1 doesn't fit the whole spectrum of data for all alloys, exemplifying that the model proposed by Sherif *et al.* [166] doesn't fully capture all of the key physics. The model being simplistic in nature is still being used in this thesis as an empirical tool to estimate the volume fraction of retained austenite as a function of tensile strain.

(a) 1. Garcia *et al.* [64]

(b) 2. Garcia *et al.* [64]

(c) 3. Garcia *et al.* [64]

(d) 4. Garcia *et al.* [64]
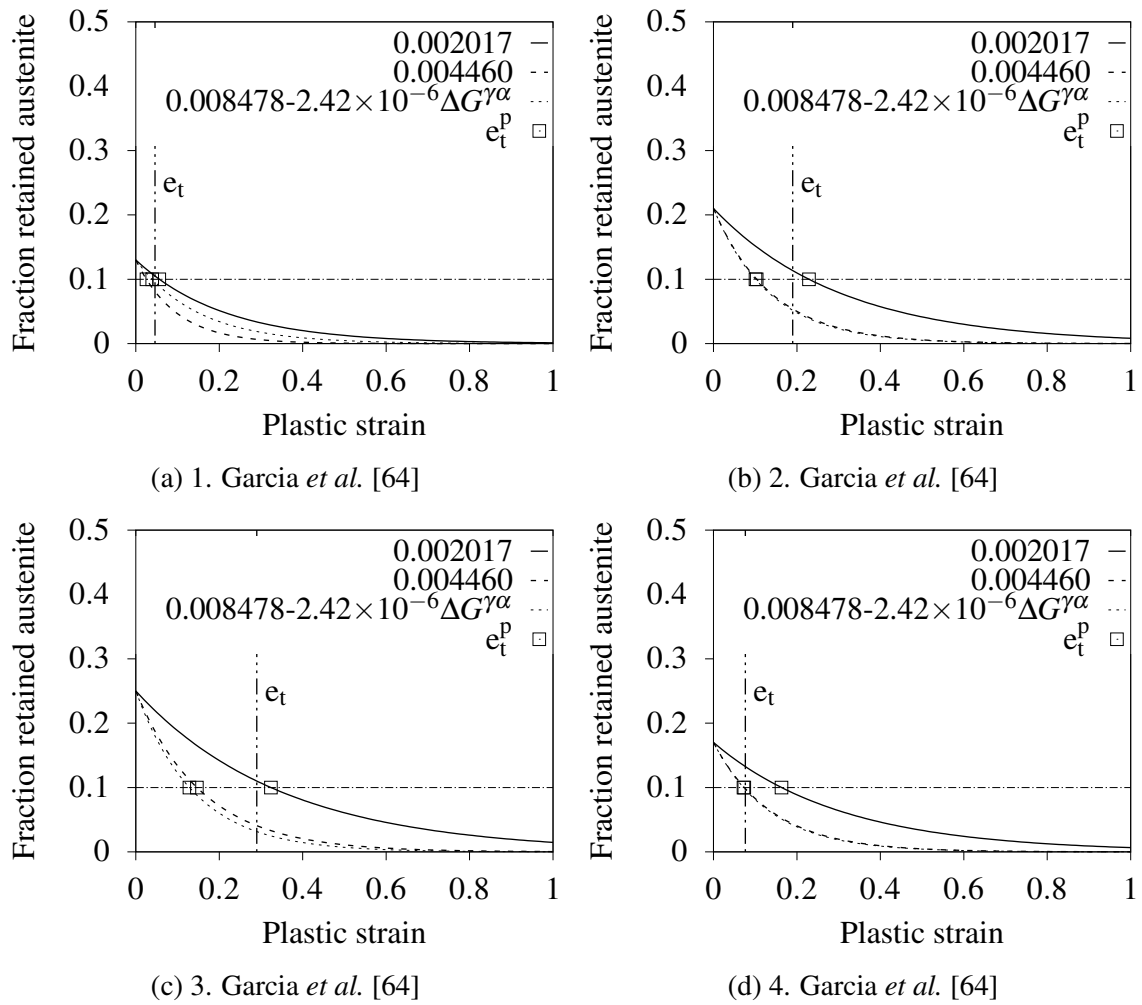
Figure 4.4 Kinetics of deformation induced transformation of γ to α' for collated published data in Table 4.3 using the model proposed by Sherif *et al.* [166] with k_1 of 0.002017, 0.00446 and 0.008478–$2.42 \times 10^{-6} \Delta G^{\alpha\gamma}$ mol J^{-1}. Vertical line representing the experimentally measured total elongation, e_t. The predicted elongation is marked by unfilled square.

(e) 5. Garcia *et al.* [64]

(f) 6. Garcia *et al.* [64]

(g) 7. Panov *et al.* [65]

(h) 8. Panov *et al.* [65]

(i) 9. Simonov *et al.* [78]

(j) 10. Simonov *et al.* [78]

Figure 4.4 *Continued from previous page*

(k) 11. Simonov *et al.* [78]

(l) 12. Caballero *et al.* [76]

(m) 13. Caballero *et al.* [76]

(n) 14. Garcia *et al.* [77]

(o) 15. Garcia *et al.* [77]

(p) 16. Gao *et al.* [176]

Figure 4.4 *Continued from previous page*

(q) 17. Duong *et al.* [74]

(r) 18. Duong *et al.* [74]

(s) 19. Duong *et al.* [74]

(t) 20. Tomita *et al.* [169]

(u) 21. Bainite 1000 TSL

(v) 22. Bainite 1000 TSL

Figure 4.4 *Continued from previous page*

(w) 23. da Cruz *et al.* [25]

(x) 24. da Cruz *et al.* [25]

(y) 25. da Cruz *et al.* [25]

(z) 26. da Cruz *et al.* [25]

(aa) 27. Caballero *et al.* [177]

(ab) 28. Caballero *et al.* [177]

Figure 4.4 *Continued from previous page*

(ac) 29. Yoozbashi *et al.* [81]

(ad) 30. Shendy *et al.* [82]

(ae) 31. Shendy *et al.* [82]

(af) 32. Shendy *et al.* [82]

(ag) 33. Avishan *et al.* [83]

(ah) 34. Avishan *et al.* [83]

Figure 4.4 *Continued from previous page*

4.1.4   Deformation–induced transformation in 1000 MPa bainitic steel

Broken tensile specimens of 1000 MPa bainitic steel were procured from Tata Steel. The composition of the steel is given in Table 4.3 (numbers 21 and 22). Multiple samples were cut along the gauge length of the tensile specimen together with one each from fractured and grip sections. The volume fraction of austenite was computed using the data from X–ray diffraction as proposed by Dickson [160] for textured samples. The lattice parameters of austenite and ferrite were computed using the profile fit in the HighScore+ software, where the peaks positions were used to determine the lattice parameter by incorporating the systematic errors. Rietveld refinement also gave similar results for lattice parameters, however, the inbuilt texture model in HighScore+ software over estimated the volume fraction of retained austenite [179].

The volume fraction of austenite plotted against reduction in area followed the trend as given in Fig. 4.5. The reduction in area was used to determine the strain in the gauge length of the sample and when plotted with the model prediction proposed by Sherif *et al.* gave good correlation, Fig. 4.5. However, the predicted elongation using the percolation theory and k_1 of 0.002017 is 9.4% as against the measured total elongation of 15.1%. The deformation induced transformation of austenite closely follows the prediction for k_1 of $0.008478 - 2.42 \times 10^{-6} \Delta G^{\gamma \alpha}$. The austenite content in the grip section was found to be 15.5% which decreased along the gauge length to a value of around 2% at the fracture surface.

The lattice parameter and the c_{γ}^{e} showed an overall increasing trend with respect to the reduction in area (Fig. 4.6). This is due to the transformation of low carbon austenite at lower strains, thus leaving the more stable high carbon austenite, as found in previous work [106–109, 57, 104, 105, 111–115].
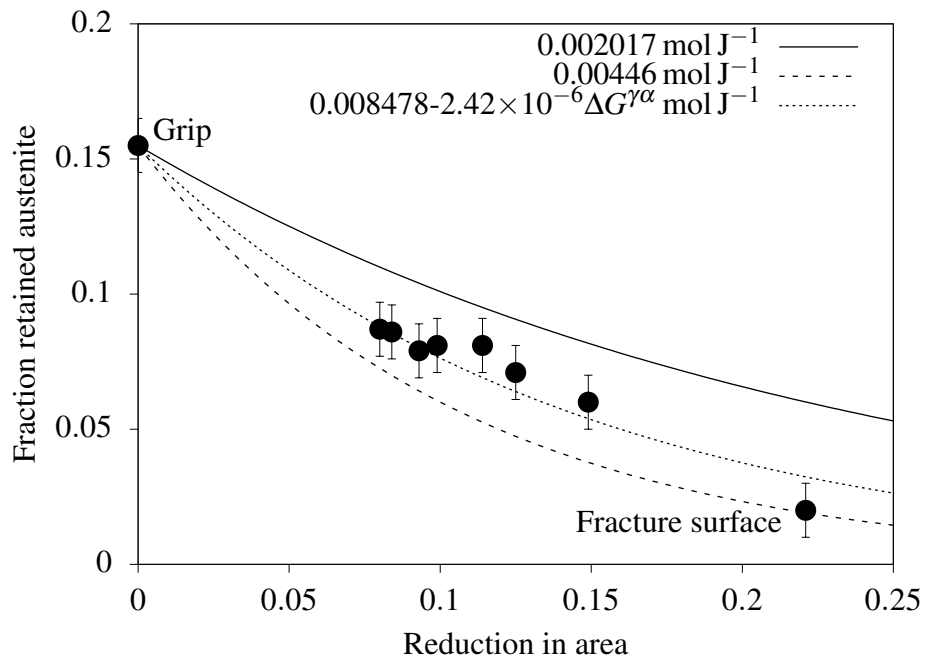
Figure 4.5 Deformation–induced transformation of austenite in 1000 MPa bainitic steel, where the strain is computed from the reduction in area. The solid dot with error bars denote the measured austenite content at various strain levels. The solid, dashed and dotted lines denote the model prediction proposed by Sherif *et al.* with k_1 of 0.002017, 0.00446 and $0.008478 - 2.42 \times 10^{-6} \Delta G^{\gamma\alpha}$ mol J^{-1} respectively.
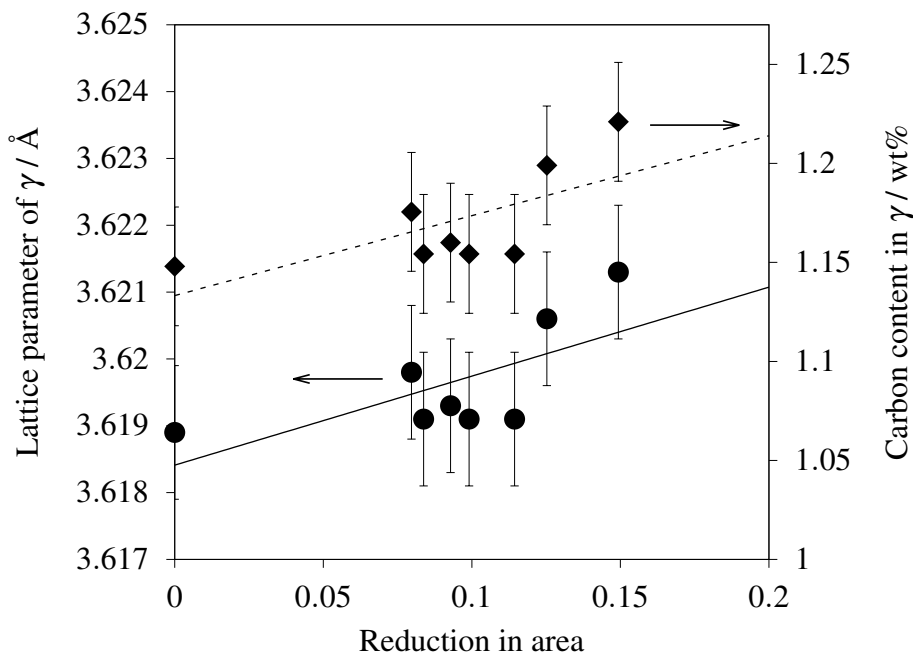

Figure 4.6 Deformation induced transformation of austenite in 1000 MPa bainitic steel showing an increase in lattice parameter of γ with increasing strain.

It was also observed that deformation in the gauge length showed reduction in intensity of $(200)_\gamma$ and $(220)_\gamma$ X-ray diffraction peaks. This can be observed in Figs. 4.7 and 4.8. The diminishing intensity of the peaks is found to be gradual with increasing reduction in area, owing to the gradual decrease of V_γ along the length of the tensile sample from the grip to the fracture surface. In Fig. 4.7 the peaks shift towards lower angles with increase in strain which confirms again, the decomposition of relatively low carbon austenite at lower strains, leading to the shift.
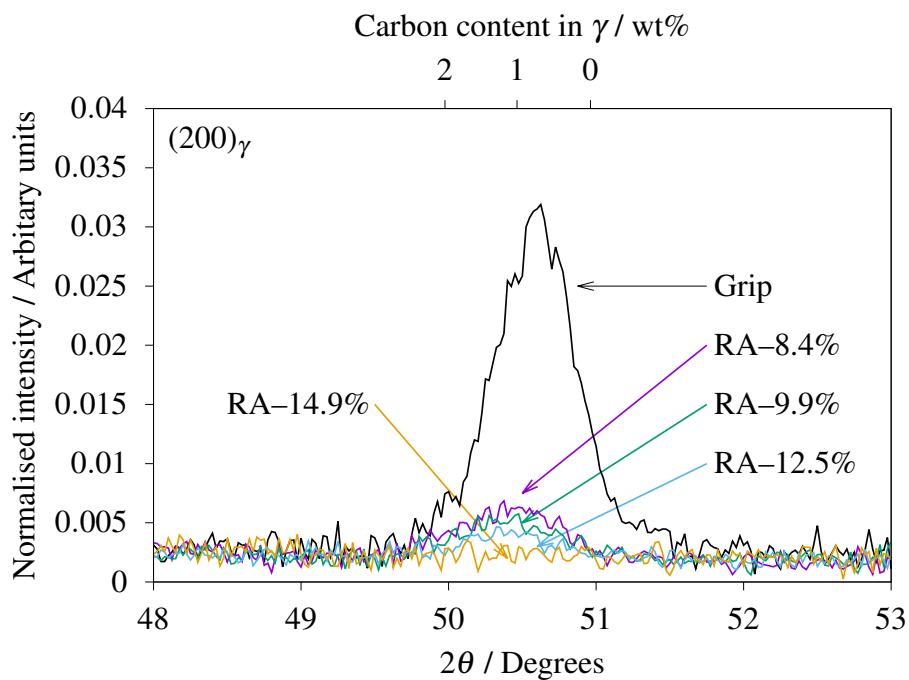
Figure 4.7 The (200) X-ray diffraction peak of austenite at different strains computed through the reduction in area. The corresponding carbon content in marked in the secondary X–axis. RA–Reduction in area.
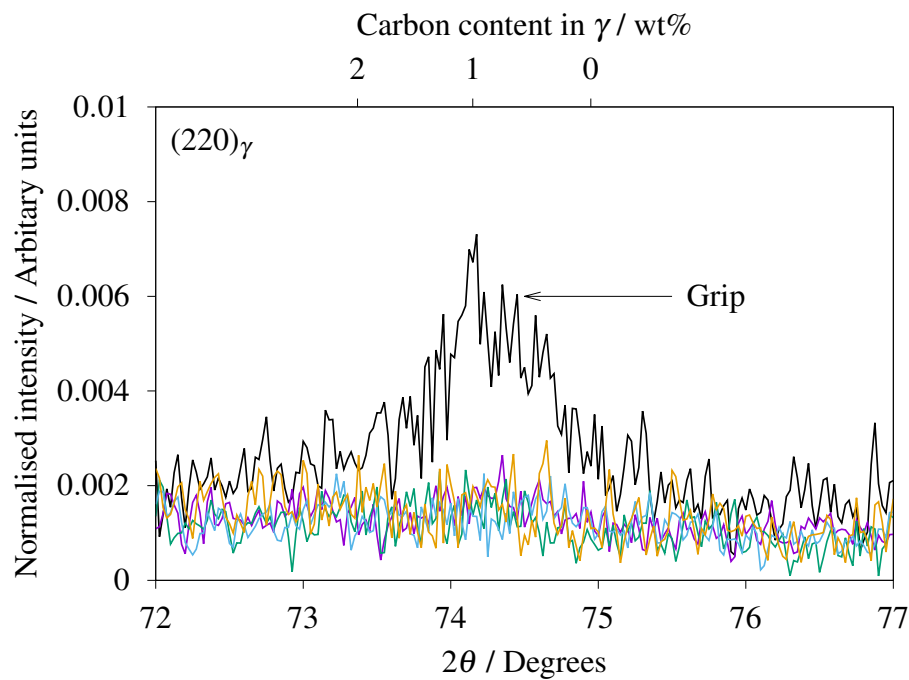
Figure 4.8 The (220) X-ray diffraction peak of austenite at different strains computed through the reduction in area. The corresponding carbon content in marked in the secondary X–axis.

Assumptions

The c_γ^e in the current context is computed using the empirical equation given by Dyson and Holmes [174], however, there exist many such empirical relationships as given in Fig. 4.8 which over predicts values of c_γ^e. For the 1000 MPa bainitic steel the carbon content of austenite in the grip section computed using the Dyson and Holmes equation [174] is 1.15 wt% which gives a value of $|\Delta G^{\gamma\alpha}|$ of 2316 J mol^{-1}. However, other equations except by Hanzaki *et al.* [180] predicts the carbon content in the range of 1.25 to 1.42 wt% and thereby the corresponding $|\Delta G^{\gamma\alpha}|$ being 1868 to 1476 J mol^{-1} respectively. However, the carbon content c_γ^e from Dyson and Holmes is the closest to x_{T_0}, so all calculations have been done accordingly [174]. A lot of these equations (except Dyson and Holmes [174]) exclude many solutes typically present in steels, rendering the usage of such equations limited.
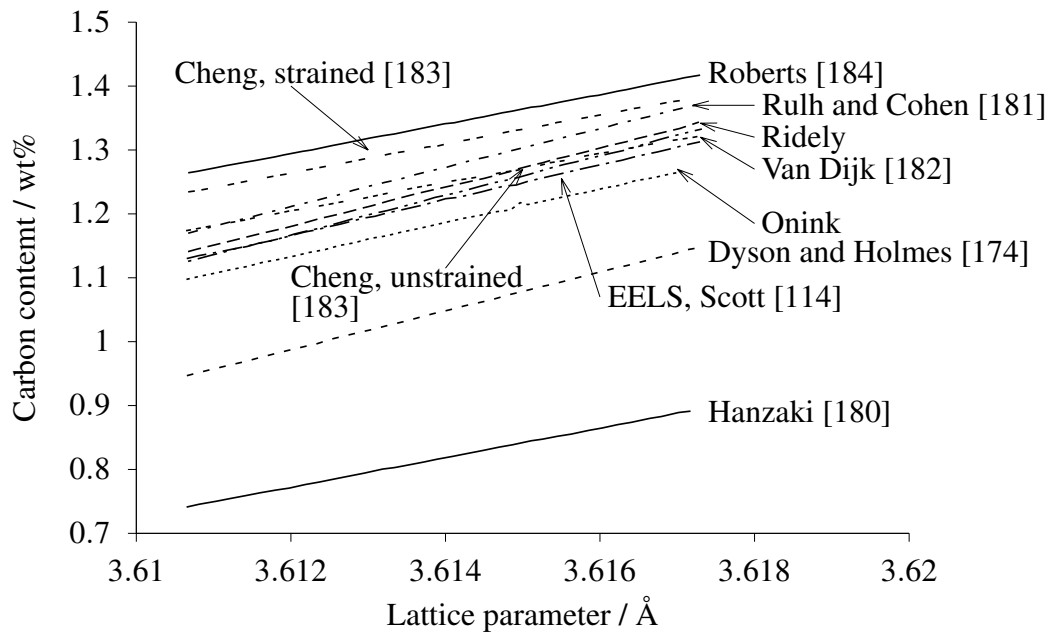
Figure 4.8 Average carbon concentration in the retained austenite measured by various authors using X–ray diffraction and the dependency on Lattice parameter of austenite.

4.2   Conclusions on elongation prediction

The following conclusions are drawn from the analysis of the literature data using the model proposed by Sherif *et al.* coupled with the percolation theory to estimate the elongation of a mixture of bainitic ferrite and retained austenite.

1. Total elongation seems to give a greater correspondence with the predicted elongation as compared to the uniform elongation.

2. The maximum error between the measured and predicted elongation was found to be around 5%, associated with just few data points.

3. The fitting parameter of k_1 given by $0.008478-2.42\times10^{-6}\Delta G^{\alpha\gamma}$ mol J^{-1} gives good general agreement with experiments but predicts poorly for low values of $|\Delta G^{\alpha\gamma}|$, where the austenite predicted to be too stable. In situation where $|\Delta G^{\alpha\gamma}|$ is small, the effect of heterogeneities in the carbon distribution is expected to be more prominent.

4. The model is sensitive to the carbon content of austenite which affects the free energy change of austenite to martensite, $\Delta G^{\alpha\gamma}$. Thus accurate measurements of the carbon content could strengthen the model.

5. The model predicts well beyond the threshold limit of 10% of austenite for the percolation theory. The prediction of the model proposed by Sherif *et al.* can also be extended to strain calculated through the reduction in area.

Chapter 5

1000 MPa bainitic steel

A commercially available steel, with the chemical composition detailed in Table 5.1, was procured from Tata Steel which was the basis for further development in the thesis.

Table 5.1 Chemical composition of a commercially available steel procured from Tata Steel. The Si content which is important in suppressing cementite has been highlighted in bold.

Steel	Chemical composition / wt%									
	C	**Si**	Mn	Cr	Mo	Nb	Al	P	S	N
Alloy	0.22	**1.01**	1.48	0.95	0.10	0.035	0.143	0.024	0.020	0.0119

5.1 Thermodynamic calculations

Thermodynamic calculations were used to determine the equilibrium phase fractions, the transition temperatures and phase compositions. These are listed in Table 5.2 together with software used along with the relevant databases. Thermodynamic calculations from all these software and corresponding databases yielded similar results, thus the choice of using one particular software depended upon the ease with which the calculations could be performed. For instance, the phase fractions of different phases versus temperature could be easily computed in THERMOCALC, however deduction of T_0 and $T_0^{'}$ was quite straight forward in MTDATA.

Table 5.2 Commercial software along with their respective databases used in this work for thermodynamic and kinetic calculations. The † indicates diffusion database for MATCALC used for the calculation of kinetics of cementite precipitation.

Software	Database	References
THERMOCALC	TCFE8	[55, 56]
MTDATA	NPL–plus for steels	[185]
MATCALC	Thermodynamic database (mc_fe_2.058)	[54]
	Diffusion database (mc_fe_2.010)†	

Fig. 5.1 shows the evolution of equilibrium phases (liquid, ferrite, austenite and cementite) with temperature. The phase mixture predicted at room temperature is of ferrite and cementite. The fractions of pearlite, which is a lamellar aggregate of ferrite and cementite, can be estimated by subtracting the ferrite phase fraction that exists before cementite precipitation becomes possible, from unity (T_α^f in Fig. 5.1). The mole fractions of pro–eutectoid ferrite and pearlite defined in this way, at room temperature are 0.55 and 0.45 respectively.
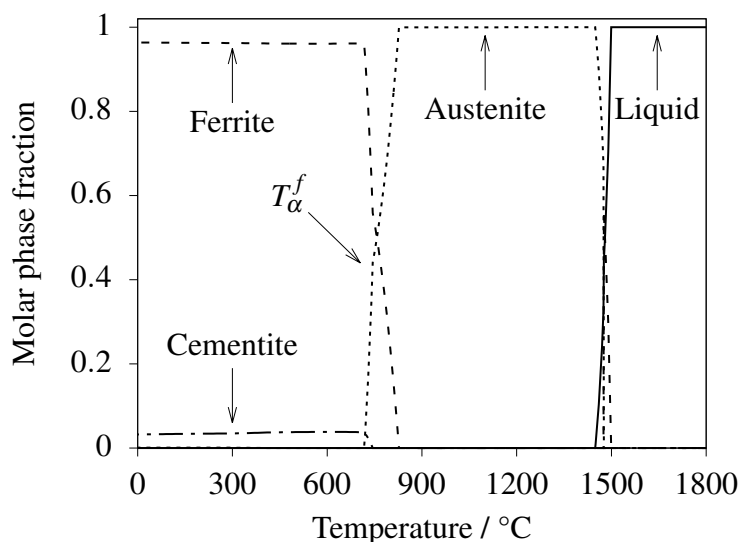
Figure 5.1 Equilibrium molar phase fraction of liquid, ferrite, austenite and cementite for the alloy using THERMOCALC with TCFE8 database.

The T_0 and $T_0^{'}$ temperatures were predicted to estimate the carbon enrichment in austenite and the maximum attainable bainite fraction during isothermal transformation. Fig. 5.2 shows the T_0 and $T_0^{'}$ predicted using MTDATA. This information can be coupled with the
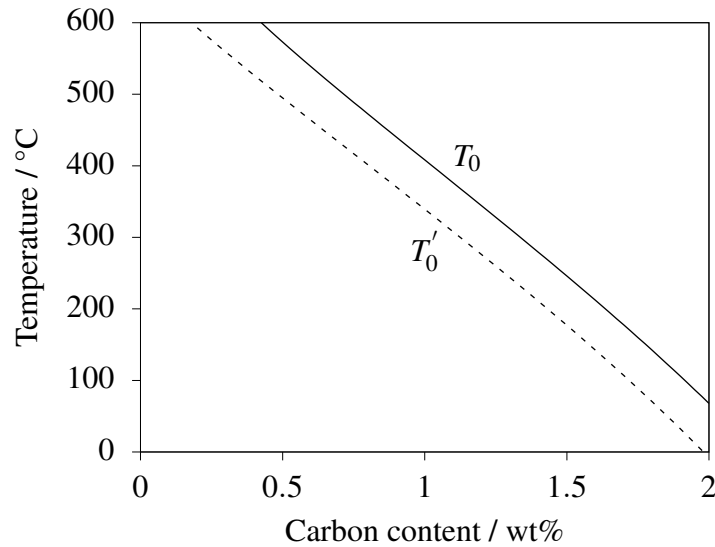
Figure 5.2 T_0 and $T_0^{'}$ calculation for the steel. Solid–line, dashed–line represents the T_0 and $T_0^{'}$ calculations done using MTDATA with its corresponding databases, Table 5.2.

dilatometry results to obtain the optimum isothermal bainitic transformation temperature needed to form stable austenite retention when the sample is cooled to ambient temperature. The x_{T_0} value was also used to evaluate the kinetics of precipitation of carbide from an enriched austenite, following bainitic transformation in the presence of dissolved silicon.

5.2 Kinetic calculations

5.2.1 Time–temperature–transformation diagram

The time–temperature–transformation (TTT) diagram for the alloy was computed using MUCG83 and MTTTDATA programs available at the Materials Algorithm Project website [186, 187]. MUCG83 is a versatile Fortran program capable of calculating the M_S, B_S and W_S temperatures for steels over a wide composition range. Other thermodynamic and kinetic parameters can also be obtained, such as the time required for the onset of diffusional and diffusionless transformations, driving force for γ to $\alpha^{'}$ transformation, driving force for allotriomorphic ferrite formation by a paraequilibrium mechanism etc. [186]. MTTTDATA is based on similar principles as MUCG83, but uses thermodynamic data from commercial databases as opposed to built in estimates of free energies [187][1]. Fig. 5.3 shows the TTT

---

[1]Note that all thermodynamic data are empirical. However, the commercially available databases are over a much wider range of composition and phases.

diagram with the separate C–curves for reconstructive and displacive transformations, and with a characteristic T_h temperature (Section 2.5). An approximate cooling rate of about $12\,°C\,s^{-1}$ was estimated to avoid the formation of allotriomorphic ferrite and pearlite, validated dilatometrically as described later. This rate constitutes one of the design parameters.
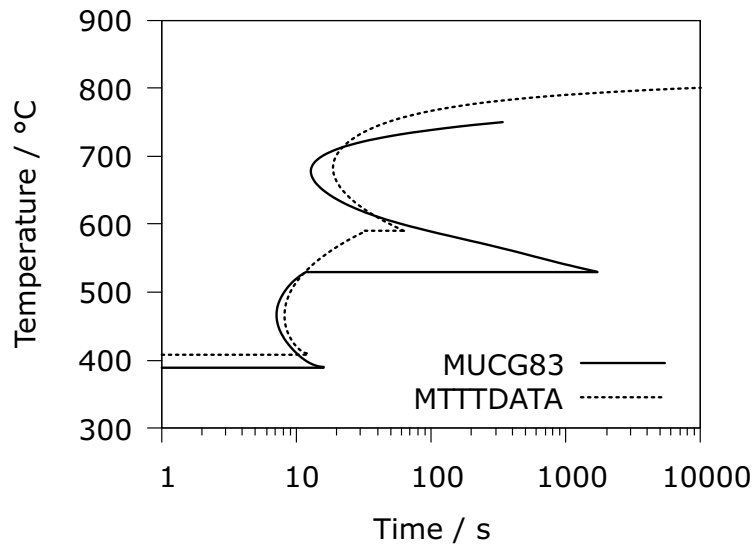

Figure 5.3

Figure 5.4 Predicted TTT using MUCG83 and MTTTDATA Fortran programs.

5.2.2   Precipitation kinetics: effect of silicon

The precipitation kinetics of cementite in austenite were estimated during isothermal transformation in the bainite range using MATCALC software and the databases listed in Table 5.2. The calculations were done for three different temperatures of 425 °C, 400 °C and 375 °C. The composition of the steel was assumed to be similar to the steel under investigation with varied silicon and carbon contents. The carbon content of the austenite was assumed to be equal to the $x_{T_0}{}^2$ with values of 0.95 wt%, 1.03 wt% and 1.10 wt% at 425 °C, 400 °C and 375 °C respectively. The thermodynamic limit for bainitic transformation during isothermal heat treatment is denoted by the T_0 line and the corresponding enrichment of austenite is given by x_{T_0} [15–17]. The silicon content was varied from 0.5 wt% to 1.5 wt% in steps of 0.25 wt%. Fig. 5.5 shows the kinetics of cementite precipitation. An increase in silicon content reduces the rate of cementite precipitation, and limits the maximum mole fraction of cementite

---

[2]Effect of silicon concentration on x_{T_0} (∼0.002 wt%/0.5 wt% Si) for composition similar to alloy under consideration, is small and thus its impact on x_{T_0} has been ignored.

available for precipitation. 1.5 wt% silicon inhibits cementite precipitation completely at all transformation temperatures. 1 wt% silicon inhibits cementite precipitation at 425 °C and retards the precipitation during transformation at 400 °C and 375 °C. Thus, it can be concluded that the presence of silicon in excess of 1 wt% for the steel under consideration is enough to prohibit cementite formation at low temperatures under paraequilibrium conditions over the time–scales of interest in the present work. All the calculations were performed under paraequilibrium conditions as previously done by Kozeschnik and Bhadeshia [28]. Babu and Hono [188–191] pointed out at low–temperature (350 °C), the diffusivity of carbon is orders of magnitude greater than the diffusivity of substitutional elements. It is said [188, 189] that during early stages of cementite precipitation no partitioning of substitutional alloying elements takes place and the growth is controlled by carbon diffusion under paraequilibrium conditions.
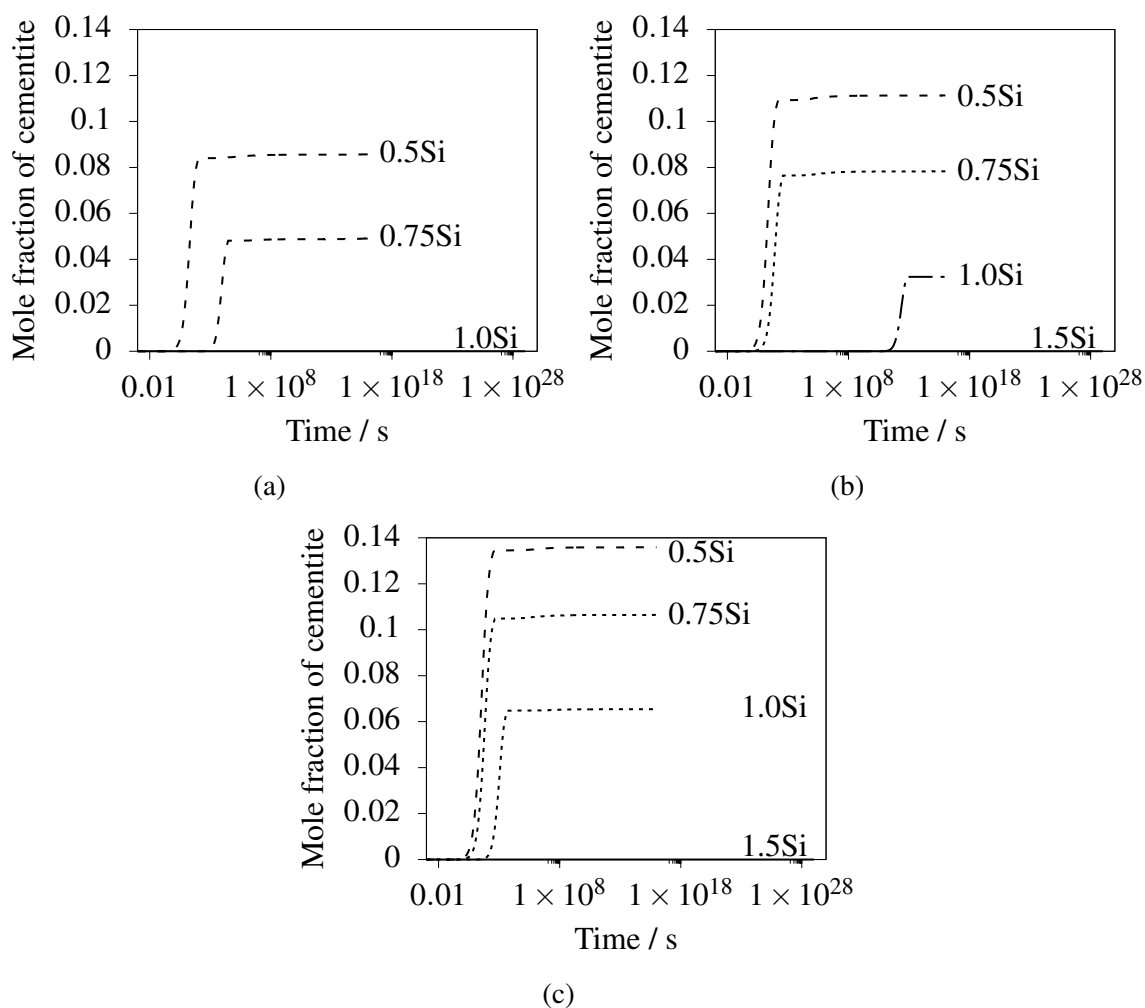
Figure 5.5 Effect of silicon (wt%) on the kinetics of cementite precipitation in austenite calculated at (a) 425°C (b) 400°C and (c) 375°C using MATCALC and Fe thermodynamic and diffusion database version 2.058 and 2.010 respectively. The calculations were done by assuming T_0 carbon content in austenite. The steel under consideration is Fe–0.20C–1.5Mn–1.0Cr–0.1Mo–0.1Al–0.0275Nb–xSi (wt%).

5.3   Analysis of dilatometry experiments

The samples were heated from room temperature to $1050\,°C$ at a rate of $10\,°C\,s^{-1}$ and held at $1050\,°C$ for $10\,min$, cooled to $900\,°C$ at $10\,°C\,s^{-1}$, and then to room temperature at various constant cooling rates of 0.5, 1, 2, 5, 10, 20 and $50\,°C\,s^{-1}$. With a similar heating cycle, cooling after $900\,°C$ was at $50\,°C\,s^{-1}$ to $400\,°C$, where the sample was held for $1\,h$ before cooling to room temperature at $10\,°C\,s^{-1}$. The thermal cycle for each of these experiments (Fig. 5.6) is reported along with the dilatation curve and microstructure obtained during the heat treatment.

Ac_1 and Ac_3 temperatures for $10\,°C\,s^{-1}$ heating rate were estimated using the offset method proposed by Yang and Bhadeshia [192] (Fig. 5.7a), the Ac_1 and Ac_3 temperatures thus obtained are $775 \pm 5\,°C$ and $891 \pm 3\,°C$ (Table 5.3) which compare with the Ae_1 and Ae_3 computed using THERMOCALC software with TCFE8 database at $747\,°C$ and $835\,°C$. As expected, the latter are lower than during heating.

Table 5.3 Transition temperatures computed from dilatometry data at various cooling rates and constant heating rate. F_S–allotriomorphic ferrite start, F_F–allotriomorphic ferrite finish, B_S–bainite start, M_S–martensite start, B_F–bainite finish, M_F–martensite finish and IBT–isothermal bainitic transformation. The transition temperatures are estimated using the offset method [192] with an error within $\pm12\,°C$.

Heat Rate $/\,°C\,s^{-1}$	Cooling Rate $/\,°C\,s^{-1}$	Heating		Cooling				
		Ac_1	Ac_3	F_S	F_F	B_S	M_S	B_F or M_F
					$/\,°C$			
10	0.5	775	890	725	651	522		390
	1	779	890			520		395
	2	782	895			506		319
	5	769	886			482		277
	10	770	888			417		252
	20	769	891				382	253
	50	780	894				374	249
	IBT $400\,°C$	775	893					

Cooling at 0.5, 1 and $2\,°C\,s^{-1}$ generated allotriomorphic ferrite, bainite and martensite, Fig. 5.7b. The allotriomorphic ferrite fraction decreased with an increase in cooling rate to zero at higher cooling rates $\geq 10\,°C\,s^{-1}$ (Fig. 5.8). Only the slowest cooling rate ($0.5\,°C\,s^{-1}$)
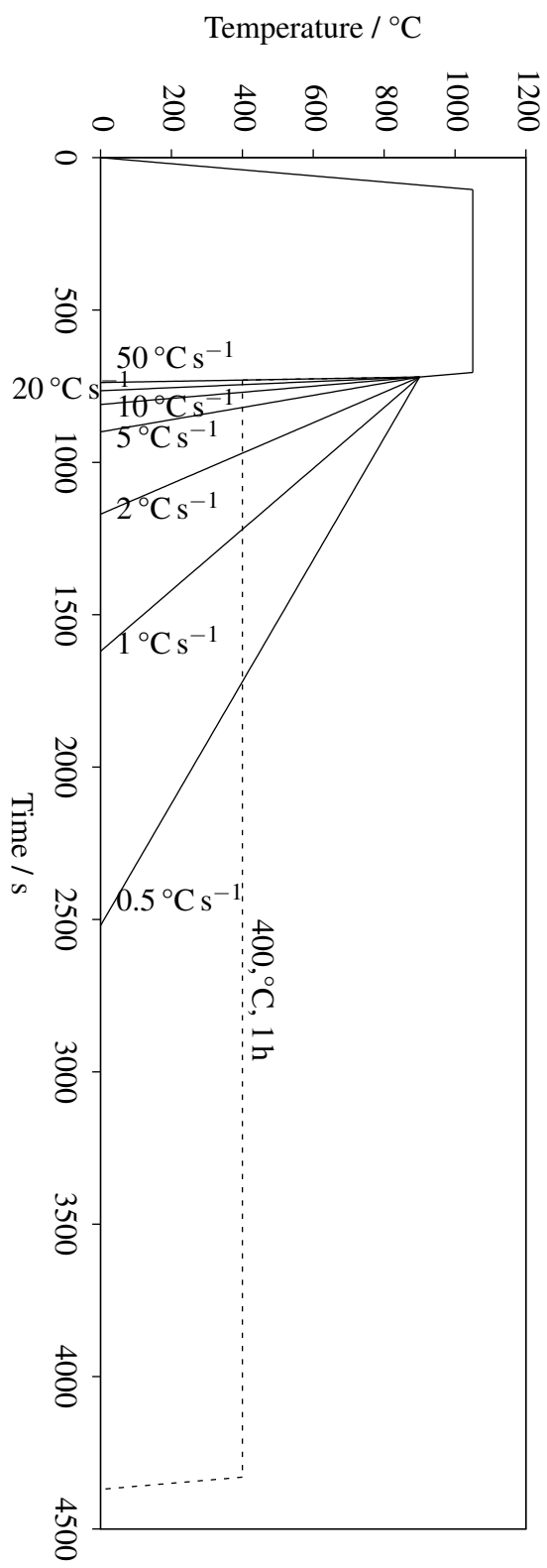
Figure 5.6 Heat treatment cycle imposed during dilatometric experiments for the alloy. IBT refers to isothermal bainitic transformation.

showed detectable deflection on the dilatation–temperature curve for allotriomorphic ferrite formation, enabling the estimation of ferrite–start and ferrite–finish temperatures (F_S and F_F, Fig. 5.7b). No such deflections were observed in the dilatation–temperature curves for 1 and $2\,°C\,s^{-1}$ (Fig. 5.7b) even with feeble presence of α in the microstructures. Cooling rates in excess of $5\,°C\,s^{-1}$ produced predominantly bainitic and/or martensitic microstructures. The amount of bainite decreased with increasing cooling rate. Bainite was absent at $50\,°C\,s^{-1}$ cooling rate. Fig. 5.8 shows the micrographs obtained for all the heat treatments.
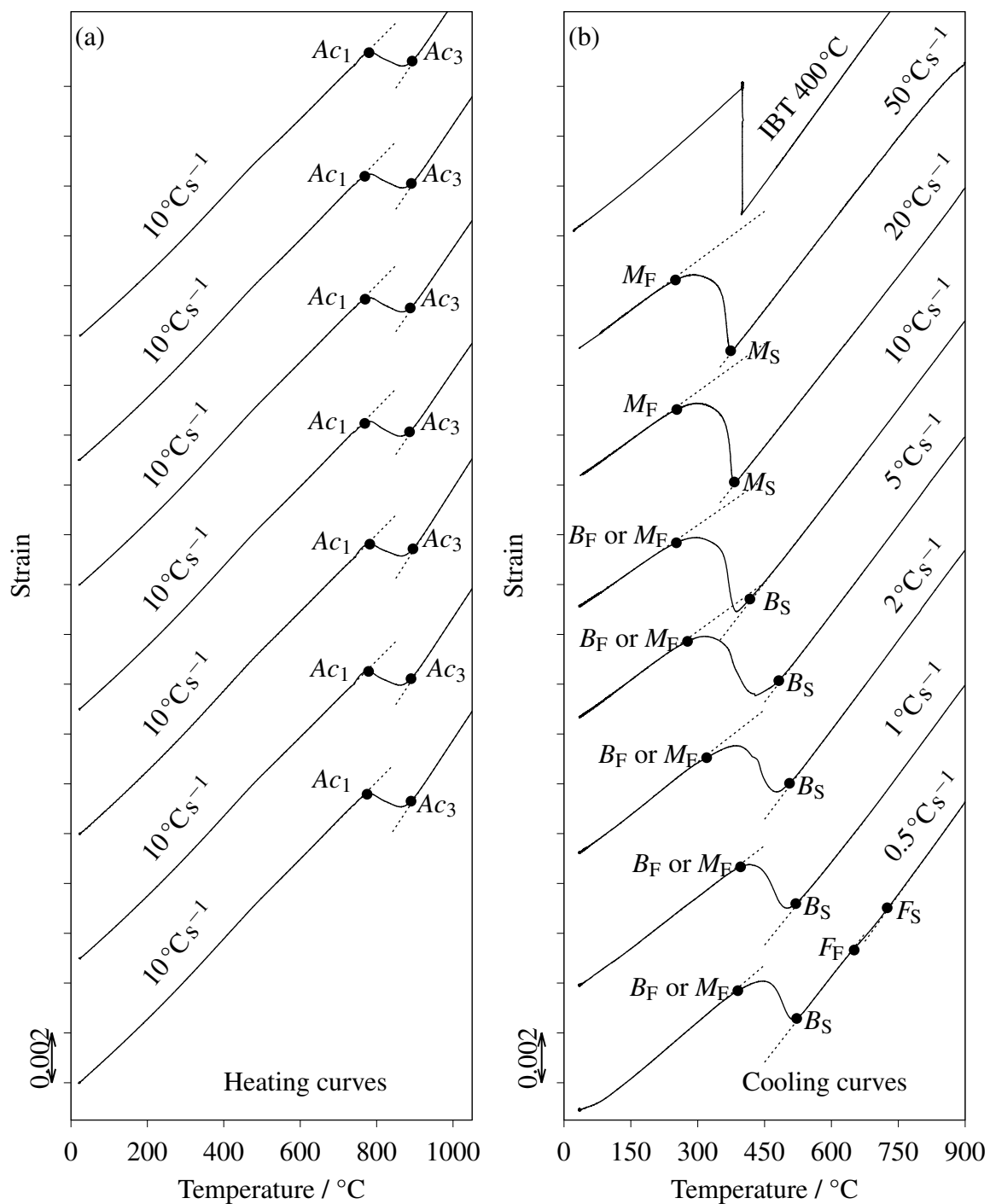
Figure 5.7 Dilatation versus temperature curves during various heating and cooling cycles.
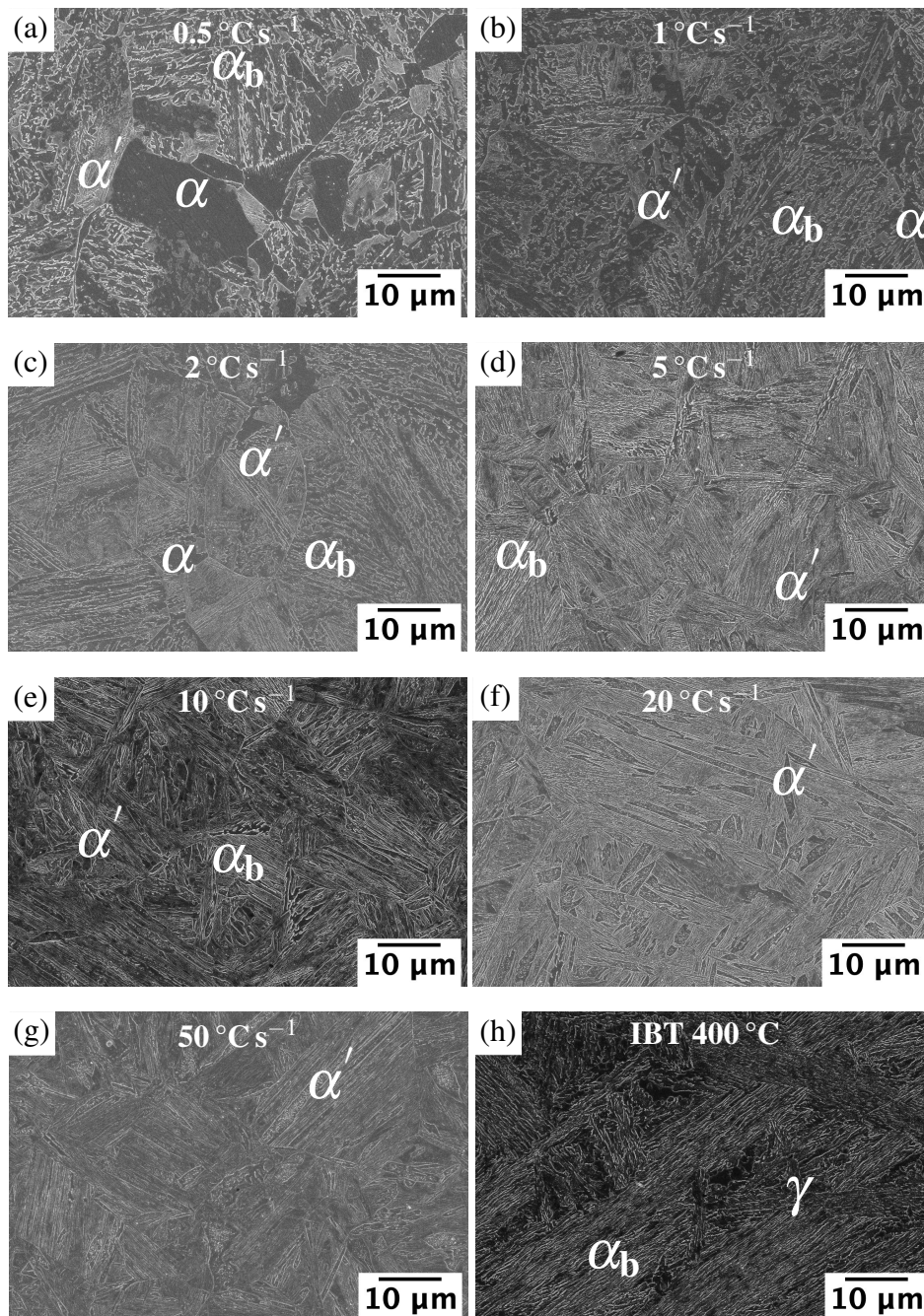
Figure 5.8 Scanning electron micrographs of the different dilatometric samples.

$10\,°\mathrm{C\,s^{-1}}$ was found to be the critical cooling rate to suppress the formation of reconstructive phases, which is close to the predicted cooling rate of $12\,°\mathrm{C\,s^{-1}}$ (TTT diagram, Fig. 5.3). Bainite was obtained during cooling over the range 522–382 °C. Fig. 5.9 is the continuous cooling transformation diagram constructed from dilatometric experiments. The predicted

CCT–start curve derived from TTT and Scheil's additivity matches well for transition temperatures at 0.5, 20 and $50\,°C\,s^{-1}$. At other rates due to the absence of allotriomorphic ferrite it is difficult to draw any correlation. The shaded area in Fig. 5.9 gives the region in which isothermal transformation would lead to a desirable bainitic ferrite and retained austenite microstructure. It is difficult to demarcate the transformation finish temperature as B_F or M_F during simultaneous formation of bainite and martensite at higher cooling rates ($>5\,°C\,s^{-1}$).

Bainitic ferrite with islands of retained austenite/martensite was the microstructure resolved following isothermal transformation at 400 °C, Fig. 5.8h. The microstructure was devoid of any cementite even after 1 h at 400 °C, which corroborates the prediction detailed in Section 5.2.2, where it would require 8×10^4 s to start, much greater than the 3600 s implemented here.
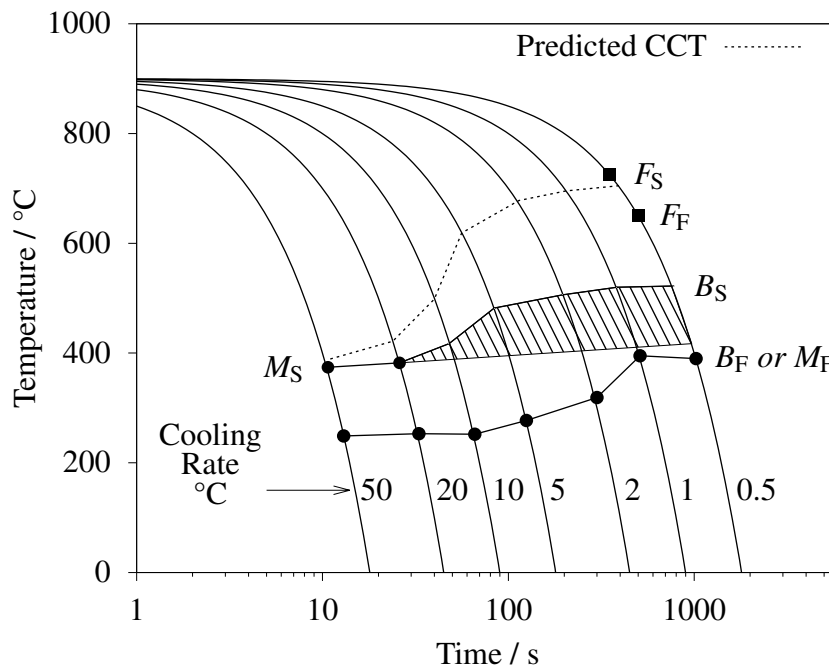
Figure 5.9 The continuous cooling transformation (CCT) diagram constructed using dilatometric data. The dotted line represents the predicted CCT–start curve computed from the TTT curve using the Scheil's additivity principle [193–195].

5.4   Rolled steel

Three tensile specimens (Table 5.4) were tested and samples were subsequently cut from the grip and gauge portions (strained to e_u) of the broken pieces for characterization. Fig 5.10 shows that T1–1 and T1–2 in their grip section are predominantly bainite with retained austenite/martensite, however $V_{\alpha_b} + V_{\alpha'}$ for T1–3 is significantly higher than the other two. Fig. 5.11 shows the fracture surface of the samples T1–1, T1–2 and T–3 after tensile failure, consisting of the expected dimples. The measured void sizes for broken tensile samples T1–1, T1–2 and T1–3 of alloy were $4.8 \pm 2.3 \, \mu m$, $3.9 \pm 2.0 \, \mu m$ and $3.7 \pm 2.6 \, \mu m$ respectively, these sizes are similar to the study by Bhadeshia [196] for untempered ($6.0 \pm 3.0 \, \mu m$) and tempered ($3.4 \pm 2.0 \, \mu m$) upper bainite. The inclusion in Fig. 5.11a was confirmed using EDAX to be a mixture of FeS and MnS, Fig. 5.12. The steel contains aluminium and nitrogen (Table 5.1) conducive to form AlN precipitates, which may act as potential nucleation sites for voids. Some of these voids were associated with large particles of AlN, Fig. 5.13. These particles are completely incoherent from the ferrite matrix and have formed at melting temperatures, consistent with their faceted hexagonal shape. Thus, the ductility (elongation) can be enhanced by the ensuring inclusion free steels. It is said [17] that few coarse particles enhances macroscopic ductility more than a large density of fine particles. Thus control of particle size and/or complete removal of AlN may improve ductility. The presence of martensite in the rolled microstructure (Fig. 5.10) may act as potential sites for void nucleation and reduce the macroscopic ductility.

Table 5.4 Mechanical properties of three samples of the steel. The data was provided by Tata Steel, India.

| Sample No.	Width mm	Thickness mm	Gauge length mm	$\sigma_{0.2}$ MPa	σ_{UTS} MPa	e_u %	e_t %	n
T1–1	12.58	5.05	50.44	618	1115	9.4	15	0.15
T1–2	12.62	5.33	49.63	625	1114	9.5	17	0.16
T1–3	12.58	5.05	50.44	660	1115	10.2	15.6	0.21
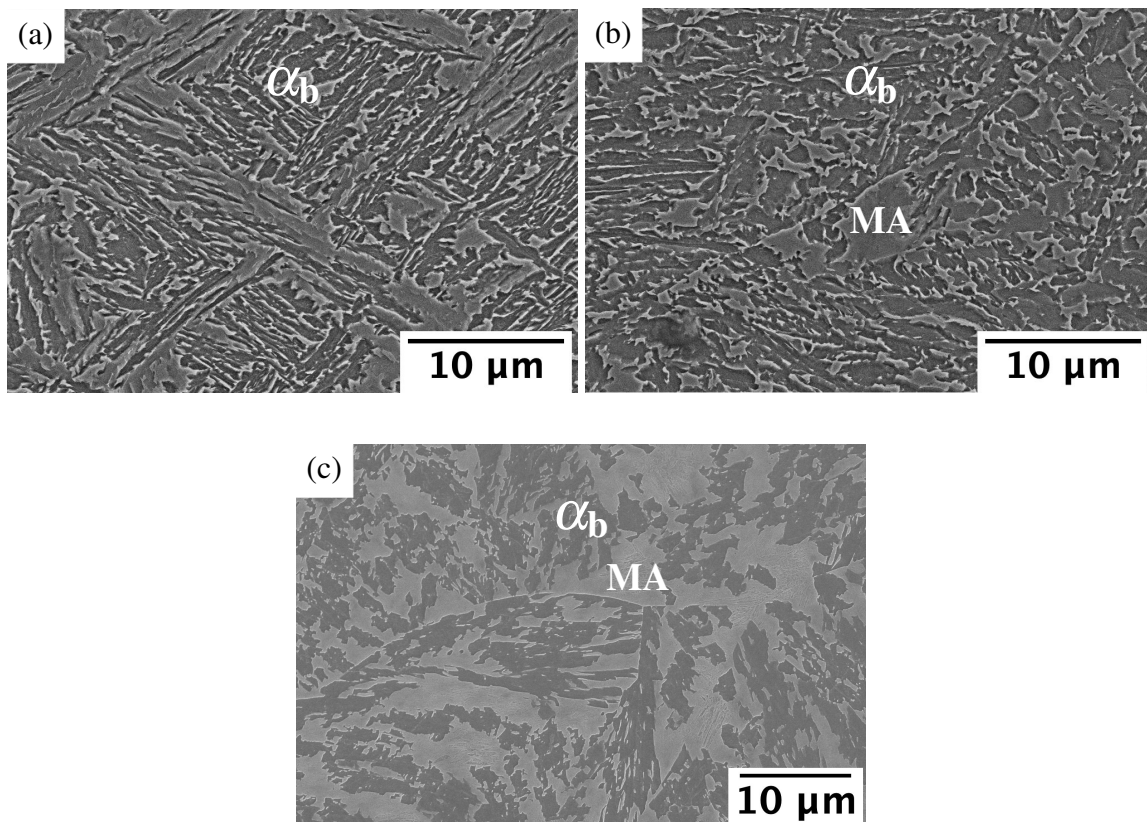
Figure 5.10 Scanning electron micrographs of grip section of tensile sample (a) T1–1, (b) T1–2 and (c) T1–3, heat treated at 1250 °C for 1 hour, followed by finish rolling at 850–930 °C and subsequently isothermally transforming at 400 °C in a salt bath post air cooling.
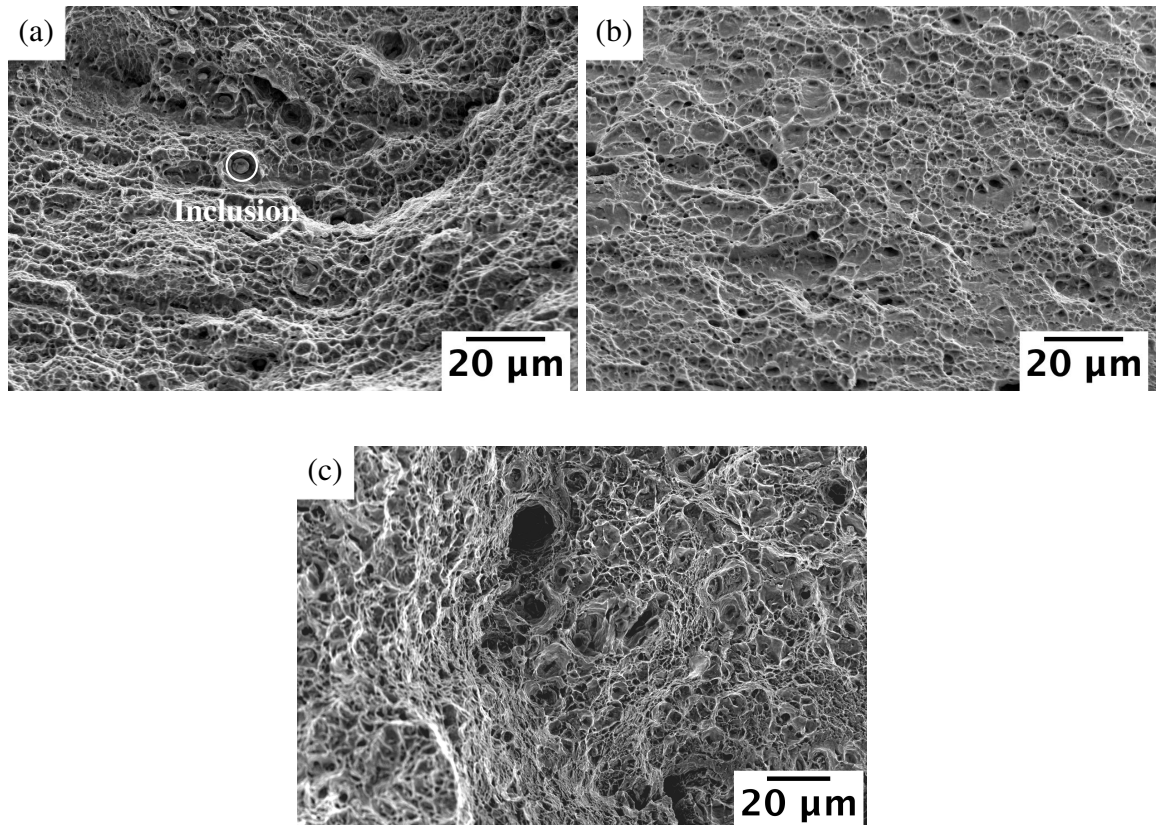
Figure 5.11 Fractography of the tensile samples T1–1, T1–2 and T1–3 showing dimples.
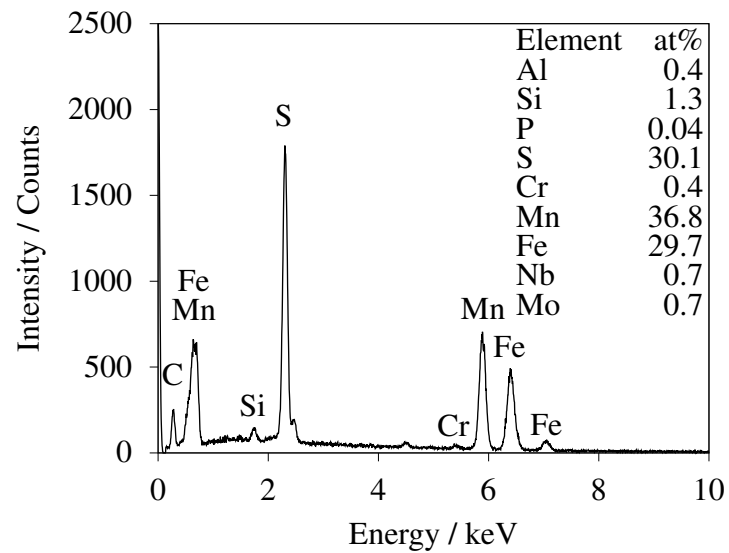
Figure 5.12 Microanalysis of the inclusion observed in sample T1–1 using energy dispersive spectroscopy.

<div align="center">(a)   (b)</div>
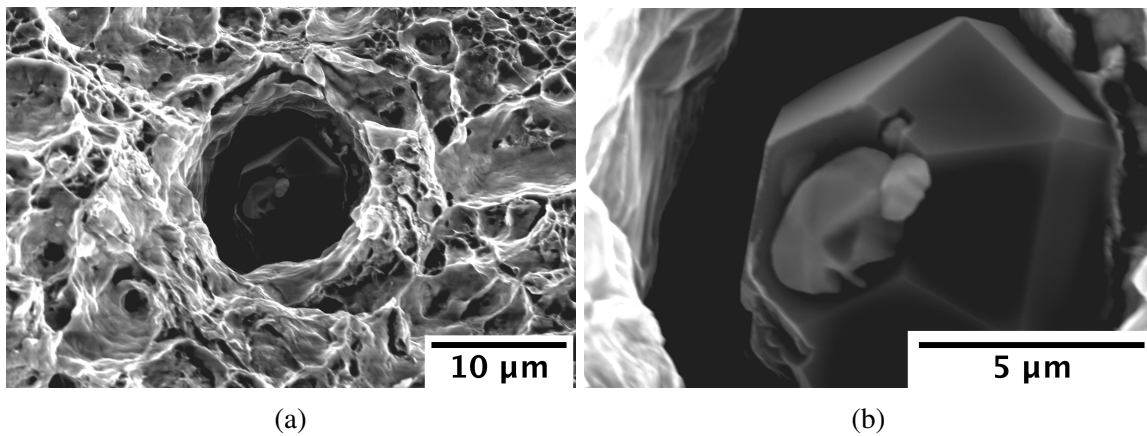
Figure 5.13 (a) Low and (b) high magnification scanning electron image of void on the fracture surface associated with large AlN particles potentially formed in melt during processing of steel. Facets of precipitates showing hexagonal symmetry consistent with the structure of AlN.

5.4.1   X–ray diffraction measurements

The fraction of retained austenite in the 400 °C isothermally treated rolled–samples, before and after tensile testing, was evaluated using X–ray diffraction. Specimens were cut from the grip (undeformed) and gauge portion (corresponding to uniform strain). Samples for X–ray diffraction measurements were prepared in accordance with the experimental procedure described in Chapter 3.

The phase fractions of retained austenite and bainitic ferrite were determined by Rietveld analysis using MAUD (Material Analysis Using Diffraction) [158] software. The raw data were assessed by the goodness of the fit and weighted profile R–factor. The difference plot, i.e. the residue between the data and fit was also examined. Figs. 5.14 and 5.15 show the Rietveld results for the alloy, listed in Table 5.4. Fig. 5.16 shows the corresponding Rietveld refinement data for sample T3–1 that has similar elongation.

As expected, the retained austenite in the grip portion of the alloy is greater than in the gauge for all samples. This confirms the deformation–induced transformation of austenite into martensite. The carbon content in ferrite computed from the lattice parameter using empirical equation [174] showed significant excess ($\sim$0.1 wt%) compared with that expected from equilibrium. This is consistent with reported synchrotron [132, 197] and atom probe tomography (Fig. 4.3) [134] measurements. The carbon content of retained austenite is less than 1 wt% for all the samples listed in Table 5.5, as compared to published data for high–carbon nanostructured bainitic steels (>1.2wt%) [64, 77]. This is attributed to the high isothermal transformational temperature (400 °C). Thus the chemical stability of retained austenite, which is dependent on its carbon content, may be detrimental to elongation. The grip section of sample T1–3 contains nearly half the austenite as observed in the cases of T1–1 and T1–2 samples, but however is 30% more enriched in carbon. This is conclusive of the formation of larger volume fraction of bainite allowing residual austenite being enriched post the transformation at 400 °C.
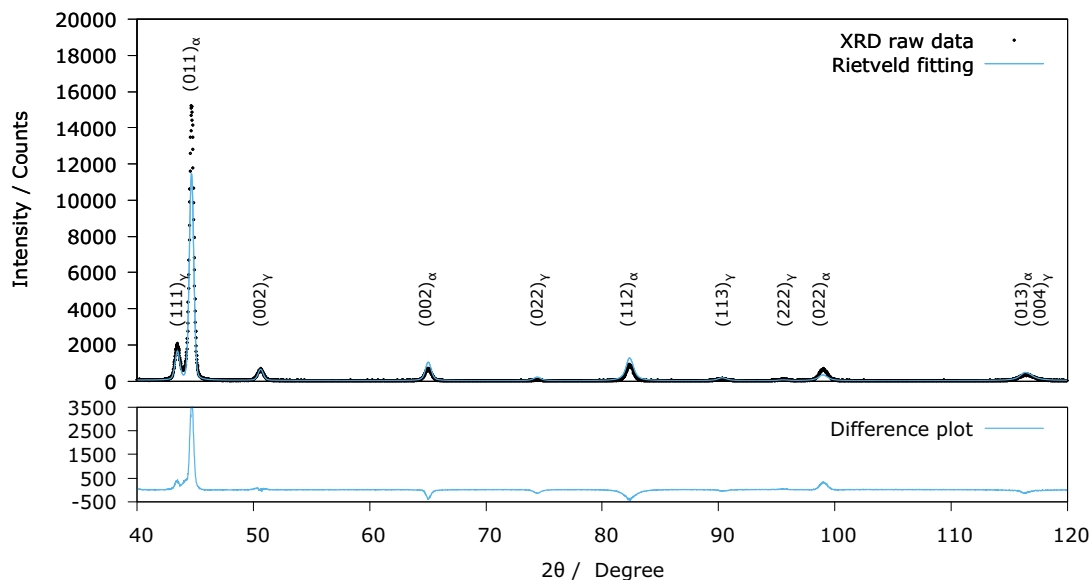
(a) Rietveld analysis of grip portion of sample T1–1.
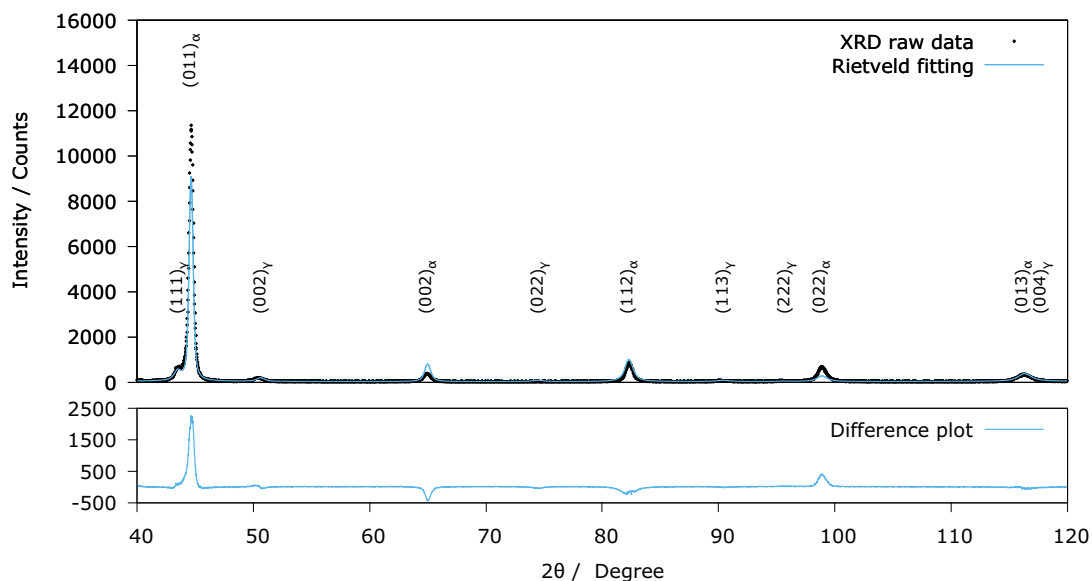
(b) Rietveld analysis of gauge portion of sample T1–1.

Figure 5.14 Raw X–ray data and Rietveld refinement using MAUD of 1000 MPa bainitic steel. Difference plot showing the gap between the raw X–ray data and the Rietveld fit. The X–ray diffraction measurements were done on a PANalytical X'Pert powder diffractometer at R&D, Tata Steel. The black dots represent the raw data and the blue curve is the fitted Rietveld curve.
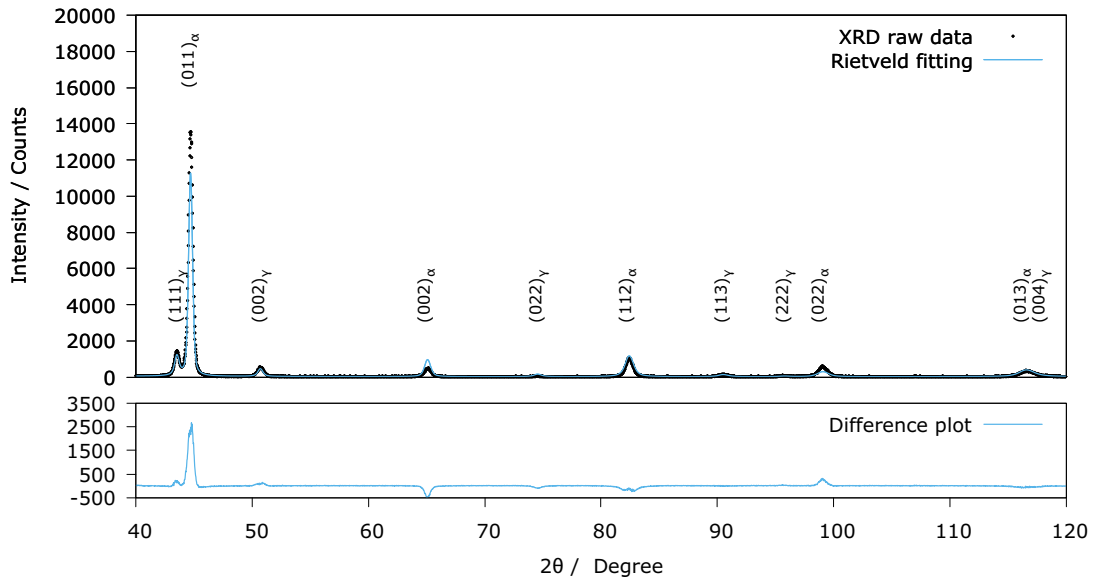
(a) Rietveld analysis of grip portion of sample T1–2..
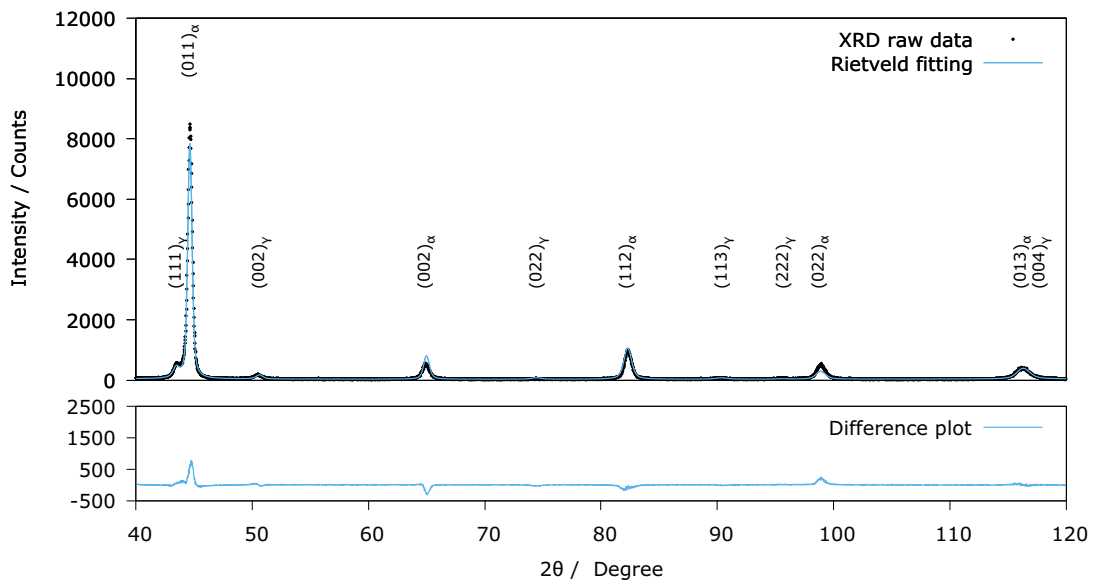
(b) Rietveld analysis of gauge portion of sample T1–2.

Figure 5.15 Raw X–ray data and Rietveld refinement using MAUD of 1000 MPa bainitic steel. Difference plot showing the gap between the raw X–ray data and the Rietveld fit. The X–ray diffraction measurements were done on a PANalytical X'Pert powder diffractometer at R&D, Tata Steel. The black dots represent the raw data and the blue curve is the fitted Rietveld curve.
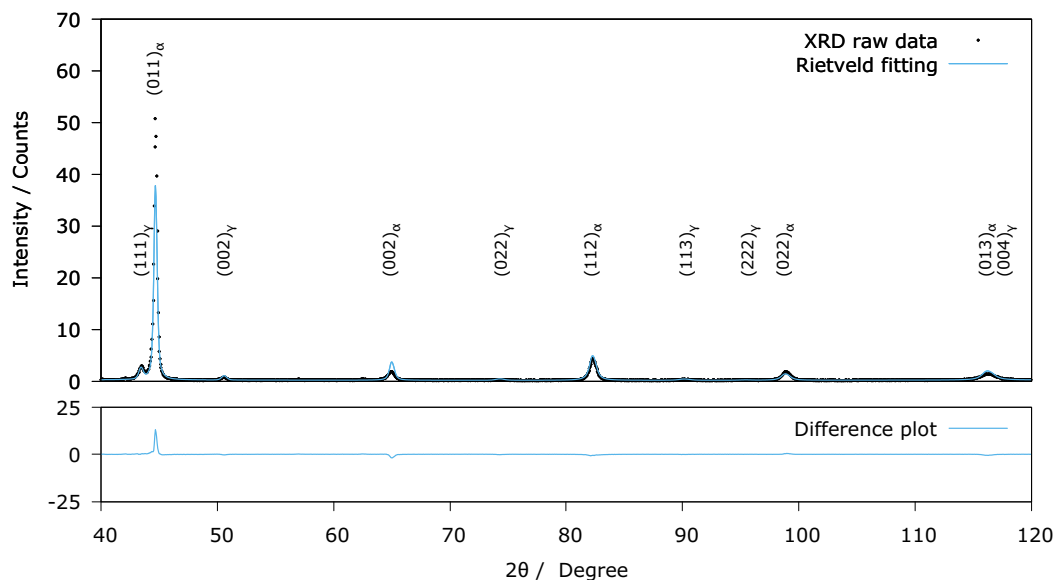
(a) Rietveld analysis of grip portion of Sample T1–3.
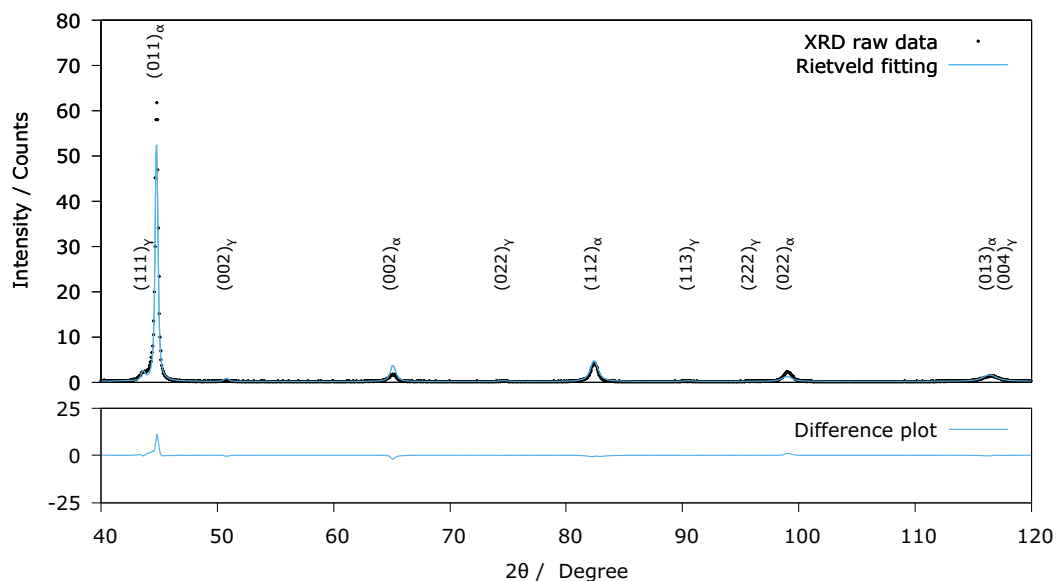
(b) Rietveld analysis of gauge portion of Sample T1–3.

Figure 5.16 Raw X–ray data and Rietveld refinement using MAUD of 1000 MPa bainitic steel. Difference plot showing the gap between the raw X–ray data and the Rietveld fit. The X–ray diffraction measurements were done on a Bruker D8 powder diffractometer at MSM, Cambridge. The black dots represent the raw data and the blue curve is the fitted Rietveld curve.

Table 5.5 Rietveld analysis of the grip and gauge portion of fractured tensile samples done using MAUD software. V_{α_b}–volume fraction of bainitic ferrite, $V_{\alpha'}$–volume fraction of martensite, V_γ–volume fraction of retained austenite, a_α–lattice parameter of ferrite in Angstroms, a_γ–lattice parameter of retained austenite in Angstroms, c_α^e and c_γ^e–carbon contents of ferrite and retained austenite computed using the empirical equation [174] respectively. 1–PANalytical X'Pert (Tata Steel) and 2–Bruker D8 (MSM, Cambridge). c_α^e was not determined in certain cases (T1–1 and T1–2) due to no solution achieved using the empirical equation.

Sample No.	Equipment	$V_{\alpha_b}+V_{\alpha'}$	V_γ	a_α Å	c_α^e wt%	a_γ Å	c_γ^e wt%
T1–1 Grip	1	0.83±0.02	0.17	2.8673±0.0002	–	3.6042±0.0006	0.70±0.02
T1–1 Gauge	1	0.90±0.03	0.10	2.8692±0.0002	0.045±0.01	3.6033±0.0006	0.67±0.02
T1–2 Grip	1	0.86±0.02	0.14	2.8643±0.0002	–	3.5983±0.0006	0.51±0.02
T1–2 Gauge	1	0.92±0.02	0.08	2.8693±0.0002	0.065±0.01	3.6056±0.0006	0.72±0.02
T1–3 Grip	2	0.91±0.05	0.09	2.8704±0.0002	0.094±0.01	3.6112±0.0004	0.91±0.01
T1–3 Gauge	2	0.95±0.03	0.05	2.8692±0.0002	0.043±0.01	3.6031±0.0004	0.66±0.01

5.5 Conclusions

1. Predicted TTT diagrams for the steel showed distinct C–curves for reconstructive and displacive transformations with a critical cooling rate of about $12\,°C\,s^{-1}$ to avoid the formation of reconstructive phases. The experimentally determined critical cooling rate using dilatometry was found to be $10\,°C\,s^{-1}$.

2. The calculated kinetics of cementite precipitation for the steel composition confirmed that 1 wt% silicon is enough to suppress cementite precipitation during isothermal transformation temperatures of 425 °C and 400 °C. When transformed at 375 °C, 1.5 wt% silicon is adequate for suppressing cementite precipitation from austenite. Dilatometry validated the predictions with no cementite following transformation at 400 °C for 1 h.

3. The predicted and measured continuous cooling transformation curves show good correspondence at slow ($0.5\,°C\,s^{-1}$) and high (20 and $50\,°C\,s^{-1}$) cooling rates. The agreement is poor at intermediate cooling rates (1, 2, 5 and $10\,°C\,s^{-1}$) with the predicted CCT curve showing less hardenability than that measured. The measured curve provides the optimum temperature range for isothermal transformation to generate bainitic ferrite with retained austenite microstructure so as to design steels with 30 GPa% characteristics.

4. Dilatometric experiments showed that the alloy possesses good hardenability for achieving tensile strength $> 1000\,\text{MPa}$. This can be confirmed by the presence of only a small amount of allotriomorphic ferrite at the slow cooling rate of $0.5\,°\text{C}\,\text{s}^{-1}$.

5. There is reasonable agreement between a variety of measured transformation–start temperatures and those expected from time–temperature–transformation diagram calculations. This augers well for the goal of the project, which is to design a strong formable steel.

6. Ductile failure is observed in tensile tests on the $400\,°\text{C}$ isothermally transformed samples. Presence of FeS/MnS inclusions leads to the void initiation and subsequent failure. Similar voids tend to nucleate from incoherent large AlN particles. Another plausible reason behind the low ductility could be the presence of martensite in the rolled microstructure. It must be accepted as well that programs such as MATCALC have two essential parameters which involve fitting, i.e. the number density of the nucleation sites and the interfacial energy per unit area during nucleation. The calculations are inevitably sensitive to these parameters.

7. X–ray measurements confirmed excess carbon in bainitic ferrite relative to equilibrium, consistent with published literature. This excess carbon is due to the tetragonal structure of bainitic ferrite which increases the solubility of carbon as compared to the body centred cubic structure.

Chapter 6

Alloy Design

The development of 30 GPa% steels requires the stability of the retained austenite to be optimised by balancing alloying elements, with some consequences on $\Delta G^{\gamma\alpha}$ illustrated in Fig. 6.1.

Cr and Si have similar and less potent effects on $\Delta G^{\gamma\alpha}$, however, Mn and Ni increase the austenite stability. All these estimations have been made using MTDATA software and NPL–Plus database at three different austenite carbon contents of 0.8, 0.9 and 1 wt%. This information was then used to readjust the composition of the alloy in Chapter 5 by reducing the chromium from 1 wt% and increasing the silicon content to compensate the loss in hardenability and increase the bainitic ferrite strength. Alloys A and B were then prepared with 2 wt% Mn and 1.65 wt% Ni respectively, Table 6.1.

The motive was to increase the strength of the commercially available alloy from Tata Steel by 100–200 MPa. This required the increment in solid solution strengthening from Si and Mn in Alloy A. However for alloy B, the same was achieved by the addition of Si and Ni. Mo was also increased to assist in obtaining this increment. The coefficients of solid solution strengthening due to addition of Si, Mn, Ni and Mo are 83, 37, 47 and 11 per wt% of alloying elements which when used as a rule of thumb leads to the design criteria for alloys A and B. Ni content of 1.65 wt% in alloy B was determined by Fig. 6.1, which achieves a $\Delta G^{\gamma\alpha} \approx 2500\,\mathrm{J\,mol^{-1}}$. Alloy C was just a variant of alloy A without containing Nb. The reason for the development of this alloy was to study the effect of austenite grain size post hot deformation on the ductility of TRIP–assisted steels. However, grain refinement in alloy A and B was achieved by changing the austenitization temperature, as a result alloy C was not studied and has not been discussed further. A high carbon variant (alloy D) was made to counter the other alloys in case they fail to achieve 30 GPa% characteristic. But this alloy was again ignored owing to its high carbon content being detrimental for spot weldability.
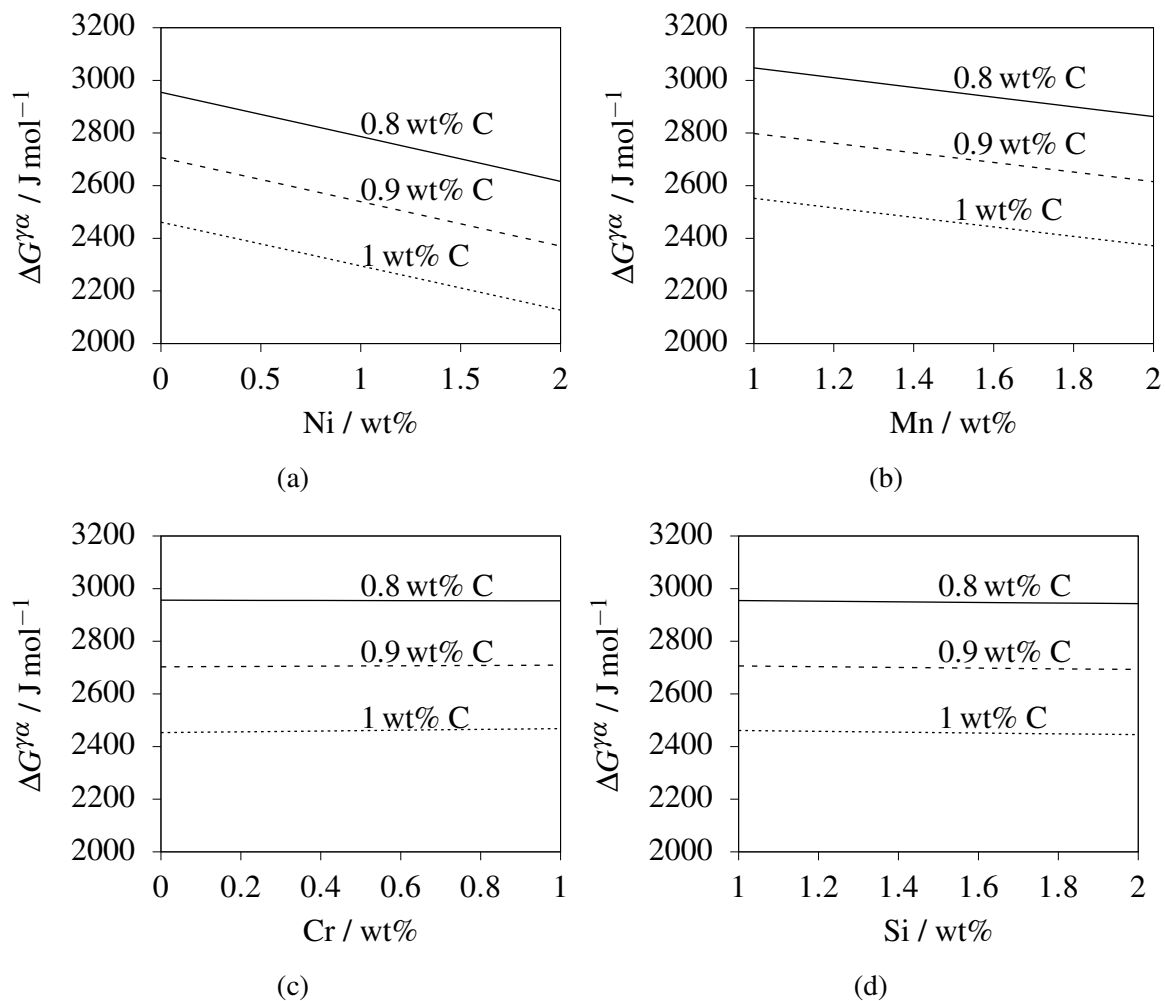
Figure 6.1 Stability of retained austenite with respect to (a) Ni, (b) Mn, (c) Cr and (d) Si added on top of the base alloy in Chapter 5 used for designing steel with 30 GPa characteristics.

Table 6.1 Chemical compositions of steels A, B, C and D .

Steel	Chemical composition / wt%											
	C	Si	Mn	Cr	Ni	Mo	Nb	Al	P	S	N	Cu
Alloy A	0.21	1.91	1.97	0.54	–	0.52	0.025	0.04	0.0023	0.0007	0.0049	–
Alloy B	0.23	1.39	1.35	0.29	1.65	0.45	0.003	0.03	0.0100	0.0100	0.0066	0.15
Alloy C	0.22	1.95	1.97	0.54	–	0.47	–	0.04	0.0026	0.001	0.0050	–
Alloy D	0.41	1.96	1.52	1.01	–	0.36	0.023	0.03	0.0037	0.0026	0.0040	–

6.1 Thermodynamics and kinetics

6.1.1 Thermodynamics

The equilibrium molar phase fractions of the experimental alloys were computed as illustrated in Fig. 6.2. 0.58 and 0.42 were the ferrite and pearlite mole fraction estimated in alloy A and compared to 0.55 and 0.45, respectively for alloy B.
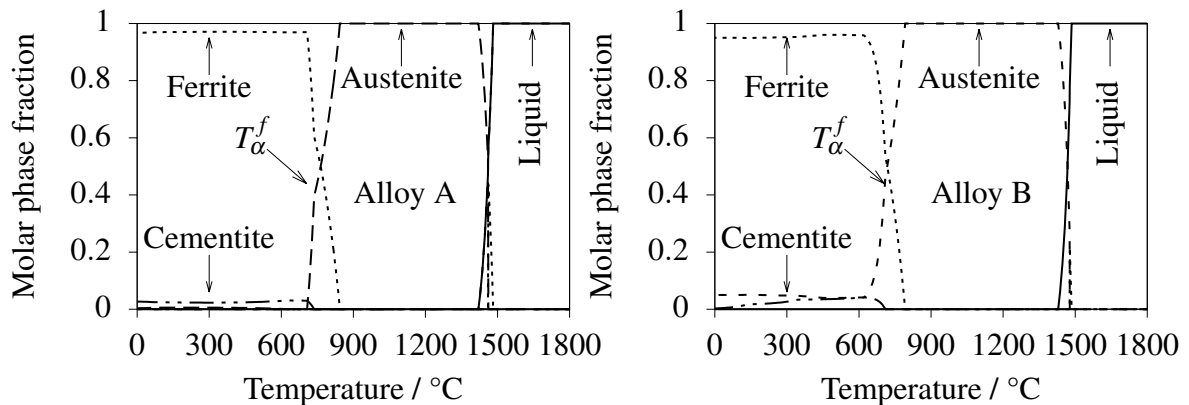

Figure 6.2 Equilibrium molar phase fraction of liquid, ferrite, austenite and cementite computed using THERMOCALC and TCFE8 database. T_α^f denotes the ferrite phase fraction that exists before cementite precipitation becomes possible.

6.1.2 Kinetics

Fig. 6.3 shows the experimentally determined continuous cooling transformation (CCT) diagrams using the DIL805 A/D dilatometer (Chapter 3). The heating rate to the austenitization temperature (T_γ) of 1050 °C was 5 °C s^{-1} followed by holding for 10 min prior to cooling at rates in the range 0.025–20 °C s^{-1}. The transition temperatures thus measured are in Table 6.2. The mean linear intercept of austenite grains ($\bar{L}_\gamma$) for alloys A and B were 48±8 and 42±9 µm respectively. The microstructure obtained at slow cooling rates (0.025–0.2 °Cs^{-1}) for alloy A is a mixture of allotriomorphic ferrite and bainite with the proportion of latter increasing with cooling rate. A similar trend was obtained in alloy B, except that allotriomorphic ferrite was almost absent at 0.2 °Cs^{-1}.

Intermediate cooling rates (0.5–5 °Cs^{-1}) generated a mixture of bainite and martensite and at the highest cooling rates of 10 and 20 °Cs^{-1}, martensite formed in both alloys. Figs. 6.4 and 6.5 show the microstructures generated using dilatometry.
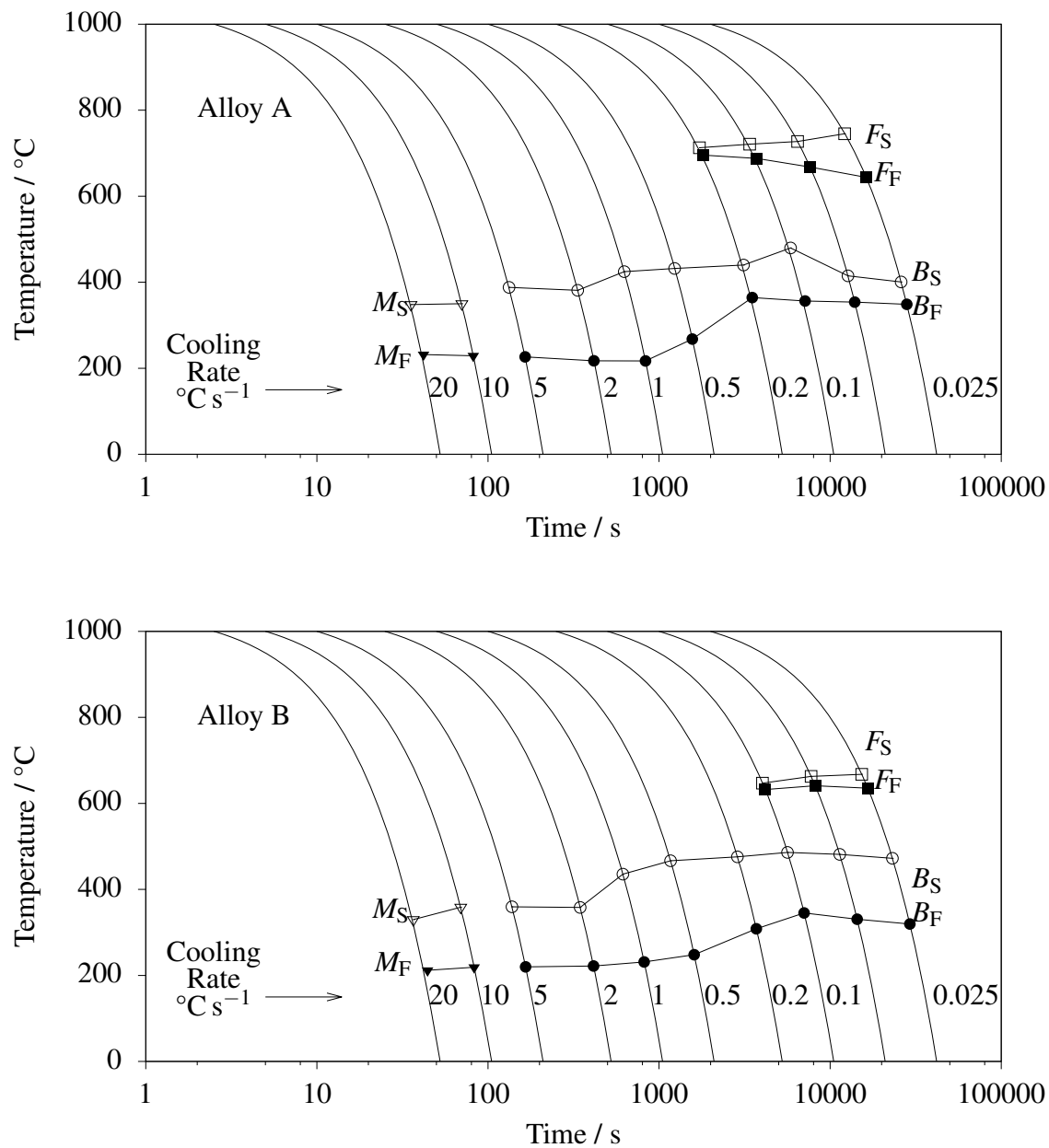
Figure 6.3 Continuous cooling transformation diagrams constructed using dilatometry. The transformation temperatures were determined using the offset method [192]

.

Table 6.2 Transition temperatures.

Alloys	Ac_1 / °C	Ac_3 / °C	M_S / °C
Alloy A	783±12	893±12	357±12
Alloy B	747±12	841±12	343±12
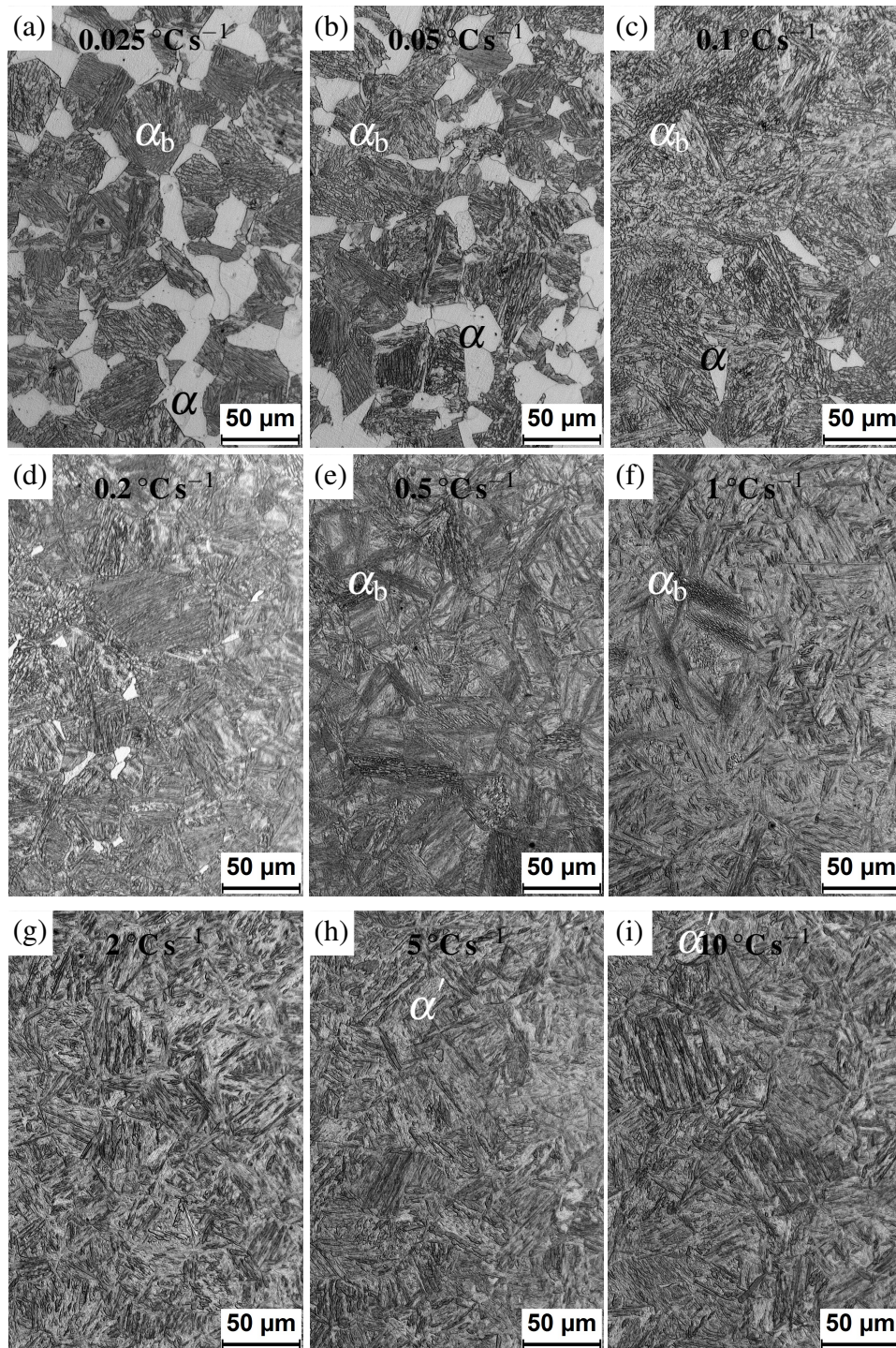
Figure 6.4 Optical microstructure of alloy A cooled at different cooling rates from austenitization temperature of 1050 °C after soaking for 10 min in dilatometer.
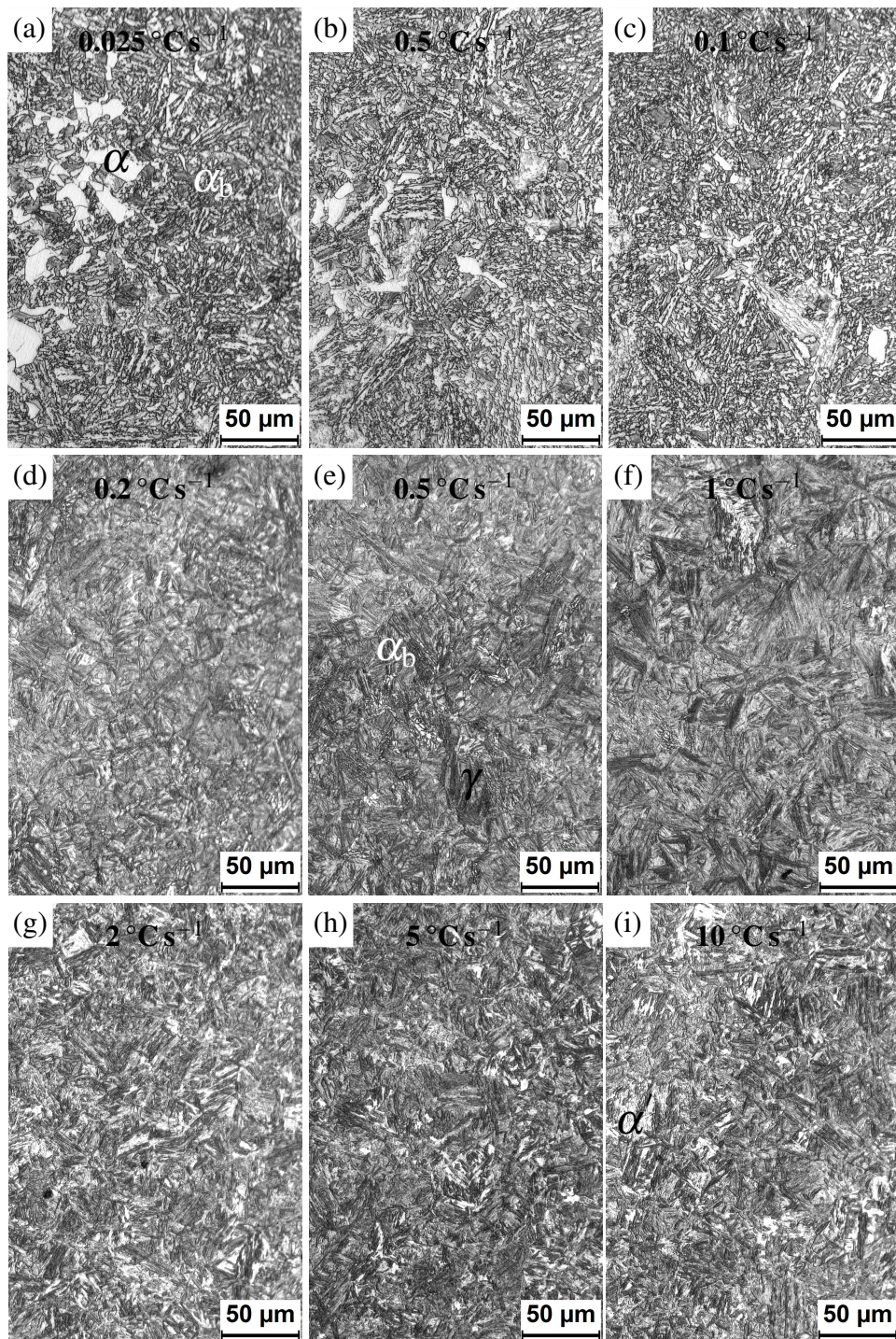
Figure 6.5 Optical microstructure of alloy B cooled at different cooling rates from austenitization temperature of 1050 °C after soaking for 10 min in dilatometer.

The dilation curve for cooling at 0.025 °C s^{-1} shows two humps (Fig. 6.6) corresponding to allotriomorphic ferrite and bainite, consistent with the metallographs in Figs. 6.4 and 6.5.

The first hump in alloy A is more prominent than alloy B, because of its greater fraction of allotriomorphic ferrite. This difference reflects the higher hardenability of alloy B. The fraction of allotriomorphic ferrite was measured using optical micrographs processed in ImageJ software, given that it is easy to distinguish it from bainite. The austenite retained was determined using X–ray diffraction and Rietveld analysis. Fig 6.7 shows the microstructural trends. Increasing the cooling rate natually leads to greater fractions of bainite or martensite. The amount of retained austenite reaches a maximum at $0.1\,°C\,s^{-1}$.
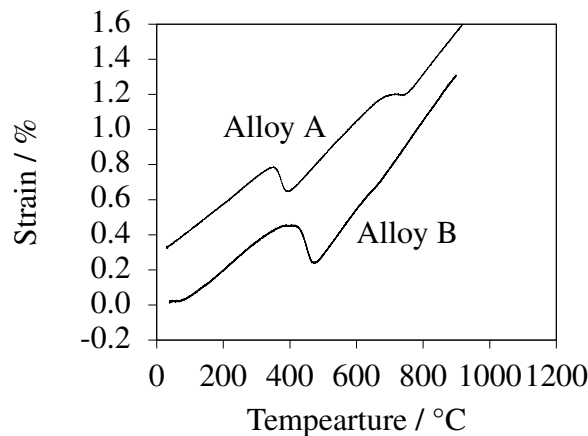

Figure 6.6 Strain due to dilatation versus temperature curve for cooling at $0.025\,°C\,s^{-1}$ showing two humps suggesting the formation of allotriomorphic ferrite followed by bainite.

Fig. 6.8 shows that the $\{110\}_\alpha$ ferrite peak splits into two when the alloys are cooled at $0.025\,°C\,s^{-1}$, with the phenomenon being more pronounced in alloy A which contains nearly 30% allotriomorphic ferrite as compared to just 10% in alloy B. Allotriomorphic ferrite is due to reconstructive transfer and hence has a lesser dislocation density than any bainite or martensite. And of course, the harder phases are likely to contain more carbon in solution. The separation of the $\{110\}$ peak can be expected only when the allotriomorphic ferrite content is large because otherwise, the peak broadening due to α_b/α' overwhelms the α.
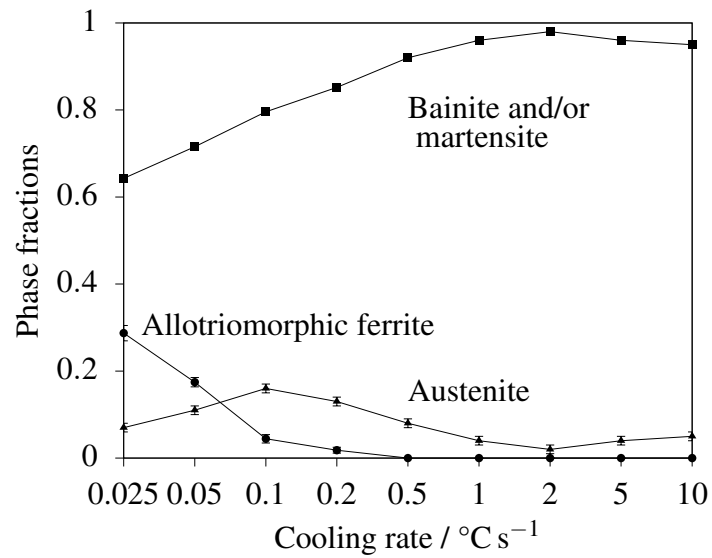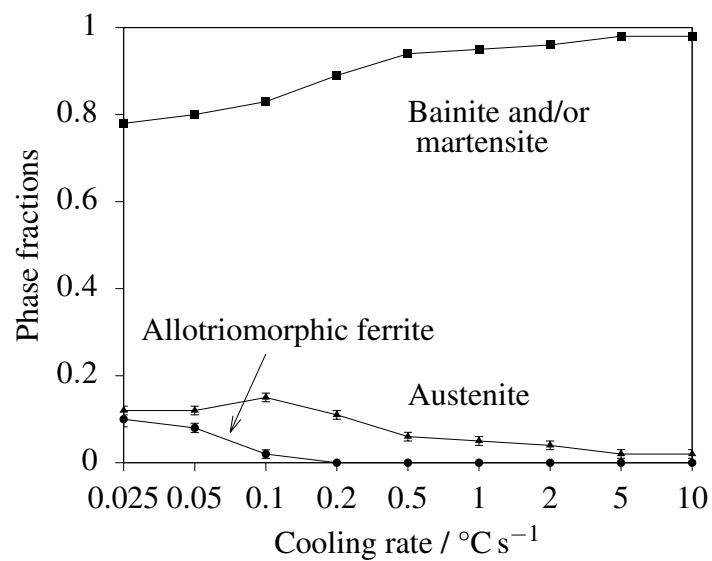
Figure 6.7 Measured volume fractions of allotriomorphic ferrite, bainite, martensite and retained austenite for (a) alloy A and (b) alloy B at different continuous cooling rates.
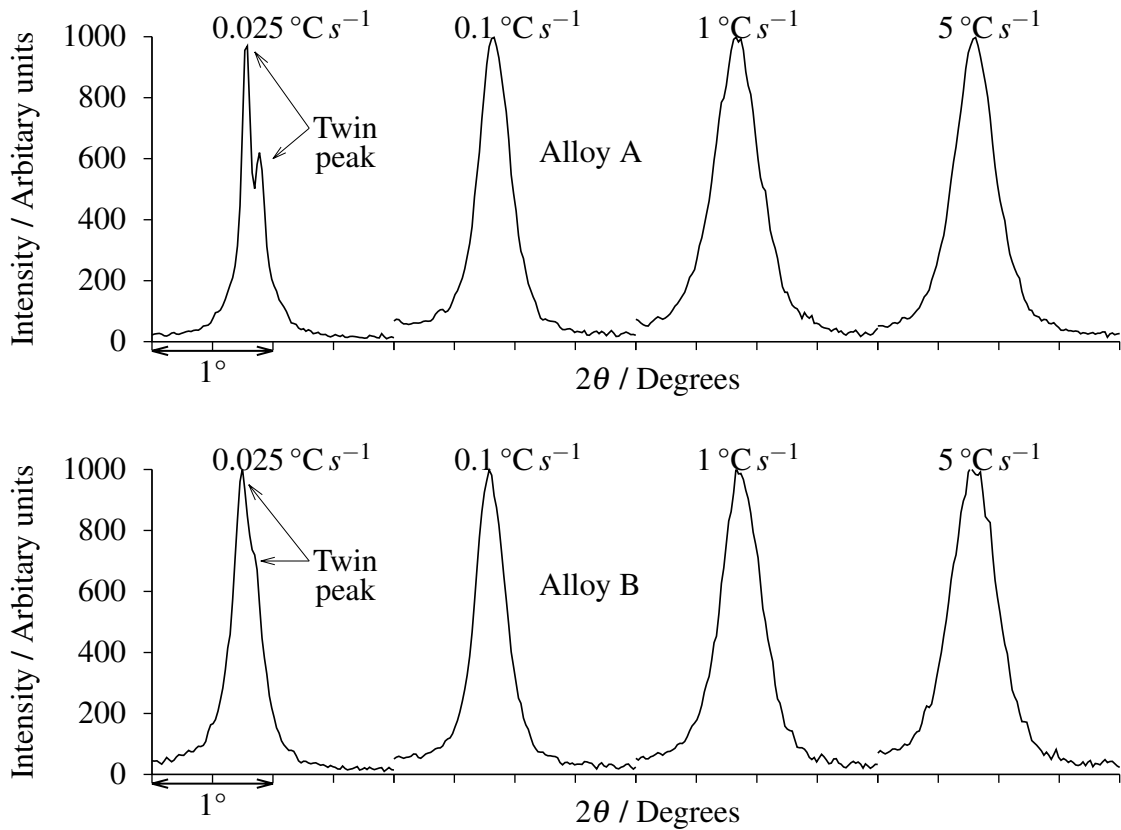
Figure 6.8 {110} peak of ferrite showing the change in shape as cooling rate increases.

The lattice parameters of retained austenite (a_γ) and inferred carbon content (c_γ^e) [174] are plotted in Fig. 6.9. Fig. 6.9a, where the microstructure is $\alpha+\alpha_b$, shows a decreasing trend in a_γ with increasing cooling rate, due to the reduction in carbon enrichment due to the formation of allotriomorphic ferrite. When the microstructure is essentially α_b, a_γ increases again. For microstructure α_b and α', a_γ is the lowest because much of the carbon is then in α'. The parameter a_γ for alloy B given in Fig. 6.9 shows similar trend as alloy A, the only difference being in the $\alpha+\alpha_b$ domain where the higher hardenability means that the carbon enrichment is reduced.

The hardness data (Fig. 6.10) correlate with the microstructures deduced metallographically.
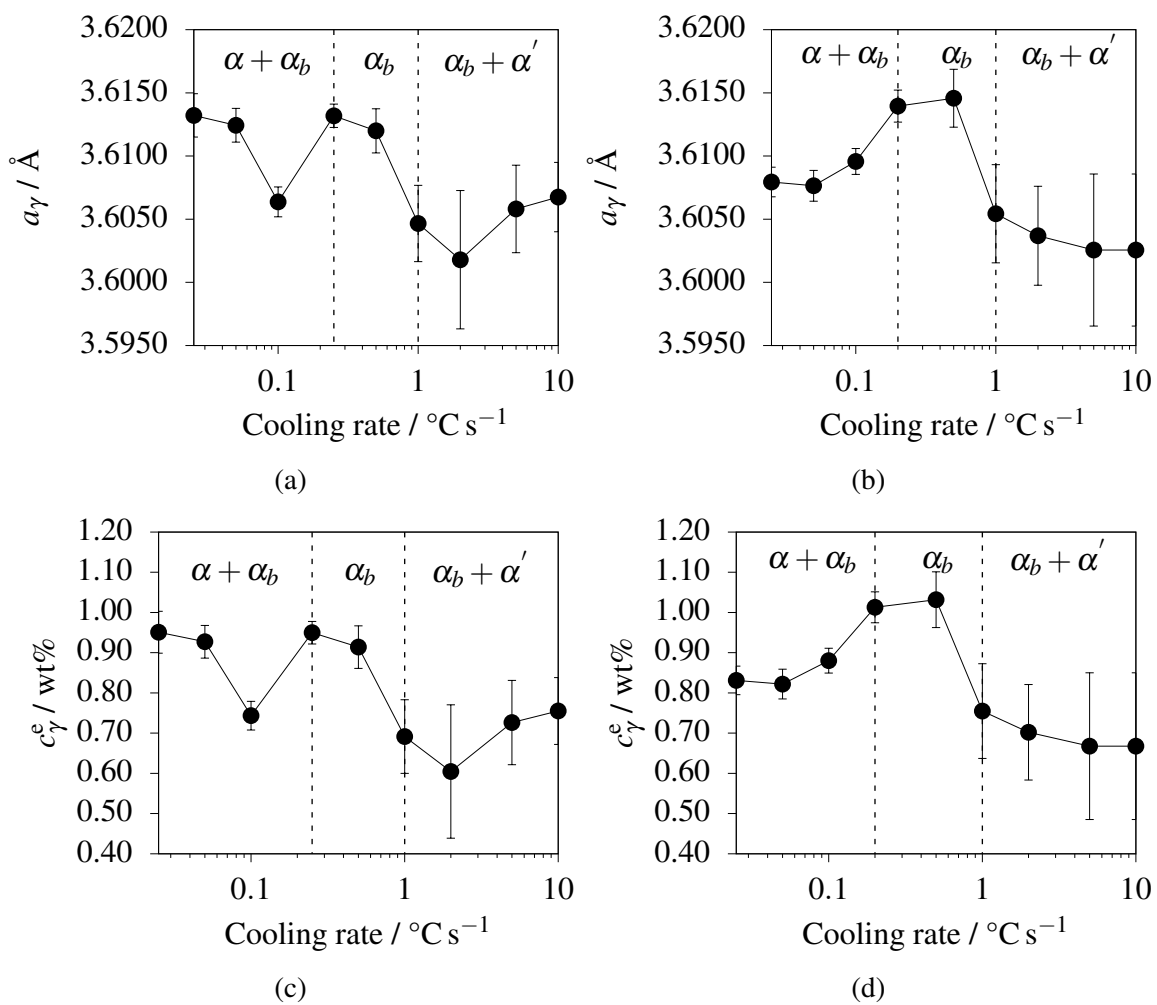
Figure 6.9 The lattice parameter of retained austenite for (a) alloy A and (b) alloy B measured form the X–ray diffraction data for various continuous cooling rates. The carbon content of the retained austenite evaluated from the the lattice parameters using the Dyson and Holmes equation [174] for (c) alloy A and (d) alloy B.
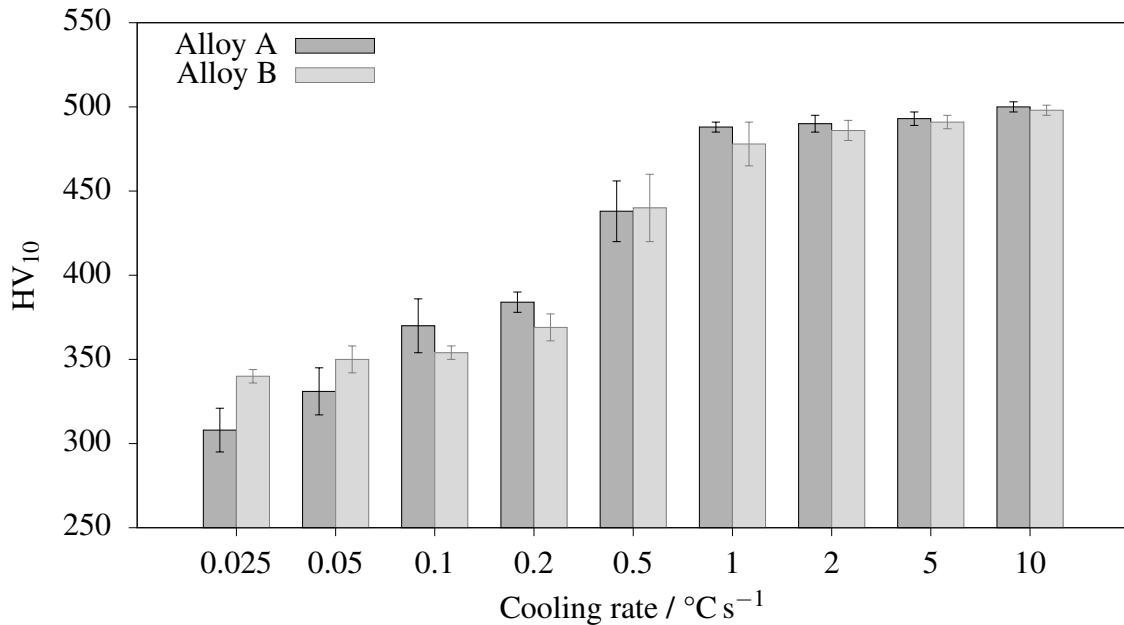
Figure 6.10 Measured bulk hardness (HV_{10}) as a function of cooling rates following austenitization at 1050 °C for 10 min.

6.2 Isothermal bainitic transformation

The dilatometer experiments helped to narrow down the temperature at which bainite can be obtained isothermally. Three temperatures of 375, 400 and 425 °C were chosen and experiments were conducted to optimise the processing parameters and subsequently used to produce bulk samples for the determination of mechanical properties.

Fig. 6.11 shows the T_0 and T_0' curves for alloys, computed using MTTTDATA program coupled with NPL–plus database for steels [187]. The experimentally determined c_γ^e points where the bainitic transformation stops at 375, 400 and 425 °C are plotted to show that the measured concentrations are much more consistent with the T_0 criteria than the paraequilibrium Ae_3. The TTT diagrams for alloys A and B are computed similarly using MTTTDATA and the time taken for the bainitic transformation to start is experimentally determined and plotted on Fig. 6.12. It can be observed that the start of the transformation is predicted well for both alloys.

The progress of the transformation as a function of time is shown in Fig. 6.13. Each heat treatment is identified, for example as follow 1050_10_375, representing the austenitization temperature (T_γ), austenitization time (t_γ) in minutes and the isothermal transformation temperature (T_I). The results are as expected, i.e., faster rate of transformation and greater fraction of transformation at lower temperatures. The further transformation takes place
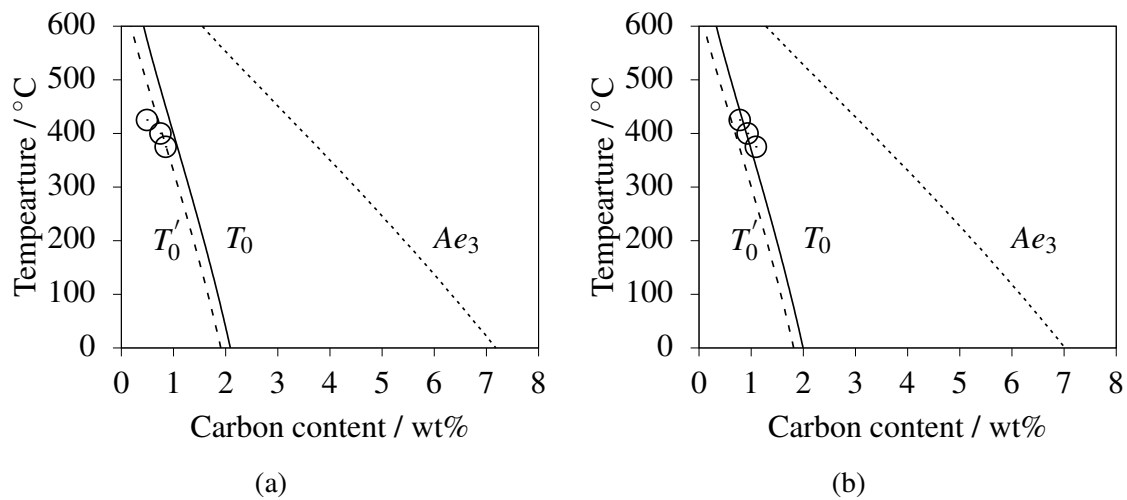
Figure 6.11 T_0, T_0' and Ae_3 curve for (a) alloy A (b) alloy B. The circles are experimentally determined carbon content in retained austenite at 375, 400 and 425 °C.
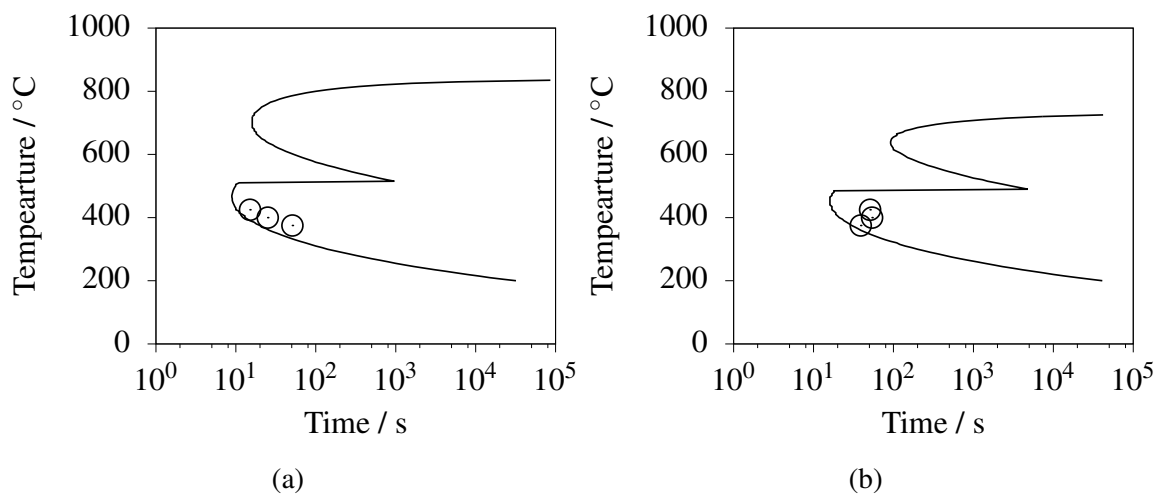

Figure 6.12 Predicted TTT curves for initiation of transformation of (a) alloy A and (b) alloy B using MTTTDATA. The circles represent the experimentally determined time for bainitic transformation start for isothermal holding at 375, 400 and 425 °C.

during cooling from the isothermal temperatures, as indicated by the deviation from the expected constant thermal contraction strain (Fig. 6.14) [192]. The onset of martensitic transformation is particularly prominent when cooling from 425 °C, because the amount of bainite at that temperature is relatively small, leaving austenite to further transform on cooling. Therefore, the retained austenite measured at the ambient temperature is not a reflection of that left untransformed at the isothermal transformation temperature.
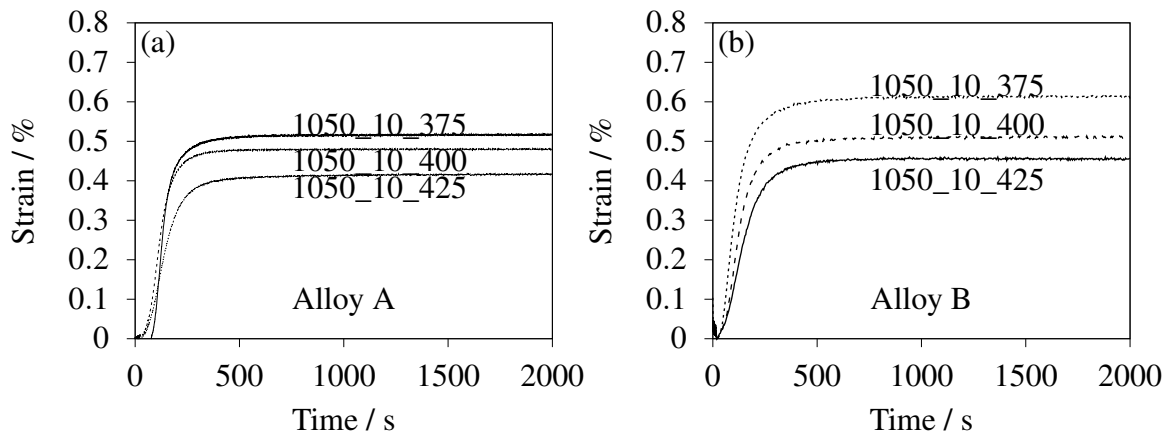
Figure 6.13 Kinetics of isothermal bainitic transformation for both alloys.
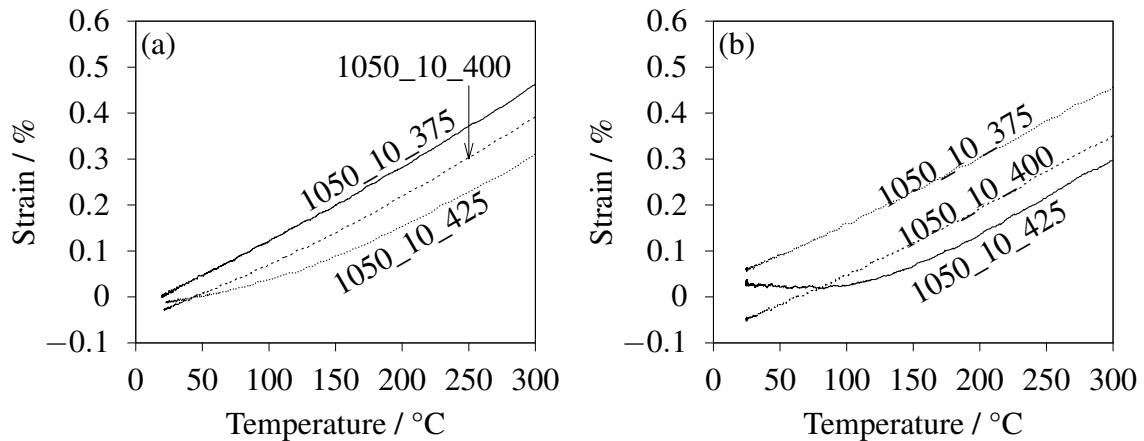

Figure 6.14 Dilatation curves during cooling to room temperature from isothermal bainitic transformation temperatures for (a) alloy A and (b) alloy B.

Larger samples for mechanical tests were austenitized in a muffle furnace then transformed isothermally in a fluidised bed containing alumina sand which is resistance heated,

and fluidized by compressed air at 30 PSI pressure. The austenitization time was increased to 30 min due to the larger sample sizes (12 mm diameter and 140 mm long). Table 6.3 lists the phase fractions and corresponding hardness data.

Table 6.3 Phase fraction and hardness data summarised. $V_{\alpha'}$ measured from, the deviation of strain (dilatation) from linearity during cooling from the isothermal transformation. V_γ estimated from X–ray diffraction. V_{α_b} then computed by subtracting V_γ and $V_{\alpha'}$ from unity.

Alloy	Heat Treatment	V_{α_b}	$V_{\alpha'}$	Dilatometer DIL805 V_γ	Hardness	Fluidised bed V_γ	Hardness
	1050 °C, 375 °C	0.89	0.02±0.01	0.09±0.02	417±12	0.13±0.02	412±4
A	1050 °C, 400 °C	0.84	0.04±0.01	0.12±0.02	398±3	0.15±0.02	392±2
	1050 °C, 425 °C	0.79	0.11±0.03	0.10±0.02	420±10	0.11±0.02	409±2
	1050 °C, 375 °C	0.88	0.03±0.01	0.09±0.02	401±13	0.14±0.03	377±4
B	1050 °C, 400 °C	0.81	0.04±0.01	0.15±0.02	362±6	0.16±0.03	358±4
	1050 °C, 425 °C	0.77	0.12±0.03	0.11±0.02	401±2	0.12±0.02	365±10

The parameter V_γ is systematically higher for the larger samples as against the dilatometer samples, Table 6.3. Also, the austenite lattice parameter is not uniform after isothermal transformation to bainite. This is evident from the deconvolution of the experimentally determined austenite peaks into two γ peaks during Rietveld refinement, Fig. 4.6. The separation between a_γ is more pronounced for dilatometer samples due to carbon inhomogeneity, due to shorter t_γ. Difference in grain size may also cause this, but at 1050 °C, increment in austenitization time from 600 s to 1800 s causes just an increase of ∼8 μm in grain size [198]. Similar nonuniform distribution of carbon in the residual austenite associated with bainitic ferrite was observed by Waugh *et al.* using atom probe [199]. Microstructures showing progressive increase in MA constituents with increasing isothermal transformation temperatures, Fig 6.16.
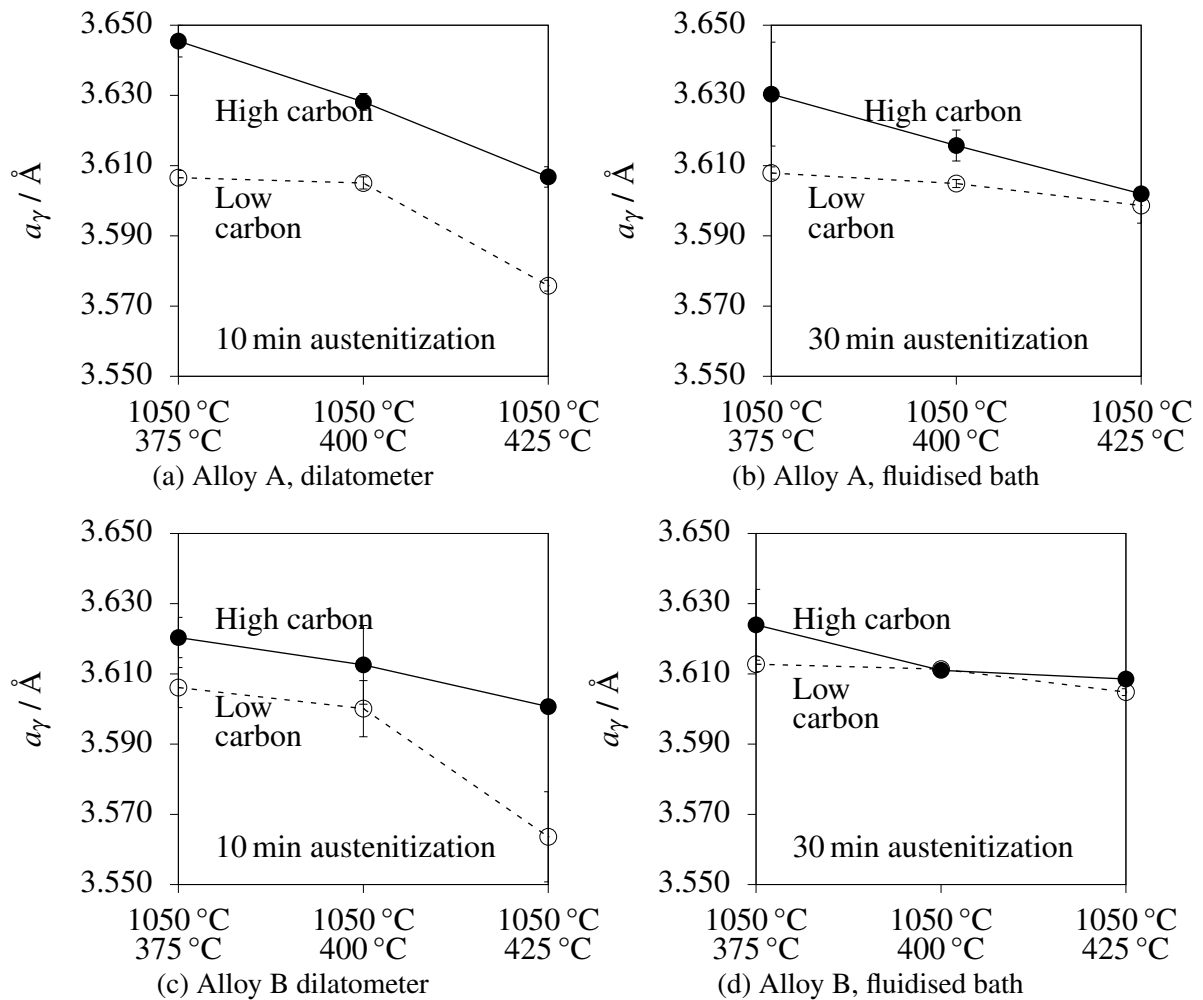
Figure 6.15 Deconvolution of austenite peak into high carbon and low carbon austenite peaks during Rietveld refinement showing greater separation for shorter austenitization time.
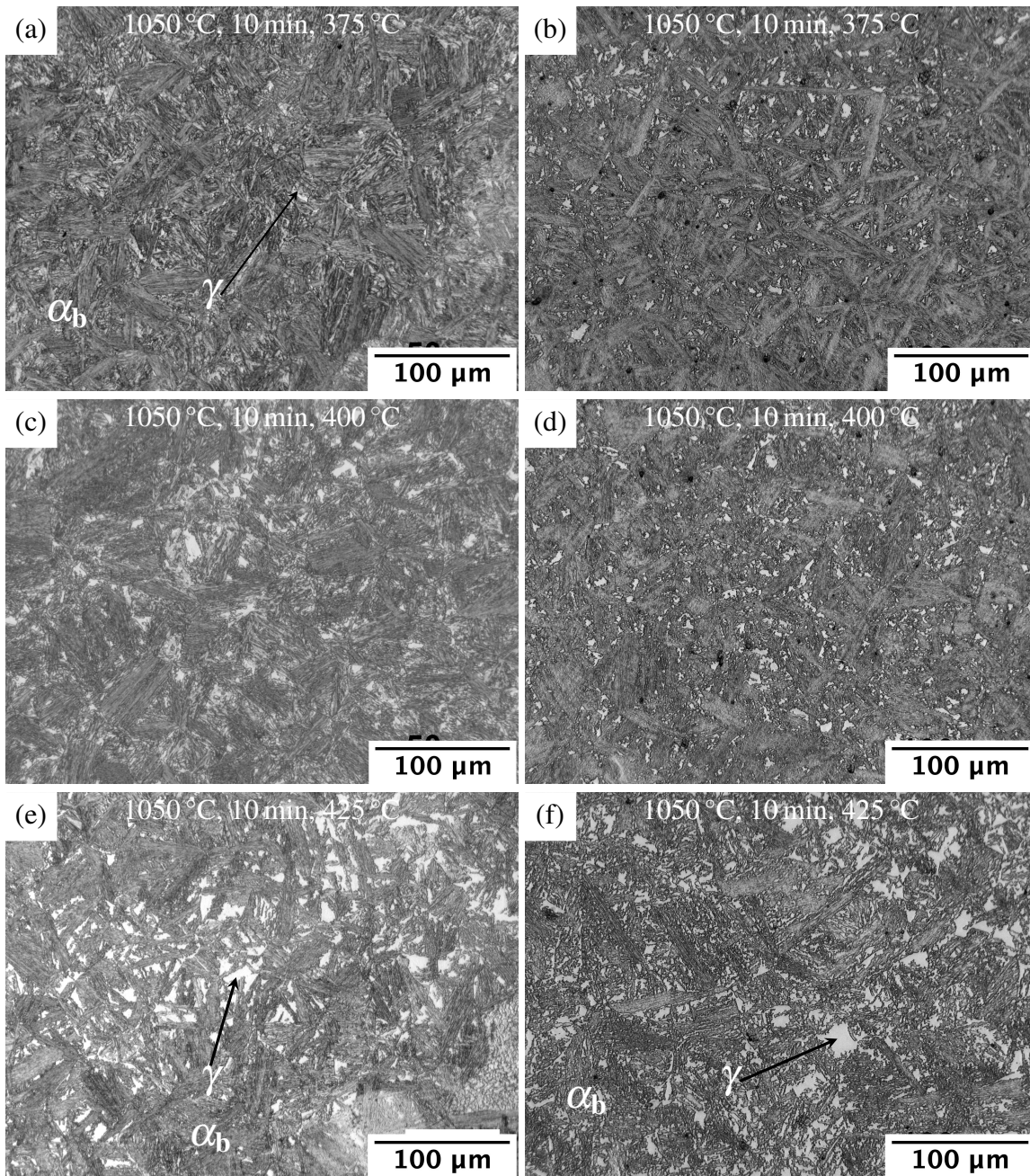
Figure 6.16 Optical micrographs of isothermally transformed samples of (a, c, e) alloy A and (b, d, f) alloy B.

6.3 Tensile properties

Tensile specimens were machined from cylindrical rods after austenitization at 1050 °C for 30 min and then isothermally transformed in a fluidised bed. The tensile tests were performed in accordance to the method outlined in experimental procedure.

6.3.1 Alloy A

For alloy A T_I was 375 and 400 °C to minimise the amount of martensite, with an austenite content of 13.4 and 14.7% respectively (Table 6.3). The tensile curves are given in Fig. 6.17. The incremental work hardening computed as n–value $=$ $d(\ln \sigma)/d(\ln \varepsilon)$ is also plotted, where σ is the stress and ε the plastic strain. Strength ductility products of 26–28 GPa% were achieved, Table 6.4. Elevated temperature (100 °C) tests were conducted to see if a change in stability of the γ has an effect on ductility. The latter increased by nearly 3% while the ultimate tensile strength dropped by 167 and 51 MPa respectively. Increment in $\sigma_{0.2}$ at 100 °C is attributed to stronger interactions between solutes and dislocations.
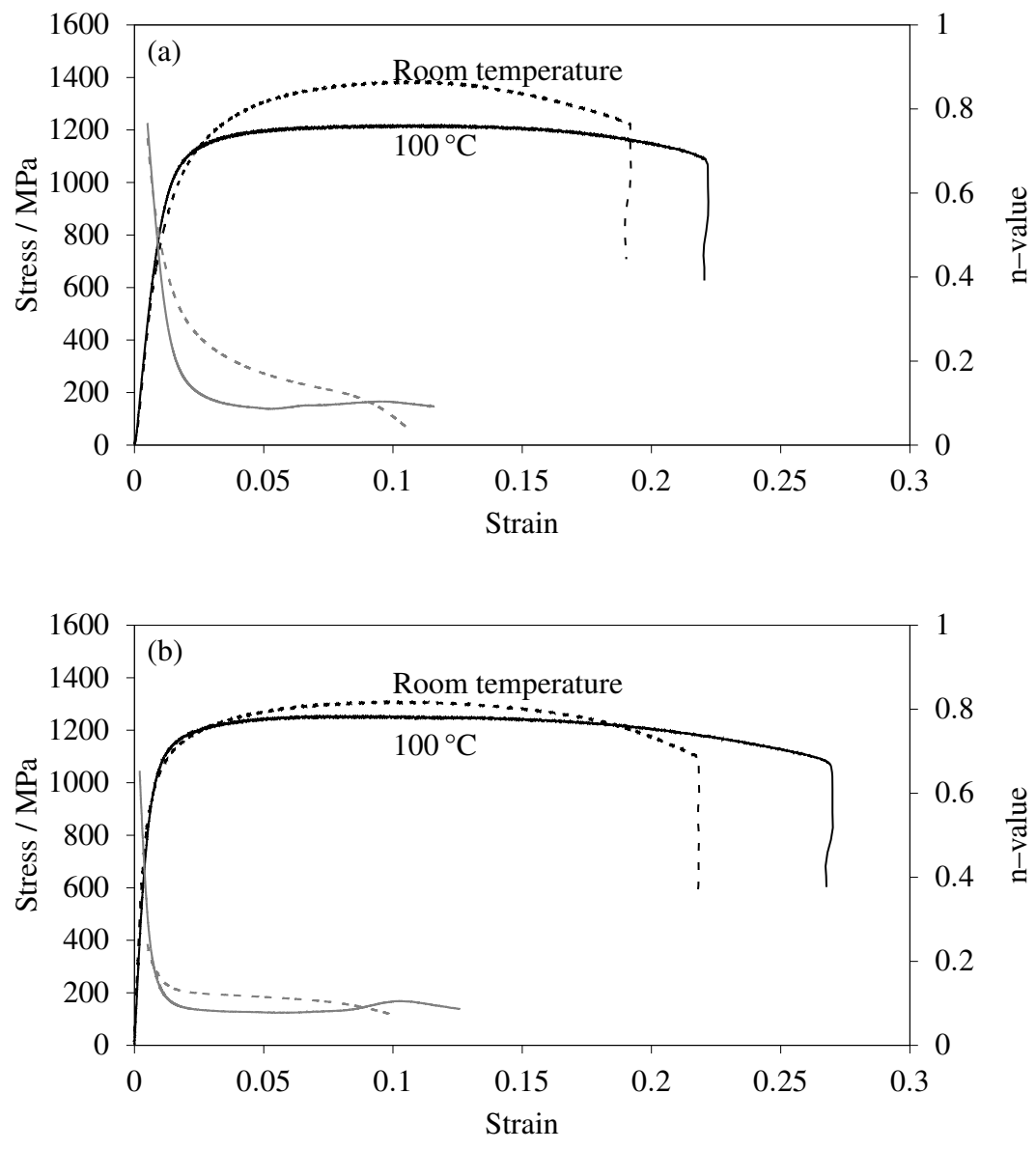
Figure 6.17 Stress–strain curve and n–value for alloy A (a) $T_I = 375\,°C$ and (b) $T_I = 400\,°C$.

Table 6.4 Proof stress ($\sigma_{0.2}$), ultimate tensile stress (σ_{UTS}), uniform elongation (e_u), total elongation (e_t), reduction in area (ε_{RA}), strain hardening exponent (n–value) and the strength–ductility product expressed in GPa% for alloy A tensile tested at room temperature (RT) and 100 °C.

Sample	$\sigma_{0.2}$ MPa	σ_{UTS} MPa	e_u %	e_t %	ε_{RA} %	GPa%
1050_30_375_RT	746	1383	10.6	19.2	37	26.6
1050_30_400_RT	916	1307	10.2	21.8	48	28.4
1050_30_375_100	846	1216	11.6	22.1	43	26.9
1050_30_400_100	948	1252	12.6	26.7	56	33.4

Table 6.5 differentiates the austenite stability at RT and 100 °C by the estimation of total free energy (ΔG_{Total}), which is the summation of chemical ($\Delta G_{Chem} = \Delta G^{\gamma\alpha}$) and mechanical ($\Delta G_{Mech} = -0.86 \times \sigma_{0.2}$) free energies. Clearly, the γ at 100 °C is more stable than at room temperature, manifesting in the increment in ductility. There seems to exist an optimum value for $|\Delta G_{Total}| \approx 2850 \, \text{J mol}^{-1}$, which maximise the elongation. To put this value of $|\Delta G_{Total}|$ into perspective, the stability of δ–TRIP steel produced by Chatterjee *et. al* [200] was compared and it was found that the elongation tend to maximise around the estimated value of 2850 J mol^{-1}.

Table 6.5 Total free energy for $\gamma \rightarrow \alpha$ transformation.

Alloy	Heat Treatment	ΔG_{Chem} J mol^{-1}	ΔG_{Mech} J mol^{-1}	ΔG_{Total} J mol^{-1}	e_u %
A	1050_30_400_RT	-2699	-787	-3486	21.8
	1050_30_400_100	-2182	-815	-2997	26.7
	1050_30_375_RT	-2541	-642	-3183	19.2
	1050_30_375_100	-2032	-728	-2760	22.1
δ–TRIP [200]	Tested at RT	-2293	-602	-2895	23
	Tested at 100	-1797	-706	-2503	14

Data from Chapter 4 were subjected to similar analyses and both total elongation and strength–ductility product tend to attain a maximum within a narrow range around 2850 J mol^{-1}, Fig 6.18. Higher values from this optimal $|\Delta G_{Total}|$ means the austenite is less stable and transforms quickly into martensite during the initial stages of deformation. However, lower free energies correspond to stable austenite which does not transform during deformation, leading to lower ductility.

Decomposition of austenite to martensite along the gauge length during tensile test at room temperature and 100 °C for alloy A, (T_I = 400 °C) is given in Fig. 6.19. Samples
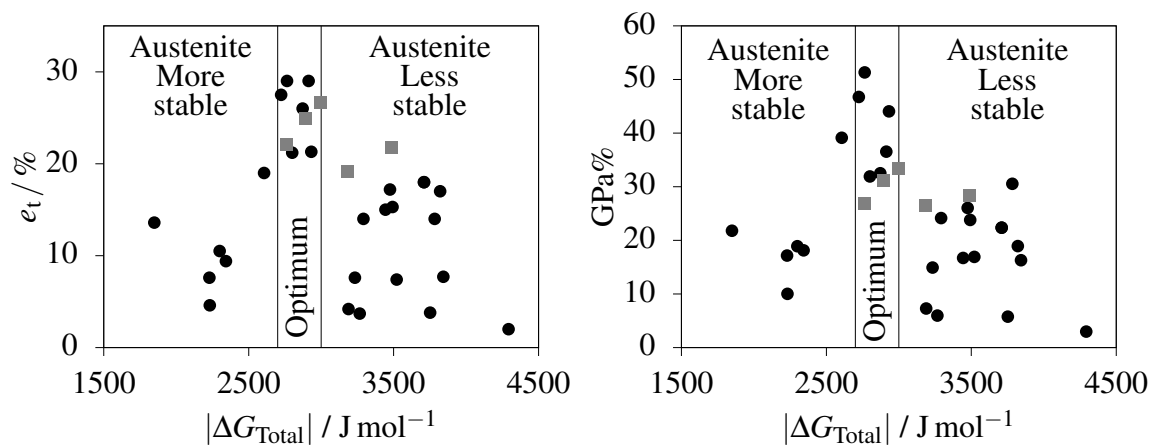
Figure 6.18 Both total elongation and strength–ductility product showing a maximum with respect to optimum austenite stability. Black circles represent the data from literature and grey squares are from the present work.

1.5 mm thick were cut from the gauge length of tensile test specimens at fixed intervals and the austenite content was measured using X–rays. $|\Delta G^{\gamma\alpha}|$ for retained austenite at room temperature and $100\,^{\circ}$C were 2699 and 2182 J mol^{-1}, respectively, also the grip austenite content were found to be 14.7$\pm$1 and 15.1$\pm$1 %. Enhanced stability of austenite at $100\,^{\circ}$C is evident in the larger V_{γ} at the fracture surface of the $100\,^{\circ}$C tested samples. Deformation induced transformation of austenite was estimated using the model proposed by Sherif *et al.* [166], where, k_1 of 0.002017 mol J^{-1} out of the three different values of constant k_1 predicted well the trend of $\gamma \rightarrow \alpha$ transformation with respect to reduction in area. The non–uniform elongation on testing at $100\,^{\circ}$C was 3% more than the room temperature test (Table 6.4).

The fractures all occurred in a ductile manner during testing at room temperature and $100\,^{\circ}$C. Clearly, the $100\,^{\circ}$C tensile tests shows a greater reduction in area. The dimple size was greater for the samples tested at $100\,^{\circ}$C, Fig 6.20. Fig. 6.21 shows the micrographs of the longitudinal section in the vicinity of the fracture surface. Flow lines are clearly visible signifying tremendous ductility. Cracks associated with MA–constituents are visible in samples tested at room temperature, indicating that these regions are susceptible to void formation.
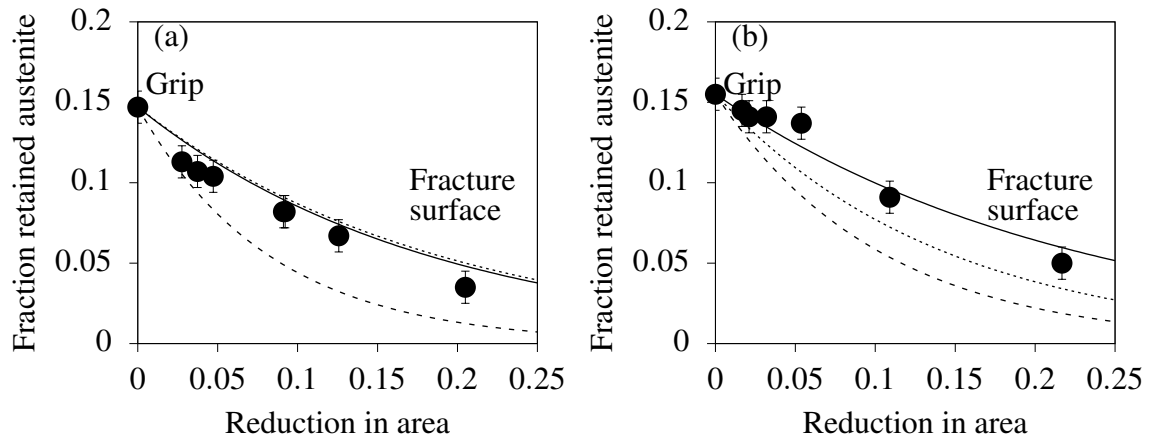
Figure 6.19 Decomposition of austenite during the tensile test for alloy A at (a) room temperature and (b) 100 °C. The solid, dashed and dotted lines represent the deformation induced transformation model proposed by Sherif *et al.* [166] with k_1 values of 0.002017, 0.00446 and 0.008478-2.42$\times 10^{-6}\Delta G^{\gamma\alpha}$ respectively.
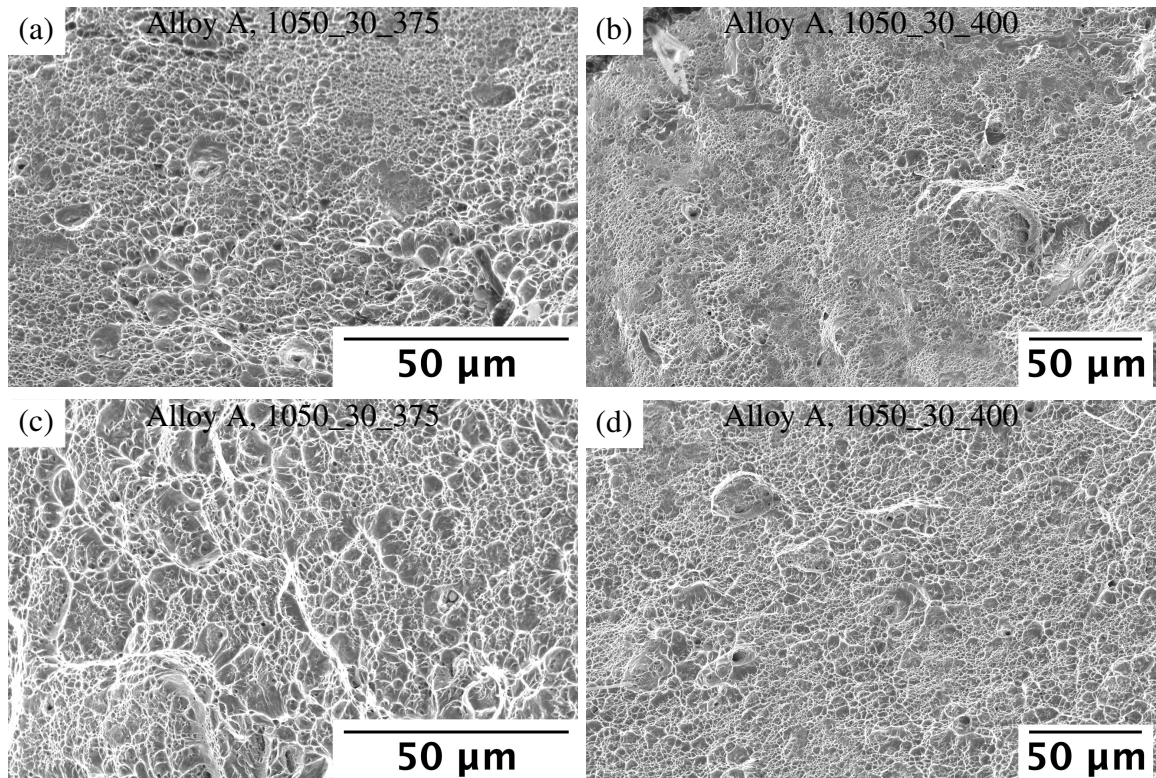
Figure 6.20 Difference in dimple size for tensile specimen tested at (a, b) room temperature and (c, d) 100 °C.

(a) 1050_30_375, tested at RT   (b) 1050_30_400, tested at RT

(c) 1050_30_375, tested at 100 °C   (d) 1050_30_400, tested at 100 °C
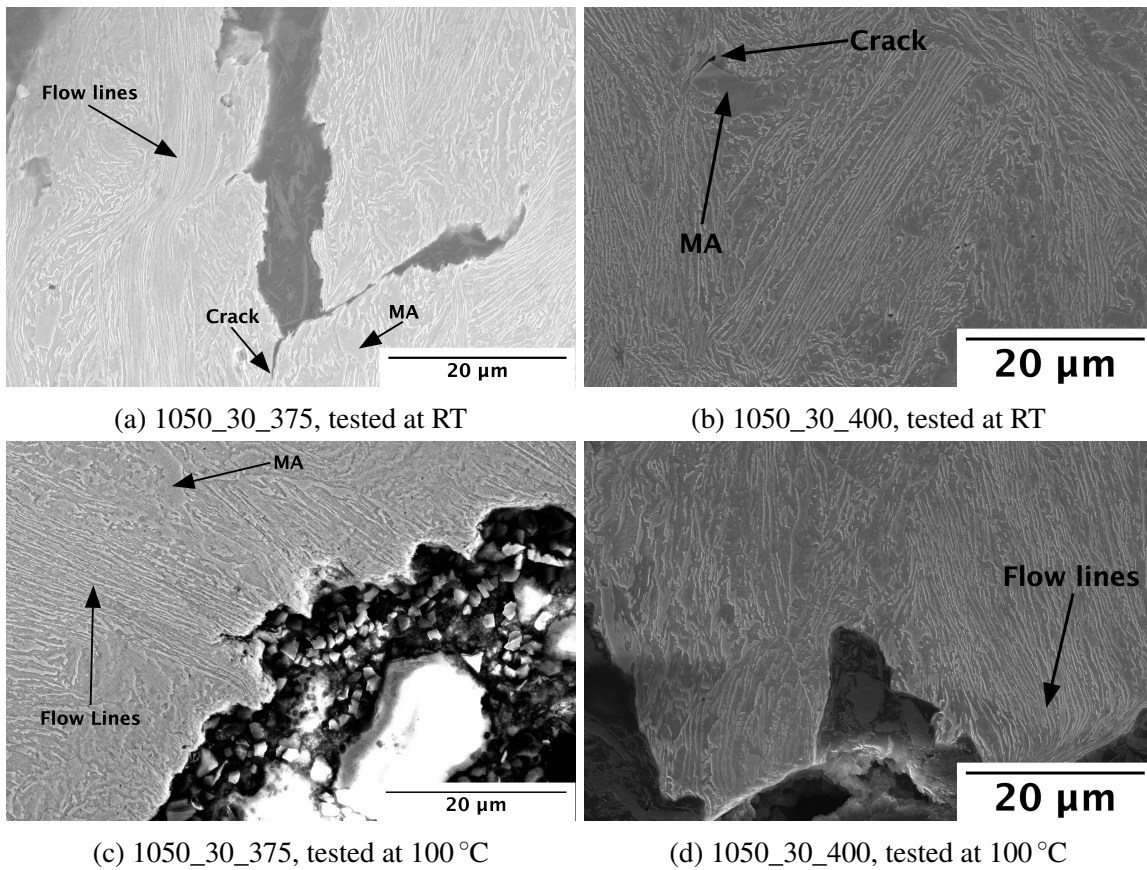
Figure 6.21 Scanning electron micrographs of longitudinal section of the fracture surface along the loading direction for tensile test specimen isothermally transformed at 375 and 400 °C. (a) and (b) are the fracture surface at room temperature and (c) and (d) at 100 °C.

6.3.2 Alloy B

Alloy B with $V_\gamma = 0.16$, reasonably low martensite content (3.6%) and hardness of 352 HV_{10} at $T_I = 400\,°C$, achieved $\approx 25\%$ elongation and crossed the 30 GPa% mark, Table 6.6. Fig. 6.22 shows the stress–strain curves for tensile tests conducted at room temperature. The stability of retained austenite, $|\Delta G_{Total}| = 2895\,Jmol^{-1}$ ($\Delta G_{Chem} = -2253\,Jmol^{-1}$ and $\Delta G_{Mech} = -642\,Jmol^{-1}$) is close to the value estimated for alloy A to maximise the elongation.

Table 6.6 Tensile parameters for alloy B tested at room temperature. Test 2 gave $\approx 2\%$ lower elongation due to the necking occurring at the extensometer grip. However, manual measurement of the gauge length before and after tensile test gave e_t as 24.5% and strength ductility product 30.6 GPa%.

Test No.	$\sigma_{0.2}$ MPa	σ_{UTS} MPa	e_u %	e_t %	ε_{RA} %	GPa%
Test 1	741	1252	14.5	24.9	45	31.2
Test 2	746	1253	14.3	22.5	46	28.1
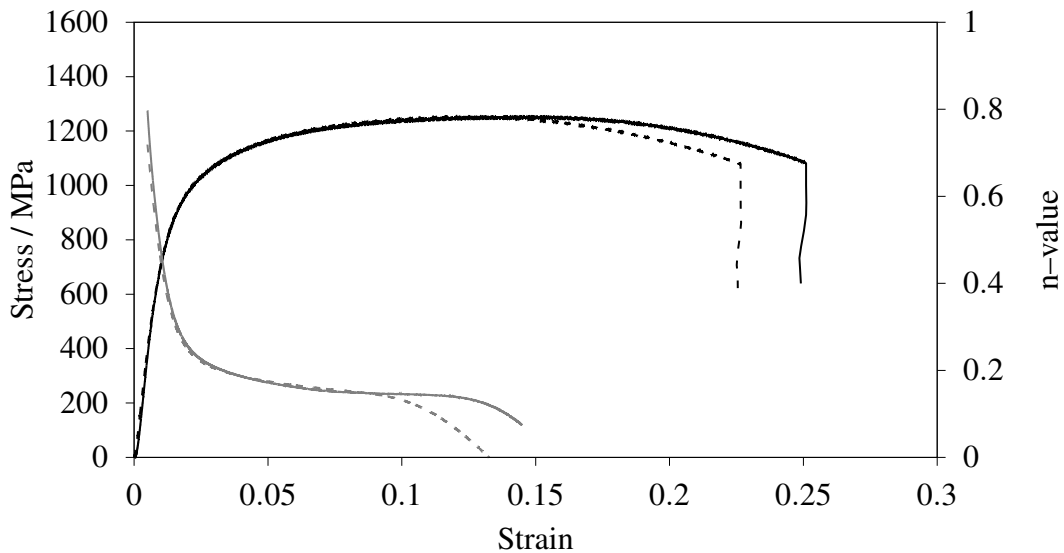
Figure 6.22 Tensile curves and incremental work hardening of alloy B, $T_I = 400\,°C$.

Deformation–induced transformation of austenite to martensite was well predicted by Sherif's model (Fig. 6.23) with k_1 of 0.002017 mol J^{-1}. The $|\Delta G^{\gamma\alpha}|$ for $\gamma \to \alpha$ transformation was used as 2253 J mol^{-1}.

The fracture surface shows similar features as that of alloy A tested at room temperature, with dimples observed in the microstructure (Fig. 6.24a). Elongated cracks with high aspect ratios associated with MA–constituents can also be found, marked in Fig. 6.24b.
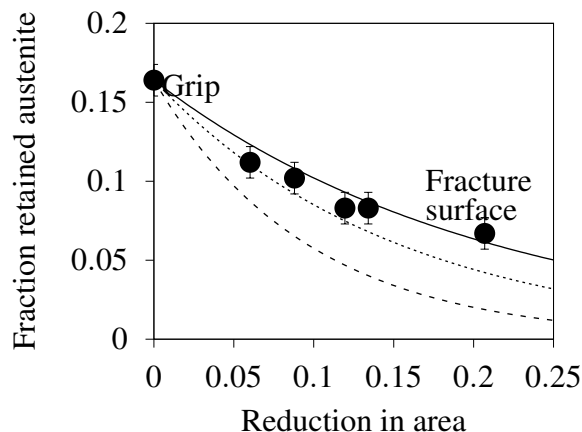
Figure 6.23 Decomposition of austenite during the tensile test at RT for alloy B at $T_I =$ 400 °C. The solid, dashed and dotted lines represent the deformation induced transformation model proposed by Sherif *et al.* [166] with k_1 values of 0.002017, 0.00446 and 0.008478-$2.42 \times 10^{-6} \Delta G^{\gamma\alpha}$ respectively.
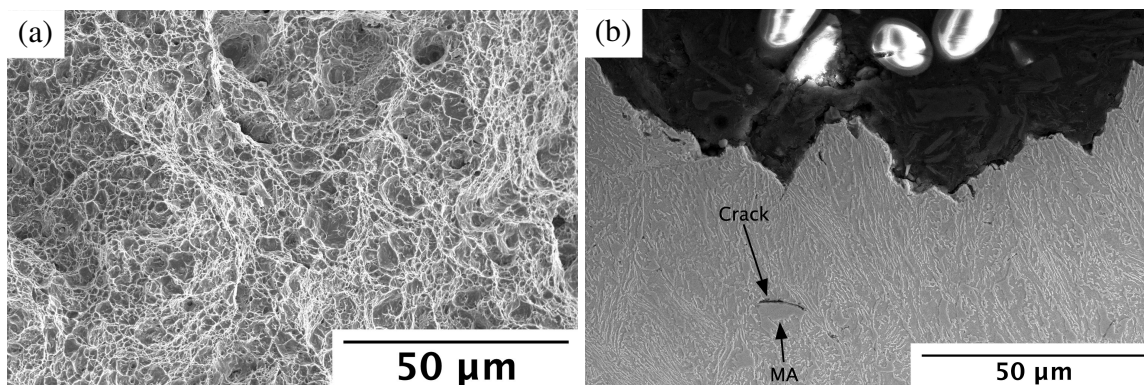
Figure 6.24 (a) Dimples showing ductile failure and (b) the longitudinal cross–section showing cracks associated with the MA–constituents.

6.3.3   Effect of tempering on tensile properties

To further increase the ductility of both alloys, tensile specimens were tempered at 150 °C for 3 h. Tempering would lead to softening of the martensite formed during cooling to ambient temperature from T_I. Stress-strain curves of the tempered specimens for both alloys A and B are given in Fig. 6.25. The corresponding tensile parameters are tabulated in Table 6.7. Both

alloys A and B achieved the required target of 30 GPa% post tempering. Tempering caused a meagre 20 MPa change to the ultimate tensile strength but increased the ductility by 2% enabling the strength–ductility product to increase.

Deformation induced transformation of $\gamma \rightarrow \alpha$ followed the trend as before and was in accordance with the model suggested by Sherif *et al.* with a constant value of k_1 of 0.002017 mol J^{-1} (Fig. 6.25). Dimples were observed on the fracture surface (Figs. 6.27a and 6.27b). Microstructure in longitudinal section were devoid of subsurface cracks in the close vicinity of MA constituents (Figs. 6.27c and 6.27d).
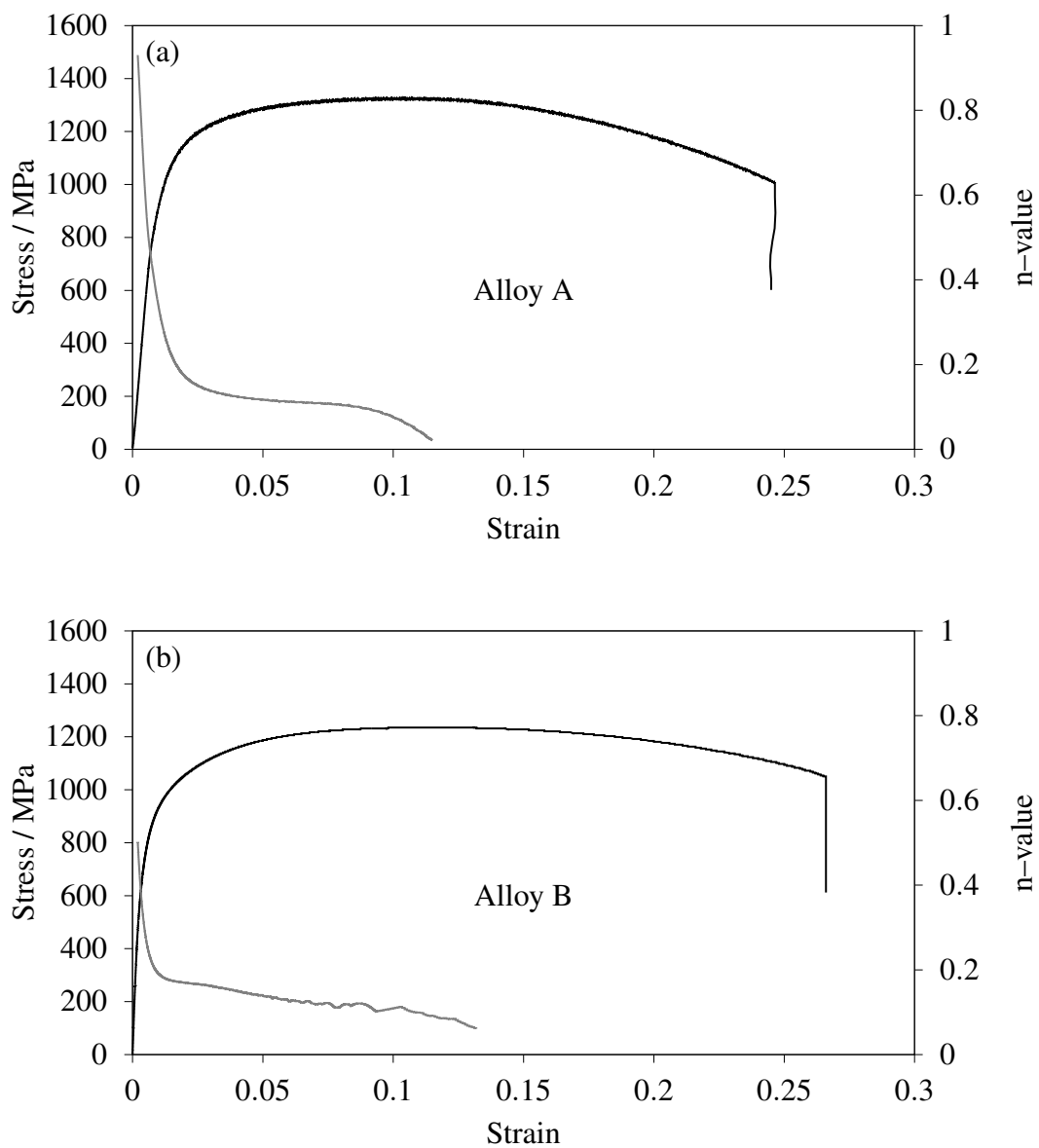
Figure 6.25 Improvement in tensile properties after tempering both alloys at 150 °C for 3 h.

Table 6.7 Tempering at 150 °C for 3 h enhanced the ductility and GPa% of both alloys.

Test No.	$\sigma_{0.2}$	σ_{UTS}	e_u	e_t	ε_{RA}	GPa%
	MPa	MPa	%	%	%	
Alloy A	899	1326	11.5	24.5	57	32.5
Alloy B	746	1235	13.2	26.6	46	32.9
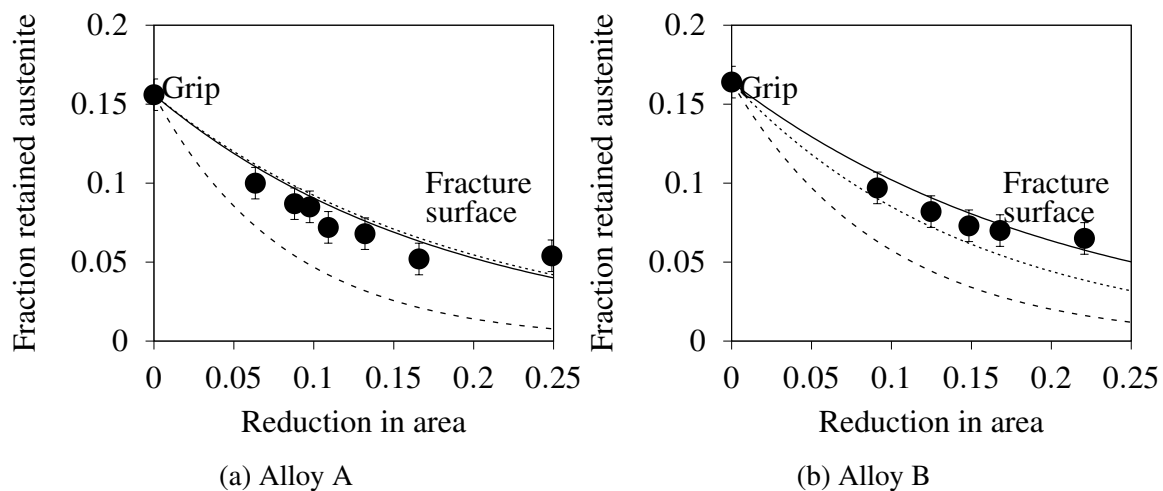
(a) Alloy A   (b) Alloy B

Figure 6.26 Decomposition of austenite during the tensile test for (a) alloy A and (b) alloy B with respect to the reduction in area. These tensile specimens were tempered at 150 °C for 3 h. The solid, dashed and dotted lines represent the deformation induced transformation model proposed by Sherif *et al.* [166] with k_1 values of 0.002017, 0.00446 and 0.008478-2..42×$10^{-6}\Delta G^{\gamma\alpha}$ respectively.
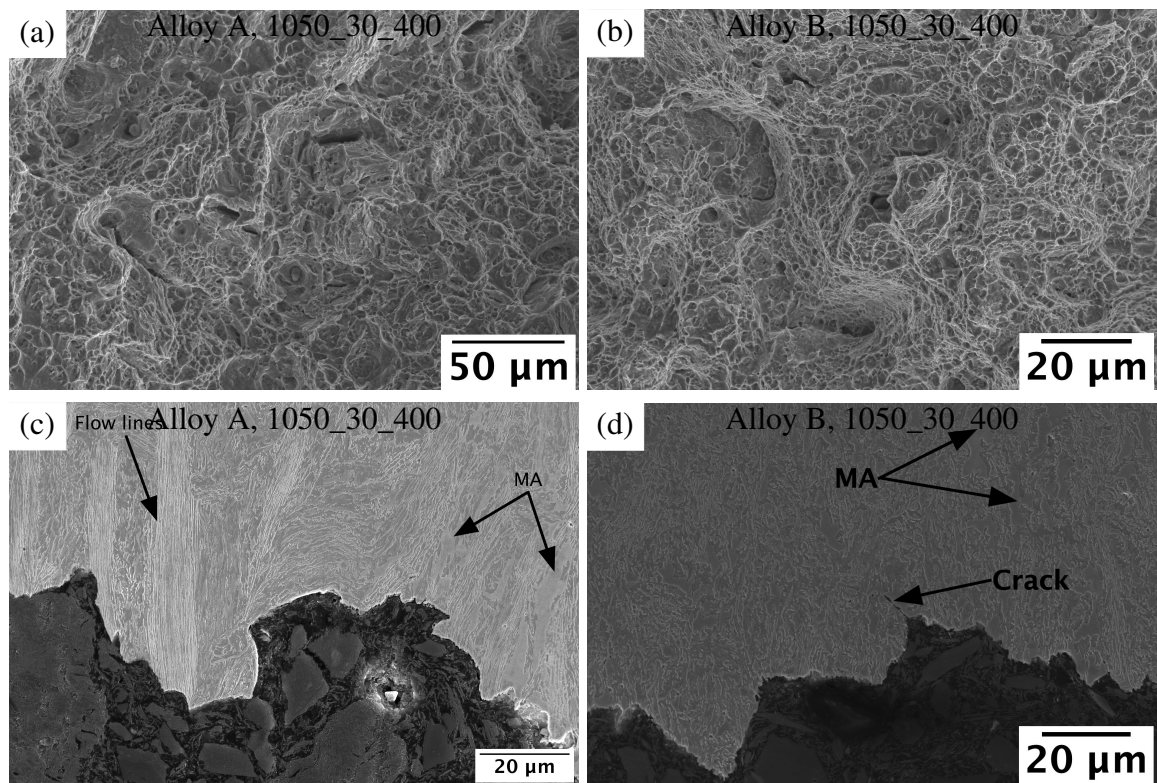
Figure 6.27 (a, b) High magnification and (c, d) longitudinal section electron micrographs of fracture surface of tempered tensile samples.

6.4   Conclusions

1. The hardenability of alloy B is greater than alloy A because it contains 1.65 wt% nickel. Although alloy B contains much less Mn and Si than alloy A, proeutectoid ferrite formation is suppressed more in alloy B at cooling rates of 0.025 and 0.05 $^\circ$C s^{-1}, resulting in a greater hardness at lower cooling rates.

2. X–ray diffraction peaks for ferrite showed distinct splitting into twin peaks during the presence of allotriomorphic ferrite and bainite in the microstructure. It is correct to say therefore that the α_b has a greater carbon concentration.

3. Short austenitization time must be avoided in dilatometer experiments because it may not be adequate for the homogenization of carbon leading to carbon rich and depleted zones. This leads to reduced retained austenite content in the final microstructure, together with more undesirable martensite.

4. Room and elevated temperature tensile tests made it possible to quantify the free energy required for optimum stability of austenite to maximise the elongation. This value was approximated as 2850 J mol^{-1}, higher free energy means, less stable austenite that transforms easily into martensite. On the contrary a lower free energy change makes the austenite too stable, leading to a reduced work hardening capacity.

5. The decomposition of austenite followed the model proposed by Sherif with respect to strain for the constant k_1 of 0.002017 mol J^{-1}, however, the reduction in area used as the parameter to determine local strain works really well with the model.

6. Low temperature tempering improved the ductility without affecting the strength of both alloys, leading to an increment in the strength–ductility product. Tempering helped in softening the martensite formed during cooling post isothermal bainitic transformation. Both alloys A and B achieved the required 30 GPa%.

7. Subsurface cracks associated with MA constituents were limited to tensile tests conducted at room temperature. High temperature tensile tests and tempering helped to minimise these crack formations thus enhancing ductility. The fracture surface of tensile tests conducted at high temperature showed larger dimple size as compared to room temperature ones, explaining the increment in ductility.

Chapter 7

Process design and enhancement of mechanical properties

Further optimisation of the properties of alloys A and B requires the careful selection of appropriate process parameters that determine the heat treatment. For example, the austenite grain size which is dependent on the austenitization temperature and time, may have an impact on mechanical properties. As a consequence parameters such as γ–grain size, segregation, pre-stressed austenite and two–step isothermal holding are considered in the work presented in this chapter with the overall aim of exceeding the 30 GPa% target.

7.1   Grain size measurement

The austenite grain size can be defined by the mean linear intercept ($\bar{L}_\gamma$), which is related conversely to the amount of grain boundary area per unit volume [182]. To determine $\bar{L}_\gamma$, dilatometer samples were prepared with a mechanically polished flat, up to diamond polishing with 0.25 µm suspension and ultrasonically cleaned with VLSI grade acetone and ethanol to ensure clean, scratch free surfaces. The samples were heated treated at various austenitization temperatures for 30 min and quenched using pure helium gas at a rate of $20\,°\text{C}\,\text{s}^{-1}$. The vacuum level during austenitization was maintained at 2.0×10^{-5} mbar to mitigate the oxidation of the polished surface. The heat treatment caused grooving of the austenite grain boundaries, grooves that are retained upon quenching (thermal grooving). The $\bar{L}_\gamma$ was then measured using multiple lines on 5 different micrographs at magnification such that at least 25 austenite grains are visible in the microstructure (Fig. 7.1).

Higher austenitization temperatures (1050, 1000 and 950 °C) led to deeper grooves which were easily visible in an optical microstructure, but for $T_\gamma = 900$ and 875 °C, the shallow

grooves were difficult to detect optically, so scanning electron microscopy was used instead. The microstructure was martensitic in all cases with accompanying surface relief which confirms that the γ boundaries do not move during cooling since the α' plates terminate at the grooves. In some cases the grooves from the prior austenite were visible along with some additional faint remnant grooves possibly from sub–grain structures (Fig. 7.2). These were excluded from the measurement of $\overline{L}_\gamma$. This is consistent with fact that the plates of martensite cross these faint boundaries. Mullins [201] showed similar traces of grain boundaries left behind due to interface motion in pure copper annealed at 940 °C for 81 h.

The measured $\overline{L}_\gamma$ values for both alloys A and B are given in Fig. 7.3 and follow the usual trend. The maximum to minimum $\overline{L}_\gamma$ changed from approximately 60 μm to 10 μm at 1050 °C and 875 °C respectively.
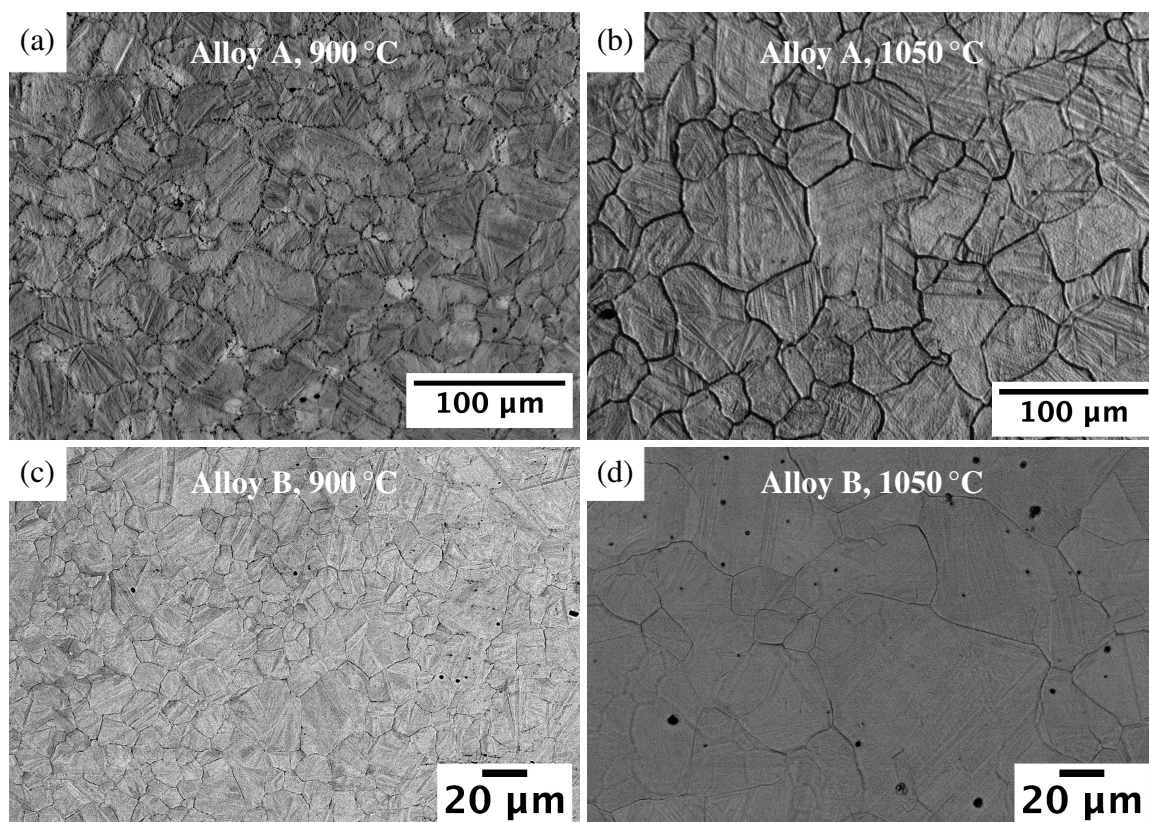

Figure 7.1 Micrographs showing thermally grooved austenite grain boundaries used for the measurement of $\overline{L}_\gamma$.
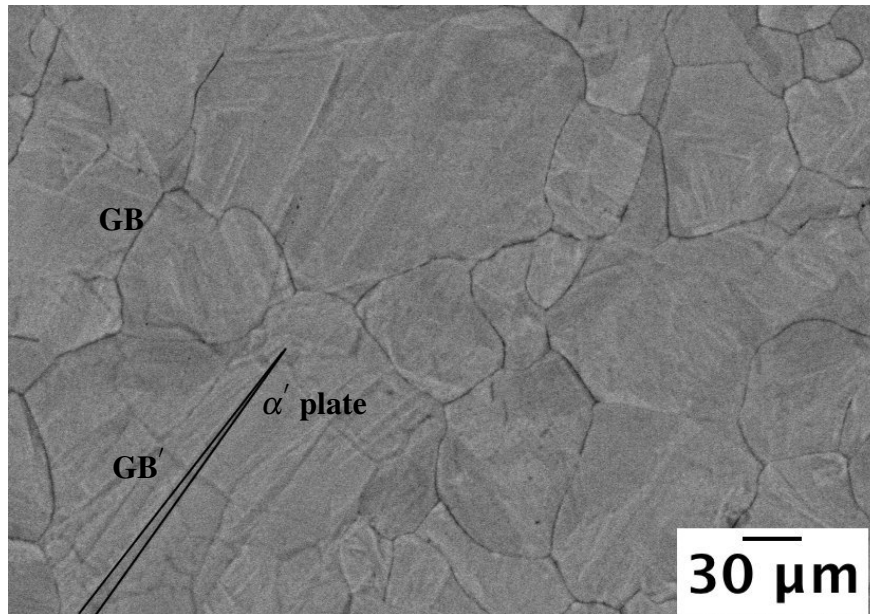
Figure 7.2 GB denotes the grain boundary grooves of prior austenite used to measure $\overline{L}_\gamma$, GB$'$ denotes the faint remnant grooves from sub–grain structures which has been excluded for the measurement of $\overline{L}_\gamma$. This is because the plate of martensite crosses GB$'$ without deviation.
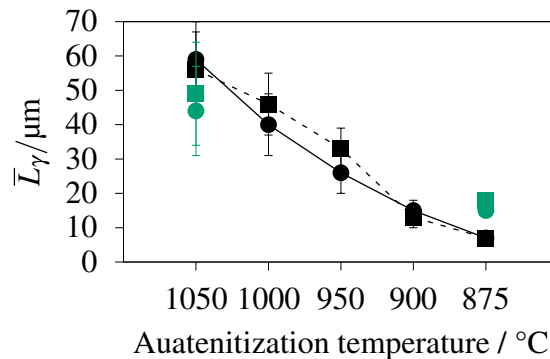
Figure 7.3 Mean linear intercepts of austenite grains after 30 min at a variety of austenitization temperatures for Alloy A and B tend to have very similar $\overline{L}_\gamma$. Green points denote the determination of $\overline{L}_\gamma$ using the electron back scattered austenitic reconstruction method discussed later. Circular data points are for alloy A and the square markers denote alloy B.

Another method adopted to determine $\overline{L}_\gamma$ exploited the bainite crystal orientations to reconstruct the parent austenite grains assuming a Kurdjumov–Sachs (KS) relationship between the two phases. The algorithm developed for the reconstruction is described in the next Chapter. Fig. 7.4 illustrates the reconstruction of the grain structure. Furthermore both alloys A and B contained retained austenite which was shown to have the same orientation as

the reconstructed austenite, giving confidence in the reconstruction algorithm. The values of $\bar{L}_\gamma$ measured through reconstruction are in agreement with those obtained from thermal grooving, Fig. 7.3. This method is particularly useful when the grooves are difficult to obtain.
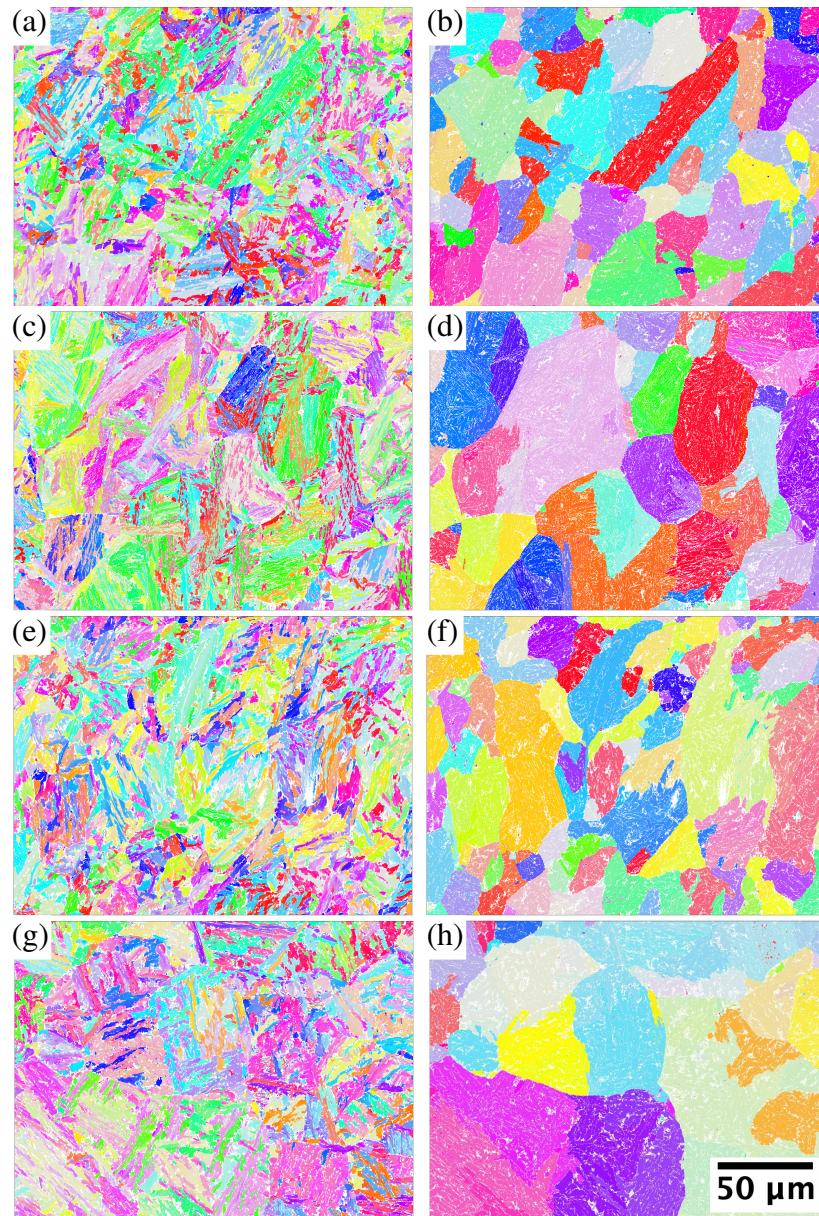
Figure 7.4 (a, c, e and g) Bainite orientation and (b, d, f and h) the corresponding reconstructed austenite showing the prior austenite grain size difference. EBSD scan from electropolished samples (a) and (c) correspond to alloy A austenitized at 875 and 1050 °C respectively. Similarly (e) and (g) are for alloy B at low and high austenitization temperatures respectively.

7.2   Grain size and consequence on blocky retained–austenite

The size distribution of blocky austenite in Si–bearing bainitic steel has been modelled [202], based on the random subdivision of austenite grains by bainite sheaves, and as a function of the prior austenite grain size and fraction of bainite. The model was validated using optical micrographs and a thresholding technique to detect the austenite blocks [203].

In the present work, the Feret diameter of blocky austenite was determined. Fig. 7.5a shows white blocky–austenite, with the processed image in Fig. 7.5c. The thresholding method helped identify blocky–austenite, which then was delineated so that the Feret diameter could be obtained by automated processing. For both alloys a larger $\overline{L}_\gamma$ gave a larger blocks of austenite (Figs. 7.6a and 7.6b). Smaller regions of austenite are desirable because they lead to a more homogeneous structure.
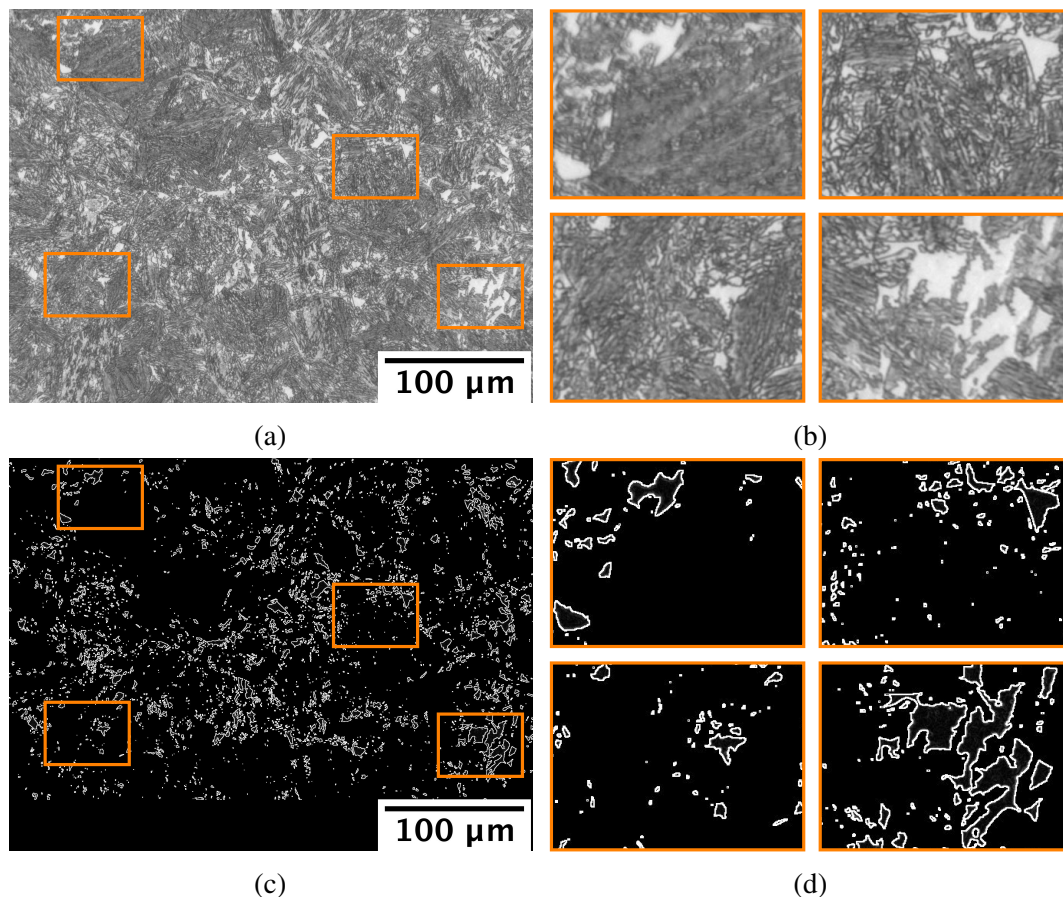

Figure 7.5 Constructed edges of blocky austenite using (a) optical image and corresponding (c) processed image for alloy A austenitized at 1050 °C. (b) Four zoomed in portions of the optical image are shown with the proportionate (d) blocky austenite features revealed to visualize the edges clearly.
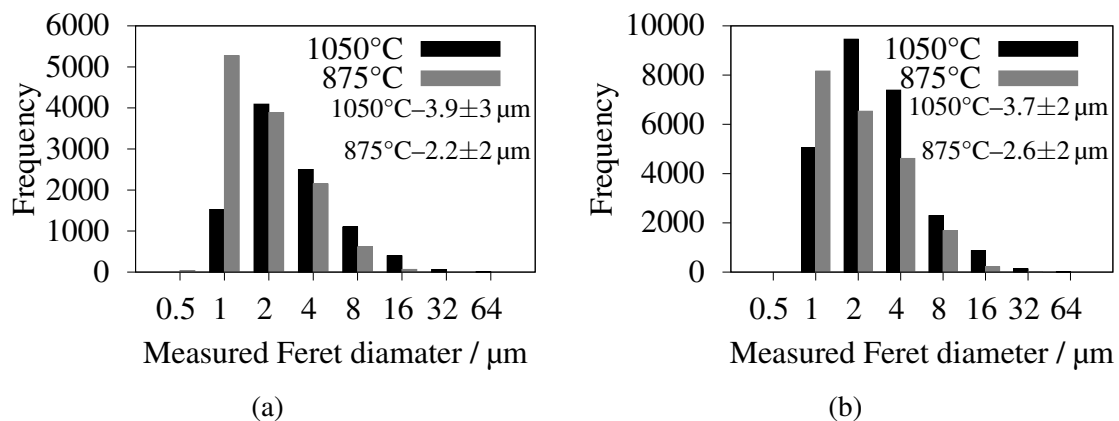
Figure 7.6 The measured Feret diameter of blocky austenite for (a) alloy A and (b) alloy B at different T_γ.

7.3 Grain size and tensile properties

Maximum (1050 °C) and minimum (875 °C) austenitization temperatures were chosen to compare the effect of the grain size on the tensile properties, with isothermal transformation to bainite at 400 °C, which from the work presented in Chapter 6 gives the best combination of strength and ductility. Fig. 7.7 shows that the higher austenitization temperature results in better ductility without compromising strength. The data are listed in Table 7.1, the differences are, however not large. The results show that the mechanical properties are not particularly sensitive to the austenite grain size. The tensile strength does not change much as the austenite grain size is increased and this might be expected since much of the strength comes from the very fine size of the bainite platelets. The thickness of the bainite plate depends on the strength of the austenite, which will not change much when the grain size is changed from something like 60 μm to 20 μm.

There is a significant drop observed in $\sigma_{0.2}$ for alloy A (916 to 769 MPa) when austenitized at lower temperature, attributed to the presence of higher amount of martensite in the microstructure.
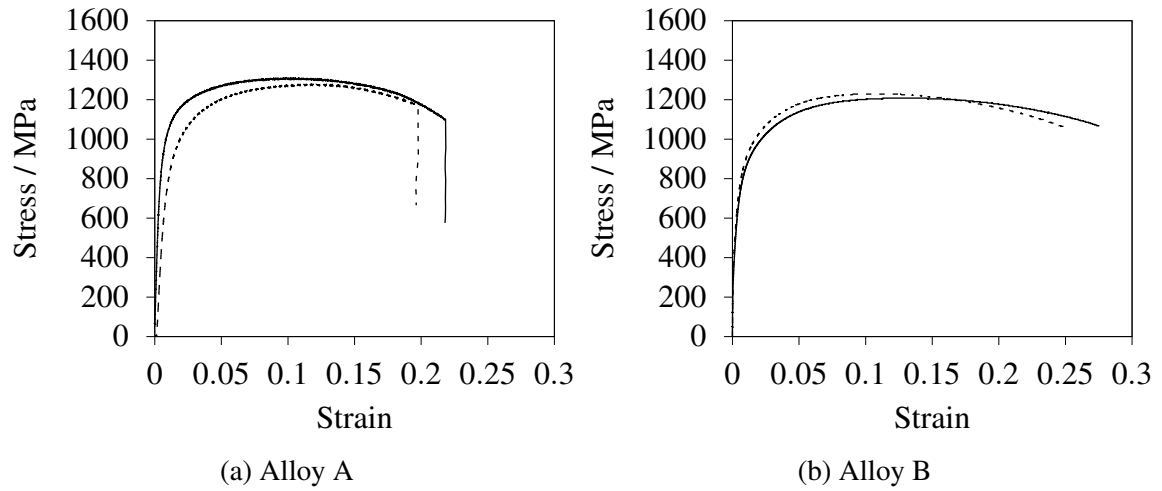
(a) Alloy A   (b) Alloy B

Figure 7.7 Tensile test of (a) alloy A and (b) alloy B with austenitization at 1050 and 875 °C for 30 min and bainitic transformation at 400 °C.

Table 7.1 Tensile parameters showing the differences due to two extreme austenitization temperature of 875 and 1050 °C.

Alloy	Austenitization Temperature	$\sigma_{0.2}$	σ_{UTS}	e_u	e_t	ε_{RA}	GPa%
	°C	MPa	MPa	%	%	%	wt%
A	875	769	1276	10.6	19.6	42	25.0
	1050	916	1307	12.2	21.8	48	28.5
B	875	743	1227	12.6	25.1	49	30.8
	1050	738	1208	14.7	27.5	52	33.2

7.3.1   Effect of austenitization temperature on banding

There is an additional interesting possibility of reducing the amount of banding in the microstructure due to chemical segregation, by increasing the austenite grain size. Mn segregation during solidification is spread out into bands during the hot processing of the steel. These bands will essentially remain as martensite in the microstructure and reduce the overall mechanical homogeneity of the steel. Experiments were therefore conducted to characterize the advantage of a coarse austenite grain size in controlling the uniformity of the microstructure. The optical microstructure of the grip sections for all the conditions were examined. Fig. 7.8 shows white bands of essentially martensite being more prevalent for the lower austenitization temperatures of $875\,^\circ$C. Fig 7.8e shows the coloured etched micrograph with light blue/green colour being α_b, speckles of white being blocky γ and patches of brown colouration predominantly α'.

Vickers hardness maps were generated using $300\,$g load as shown in Figs. 7.9–7.10. Fig. 7.11 shows the microhardness data at $1050\,^\circ$C and $875\,^\circ$C. It is evident that there is a wider variation in hardness for the samples transformed at $875\,^\circ$C, with occasional hard regions that cannot be conducive to good toughness.
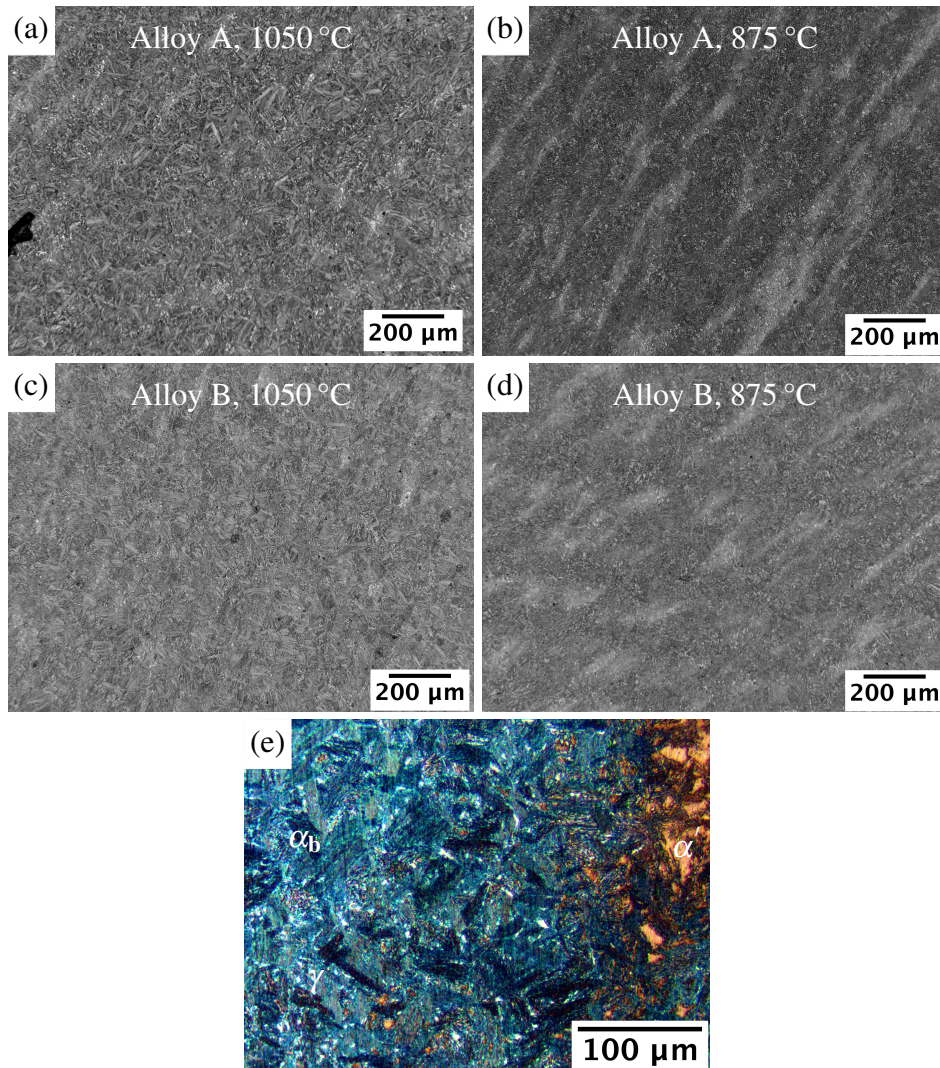
Figure 7.8 Optical microstructure of grip section of tensile specimen showing negligible segregation at higher austenitization temperature for both alloys. The white bands seen at lower austenitization temperature is due to formation of hard phase (MA constituents) in the segregated regions.
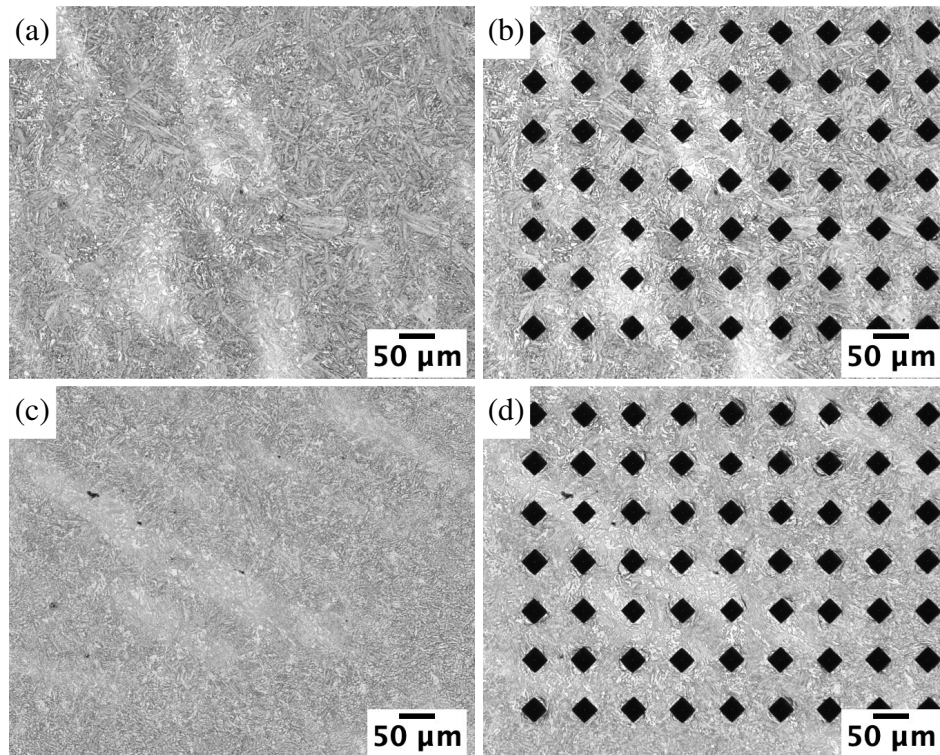
Figure 7.9 Micro hardness ($HV_{0.3}$) of tensile samples transformed at $400\,°C$ for alloy A after austenitization at (a, b) $1050\,°C$ and (c, d) $875\,°C$. The microstructures show patches of segregated regions which have varying hardness at the two different austenitization temperatures.
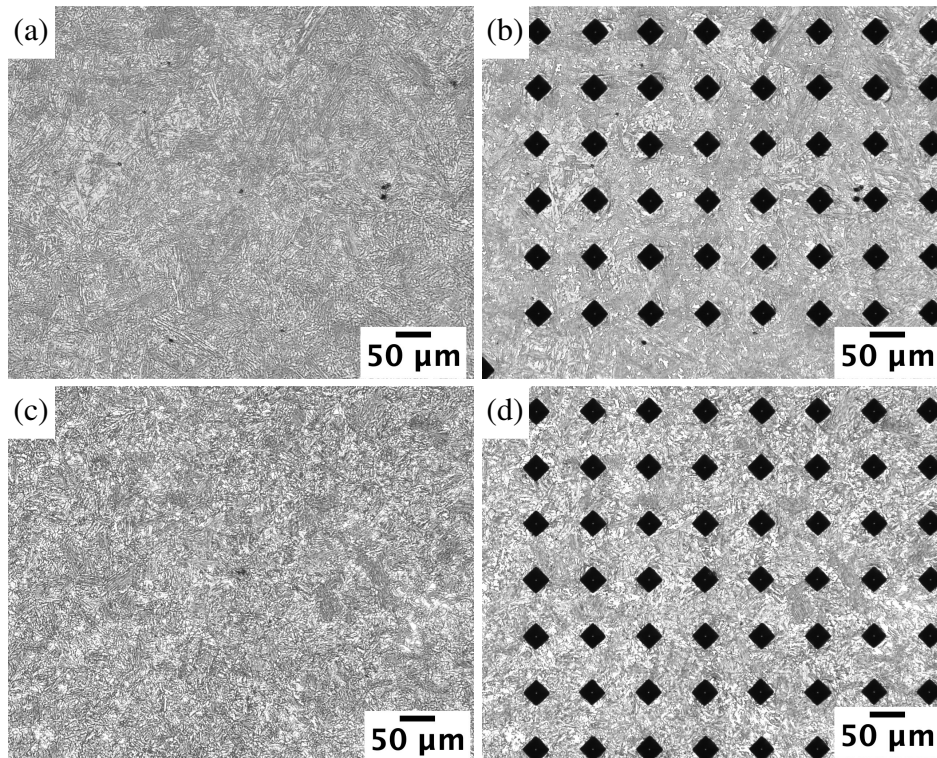
Figure 7.10 Micro hardness ($HV_{0.3}$) of tensile samples transformed at 400 °C for alloy B after austenitization at (a, b) 1050 °C and (c, d) 875 °C. The microstructures show negligible segregated regions and thus possess lesser variation at the different austenitization temperatures.
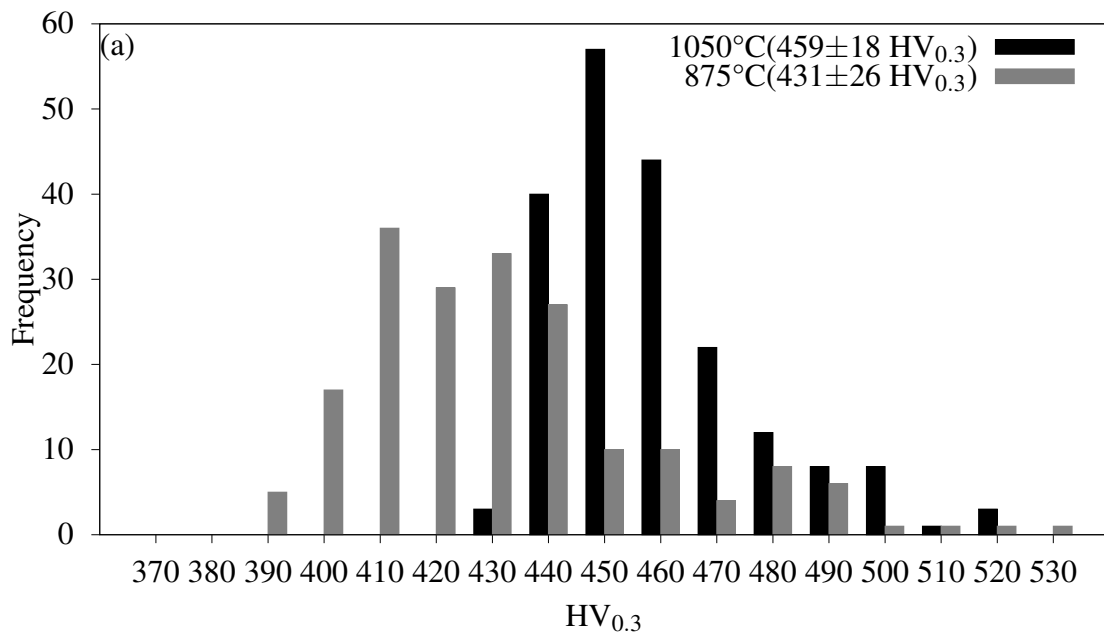
(a)
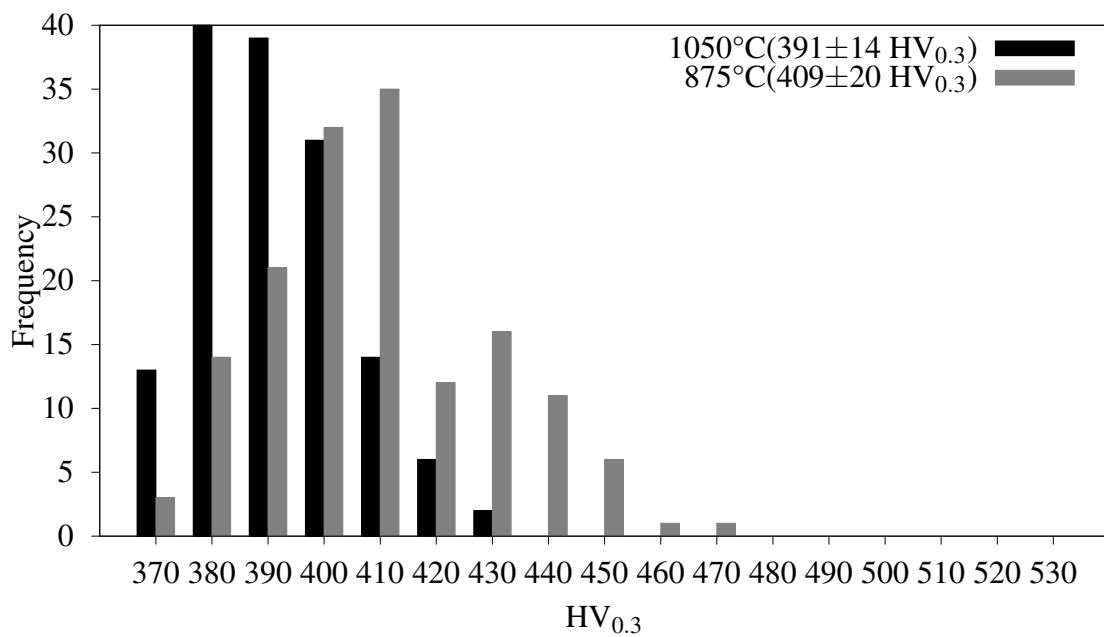
(b)

Figure 7.11 Measured micro hardness ($HV_{0.3}$) of tensile specimen austenitized at 1050 °C and 875 °C and isothermally transformed to bainite at 375 °C for 1 h. The plot showing greater spread of hardness for 875 °C (130 $HV_{0.3}$) as compared to 1050 °C (90 $HV_{0.3}$).

The "entropy" is a more robust measure of the heterogeneity or homogeneity in data; for instance in a bimodal distribution with two peaks, the increase in the separation of the peaks leads to an increase in standard deviation. However, the entropy as defined by Equation 7.1 does not because it does not depend on the location of the peaks. This is because the entropy depends on probabilities (phase fractions), whereas the standard deviation is a function of the actual hardness values. However, it is noted that in the present case, the dispersion, especially the ranking, in the hardness values is reasonably represented by entropy:

$$S_{\text{HV}} = \sum_{n=1}^{17} -x_n \ln(x_n) \times \frac{1}{\ln(n)} \tag{7.1}$$

where, S_{HV} is the hardness entropy, n is the number of bins and x_n is the fraction of hardness in the nth bin. The entropy ranges from 0 and 1, corresponding to homogeneous and heterogeneous samples. The data were in each case binned into 17 groups of consistent size, ranging from 370 to 530 $\text{HV}_{0.3}$ in steps of 10 $\text{HV}_{0.3}$. As shown in Table 7.2 alloy B is more homogeneous than alloy A, which contains a greater Mn concentration. Both alloys show lower hardness entropy at the higher austenitization temperature. Clearly, higher austenitization temperature leads to better homogenization and lesser segregation as compared to austenitization at lower temperatures, thus proving the hypothesis.

Table 7.2 Hardness entropy, S_{HV}, computed using equation analogous to configurational entropy. Alloy A and B showing significantly different hardness entropy at the two different austenitization temperatures. The range of hardness which is the difference between the maximum and minimum hardness is also mentioned.

Sample	Hardness entropy, ΔS_{HV}	Range of hardness ($\text{Max}_{\text{HV}} - \text{Min}_{\text{HV}}$)
Alloy A, 1050 °C	0.65	90
Alloy A, 875 °C	0.79	140
Alloy B, 1050 °C	0.59	60
Alloy B, 875 °C	0.73	100

7.4   Fractography as a function of grain size

All tensile fractures were ductile so the purpose was to study the dimple sizes as a function of $\overline{L}_\gamma$. Scanning electron fractographs were subjected to image processing using MATLAB software. Contrast and brightness were adjusted to increase the definition of the dimples.

The images were then "skeletonized" to visualize the dimples. Isolated segments of size less than 20 pixels were removed (Fig. 7.12). Dimple size measurements were carried out by using the mean linear intercept $\overline{L}_D$, Fig. 7.13.

The histograms delineating the L_D for both alloys A and B at course and fine austenite grain sizes. Dimple size of Alloy B is 10% greater than Alloy A, which correlates with greater elongation in Alloy B. At higher austenitization temperature, $\overline{L}_D$ is nearly 4% greater than the fine grained counterparts, though the increment in not substantial, it again correlates with improved ductility.

Banded structures are of course detrimental for ductility. Alloy A which is significantly heterogeneous due to the presence of large patches of α', which may crack during tensile loading. The dimple size is a measure of density of void nucleation sites in the microstructure, greater is the void nucleation, the smaller will be the dimples. This is clearly evident from $\overline{L}_D$ which for alloy A and B having values of 1.45 ± 0.24 and $1.59\pm0.24\,\mu m$, respectively. The histogram of alloy B at $1050\,°C$ (Fig 7.13b) also shows some few very big dimples with intercept length greater than $2.5\,\mu m$ which tend to be absent in alloy A. This confirms that α' definitely is a potential void nucleation site, Fig 7.14.

(a)

(b)

(c)

(d)
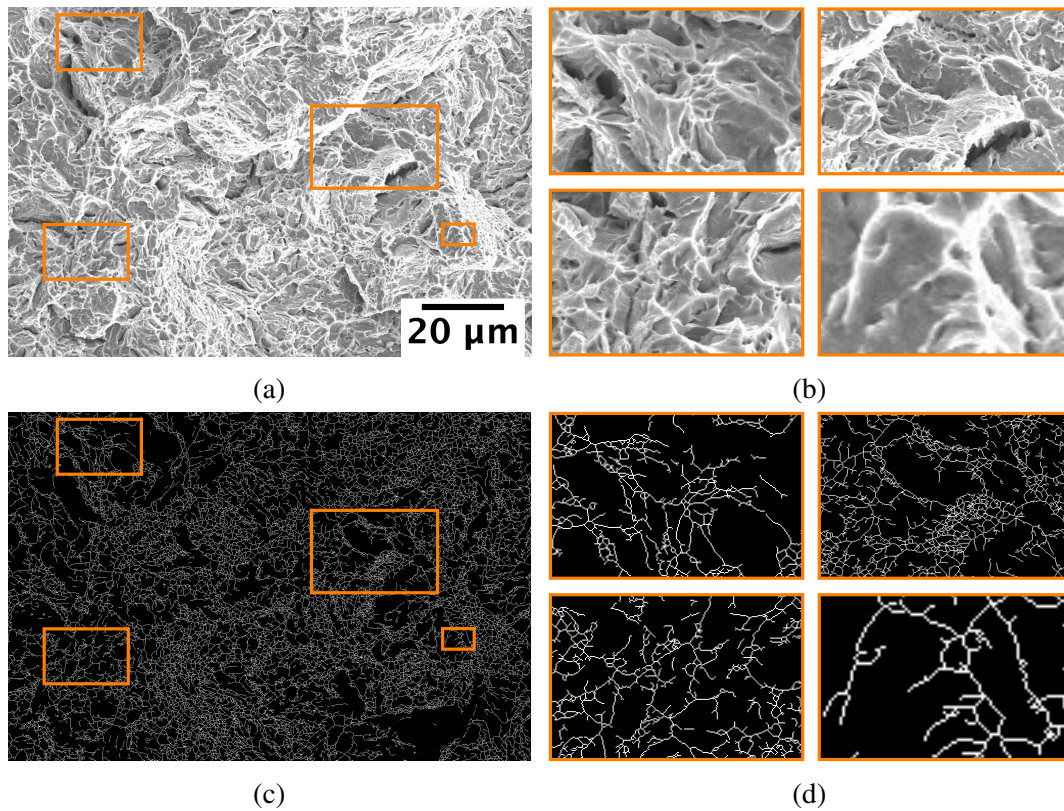
Figure 7.12 Dimple features determined using image processing from (a) fractograph of the tensile specimen to generate (c) the skeletonized image. (b) and (d) are the zoomed regions of (a) and (b) respectively, showing the capability of the method to identify intricate features of the dimples.
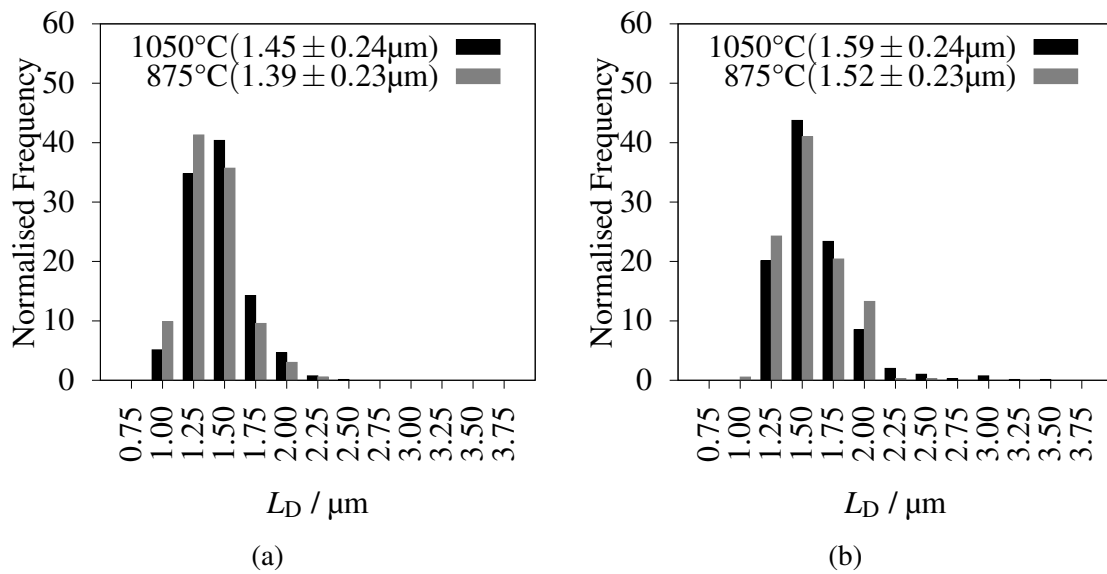
Figure 7.13 The linear intercept of dimple size at the fracture surface of (a) alloy A and (b) alloy B showing a shift towards higher values for samples displaying improvement in ductility.
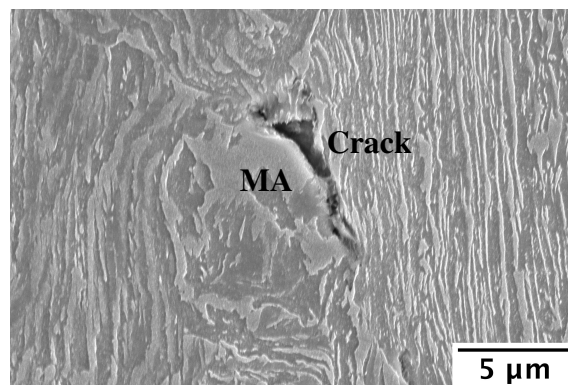
Figure 7.14 Crack associated with MA–constituent showing void nucleation.

7.5 Two–step heat treatment

In a two step heat treatment, samples after austenitization are isothermally transformed at two different temperatures to promote transformation, Table 7.3.

Table 7.3 Volume fraction of all phases for the two-step heat treatments and the comparison with single step heat treatment at 400 °C. Hardness variation also presented showing significant increase by incorporating two–step heat treatments. V_γ measured from analysis of X–ray diffraction data. $V_{\alpha'}$ is estimated from the dilatometry. $V_{\alpha_b} = 1 - V_\gamma - V_{\alpha'}$.

| Isothermal temperature | | | | Alloy A | | | | Alloy B |
| | | | | | | | | |
°C	V_{α_b}	$V_{\alpha'}$	V_γ	HV_{10}	V_{α_b}	$V_{\alpha'}$	V_γ	HV_{10}
400	0.84	0.04±0.01	0.12±0.02	398±4	0.81	0.04±0.02	0.15±0.02	358±4
475–400	0.78	0.14±0.01	0.08±0.02	421±11	0.75	0.11±0.01	0.14±0.02	382±6
450–400	0.81	0.09±0.02	0.10±0.02	415±9	0.73	0.13±0.02	0.13±0.02	395±11
425–400	0.81	0.10±0.02	0.09±0.02	415±9	0.75	0.12±0.01	0.13±0.02	387±9

Fig. 7.15 gives the V_{α_b}, determined from the dilatometric strain and the isothermal holding time duration. A Fortran program to analyse dilatometric data by Bhadeshia [204] was used. V_{α_b} estimated from dilatometry and from Table 7.3 using $1 - V_\gamma - V_{\alpha'}$ were consistent. It is evident that two distinct sigmoidal curves exist for some of the two–step heat treatments. Sufficient time was given for bainitic reaction to stop at the first time step, which occurred at x_{T_0}. The enriched austenite after the first bainitic transformation followed different kinetics. $V_{\alpha'}$ increased substantially over the single step isothermal transformation. This manifested in increase hardness for all the two–step heat treatments, the observation is similar to the work done by Duong *et al.* [74], where they have shown a deterioration of mechanical properties due to the formation of α'.
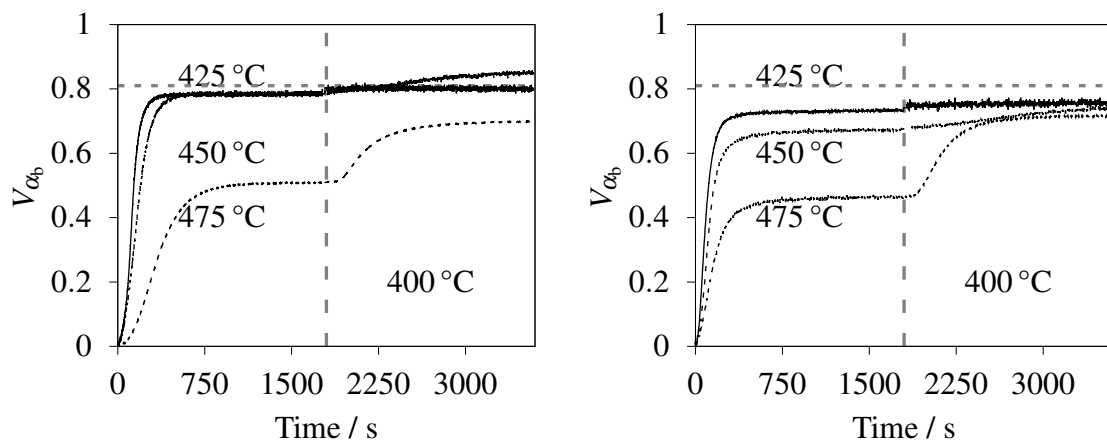

Figure 7.15 Volume fraction of bainite estimated from the dilatation curves [204]. The horizontal line denotes the maximum dilatation observed by one step heat treatment, and the vertical line separates the two halves of the two step heat treatment.

It is worth mentioning that a heat treatment where the first step temperature is less than the second step in cast iron helped improve toughness [205]. However, this experiment was based on incomplete reaction at the first step, which has very less applicability in present alloys as the bainitic reaction completion occurs by lowering the temperature.

7.6   Bainitic transformation in deformed austenite

The growth of bainite can be retarded or stopped when the austenite is plastically deformed prior to transformation. This phenomenon is known as mechanical stabilization [206]. Deformed austenite contains dislocations which interfere with the motion of the glissile transforming interface. Since steels are sometimes processed by hot rolling or hot forging it is possible that the austenite is then left in a deformed state before it is allowed to transform into bainite at a lower temperature. To study the consequences, the alloys were processed as shown in Fig. 7.16. The austenite was deformed at 900 and 850 °C before isothermal transformation at 400 °C. The true strains implemented were 0.4 (low) and 0.6 (high), applied at a strain rate of $5\,\mathrm{s}^{-1}$.
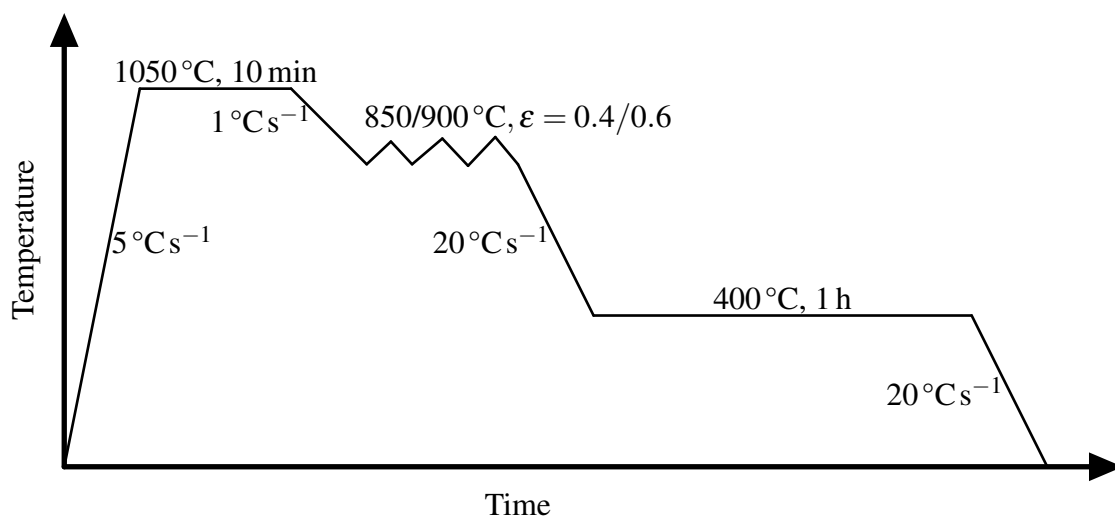
Figure 7.16 The processing cycle adopted for simulating mechanical stabilization on the dilatometer.

As expected, the deformation led to a decrease in the amount of bainitic transformation and the effect was more pronounced with greater strain, $\varepsilon = 0.6$. Fig. 7.18 shows the transformation strains for alloy A, indicating that both the total amount of transformation and its rate are reduced when the γ is in a deformed state [207, 208]. There are of course

contradicting effects when transformation occurs from deformed austenite. The first is that the number density of nucleation sites increases both because of the greater dislocation density in the austenite and because the amount of surface per unit volume increases. These should lead to an acceleration of transformation. However, this effect can be overwhelmed by mechanical stabilization which retards or arrests the growth of individual platelets. The increase in the amount of surface per unit volume, can be estimated as follows [207, 208]:

$$\frac{S_V}{S_{V_0}} = \frac{1}{2} \left(0.0429 \times \exp\left(-\varepsilon_{11}\right) + 0.571 \times \exp\left(-\varepsilon_{22}\right) + \exp\left(-\varepsilon_{33}\right) \right) \tag{7.2}$$

where, S_V and S_{V_0} are the grain boundary per unit volume in deformed and undeformed austenite respectively. ε_{11}, ε_{22} and ε_{33} are the principal strains with $\varepsilon_{11} = \varepsilon_{22} = -0.5\varepsilon_{33}$ for axisymmetric compression. Substituting the values of -0.4 and -0.6 as ε_{33} in the above equation gives a value of S_V/S_{V_0} of 1.16 and 1.28 respectively. Although this is significant, Fig. 7.17 shows that the volume transformed by each platelet is dramatically reduced when transformation is from deformed austenite. For example, the apparent sheaf length of α_b changes form $17\pm10\,\mu$m to $10\pm5\,\mu$m due to deformation of austenite at $850\,^\circ$C and $\varepsilon = 0.6$, Fig 7.17. Figs. 7.18 and 7.19 also show that because of the reduced fraction of α_b due to mechanical stabilization, more α' is obtained on cooling to ambient temperature. It must be noted that if untempered hard martensite is to be avoided, then bainitic transformation must occur from recrystallized austenite rather than deformed austenite. Excess martensite in the mechanically stabilized samples is reflected in the higher hardness values, Figs 7.18 and 7.19.
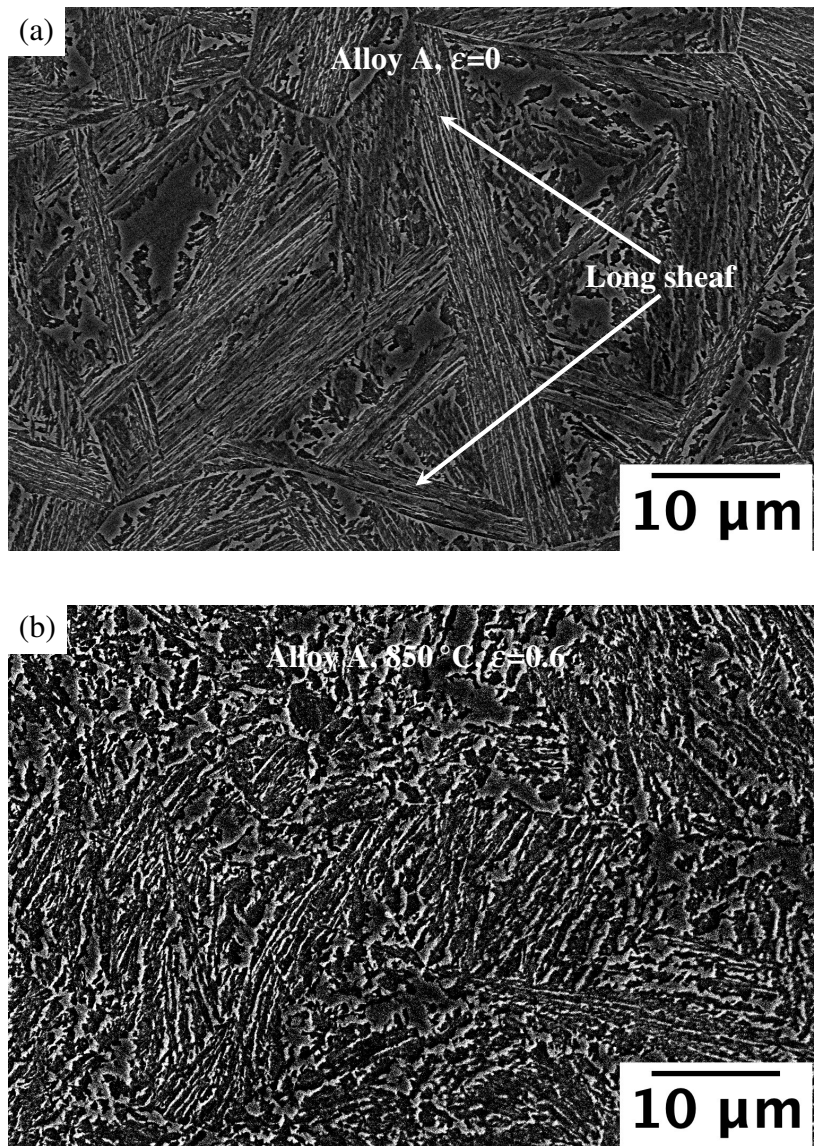
Figure 7.17 Micrographs showing length of sheaves drastically shortened in strained austenite. Bainitic sheaves are clearly visible in (a) undeformed sample as compared to (b) deformed sample at $\varepsilon=0.6$.
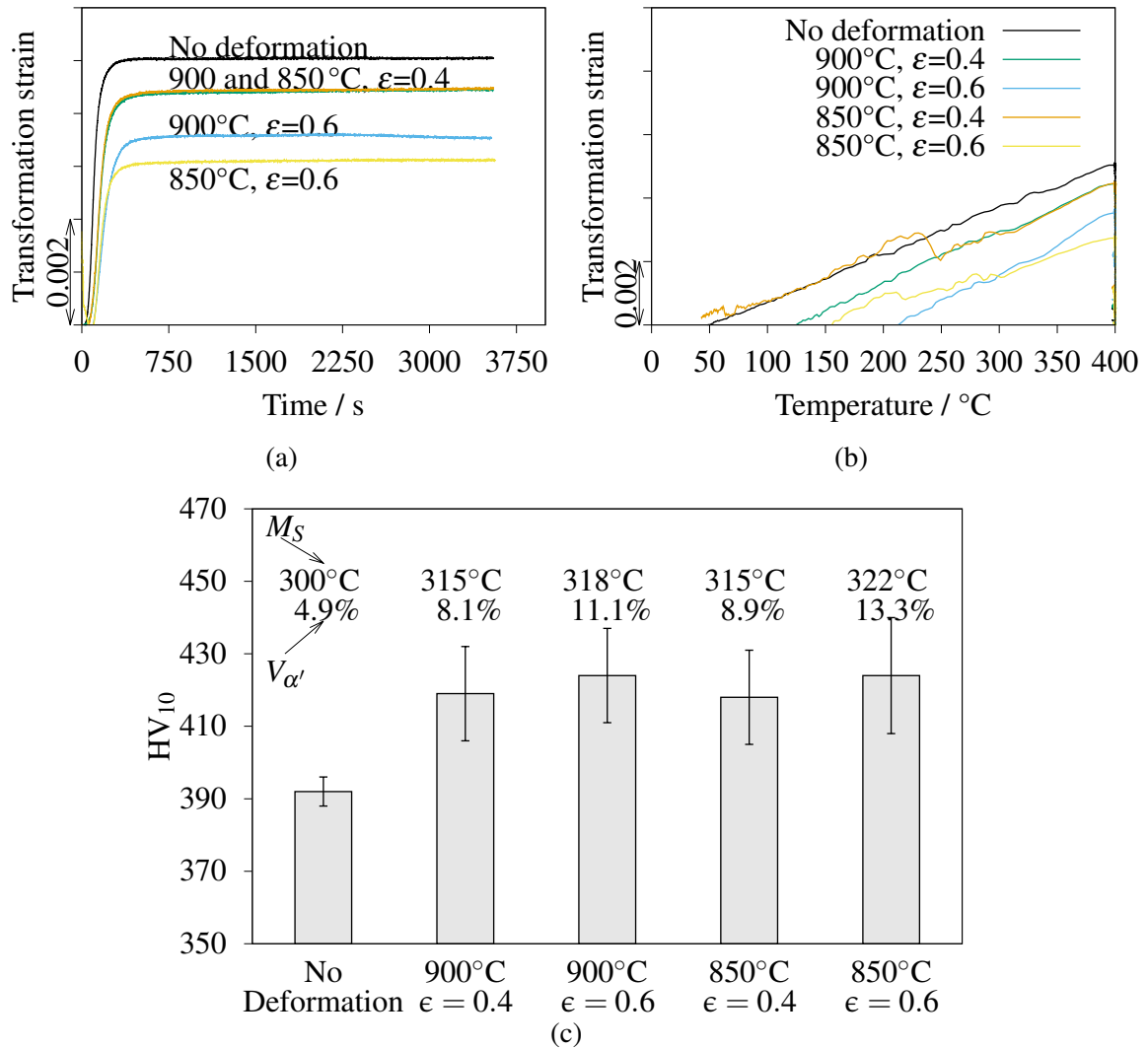
Figure 7.18 Deformation in austenite causing (a) mechanical stabilization and delayed kinetics, (b) increase in $V_{\alpha'}$ and (c) increase in bulk hardness in alloy A. Plots (a) and (b) were obtained from the dilatometric measurements.
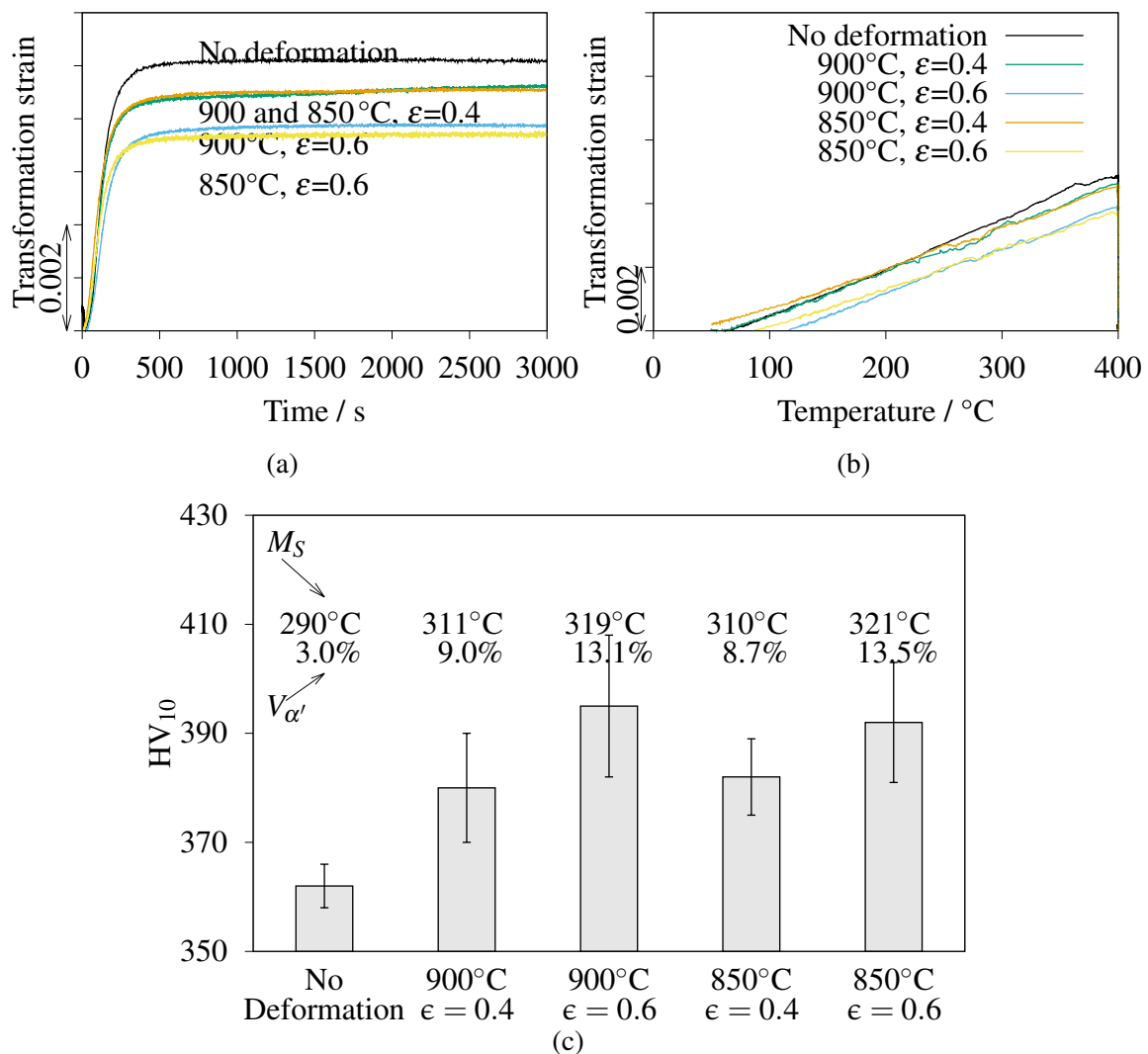
Figure 7.19 Deformation in austenite causing (a) mechanical stabilization and delayed kinetics, (b) increase in $V_{\alpha'}$ and (c) increase in bulk hardness in alloy B. Plots (a) and (b) were obtained from the dilatometric measurements.

X–ray diffraction of a deformed sample showed γ and α to be textured, which is noticeable from the varying intensity of various reflections with respect to strain in Fig. 7.20a. Intensities of all the X–ray diffraction scans have been normalized to the same value of $\{110\}_\alpha$. The intensity of X–rays scattered from the closed–packed planes of austenite $\{111\}_\gamma$ reduces due to deformation, however the intensity of $\{022\}_\gamma$ reflection increases. Exactly similar observations made for ferrite peaks.

Information from the analysis of X–ray diffraction scans is listed in Table 7.4. The fraction of austenite is similar for all the cases, so are the corresponding lattice parameters and carbon in the retained austenite. The major difference was in the proportion of bainite and martensite formed in the deformed samples which led to an overall increase in hardness and M_S temperature with respect to the undeformed samples. Values of c_α^e for alloy A ($\approx$ 0.15 wt%) show that the carbon in bainitic ferrite is greater compared to alloy B ($\approx$ 0.04 wt%), arising from the difference in T_0.
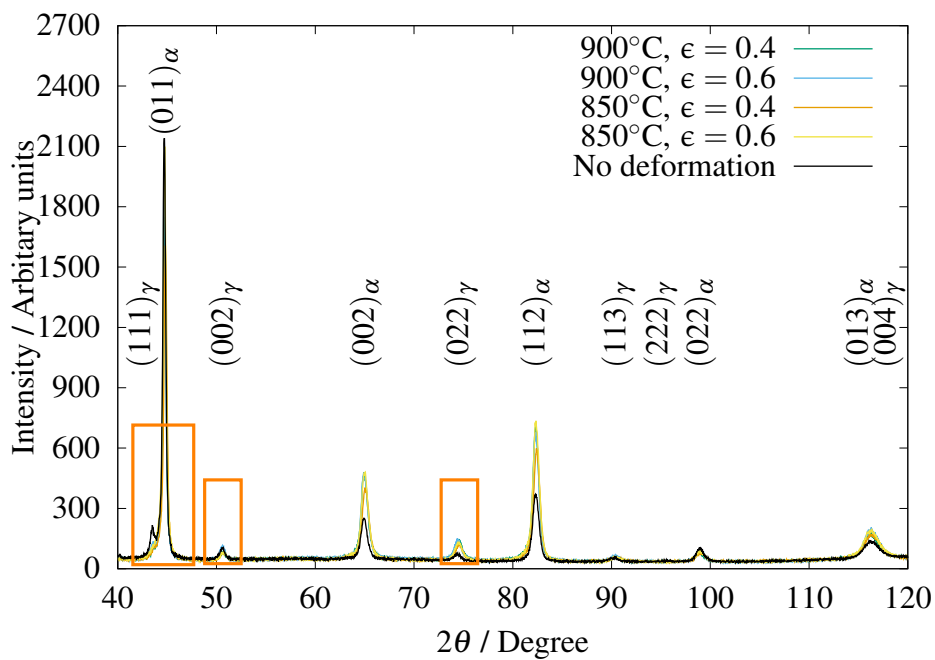
(a)
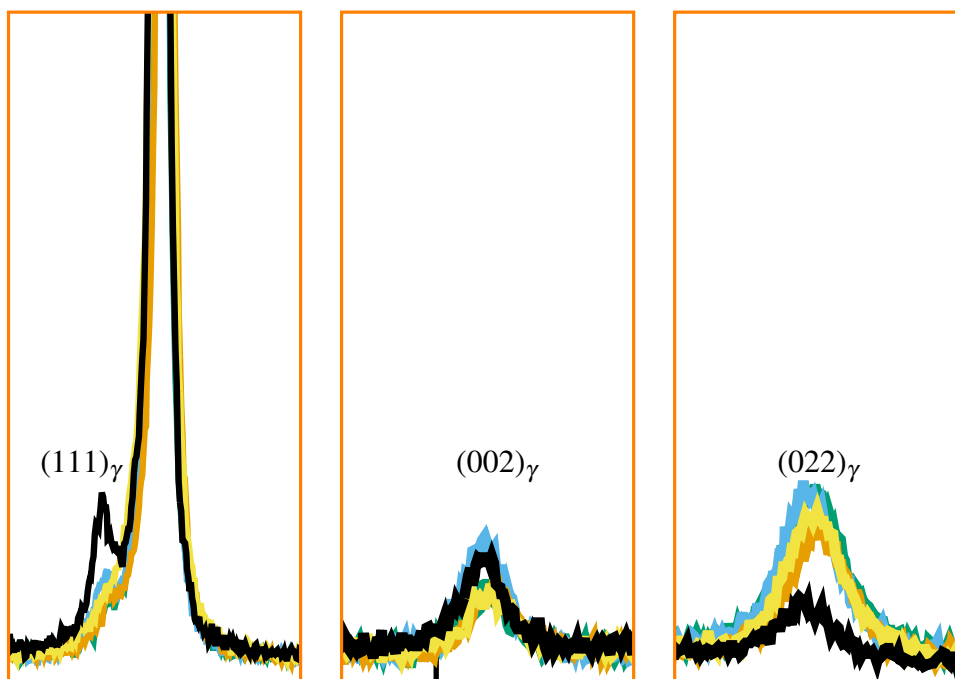
(b)

Figure 7.20 X–ray diffraction scans of samples of alloy A subjected to deformation in the austenitic region at 900 and 850 °C with a true strain of 0.4 and 0.6.
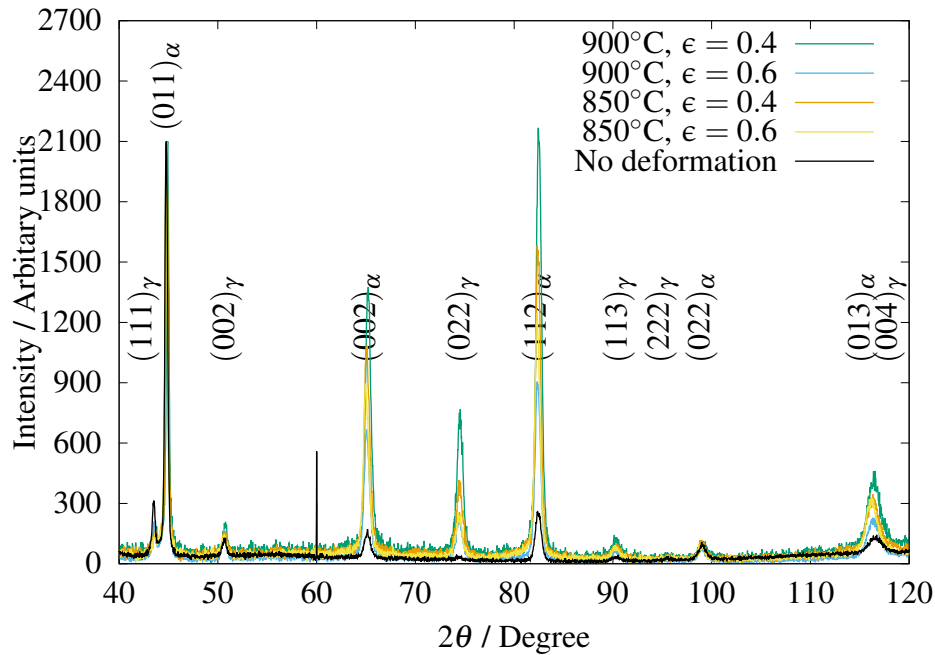
Figure 7.21 X–ray diffraction scans of deformed and undeformed alloy B showing significant decrease in $(111)_\gamma$ peaks, increase in $(022)_\gamma$ reflections and unchanged $(002)_\gamma$ at ε=0.4/0.6.

Table 7.4 Measured volume fraction of ferrite and austenite for both alloys using integrated intensity of (011), (002) and (112) peaks of ferrite and (111), (002) and (022) peaks of austenite. The effect of texture in determining the volume fraction of various phases has been dealt in accordance to the method proposed by Dickson *et al.* [160].

Alloy–Condition	$V_{\alpha_b}+V_{\alpha'}$	V_γ	a_α / Å	a_γ / Å	c_α / wt%	c_γ / wt%
A–900 °C, $\varepsilon = 0.4$	0.88	0.12±0.03	2.8728±0.0002	3.6074±0.0004	0.18±0.01	0.78±0.01
A–900 °C, $\varepsilon = 0.6$	0.87	0.13±0.03	2.8714±0.0002	3.6084±0.0004	0.13±0.01	0.81±0.01
A–850 °C, $\varepsilon = 0.4$	0.88	0.12±0.02	2.8719±0.0002	3.6073±0.0005	0.14±0.01	0.78±0.01
A–850 °C, $\varepsilon = 0.6$	0.86	0.14±0.03	2.8720±0.0002	3.6064±0.0005	0.15±0.01	0.75±0.01
A–No deformation	0.85	0.15±0.02	2.8715±0.0002	3.6092±0.0006	0.13±0.01	0.83±0.02
B–900 °C, $\varepsilon = 0.4$	0.85	0.15±0.02	2.8700±0.0002	3.6103±0.0004	0.06±0.01	0.91±0.01
B–900 °C, $\varepsilon = 0.6$	0.85	0.15±0.02	2.8697±0.0002	3.6107±0.0004	0.05±0.01	0.93±0.01
B–850 °C, $\varepsilon = 0.4$	0.86	0.14±0.02	2.8695±0.0002	3.6111±0.0005	0.04±0.01	0.94±0.01
B–850 °C, $\varepsilon = 0.6$	0.86	0.14±0.03	2.8700±0.0002	3.6110±0.0005	0.06±0.01	0.90±0.01
B–No deformation	0.84	0.16±0.02	2.8691±0.0001	3.6113±0.0007	0.03±0.01	0.95±0.02

Chatterjee *et al.* [206] developed a mathematical formulation of mechanical stabilization by balancing the force driving the transformation interface against the dislocation debris in

the austenite,

$$b\Delta G = \frac{1}{8\pi(1-\nu)}Gb^{3/2}\left(\frac{\varepsilon}{L}\right)^{1/2} + \tau_{s}b \tag{7.3}$$

where, b is the magnitude of the Burgers vector (2.52 Å), ΔG is chemical driving force, ν is the Poisson's ratio (0.27), G is the shear modulus of austenite (80 GPa), L is the average distance traversed by dislocations, τ_{s} is the shear stress due to solid solution hardening computed from the tensile strength using the Tresca criterion. It is evident from Fig 7.22 that the strains used in the present work are sufficient to cause mechanical stabilization.
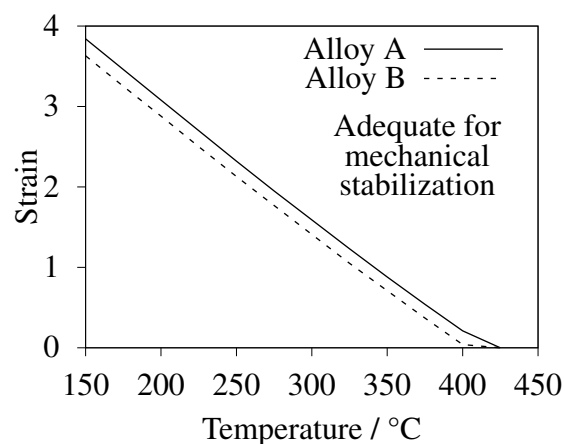
Figure 7.22 The critical strain for achieving mechanical stabilization in deformed austenite at various temperatures. The upper triangle denotes the region where the strain–temperature combination is adequate for mechanical stabilization.

7.7   Conclusions

Careful control of process parameters such as austenitization/isothermal bainitic transformation temperature, austenite grain size, amount of prior deformation is essential to achieve stable retained austenite and an optimum TRIP effect. The following interpretations can be drawn:

1. As expected, grain size scales with austenitization temperature and time of austenitization. Thermal grooving is a powerful technique to determine the grain size, however, smaller austenitization temperature and time leads to inadequate grooving which is not perceptible through microscopy. Remnant grooves from subgrain boundaries in the microstructure should be avoided in measurement of $\overline{L}_{\gamma}$. Reconstruction of the

prior austenite orientation from the bainite/martensite plates can be used to eradicate this problem of determining grain size at lower austenitization temperatures. The only demerit of the EBSD reconstruction is that it is time consuming to obtain statistically significant values of $\overline{L}_\gamma$.

2. Smaller austenite grain size ensures finer austenite block size which is supposed to be beneficial for ductility, but segregation diminished this impact. Lowering the austenitization temperature, reduced the scale of microstructure but it wasn't too beneficial for eradication of segregated regions.

3. Hardness entropy can be used to quantify the homogeneity of the microstructure which is susceptible to segregation due to the presence of higher weight fraction of alloying elements like Mn, Ni and Cr. The microhardness map of the segregated regions with load around 300 g is adequate to express the difference in local mechanical properties.

4. Highly segregating alloying elements like Mn can be detrimental to elongation due to formation of hard phase with larger proportion of martensite in MA constituents. This was the sole reason for the decrease in elongation while austenitization at low temperatures, was insufficient for homogenization. There is therefore a trade off between enhancement in properties through formation of finer scales of structure, and the elimination of hard phase formation due to segregation.

5. Two step isothermal transformation failed in improving the stability of retained austenite in both alloys and subsequently leading to formation of excessive martensite during cooling.

6. Plastically deformed austenite lead to mechanical stabilization, the extent of which depended on the temperature and the amount of deformation. Bainitic transformation was suppressed in strained austenite and the corresponding retained austenite was not stable enough for prohibiting martensite formation. Driving force for martensite formation is higher and the critical strain required for prohibiting $\alpha^{'}$ is in excess of 1 at the M_S temperature.

7. Mechanical stabilization didn't achieve the stable austenite required for optimum TRIP effect as the volume fraction of martensite increased substantially negating the whole objective of improving the strength–ductility product. Thus, it should be noted that in order to prohibit martensite formation, the bainitic transformation should be done in recrystallized austenite rather than in deformed austenite.

Chapter 8

Revisiting bainite crystallography and prior austenite reconstruction

Many attempts have been made previously to determine simultaneously the true transformation strain, orientation relationship and habit plane of a single plate of α'; however, similar assessment of an individual platelet of α_b has rather never been dealt with. All previous studies have dealt with the determination of the habit plane, the orientation relationship and the shape deformation as independent parameters measured on different plates and different alloys. However, these quantities are mathematically connected by the crystallographic theory of displacive transformations and cannot in principle be treated as independent quantities to obtain a closure between theory and experiment. The problem arises because the bainite platelets are extremely small in size, making it incredibly difficult to conduct all the measurements on a single plate [209–213]. This section addresses this problem and tries to fill the gap by determining all the three parameters together on a single plate of bainite. A high carbon, carbide–free nanostructured bainitic steel was chosen to carry out the experiments for two reasons. The absence of cementite in bainitic ferrite helps in the determination of habit plane directly with respect to austenite that is retained, along with the orientation relationship between the parent and product phases [17]. The chemical composition of the steel used is given in table 8.1 [214].

Alloy	C	Si	Ni	Al	Mo	Mn	Co	Cr
Nanostructured bainite	0.72	3.87	3.40	1.39	0.21	0.02	<0.01	<0.01

Table 8.1 Chemical compositions of alloy, wt%.

The samples were prepared as described in Chapter 3 for thermal grooving experiments. However, two mutually perpendicular surfaces were prepared for the two–surface analysis. Perpendicularity was obtained by precision machining using the ATM Brilliant cutting machine. Heat treatment consisted of austenitization at 1050 °C, followed by cooling to the isothermal temperature of 400 °C at an approximate rate of $5\,°C\,s^{-1}$. The time of isothermal bainitic transformation was 3 h, after which the sample was cooled to room temperature. The dilatometric response during this heat treatment given [214] showed no martensitic transformation during cooling. The microstructure thus obtained only contains bainite and retained austenite.

8.1 Experimental determination of habit plane

The determination of habit plane was carried out by two–surface analysis as described elsewhere [209, 212]. The traces of the bainitic plate at two adjacent, non parallel surfaces were used to compute the habit plane. Fig. 8.1 shows the two perpendicular surfaces on which the traces of the plate used for analysis have been marked ($\mathbf{t}_{11}$ and $\mathbf{t}_{21}$). The angles between the edge (intersection of the two surfaces) and the traces $\mathbf{t}_{11}$ and $\mathbf{t}_{21}$ are measured in the anticlockwise sense, to determine the unit vectors of each of the two traces. The cross product of these two vectors gives the normal to the habit plane in the sample frame denoted by basis "S". Conversion of the habit plane into the crystal frame (basis γ), requires the multiplication of the vector with the rotation matrix given by ($\gamma\,J\,S$). This rotation matrix is derived from the Euler angles of the austenite measured through EBSD. Similar two surface analyses have been done for two further plates of bainite.
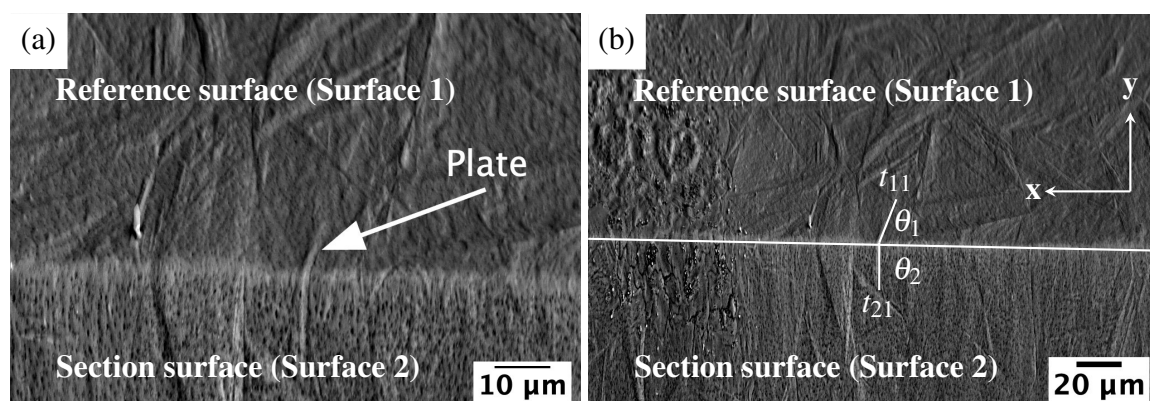
Figure 8.1 Plate P1 and the definitions of θ_1 and θ_2 respectively. The directions in the sample frame are marked in the second image.

Unit vectors $\mathbf{t}_{11}$ and $\mathbf{t}_{21}$ are given by:

$$\mathbf{t}_{11} = [\cos(\theta_1) \quad \sin(\theta_1) \quad 0]$$
$$\mathbf{t}_{21} = [\cos(\theta_2) \quad 0 \quad \sin(\theta_2)]$$

It follows that:

$$[S;\mathbf{t}_{11}] = [\text{-}0.33840947 \quad 0.94099895 \quad 0]$$
$$[S;\mathbf{t}_{21}] = [0.01560261 \quad 0 \quad \text{-}0.99987827]$$
$$[S;\mathbf{p}_1 = \mathbf{t}_{21} \times \mathbf{t}_{11}] = [\text{-}0.940884 \quad \text{-}0.338368 \quad \text{-}0.014682]$$

$$(\gamma \, J \, S) = \begin{pmatrix} -0.2470 & -0.6069 & 0.7554 \\ 0.7788 & -0.5882 & -0.2179 \\ 0.5766 & 0.5345 & 0.6180 \end{pmatrix}$$

$$[\gamma;\mathbf{p}_1] = (\gamma \, J \, S) \, [S;\mathbf{p}_1] = [0.426613 \quad \text{-}0.530507 \quad \text{-}0.732485]$$

The habit plane normal therefore is [0.426613   -0.530507   -0.732485]. Other two surface analyses carried out are shown in Fig. 8.2. Fig. 8.3 shows the inverse pole figure of the experimentally determined habit plane for the current alloy, compared with literature of carbide–free bainitic steels.

(a)
Reference surface (Surface 1)
Plate P2
θ_1=**95.05°**
θ_2=**105.02°**
Section surface (Surface 2)   **20 µm**

(b)
Reference surface (Surface 1)
Plate P3
θ_1=**91.89°**
θ_2=**102.36°**
Section surface (Surface 2)   **20 µm**
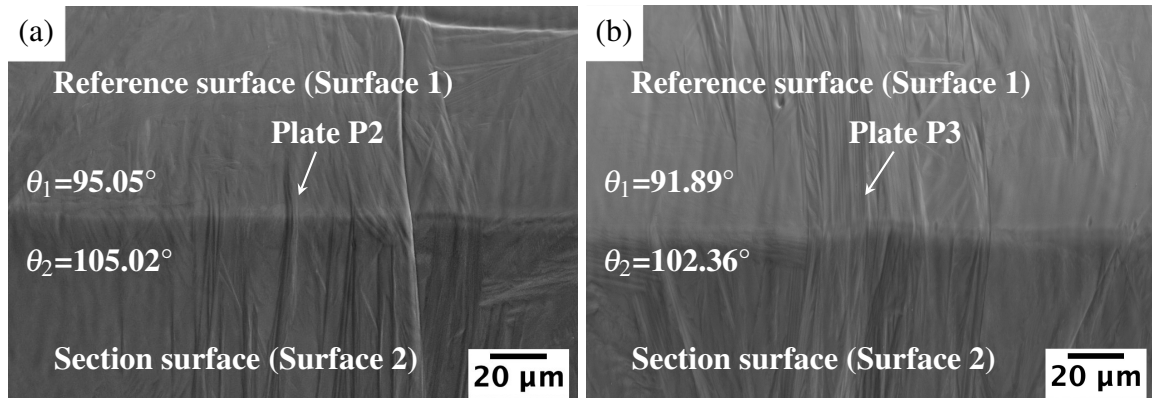
Figure 8.2 Other plates of bainite analysed similarly like plate P1 to determine the habit plane.
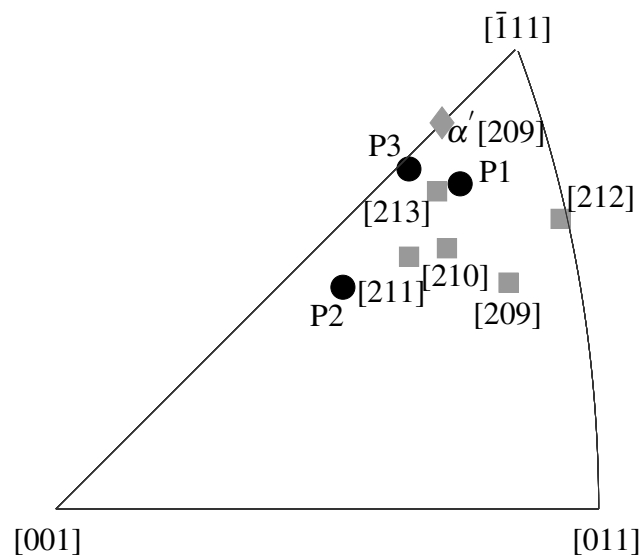
Figure 8.3 The inverse pole figure showing the experimentally determined habit plane of bainite plates P1, P2 and P3 for carbide free bainitic steel in the present work denoted in black circular dots. Grey square points denote the data collated from literature [209–213]. The grey diamond denotes the habit plane of α', $\{557\}_\gamma$ measured by Srinivasan and Wayman [209]. Plate P2 is a little off from the other two plates but angular deviation is less than 7°. This is attributed to the error associated in measurement of traces $\mathbf{t}_{11}$ and $\mathbf{t}_{21}$ from scanning electron micrographs. Except for author [209], all other measurements pertain to sheaves of bainite.

8.2 The orientation relationship

The orientation relationship between austenite and bainitic ferrite was measured through electron back scattered diffraction. Fig 8.4 shows the EBSD map overlayed on the secondary electron image of the single plate of bainite, and the orientation relationships are illustrated in Fig 8.5. The actual orientation relationship is likely to be irrational but it is noted that there is a certain amount of uncertainty as indicated by the angular spread of the EBSD data in each case. Nevertheless, it is evident that there is a $\{111\}_\gamma$ plane approximately parallel to a $\{110\}_\alpha$ plane and corresponding close–packed directions within those planes approximately parallel.
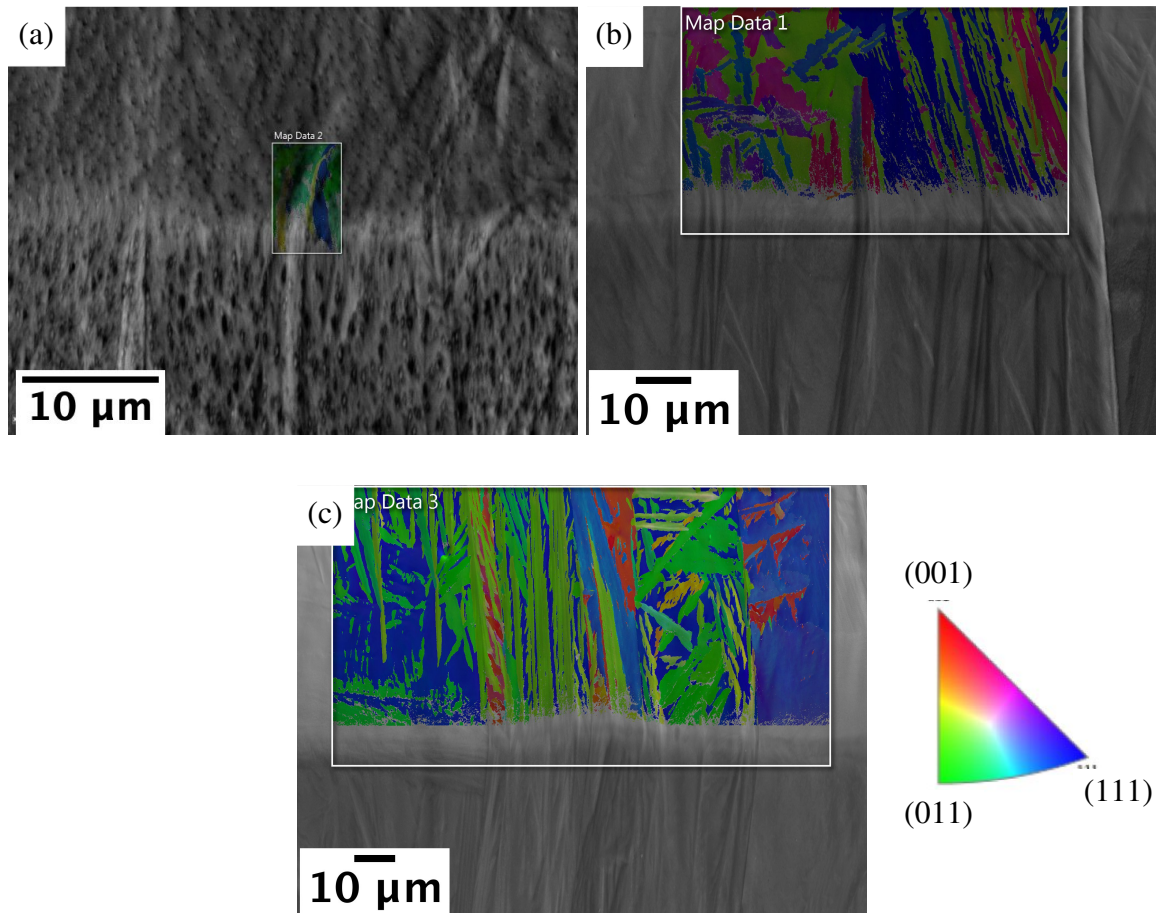
Figure 8.4 Inverse pole figure map measured by electron back scattered diffraction for the plates (a) P1, (b) P2 and (c) P3 overlayed on the scanning electron image.

Plate P1

Plate P2

X

A

B

Y

X

A

B

Y

Plate P3

X

A

B

Y
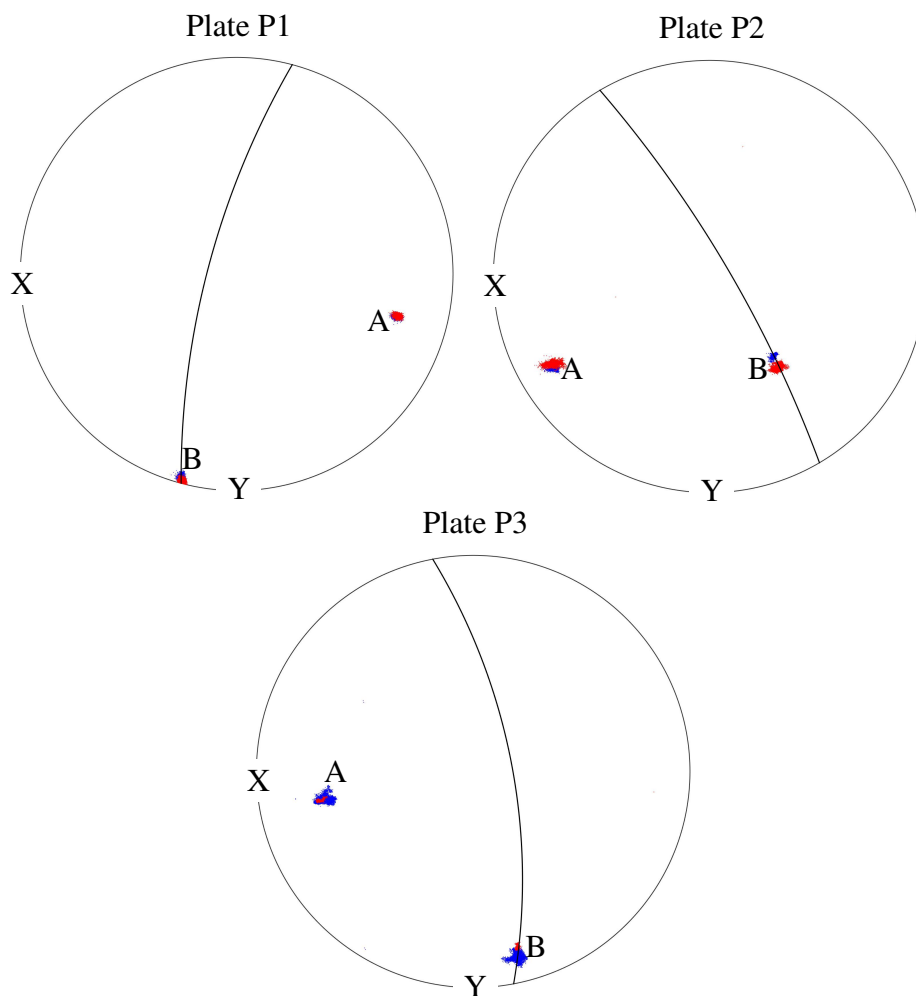
Figure 8.5 KS relationship between γ and α. A denotes the planes almost overlapping and B shows the directions within the misorientation angle of 5°. Blue and red coloured poles correspond to γ and α respectively.

The irrational orientation relationship and the corresponding rotation matrices are converted into Euler angles and have been plotted in Fig. 8.6 to show the deviation from standard KS and NW orientation relationship.
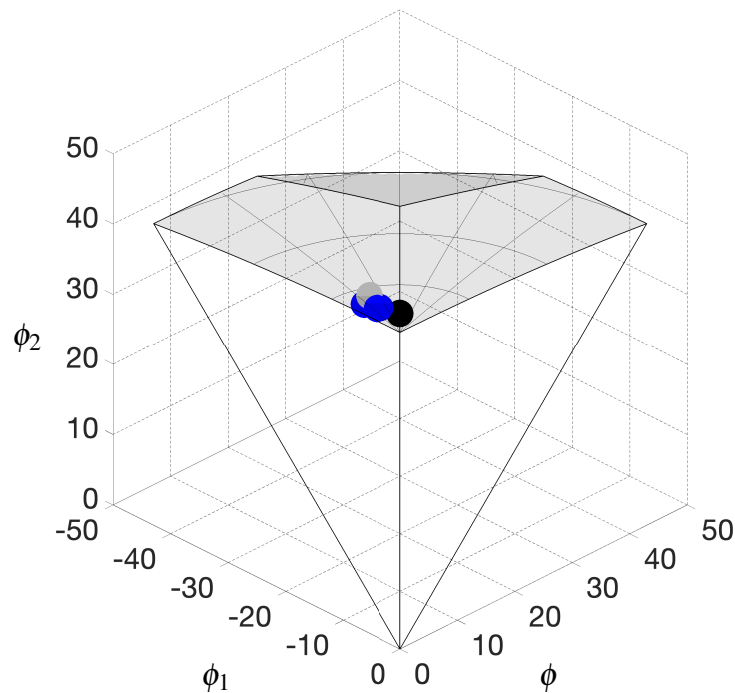
Figure 8.6 Standard KS and NW orientation relationships with the irrational orientation relationships measured for each of the plates P1, P2 and P3. Black point–KS, grey point–NW and the blue points refer to plates P1, P2 and P3 respectively.

Table 8.2 tabulates the two standard orientation relationships along with the measured ones for the three plates represented in Euler angles (Bunge convention) and axis angle pairs. The misorientation from the standard OR has also been reported to observe that measured relationships are irrational and offset by around $5°$. The systematic error associated with the spread in the orientations of a pole measured through EBSD is $\pm 5°$.

Table 8.2 Standard KS and NW orientation relationships between γ and α expressed in Euler angles (Bunge convention) and axis–angle pairs. Also the orientation relationship measured from EBSD scans for the three plates under consideration has been tabulated, with the misorientation with the standard orientation relationship been compiled. Error associated with the measurement is within $\pm 5°$.

Orientation relationship	Euler angles / °			Axis–angle pair	Misorientation/ °	
	ϕ_1	ϕ	ϕ_2		KS	NW
KS	355.80	10.53	65.80	$\langle$-0.1766 0.1766 0.9679$\rangle$ 42.85°	0	5.26
NW	180	99.74	45	$\langle$-0.2007 0.0831 0.9761$\rangle$ 45.99°	5.26	0
Plate 1	89.90	82.56	45.63	$\langle$-0.1562 0.0622 0.9855$\rangle$ 44.96°	5.35	2.38
Plate 2	86.71	9.83	229.38	$\langle$-0.2124 0.0717 0.9745$\rangle$ 44.95°	5.22	1.27
Plate 3	259.48	43.49	91.90	$\langle$-0.1851 0.1063 0.9770$\rangle$ 44.30°	3.40	2.09

Pole figures showing the irrational $\gamma \rightarrow \alpha$ orientation relationship along with the habit plane of the various plates P1, P2 and P3 in the basis γ are shown in Figs. 8.7, 8.8 and 8.9, respectively. It is evident that the closest packed planes and directions of bainitic ferrite and austenite are related closely and the habit planes measured from two surface analyses are within 7°, with the trace being nearly similar for all the plates. The habit plane is also found to be close to that of martensite data at about $\{557\}_\gamma$ [209]. The spread in the black austenite orientation seems more as compared to that of ferrite due to the difference in the number the data points plotted for austenite is greater than ferrite.
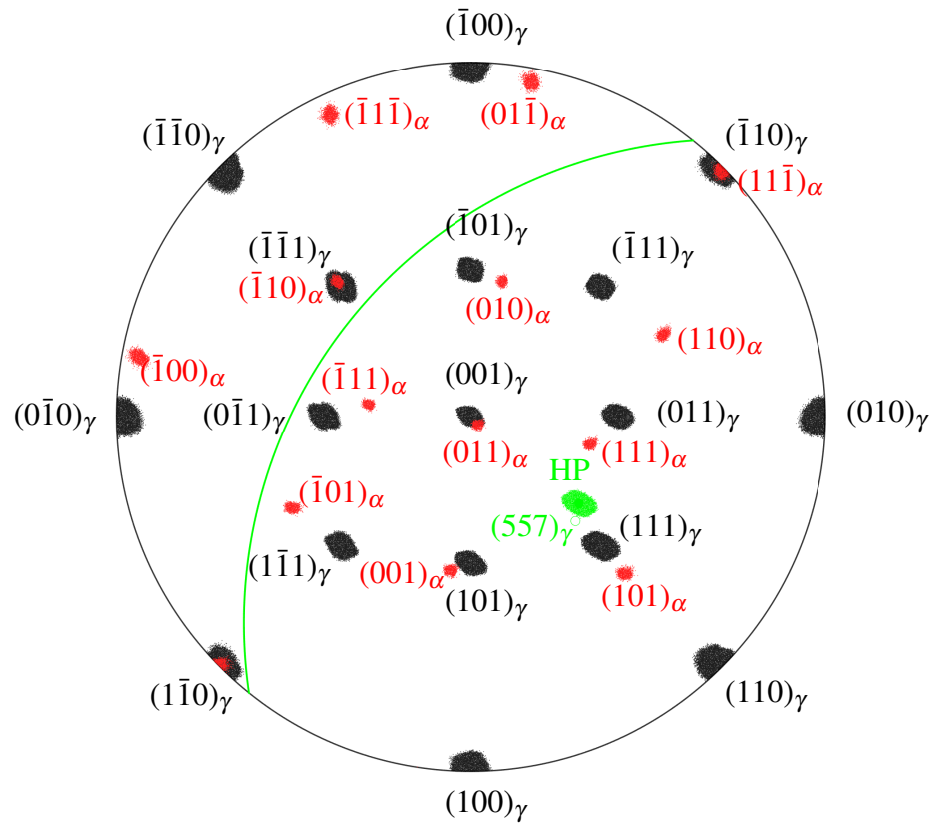
Figure 8.7 Orientation relationship and the habit plane for plate P1 along with the trace of the habit plane has been marked on a stereogram. Black points denote the austenite, red points refer to the bainitic ferrite and green points indicate the habit plane orientations. There is a spread associated with each pole which is due to the fact that the structures observed are not free from defects and strain fields. This spread gives an uncertainty in the stated crystallographic data. The green pole is the habit plane of martensite $(557)_\gamma$ [209]. The trace of the mean habit plane orientation is marked in green.
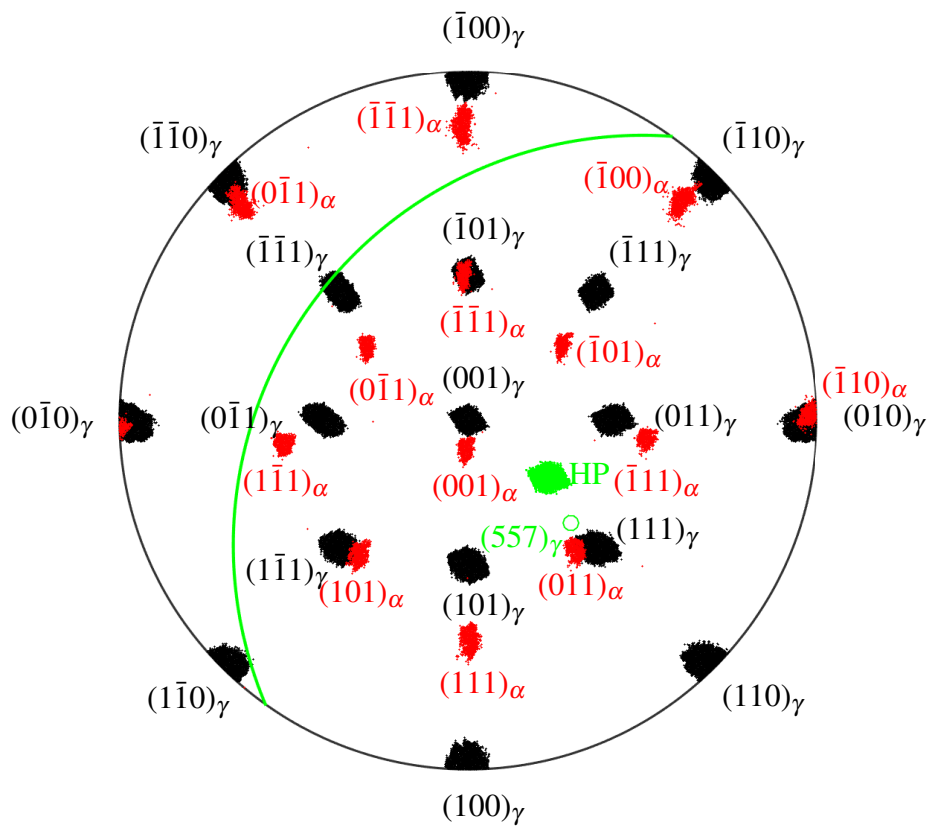
Figure 8.8 Orientation relationship and the habit plane for plate P2.

Figure 8.9 Orientation relationship and the habit plane for plate P3.

8.3   Determination of true strain

The transformation is accompanied by displacements that can be measured on a pre–polished sample of austenite using a Atomic Force Microscopy (AFM).

Fig. 8.10 shows the AFM scan of the first bainitic plate P1. The line scan (A–B, Fig. 8.10a) showing the height and width of the plate is shown in Fig. 8.11. The exaggerated Y-scale shows the sharp ascent on one side of the line profile associated with the bainitic plate. However, the adjacent side of the line profile shows a gradual slope due to the plastic accommodation in the austenite. Similar features can be seen in all the three line profiles for plates P1, P2 and P3. Figs. 8.12 and 8.14 give the top and isometric view of plates P2 and P3 respectively. The corresponding extracted line profiles for plates P2 and P3 are given in Figs. 8.13 and 8.15 respectively. The apparent strain is measured by the ratio of the height to the width of the surface relief caused by the displacive transformation and is also given by the slope of sharp ascent.

The measured apparent strains for plates P1, P2 and P3 are 0.31, 0.21 and 0.22 respectively. This strain needs to be corrected to determine the true strain by incorporating the direction of shear and the orientation of the plate. The latter can be determined by the two surface analysis where the angle made by the trace $\mathbf{t}_{21}$ with the reference surface (surface 1) as discussed previously in Fig. 8.1 is used to correct the strain value, Fig. 8.16. The corrected strains are found to be 0.30±0.05, 0.23±0.03 and 0.24±0.04 for P1, P2 and P3, respectively.
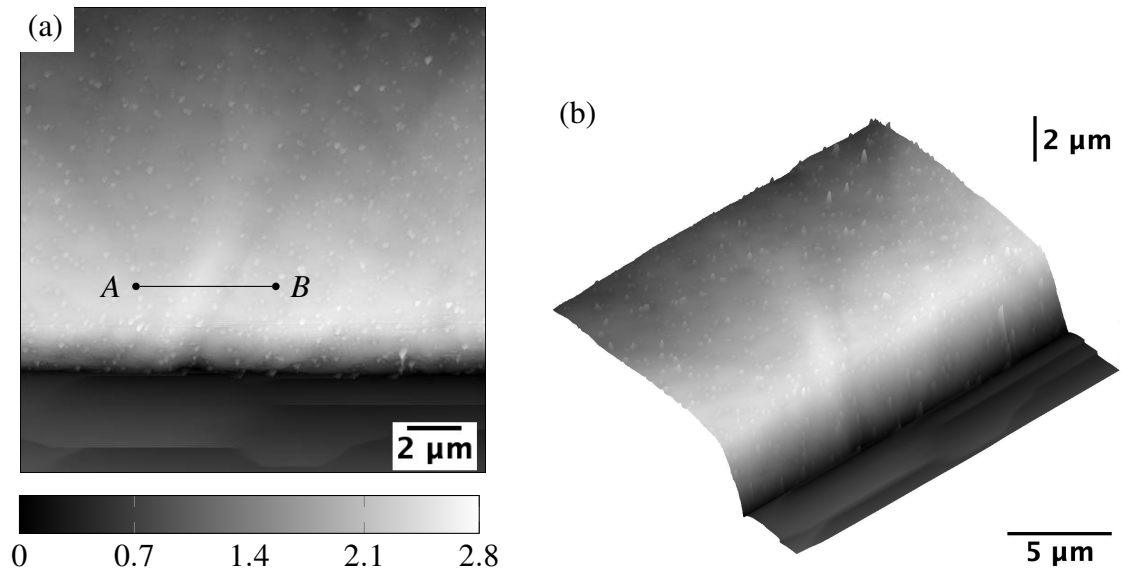
Figure 8.10 The AFM scan of bainitic plate P1 shown from (a) top view and (b) isometric view, exhibiting the surface relief caused by the displacive transformation. The line profile across the plate of bainite is extracted and plotted in Fig. 8.11.
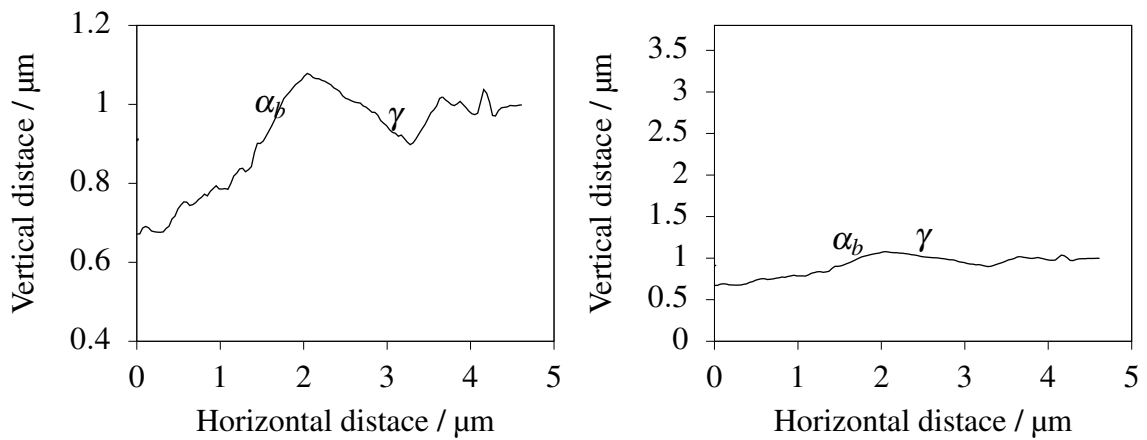
Figure 8.11 Line profile of surface relief of bainitic plate P1 plotted on (a) exaggerated Y–axis scale and (b) 1:1 scale, giving a strain value of 0.31. The corrected strain value is 0.30±0.05. The austenite side of the scan is associated with irregular relief, caused as a result of plastic accommodation which involves multiple slip systems resulting in intense dislocations [215].
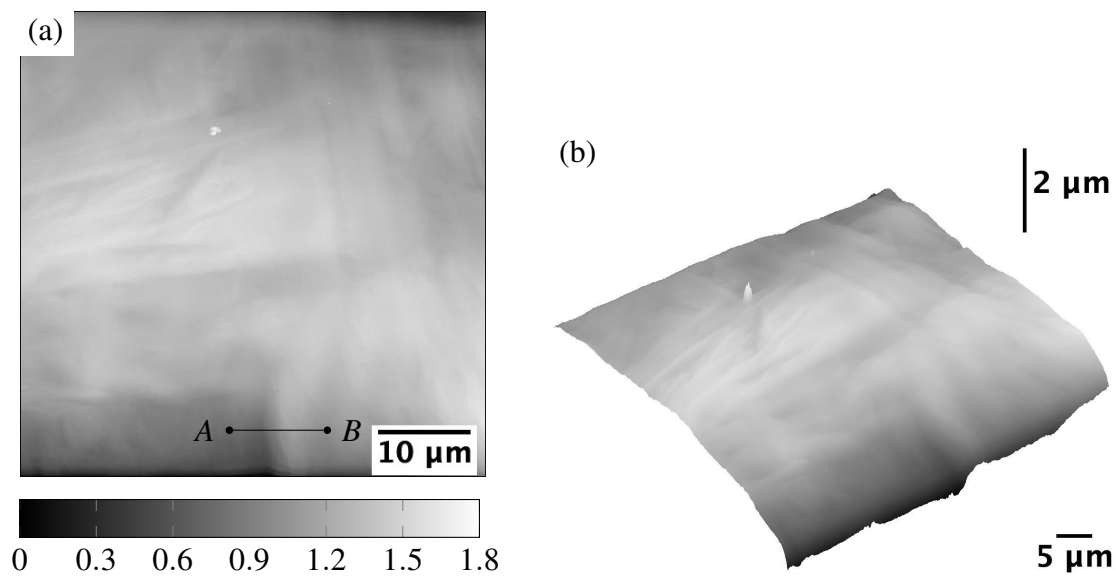
Figure 8.12 The AFM scan of bainitic plate P2 shown from (a) top view and (b) isometric view, exhibiting the surface relief caused by the displacive transformation. The line profile across the plate of bainite is extracted and plotted in Fig. 8.13.
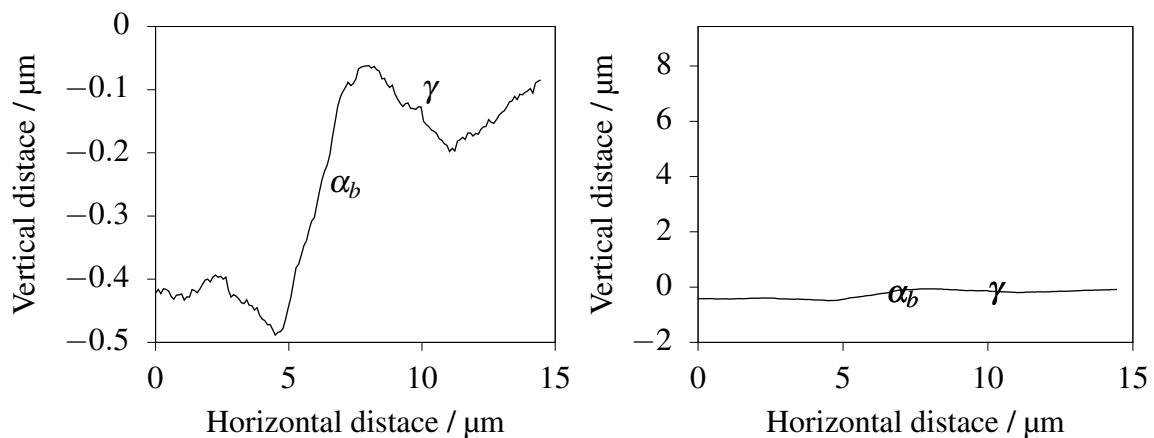
Figure 8.13 Line profile of surface relief of bainitic plate P2 plotted on (a) exaggerated Y–axis scale and (b) 1:1 scale, giving a strain value of 0.21. The corrected strain value is 0.23 ± 0.03.
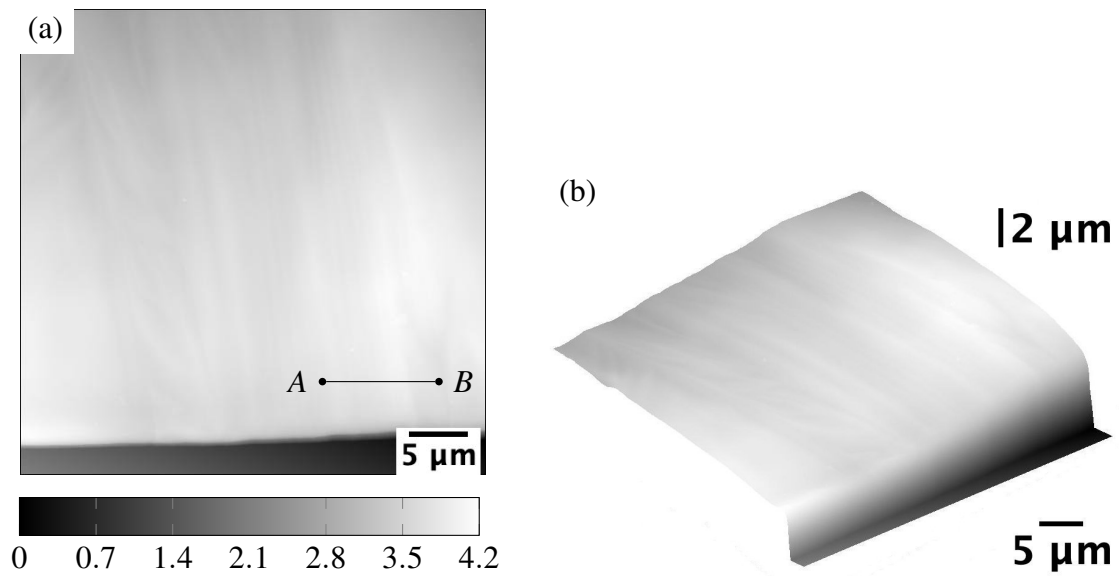
Figure 8.14 The AFM scan of bainitic plate P3 shown from (a) top view and (b) isometric view, exhibiting the surface relief caused by the displacive transformation. The line profile across the plate of bainite is extracted and plotted in Fig. 8.15.
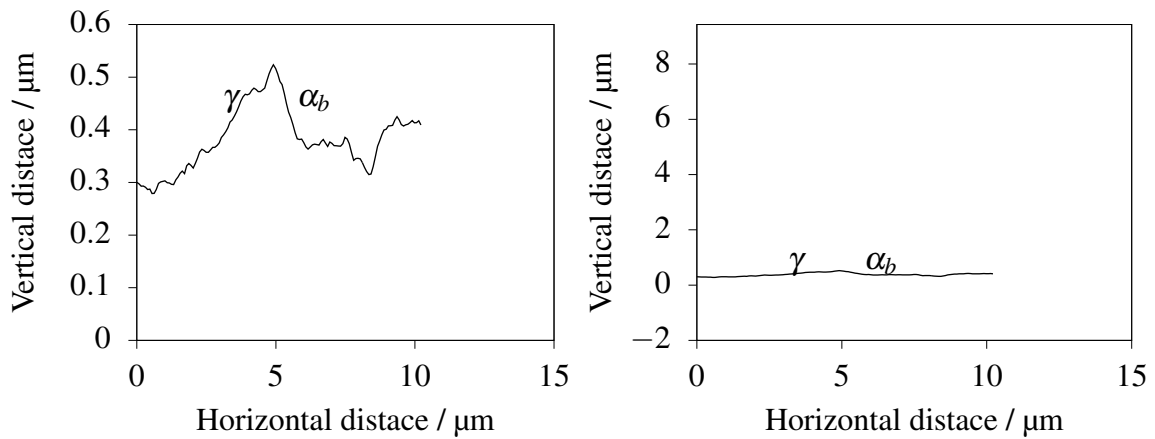

Figure 8.15 Line profile of surface relief of bainitic plate P3 plotted on (a) exaggerated Y–axis scale and (b) 1:1 scale, giving a strain value of 0.22. The corrected strain value is 0.24±0.04.
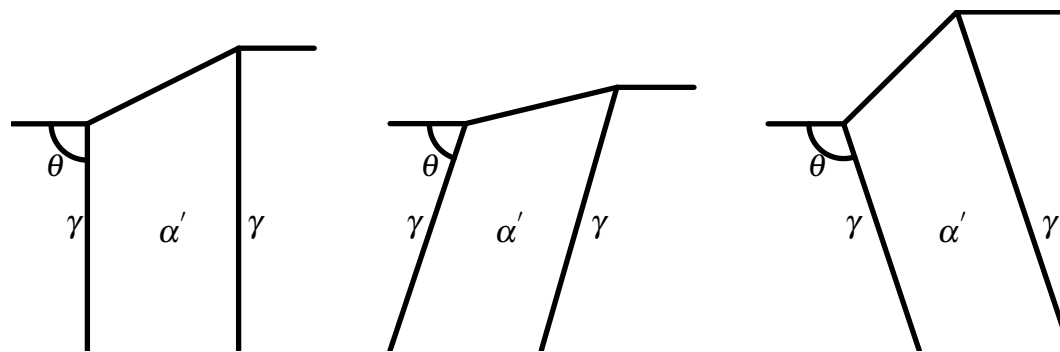
Figure 8.16 Schematic of plate of bainite making (a) right, (b) acute and (c) obtuse angles to the surface of the specimen showing surface relief. The amount of true strain is the same for all the three cases but the apparent strain varies significantly as a function of the inclination angle.

8.4   Austenite reconstruction from bainite ferrite orientation

There have been many successful attempts at reconstructing the austenite grain orientation from the martensite or bainitic plate orientations [216, 217]. The most recent work is by Tuomo Nyyssönen who used the Matlab and MTEX toolbox for this [218–220]. This method has been adopted here:

8.4.1   Principles of reconstruction

The method by Nyyssönen *et al.* [218–220] consists of four components:

1. Determination of the orientation relationship between bainitic ferrite and austenite by an iterative approach. The KS orientation relationship was assumed to be the starting orientation relationship. Next, the actual orientation (from EBSD data) and assumed KS orientation are compared to determine the minimum deviation angles. Multiple iterations then allow the angle between the closest packed planes of ferrite and austenite to converge to a constant value [218, 219].

2. Each plate misorientation is assigned a value depending upon whether the misorientation between two variants (plates) originates from the same prior austenite. Accordingly a value of between 0 and 1 is assigned by using a cumulative distribution function [220, 219].

3. A clustering algorithm is used to classify each of the martensitic variants into one parent austenite depending upon the plate boundaries shared. These plates considered as nodes possess many boundaries within one cluster and relatively fewer boundaries between clusters [220, 219].

4. Reconstruction of austenite using the clusters from step 3 and the orientation relationship determined in step 1. The determined austenite orientations are then used to reconstruct the prior austenite grains.

The flowchart of the entire working script is given in Fig. 8.17. The raw EBSD file is imported into MTEX toolbox in MATLAB (8.18a), depending upon the presence of retained austenite or not the crystal symmetries of α and γ are either imported or defined. Each martensitic/bainitic variant is converted into a plate (which is analogous to a grain) and an optional cleaning up of the grains smaller than a threshold value is done. The plate boundaries are determined with a misorientaion angle less than the minimum of all possible misorientations in 24 variants following the KS orientation relationship (Fig. 8.18c).

An iterative loop is used to solve the following two equations simultaneously using the KS orientation relationship as the starting point.

$$(C_i T_{\gamma \to \alpha})^{-1}(C_j T_{\gamma \to \alpha}) = M \tag{8.1}$$

$$T_{n+1,k} = C_j^{-1} C_i \overline{T}_n M_k \tag{8.2}$$

where, $T_{\gamma \to \alpha}$ is the rotation matrix defining the orientation relationship between γ and α, C_i and C_j denote one of the 24 mutually equivalent symmetry elements in a cubic system, M is the theoretical misorientation between the different variants of KS orientation relationship, Equation 8.1 can be rearranged and expressed as Equation 8.2. The definitions of the terms remain the same, however, Equation 8.2 is used for the experimental misorientation between intermartensitic plates (M_k), with $T_{n+1,k}$ and $\overline{T}_n$ denoting the experientially determined orientation relationship between γ and α at iteration step $n+1$ and n respectively. Note the orientation relationship at iteration n (i.e. right hand side of 8.2) is a mean value. The value of $\overline{T}_n$ at $n = 0$ is simply the starting KS orientation relationship.

The intermartensitic plate misorientation is assigned a value using the following cumulative density function equation:

$$S(x) = \frac{1}{[1 + (\frac{M_{\text{dev}}}{2})^5]} \tag{8.3}$$

where, M_{dev} is the minimum deviation angle between the experimentally determined inter-martensitic plate misorientation (from EBSD data), and the theoretically generated set of

martensitic misorientations (*M*). The martensitic plates and plate boundaries in Figs. 8.18b and 8.18c respectively, are then converted into a sparse array using Equation 8.3 and subjected to a clustering algorithm discussed in detail elsewhere [221]. Post clustering the indices of each plate of martensite are linked to the orientation of the parent austenite, which is chosen on the basis of the most intense orientation in the ODF (orientation distribution function).
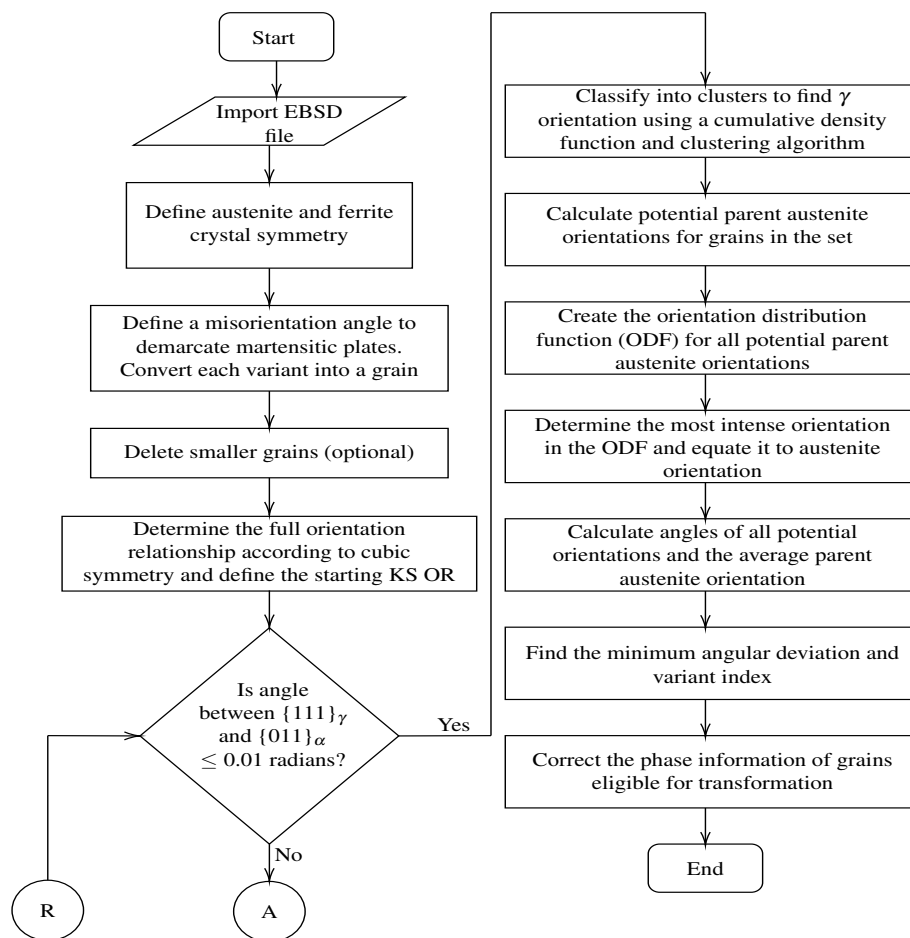
Figure 8.17 Flowchart showing the steps involved in the reconstruction algorithm.

R

A

Determine intermartensitic misorientations
with respect to all KS variants

Determine the interferritic grain boundaries
and all neighboring grain pairs

Determine the angles between the
possible misorientation set and the grain
pair misorientations

Determine the minimum angle and
corresponding index of all the angles
in the above step

Determine cutoff as value encompassing
90 % of misorientations

Limit the list of indexes of the
misorientations to minimum angle between
the % misorientation $\leq$ the cutoff value

Return all misorientations to "primary"
misorientation

The reconstructed EBSD map of austenite is given in Fig. 8.18d. One portion of the EBSD map of ferrite from Fig. 8.18a is cropped and magnified and the corresponding reconstructed austenite is also shown in Figs. 8.19a and 8.19b, respectively. The measured and calculated pole figures of ferrite are shown in Figs. 8.19c and 8.19d, respectively. Both the pole figures match well, validating the reconstruction algorithm.
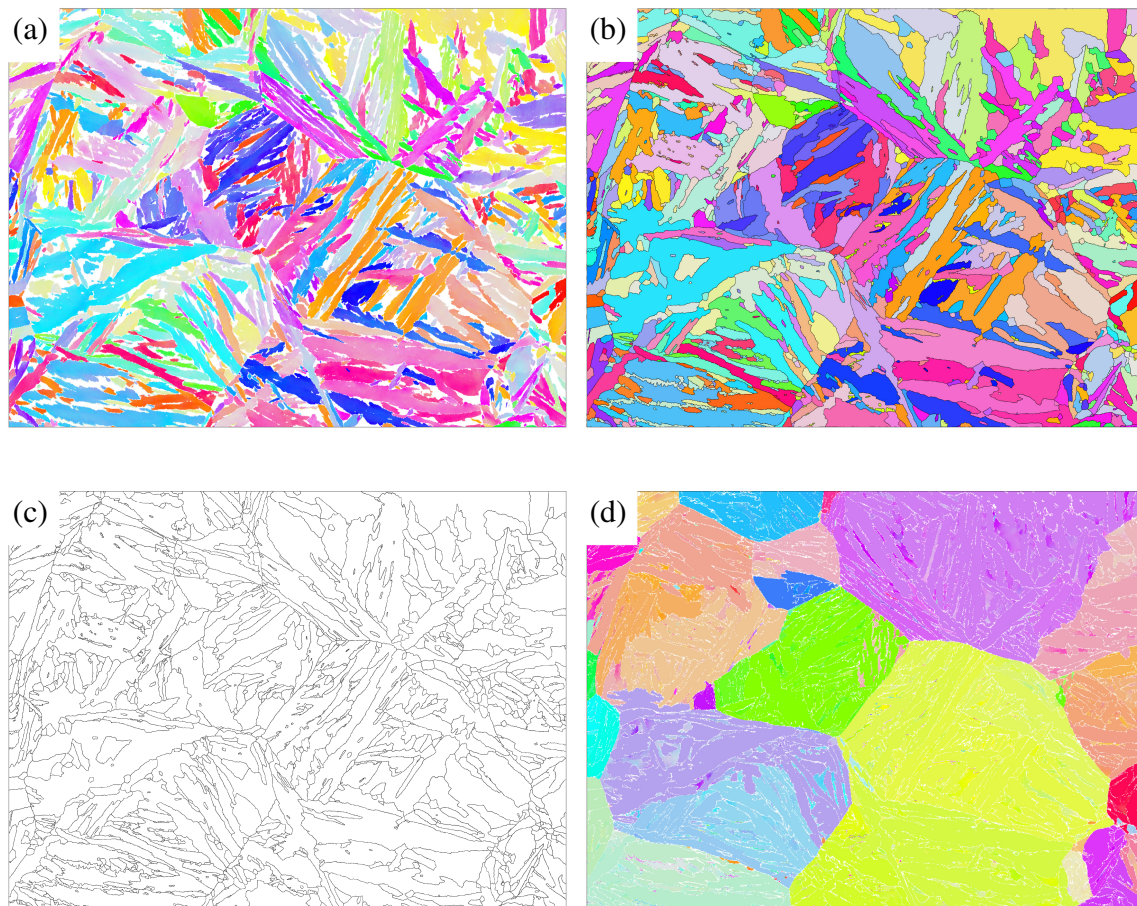
Figure 8.18 The reconstruction steps showing the (a) raw EBSD martensitic orientation map, (b) plates of martensite delineated from the raw map using misorientation angle less than the minimum of misorientations of KS variants, (c) the edges of the plates used to build the boundary information used to derive the irrational $\gamma \rightarrow \alpha$ orientation relationship, (d) the constructed γ orientation.
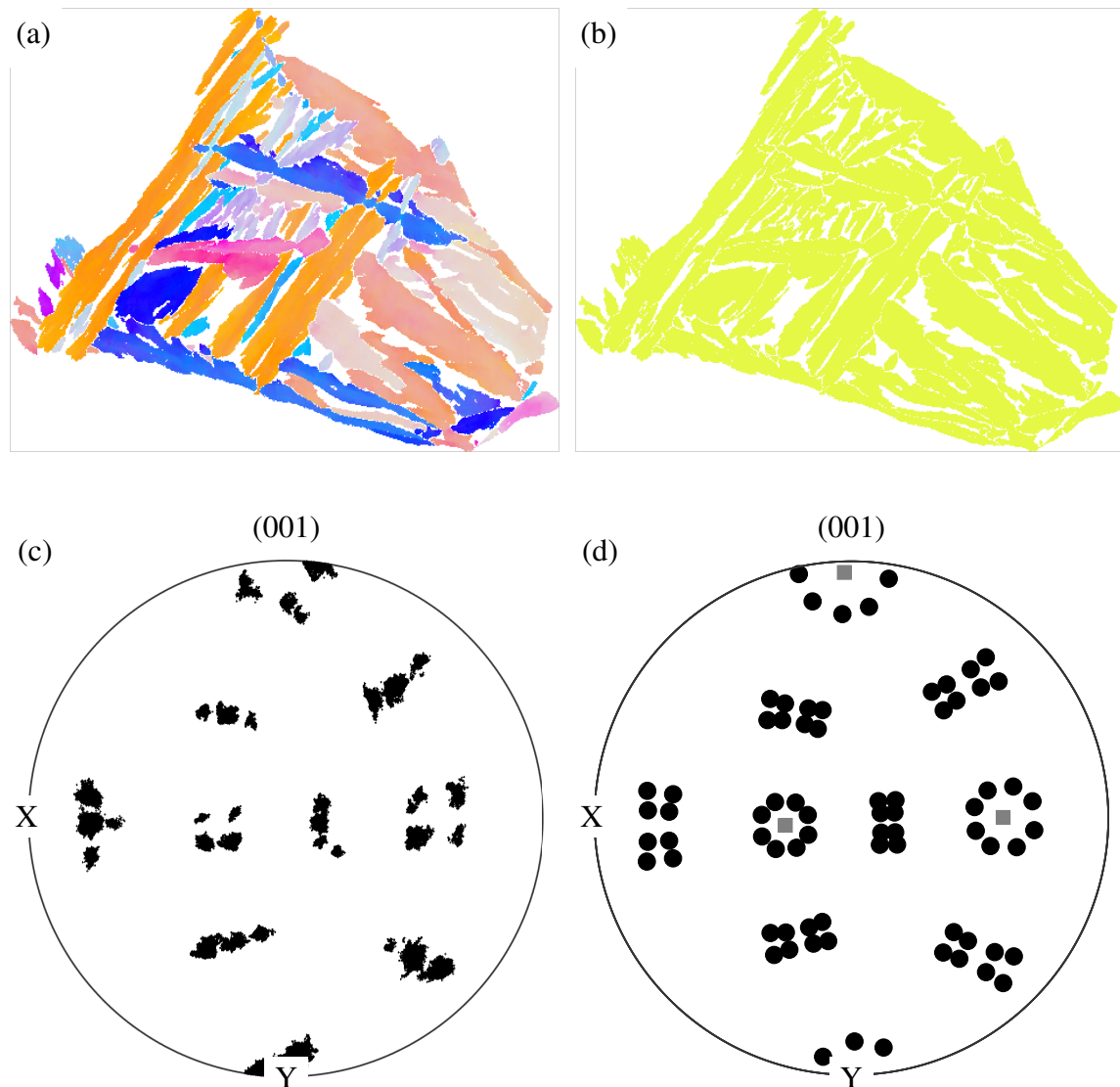
Figure 8.19 Cropped grain from the complete EBSD map exploded and shown in (a) with all bainitic ferrite variants, (b) is the corresponding reconstructed austenite map. (c) and (d) are the experimental and calculated pole figures of (001) ferrite showing all the 24 variants. In (d) the mean orientation of austenite from which the ferrite variants are calculated is marked in grey squares.

8.5 Conclusions

Bainite crystallography has been revisited with emphasis on the simultaneous determination of habit plane, orientation relationship and strain due to shape deformation on individual plates of bainite. The reconstruction of an austenite orientation map from the experimentally

determined map of bainite plate has also been outlined. The following inferences can be drawn:

1. Traces of an individual bainitic plate on two perpendicular surfaces have been used to determine the habit plane of bainite by two surface analysis. The determined habit plane of bainite is quite close to that reported for lath martensite.

2. An irrational orientation relationship has been determined for all the plates studied and is in agreement with the rigid body rotation required for converting the Bain orientation to contain a line unrotated and undistorted.

3. The shape deformation has been measured using atomic force microscopy for all the plates is well around the value estimated by phenomenological theory for martensite of 0.26. Some authors [222] reported shear strains of ≈ 0.46 associated with plate of bainite in nanostructured steels transformed at low temperatures (200 °C). Slenderness of the plates transformed at such low temperatures causes this. In the current work the bainitic transformation temperature is 400 °C, much higher than reported in literature for nanostructured steels.

4. The austenite reconstruction script performs well and generates the entire prior austenite grain orientation from bainite variants. The reconstruction has also been compared against the retained austenite and shows a very good match. The experimentally determined pole figure of bainitic ferrite variants with the 24 variants of α_b computed using the parent austenite orientation also matches quite well, signifying the correctness of the method.

Chapter 9

Conclusions and future work

Strength is relatively easy to achieve, but an actual automotive component requires a basket of parameters to be satisfied. Key amongst these parameters is of course ductility, with the combined requirement often expressed as a strength–ductility product. This is because the product is a representation of the energy absorbed during plastic deformation. Strength and ductility feature in the ability to form shapes: too high a strength causes elastic springback when a formed component is removed from the embrace of the forming tool. Ductility is essential in avoiding fracture during shaping. Many other parameters, for example, crack–free hole expansion during forming operations on blanks containing circular openings for bolts. Then there is the fact that the forming process itself will not in general impart equal plastic strain in all regions, so the final strength will not be homogeneous in the component. Furthermore, individual components must be joined by high-productivity processes such as spot welding, which takes milliseconds and therefore subjects the steel locally to rapid heating and cooling cycles. Such joints must survive fatigue loading during service and have sufficient tearing resistance during any crash impacts. Most of these aforementioned parameters can crudely be correlated to the strength–ductility product and the carbon equivalent of the steel. Two steels have been developed keeping in mind the restriction on carbon equivalent while achieving the desired 30 GPa% characteristic.

It is proposed that uniformity, which is the holy grail of achieving properties such as hole expansion etc., can be achieved not by thinking about the final microstructure, but by greatly refining the parent austenite grain size so that any subsequent transformations cannot exceed the size of the parent phase. Work done by Chatterjee some time ago [200] proved that fine plates of martensite do not crack easily even though they contain large concentrations of carbon. Similar principles should apply in TRIP steel, where the retained austenite is induced during deformation to transform into high–carbon martensite that should by convention be

brittle. Such martensite can be made less brittle if the parent grain size is small. Recent work by Peet [223] has proven that using vanadium microalloying it is possible to obtain an effective austenite grain size which is less than 4 µm, either in an equiaxed or in a pancaked morphology. Vanadium is used because it precipitates at the low finish–rolling temperature that is essential in achieving fine austenite grain structures. The goal here is the same concept in TRIP–assisted steel and is achieved by the following procedures:

1. Enhancement of austenite stability along with an increase in retained austenite content was achieved by using the percolation concept. This theory indicated the minimum free energy for austenite to ferrite transformation, required to ascertain the required strength–ductility combination. The method was particularly helpful in designing two new steels from the base composition by weighing the effect of each element on austenite stability.

2. A comprehensive study of the transformation behaviour of the new alloys helped to focus on the parameters conducive to the highest amount of stable retained austenite. Once these parameters established, bulk samples were prepared using the optimum processing, leading to the achievement of the 30 GPa% strength–ductility product.

3. Some samples narrowly missed the 30 GPa% target, but after treatment at a low temperature (150°C) for a few hours (3 h) to temper any martensite formed during cooling to room temperature helped recover the target properties. The retained austenite was not affected by the low temperature heat–treatment.

4. Extensive high resolution electron microscopy helped understand the generic damage mechanisms involved during the failure in tension of carbide–free bainitic TRIP–assisted steels. It was also interesting to look into deformation of microstructure containing both carbide–free bainite and austenite to pin point the instability post the saturation of TRIP–effect. Comprehensive fractography helped characterize crack initiation and the mode of failure.

5. The fine grained structure which was supposed to enhance ductility fell short of expectations due to chemical segregation–induced banding, the effects of which manifested particularly at the low austenitization temperatures. The degree of inhomogeneity was measured using the hardness entropy and helped in the quantification of the extent of banding caused at fine austenite grain sizes.

6. Image processing techniques were used to quantify features such as blocky austenite size or dimple size of ductile failure fracture surfaces. This information was later found to correlate with the grain size. Dimple size, which is sensitive to the presence of martensite, was found to be small for banded samples of alloy A, exemplifying the potency of these site for void nucleation.

7. The effect of fine, deformed austenite grains on the stability of retained austenite was studied using deformation dilatometry. Hot deformation below the non recrystallization temperature coupled with transformation in the bainitic temperature range led to a finer bainitic ferrite plates, but mechanical stabilization hindered the deformation–induced transformation of the retained austenite, thus impairing ductility.

8. Two–surface analysis of individual bainitic plates was attempted for the first time to reveal simultaneously the habit plane, orientation relation and shape deformation.

9. An algorithm to reconstruct prior austenite grains from the orientation maps of plates of martensite and bainite has been discussed with appropriate examples and the steps of reconstruction have been outlined. While this in itself is not novel, the technique proved essential in conducting grain size measurements in samples which were immune to thermal grooving.

Particular experiments to be done in the future should include:

1. The characterization of complex properties such as hole expansion and crash performance in order to test the viability of the alloys in more realistic scenarios.

2. A measure of spot weldability is needed to assess the performance of actual components using the peel or chisel tests as stated in ISO 10477:2015 standard [224]. Weldability needs to be quantified for the current steels which have been produced having a carbon equivalent low enough to achieve strong spot welds.

3. The performance of the new steels against hydrogen embrittlement needs to be investigated and the role of Nb in alloy A in improving susceptibility towards hydrogen embrittlement can be studied.

Bibliography

[1] Y. Weng, H. Dong, and Y. Gan. *Advanced Steels: The recent scenario in steel science and technology*. Springer Science & Business Media, 2011.

[2] D. MacKenzie, S. Zoepf, and J. Heywood. Determinants of US passenger car weight. *International Journal of Vehicle Design*, 65:73–93, 2014.

[3] N. Yurioka. Physical metallurgy of steel weldability. *ISIJ international*, 41:566–570, 2001.

[4] M. J. Peet. *Transformation and tempering of low-temperature bainite*. PhD thesis, University of Cambridge, 2010.

[5] H. Oikawa, G. Murayama, T. Sakiyama, Y. Takahashi, and T. Ishikawa. Resistance spot weldability of high strength steel (HSS) sheets for automobile. Technical report, 2006.

[6] Z.H. Cai, H. Ding, R.D.K. Misra, and Z.Y. Ying. Austenite stability and deformation behavior in a cold-rolled transformation-induced plasticity steel with medium manganese content. *Acta Materialia*, 84:229 – 236, 2015.

[7] H.F. Xu, J. Zhao, W.Q. Cao, J. Shi, C.Y. Wang, C. Wang, J. Li, and H. Dong. Heat treatment effects on the microstructure and mechanical properties of a medium manganese steel (0.2C–5Mn). *Materials Science and Engineering: A*, 532:435 – 442, 2012.

[8] D. W. Suh, S. J. Park, T. H. Lee, C. S. Oh, and S. J. Kim. Influence of Al on the microstructural evolution and mechanical behavior of low-carbon, manganese transformation-induced-plasticity steel. *Metallurgical and Materials Transactions A*, 41(2):397, Dec 2009.

[9] S.-J. Park, B. Hwang, K.H. Lee, T.-H. Lee, D.-W. Suh, and H.N. Han. Microstructure and tensile behavior of duplex low-density steel containing 5 mass% aluminum. *Scripta Materialia*, 68(6):365 – 369, 2013. Viewpoint Set 53: Low-Density Steels.

[10] Z.C. Li, H. Ding, R.D.K. Misra, and Z.H. Cai. Deformation behavior in cold-rolled medium-manganese TRIP steel and effect of pre-strain on the lüders bands. *Materials Science and Engineering: A*, 679:230 – 239, 2017.

[11] O. Grässel, L. Krüger, G. Frommeyer, and L. W. Meyer. High strength Fe–Mn–(Al, Si) TRIP/TWIP steels development–properties–application. *International Journal of Plasticity*, 16:1391–1409, 2000.

[12] Y. G. Kim, J. M. Han, and J. S. Lee. Composition and temperature dependence of tensile properties of austenitic Fe–Mn–Al–C alloys. *Materials Science and Engineering A*, 114:51–59, 1989.

[13] O. Grässel and G. Frommeyer. Effect of martensitic phase transformation and deformation twinning on mechanical properties of Fe–Mn–Si–Al steels. *Materials science and Technology*, 14:1213–1217, 1998.

[14] L. Cretteur, A. I. Koruk, and L. Tosal-Martínez. Improvement of weldability of TRIP steels by use of in–situ pre– and post–heat treatments. *Steel Research*, 73:314–319, 2002.

[15] R. W. K. Honeycombe and H. K. D. H. Bhadeshia. *Steels: Microstructure and Properties, 4nd edition*. Butterworths–Hienemann, London, 2017.

[16] R. W. K. Honeycombe and H. K. D. H. Bhadeshia. *Steels: Microstructure and Properties, 2nd edition*. Butterworths–Hienemann, London, 1995.

[17] H. K. D. H. Bhadeshia. *Bainite in Steels, 2nd edition*. Institute of Materials, London, U.K., 2001.

[18] G. Gao, H. Zhang, Z. Tan, W. Liu, and B. Bai. A carbide-free bainite/martensite/austenite triplex steel with enhanced mechanical properties treated by a novel quenching–partitioning–tempering process. *Materials Science & Engineering A*, 559:165–169, 2013.

[19] X. Zhang, H. Gao, X. Zhang, and Y. Yang. Effect of volume fraction of bainite on microstructure and mechanical properties of X80 pipeline steel with excellent deformability. *Materials Science & Engineering A*, 531:84–90, 2012.

[20] H. S. Hasan. Effect of transformation temperature on microstructure and mechanical properties of bainite. *Engineering and Technology Journal*, 30:2165–2174, 2012.

[21] M. H. Cai, H. Ding, Y. K. Lee, Z. Y. Tang, and J. S. Zhang. Effects of Si on microstructural evolution and mechanical properties of hot-rolled ferrite and bainite dual-phase steels. *ISIJ International*, 51:476–481, 2011.

[22] Y. Sakuma, O. Matsumura, and H. Takechi. Mechanical-properties and retained austenite in intercritically heat-treated bainite-transformed steel and their variation with Si and Mn additions. *Metallurgical & Materials Transactions A*, 22:489–498, 1991.

[23] Y. Tomita and K. Okabayshi. Mechanical properties of 0.4C–Ni–Cr–Mo high strength steel having a mixed structure of martensite and bainite. *Metallurgical Transactions A*, 16:73–82, 1985.

[24] M. Sudo and T. Iwai. Deformation behaviour and mechanical properties of ferrite-bainite-martensite (triphase) steel. *Transactions of the Iron and Steel Institute of Japan*, 23:294–302, 1983.

[25] J. A. da Cruz, T. F. M. Rodrigues, V. D. C. Viana, and D. B. Santos. Bainite formation at low temperatures in high C-Si steel and its mechanical behavior. In *Materials Science Forum*, volume 706, pages 173–180. Trans Tech Publ, 2012.

[26] S. Chatterjee. *TRIP–assisted steels*. PhD thesis, University of Cambridge, 2006.

[27] P. J. Jacques, E. Girault, A. Martens, B. Verlinden, J. van Humbeeck, and F. Delannay. The development of cold rolled TRIP–assisted multiphase steels. Al-alloyed TRIP-assisted multiphase steels. *ISIJ International*, 41:1068–1074, 2001.

[28] E. Kozeschnik and H. K. D. H. Bhadeshia. Influence of silicon on cementite precipitation in steels. *Materials Science and Technology*, 24:343–347, 2008.

[29] J. H. Jang, I. G. Kim, and H. K. D. H. Bhadeshia. Substitutional solution of silicon in cementite: A first–principles study. *Computational Materials Science*, 44:1319–1326, 2009.

[30] J. H. Jang, I. G. Kim, and H. K. D. H. Bhadeshia. ε–carbide in alloy steels: First–principles assessment. *Scripta Materialia*, 63:121–123, 2010.

[31] J. H. Jang, I. G. Kim, and H. K. D. H. Bhadeshia. First–principles calculations and the thermodynamics of cementite. In *Materials Science Forum*, volume 638, pages 3319–3324. Trans Tech Publ, 2010.

[32] C. J. McMahon. Temper brittleness–an interpretive review. In *Temper Embrittlement in Steel*, pages 127–167. ASTM International.

[33] R. A. Mulford, C. J. Mcmahon, D. P. Pope, and H. C. Feng. Temper embrittlement of Ni–Cr steels by phosphorus. *Metallurgical Transactions A*, 7:1183–1195, 1976.

[34] W. D. Callister and D. G. Rethwisch. *Fundamentals of materials science and engineering: an integrated approach*. John Wiley & Sons, 2012.

[35] W. T. Lankford, S. C. Snyder, and J. A. Bauscher. New criteria for predicting the press performance of deep drawing sheets. *Transactions of the American Society of Metals*, 42:1197–1205, 1950.

[36] Advanced vehicle concepts : Overview report. Technical report, ULSAB-AVC, January 2002.

[37] *ASM Handbook: Irons, Steels, and High-Performance Alloys*, volume 1–23. ASM International, 2016.

[38] H. K. D. H. Bhadeshia. High–performance bainitic steels. *Materials Science Forum*, 500-501:63–74, 2005.

[39] H. K. D. H. Bhadeshia. Steels for rails. In *Encyclopedia of Materials Science*, pages 1–7. Pergamon Press, Oxford, Elsevier Science, 2007.

[40] H. K. D. H. Bhadeshia. Bulk nanocrystalline steel. *Ironmaking and Steelmaking*, 32:405–410, 2005.

[41] E. DeMoor, S. Lacroix, A. J. Clarke, J. Penning, and J. G. Speer. Effect of retained austenite stabilized via quench and partitioning on the strain hardening of martensitic steels. *Metallurgical and Materials Transactions A*, 39:2586–2595, 2008.

[42] M. J. Santofimia, T. Nguyen-Minh, L. Zhao, R. Petrov, I. Sabirov, and J. Sietsma. New low carbon Q&P steels containing film–like intercritical ferrite. *Materials Science and Engineering A*, 527:6429–6439, 2010.

[43] N. Zhong, X. D. Wang, L. Wang, and Y. H. Rong. Enhancement of the mechanical properties of a Nb-microalloyed advanced high-strength steel treated by quenching–partitioning–tempering process. *Materials Science and Engineering: A*, 506:111–116, 2009.

[44] H. Y. Li, X. W. Lu, W. J. Li, and X. J. Jin. Microstructure and mechanical properties of an ultrahigh-strength 40SiMnNiCr steel during the one-step quenching and partitioning process. *Metallurgical and Materials Transactions A*, 41:1284–1300, 2010.

[45] T. Y. Hsu and X. Jin. *Ultra–high strength steel treated by using quenching–partitioning–tempering process*, pages 67–73. Springer Berlin Heidelberg, Berlin, Heidelberg, 2011.

[46] H. K. D. H. Bhadeshia. *Geometry of Crystals*. 2nd edition, Institute of Materials, 2001.

[47] C. M. Wayman. *Introduction to the crystallography of martensitic transformations*. Macmillan, New York, 1964.

[48] C. M. Wayman. The phenomenological theory of martensite crystallography: Interrelationships. *Metallurgical and Materials Transactions A*, 25:1787–1795, 1994.

[49] E. C. Bain. The nature of martensite. *Transactions of the Metallurgical Society of AIME*, 70:25–46, 1924.

[50] J. W. Christian. Basic crystallography and kinetics. *Martensite: fundamentals and technology by Petty, ER, Longman Ltd., London, United Kingdom.*, 1970.

[51] G. V. Kurdjumov and G. Sachs. Über den mechanismus der stahlhärtung. *Zietschrift für Physik A Hadrons and Nuclei*, 64:325–343, 1930.

[52] Z. Nishiyama. X–ray investigation of the mechanism of the transformation from face centered cubic lattice to body centered cubic. *Science Reports of Tohoku Imperial University*, 23:637–634, 1934.

[53] D. P. Koistinen and R. E. Marburger. A general equation prescribing the extent of the austenite–martensite transformation in pure iron–carbon alloys and plain carbon steels. *Acta Metallurgica*, 7:59–60, 1959.

[54] H. Davies. MTDATA–a tool for research and development in materials. *National Physical Laboratory, Teddington, UK*, 2003.

[55] J. O. Andersson, T. Helande, L. Hoglund, P. Shi, and B. Sundman. Thermo-Calc &
DICTRA, computational tools for materials science. *CALPHAD*, 26:273–312, 2002.

[56] B. Sundman, B. Jansson, and J. O. Andersson. The Thermo–Calc databank system.
CALPHAD, 9:153–190, 1985.

[57] E. Pereloma, A. Gazder, and I. Timokhina. Retained austenite: Transformation-
induced plasticity. *Encyclopedia of Iron, Steel and their Alloys*, pages 3088–3103,
2016.

[58] J. R. Patel and M. Cohen. Criterion for the action of applied stress in the martensitic
transformation. *Acta Metallurgica*, 1:531–538, 1953.

[59] L. Delaey and H. Warlimont. Crystallography and thermodynamics of SME-
martensites. In J. Perkins, editor, *Shape Memory Effects in Alloys*, pages 89–114,
U.S.A., 1975. Springer.

[60] H. K. D. H. Bhadeshia. TRIP–assisted steels? *ISIJ International*, 42:1059–1060,
2002.

[61] J. K. Mackenzie and J. S. Bowles. The crystallography of martensite transformations
II. *Acta Metallurgica*, 2:138–147, 1954.

[62] J. S. Bowles and J. K. Mackenzie. The crystallography of martensite transformations,
part I. *Acta Metallurgica*, 2:129–137, 1954.

[63] G. K. Tirumalasetty, M. A. Van Huis, C. Kwakernaak, J. Sietsma, W. G. Sloof, and
H. W. Zandbergen. Deformation–induced austenite grain rotation and transformation
in TRIP–assisted steel. *Acta Materialia*, 60:1311–1321, 2012.

[64] C. Garcia-Mateo and F. G. Caballero. Role of retained austenite on tensile properties
of steels with bainitic microstructures. *Materials Transactions*, 46:1839–1846, 2005.

[65] D. O. Panov, Yu. N. Simonov, P. A. Leont'ev, A. Yu. Kaletin, and M. N. Georgiev.
Formation of structure and properties of carbide-free bainite in steel 30KhGSA. *Metal
Science and Heat Treatment*, 58:71–75, 2016.

[66] K. W. Andrews. Empirical formulae for the calculation of some transformation
temperatures. *Journal of the Iron and Steel Institute*, 203:721–727, 1965.

[67] I. Tamura and C. M. Wayman. Martensitic transformations and mechanical effects. In *Martensite*, pages 228–242, Metals Park, Ohio, USA, 1992. ASM International.

[68] K. Sugimoto, N. Usui, M. Kobayashi, and S. Hashimoto. Effects of volume fraction and stability of retained austenite on ductility of TRIP–aided dual–phase steels. *ISIJ International*, 32:1311–1318, 1992.

[69] K. Sugimoto, M. Kobayashi, and S. Hashimoto. Ductility and strain-induced transformation in a high–strength TRIP aided dual phase steel. *Metallurgical Transactions A*, 23A:3085–3091, 1992.

[70] I. Tamura, T. Maki, H. Hoto, Y. Tomota, and M. Okada. Strength and ductility of austenitic iron alloys accompanying strain–induced martensitic transformation. In *2nd International Conference on Strength of Metals and Alloys*, volume 3, pages 894–899, Ohio, U. S. A., 1970. ASM.

[71] B. C. DeCooman. Structure–properties relationship in TRIP steels containing carbide–free bainite. *Current Opinion in Solid State and Materials Science*, 8:285–303, 2004.

[72] K. Sugimoto, N. Usui, M. Kobayashi, and S. Hashimoto. Effects of volume fraction and stability of retained austenite on ductility of TRIP-aided dual-phase steels. *ISIJ International*, 32:1311–1318, 1992.

[73] O. A. Zambrano. Stacking fault energy maps of Fe–Mn–Al–C–Si steels: Effect of temperature, grain size, and variations in compositions. *Journal of Engineering Materials and Technology*, 138:041010, 2016.

[74] V. T. Duong, Y. Y. Song, K. S. Park, H. K. D. H. Bhadeshia, and D. W. Suh. Austenite in transformation-induced plasticity steel subjected to multiple isothermal heat-treatments. *Metallurgical & Materials Transactions A*, 45:4201–4209, 2014.

[75] O. Matsumura, Y. Sakuma, and H. Takechi. TRIP and its kinetic aspects in austempered 0.4C–1.5Si–0.8Mn steel. *Scripta Metallurgica*, 27:1301–1306, 1987.

[76] C. Garcia-Mateo, F. G. Caballero, J. Chao, C. Capdevila, and C. Garcia de Andres. Mechanical stability of retained austenite during plastic deformation of super high strength carbide free bainitic steels. *Journal of Materials Science*, 44:4617–4624, 2009.

[77] C. Garcia-Mateo, F. G. Caballero, T. Sourmail, M. Kuntz, J. Cornide, V. Smanio, and E. Elvira. Tensile behaviour of a nanocrystalline bainitic steel containing 3 wt% silicon. *Materials Science & Engineering A*, 549:185–192, 2012.

[78] Yu. N. Simonov, M. Yu. Simonov, D. O. Panov, V. P. Vylezhnev, and A. Yu. Kaletin. Formation of structure of lower carbide-free bainite due to isothermal treatment of steels of types Kh3G3MFS and KhN3MFS. *Metal Science and Heat Treatment*, 58:61–70, 2016.

[79] F. G. Caballero, M. K. Miller, S. S. Babu, and C. Garcia-Mateo. Atomic scale observations of bainite transformation in a high carbon high silicon steel. *Acta Materialia*, 55:381–390, 2007.

[80] F. G. Caballero, H. Roelofs, S. Hasler, C. Capdevila, J. Chao, J. Cornide, and C. Garcia-Mateo. Influence of bainite morphology on impact toughness of continuously cooled cementite free bainitic steels. *Materials Science and Technology*, 28:95–102, 2012.

[81] M. N. Yoozbashi and S. Yazdani. Mechanical properties of nanostructured, low temperature bainitic steel designed using a thermodynamic model. *Materials Science and Engineering: A*, 527:3200–3205, 2010.

[82] B. R. Shendy, M. N. Yoozbashi, B. Avishan, and S. Yazdani. An investigation on rotating bending fatigue behavior of nanostructured low–temperature bainitic steel. *Acta Metallurgica Sinica (English Letters)*, 27:233–238, 2014.

[83] B. Avishan, C. Garcia-Mateo, L. Morales-Rivas, S. Yazdani, and F. G. Caballero. Strengthening and mechanical stability mechanisms in nanostructured bainite. *Journal of Materials Science*, 48:6121–6132, 2013.

[84] J. W. Christian. Thermodynamics and kinetics of martensite. In G. B. Olson and M. Cohen, editors, *International Conference on Martensitic Transformations ICOMAT '79*, pages 220–234, Massachusetts, USA, 1979. Alpine Press.

[85] K. Sugimoto, M. Tsunezawa, T. Hojo, and S. Ikeda. Ductility of 0.1–0.6C–1.5Si–1.5Mn ultra high-strength TRIP–aided sheet steels with bainitic ferrite matrix. *ISIJ International*, 44:1608–1614, 2004.

[86] A. Pichler, P. Stiaszny, R. Potzinger, R. Tikal, and E. Werner. TRIP steels with reduced Si content. In *40th Mechanical Working and Steel Processing Conference Proceedings*, volume 36, pages 259–274, 1998.

[87] H. C. Chen, H. Era, and M. Shimizu. Effect of phosphorus on the formation of retained austenite and mechanical properties in Si–containing low–carbon steel sheet. *Metallurgical Transactions A*, 20:437–445, 1989.

[88] F. B. Pickering. *Physical Metallurgy and the Design of Steels*. Applied Science Publishers, Essex, U. K., 1978.

[89] H. C. Chen, H. Era, and M. Shimizu. Effect of phosphorus on the formation of retained austenite and mechanical properties in Si–containing low-carbon steel sheet. *Metallurgical Transactions A*, 20:437–445, Mar 1989.

[90] C. Jing, D. Suh, C. Oh, Z. Wang, and S. Kim. Effects of phosphorous addition on mechanical properties and retained austenite stability of 0.15C-1.5Mn-1.5Al TRIP–aided cold rolled steels. *Metals and Materials International*, 13:13, Feb 2007.

[91] D. Krizan and B. C. De Cooman. Mechanical properties of TRIP steel microalloyed with Ti. *Metallurgical and Materials Transactions A*, 45:3481–3492, Jul 2014.

[92] K. Hausmann, D. Krizan, K. Spiradek-Hahn, A. Pichler, and E. Werner. The influence of Nb on transformation behavior and mechanical properties of TRIP–assisted bainitic–ferritic sheet steels. *Materials Science and Engineering: A*, 588:142–150, 2013.

[93] K. Sugimoto, T. Muramatsu, S. Hashimoto, and Y. Mukai. Formability of Nb bearing ultra high-strength TRIP–aided sheet steels. *Journal of Materials Processing Technology*, 177:390–395, 2006.

[94] S. Kim, C. G. Lee, T. Lee, and C. Oh. Effects of copper addition on mechanical properties of 0.15C–1.5Mn–1.5Si TRIP–aided multiphase cold-rolled steel sheets. *ISIJ International*, 42:1452–1456, 2002.

[95] S. Kim, C. G. Lee, T. Lee, and C. Oh. Effect of Cu, Cr and Ni on mechanical properties of 0.15 wt.% C TRIP–aided cold rolled steels. *Scripta Materialia*, 48:539–544, 2003.

[96] K. Sugimoto, M. Murata, and S. Song. Formability of Al–Nb bearing ultra high-strength TRIP-aided sheet steels with bainitic ferrite and/or martensite matrix. *ISIJ International*, 50:162–168, 2010.

[97] S. Kim, C. G. Lee, I. Choi, and S. Lee. Effects of heat treatment and alloying elements on the microstructures and mechanical properties of 0.15 wt pct C transformation-induced plasticity-aided cold-rolled steel sheets. *Metallurgical and Materials Transactions A*, 32:505–514, Mar 2001.

[98] K. Sugimoto, M. Murata, T. Muramatsu, and Y. Mukai. Formability of C–Si–Mn–Al–Nb–Mo ultra high-strength TRIP–aided sheet steels. *ISIJ international*, 47:1357–1362, 2007.

[99] K. Sugimoto, B. Yu, Y. Mukai, and S. Ikeda. Microstructure and formability of aluminum bearing TRIP–aided steels with annealed martensite matrix. *ISIJ International*, 45:1194–1200, 2005.

[100] H. S. Yang and H. K. D. H. Bhadeshia. Austenite grain size and the martensite–start temperature. *Scripta Materialia*, 60:493–495, 2009.

[101] I. Tamura. Deformation–induced martensitic transformation and transformation-induced plasticity in steels. *Metal Science*, 16:245–253, 1982.

[102] A. Rosen, R. Jago, and T. Kjer. Tensile properties of metastable stainless steels. *Journal of Materials Science*, 7:870–876, Aug 1972.

[103] T. Maki, Y. Tomota, and I. Tamura. Effect of grain size on the transformation-induced plasticity in metastable austenitic Fe–Ni–C alloy. *Journal of the Japan Institute of Metals*, 38:871–876, 1974.

[104] H. K. D. H. Bhadeshia and D. V. Edmonds. Bainite in silicon steels: a new composition property approach I. *Metal Science*, 17:411–419, 1983.

[105] H. K. D. H. Bhadeshia and D. V. Edmonds. Bainite in silicon steels: a new composition property approach II. *Metal Science*, 17:420–425, 1983.

[106] I. B. Timokhina, P. D. Hodgson, and E. V. Pereloma. Effect of deformation schedule on the microstructure and mechanical properties of a thermomechanically processed C–Mn–Si transformation-induced plasticity steel. *Metallurgical and Materials Transactions A*, 34:1599–1609, 2003.

[107] D. Q. Bai, A. Di Chiro, and S. Yue. Stability of retained austenite in a Nb microalloyed Mn-Si TRIP steel. *Materials Science Forum*, 284–286:253–260, 1998.

[108] Y. Tomota, H. Tokuda, Y. Adachi, M. Wakita, N. Minakawa, A. Moriai, and Y. Morii. Tensile behavior of TRIP–aided multi-phase steels studied by in situ neutron diffraction. *Acta Materialia*, 52:5737–5745, 2004.

[109] J. B. Seol, D. Raabe, P. P. Choi, Y. R. Im, and C. G. Park. Atomic scale effects of alloying, partitioning, solute drag and austempering on the mechanical properties of high-carbon bainitic–austenitic TRIP steels. *Acta Materialia*, pages 6183–6199, 2012.

[110] M. X. Zhang and P. M. Kelly. Determination of carbon content in bainitic ferrite and carbon distribution in austenite by using CBKLDP. *Materials Characterisation*, 40:159–168, 1998.

[111] E. Pereloma, H. Beladi, L. Zhang, and I. Timokhina. Understanding the behavior of advanced high-strength steels using atom probe tomography. *Metallurgical and Materials Transactions A*, 43:3958–3971, 2012.

[112] E. V. Pereloma, E. V. Timokhina, M. K. Miller, and P. D. Hodgson. Three-dimensional atom probe analysis of solute distribution in thermomechanically processed TRIP steels. *Acta Materialia*, 55:2587–2598, 2007.

[113] I. B. Timokhina, E. V. Pereloma, S. P. Ringer, R. K. Zheng, and Peter D. Hodgson. Characterization of the bake-hardening behavior of transformation induced plasticity and dual-phase steels using advanced analytical techniques. *ISIJ international*, 50:574–582, 2010.

[114] C. P. Scott and J. Drillet. A study of the carbon distribution in retained austenite. *Scripta Materialia*, 56:489–492, 2007.

[115] X. C. Xiong, B. Chen, M. X. Huang, J. F. Wang, and L. Wang. The effect of morphology on the stability of retained austenite in a quenched and partitioned steel. *Scripta Materialia*, 68:321–324, 2013.

[116] N. Tsuchida, S. Okura, T. Tanaka, and Y. Toji. High-speed tensile deformation behavior of 1 gpa-grade TRIP-aided multi-phase steels. *ISIJ International*, 58:978–986, 2018.

[117] S. V. Radcliffe and M. Schatz. The effect of high pressure on the martensitic reaction in iron-carbon alloys. *Acta Metallurgica*, 10:201–207, 1962.

[118] K. Sugimoto, M. Misu, M. Kobayashi, and H. Shirasawa. Effect of second phase morphology on retained austenite morphology and tensile properties in a TRIP–aided–dual phase steel sheet. *ISIJ International*, 33:775–782, 1993.

[119] I. Tsukatani, S. Hashimoto, and T. Inoue. Effects of Si & Mn addition on mech. properties of high strength ot rolled sheet steel containing retained austenite. *ISIJ International*, 31:992–1000, 1991.

[120] R. F. Hehemann, K. R. Kinsman, and H. I. Aaronson. Debate on the bainite reaction. *Metallurgical Transactions*, 3:1077–1094, 1972.

[121] H I Aaronson, W. T. Reynolds, G.J. Shiflet, and G. Spanos. Bainite viewed three different ways. *Metall Trans A*, 21A:1343–1380, 1990.

[122] L. C. D. Fielding. The bainite controversy. *Materials Science and Technology*, 29:383–399, 2013.

[123] H. K. D. H. Bhadeshia and D. V. Edmonds. The mechanism of bainite formation in steels. *Acta Metallurgica*, 28:1265–1273, 1980.

[124] L. C. Chang and H. K. D. H. Bhadeshia. Metallographic observations of bainite transformation mechanism. *Materials Science and Technology*, 11:106–108, 1995.

[125] M. Takahashi and H. K. D. H. Bhadeshia. Model for transition from upper to lower bainite. *Materials Science and Technology*, 6:592–603, 1990.

[126] A. Ali. *Widmanstätten ferrite and bainite in ultra–high strength steels*. PhD thesis, University of Cambridge, Cambridge, U. K., 1990.

[127] A. Ali and H. K. D. H. Bhadeshia. Aspects of the nucleation of Widmanstätten ferrite. *Materials Science and Technology*, 6:781–784, 1990.

[128] H. K. D. H. Bhadeshia. Rationalisation of shear transformations in steels. *Acta Metallurgica*, 29:1117–1130, 1981.

[129] C. H. Young and H. K. D. H. Bhadeshia. Strength of mixtures of bainite and martensite. *Materials Science and Technology*, 10:209–214, 1994.

[130] G. R. Speich and H. Warlimont. Yield strength and transformation substructure of low carbon martensite. *J. Iron and Steel Institute*, 206:385–392, 1968.

[131] J. W. Christian. The strength of martensite. In A. Kelly and R. Nicholson, editors, *Strengthening Methods in Crystals*, pages 261–329, Netherlands, 1971. Elsevier.

[132] C. N. Hulme-Smith, I. Lonardelli, A. C. Dippel, and H. K. D. H. Bhadeshia. Experimental evidence for non–cubic bainitic ferrite. *Scripta materialia*, 69:409–412, 2013.

[133] H. K. D. H. Bhadeshia. Anomalies in carbon concentration determinations from nanostructured bainite. *Materials Science and Technology*, 31:758–763, 2015.

[134] F. G. Caballero, M. K. Miller, C. Garcia-Mateo, J. Cornide, and M. J. Santofimia. Temperature dependence of carbon supersaturation of ferrite in bainitic steels. *Scripta Materialia*, 67:846–849, 2012.

[135] L. C. Chang and H. K. D. H. Bhadeshia. Austenite films in bainitic microstructures. *Materials Science and Technology*, pages 874–881, 1995.

[136] K. J. Irvine, F. B. Pickering, W. C. Heselwood, and M. Atkins. The physical metallurgy of low-C low-alloy steels containing boron. *Journal of the Iron and Steel Institute*, 186:54–67, 1957.

[137] K. J. Irvine and F. B. Pickering. Low carbon bainitic steels. *Journal of the Iron and Steel Institute*, 187:292–309, 1957.

[138] D. B. McCutcheon, T. W. Trumper, and J. D. Embury. Controlled rolling of acicular ferrite plate. *Revue de Métallurgie*, 73:143–174, 1976.

[139] L. Zhao, M. K. Wibowo, M. J. M. Hermans, S. M. C. van Bohemen, and J. Sietsma. Retention of austenite in the welded microstructure of a 0.16C–1.6Mn–1.5Si (wt%) TRIP steel. *Journal of Materials Processing Technology*, 209:5286–5292, 2009.

[140] H. K. D. H. Bhadeshia. Nanostructured bainite. In *Proceedings of the Royal Society of London A: Mathematical, Physical and Engineering Sciences*, volume 466, pages 3–18. The Royal Society, 2010.

[141] H. K. D. H. Bhadeshia. The first bulk nanostructured metal. *Science and Technology of Advanced Materials*, 14:014202, 2013.

[142] H. K. D. H. Bhadeshia and L. E. Svensson. Modelling the evolution of microstructure in steel weld metal. *Mathematical Modeling of Weld Phenomena*, 1:109–182, 1993.

[143] G. Shi and S. A. Westgate. Techniques for improving the weldability of TRIP steel using resistance spot welding. In *Paper for 1st International Conference of the High Strength Steel*, pages 1–13, 2005.

[144] L. Tosal-Martínez, L. Cretteur, O. Moriau, and A. I. Koruk. Characterization of cold rolled TRIP steels for structural crash-relevant applications in the automotive industry. In *International Body Engineering Conference Exhibition and Automotive Transportation Technology Congress*. SAE International, jul 2002.

[145] L. Cretteur, A. T. Koruk, and L. Tosal-Martínez. Improvement of weldability of TRIP steels by use of in-situ pre-and post-heat treatments. *Steel Research*, 73:314–319, 2002.

[146] D. B. Im, C. G. Lee, B. H. Song, S. J. Kim, and I. M. Park. Formability of low carbon TRIP–aided high strength cold rolled steel sheets containing tramp elements. *Journal of the Korean Institute of Metals and Materials (South Korea)*, 38:1328–1335, 2000.

[147] C. G. Lee, S. J. Kim, B. H. Song, and S. Lee. Effect of heat treatment on formability in 0.15C–1.5Si–1.5Mn multiphase cold–rolled steel sheet. *Metals and Materials International*, 8:435–441, 2002.

[148] C. G. Lee, S. J. Kim, T. H. Lee, and S. Lee. Effects of volume fraction and stability of retained austenite on formability in a 0.1C–1.5Si–1.5Mn–0.5Cu TRIP–aided cold–rolled steel sheet. *Materials Science and Engineering: A*, 371:16–23, 2004.

[149] K. Sugimoto, M. Kobayashi, A. Nagasaka, and S. Hashimoto. Warm stretch-formability of TRIP aided dual-phase sheet steels. *ISIJ International*, pages 1407–1414, 2002.

[150] The limiting dome height test. http://www.msm.cam.ac.uk/phase-trans/2016/Tata1/Pages/41.html. Accessed: 2016-12-31.

[151] C. G. Lee, S.-T. Kim, T.-H. Lee, and C.-S. Oh. Effects of tramp elements on formability of low-carbon TRIP–aided multiphase cold-rolled steel sheets. *ISIJ International*, 44:737–743, 2004.

[152] P. Larour, J. Freudenthaler, A. Grünsteidl, and K. Wang. Evaluation of alternative stretch flangeability testing methods to iso 16630 standard. pages 188–193, 2014.

[153] M. Mukherjee, A. R. Chintha, S. Kundu, S. Misra, J. Singh, C. Bhanu, and T. Venugopalan. Development of stretch flangeable ferrite-bainite grades through thin slab casting and rolling. *Materials Science and Technology*, 32:348–355, 2016.

[154] K. Sugimoto, J. Sakaguchi, T. Iida, and T. Kashima. Stretch-flangeability of a high-strength TRIP type bainitic sheet steel. *ISIJ International*, 40:920–926, 2000.

[155] The hole expansion test: Initial blank. http://www.msm.cam.ac.uk/phase-trans/2016/Tata1/Pages/45.html. Accessed: 2016-12-31.

[156] The hole expansion test: Final blank. http://www.msm.cam.ac.uk/phase-trans/2016/Tata1/Pages/46.html. Accessed: 2016-12-31.

[157] T. Degen, M. Sadki, E. Bron, U. König, and G. Nénert. The highscore suite. *Powder Diffraction*, 29:S13–S18, 2014.

[158] L. Lutterotti. Materials analysis using diffraction. http://www.ing.unitn.it/ maud/index.html, 2013.

[159] B. D. Cullity and S. R. Stock. *Elements of X–ray Diffraction*, volume 3. Prentice hall New Jersey, 2001.

[160] M. J. Dickson. The significance of texture parameters in phase analysis by X–ray diffraction. *Journal of applied Crystallography*, 2:176–180, 1969.

[161] ASTM E8/E8M-16a. Standard test methods for tension testing of metallic materials, 2016.

[162] G. B. Olson and M. Cohen. Kinetics of strain–induced martensitic transformation. *Metallurgical Transactions A*, 6A:791–795, 1975.

[163] J. R. C. Guimaraes. The deformation–induced martensitic reaction in polycrystalline Fe–30.7Ni–0.06C. *Scripta Metallurgica*, 6:795–798, 1972.

[164] W. W. Gerberich, G. Thomas, E. R. Parker, and V. F. Zackay. Metastable austenites: decomposition and strength. In *Second International Conference on Strength of Metals and Alloys*, pages 894–899, Ohio, USA, 1970. ASM International.

[165] D. C. Ludwigson and J. An. Berger. Plastic behaviour of metastable austenitic stainless steels. *Journal of the Iron and Steel Institute*, 207:63–69, 1969.

[166] M. Sherif, C. Garcia-Mateo, T. Sourmail, and H. K. D. H. Bhadeshia. Stability of retained austenite in TRIP–assisted steels. *Materials Science and Technology*, 20:319–322, 2004.

[167] J. R. McDermid, H. S. Zurob, and Y. Bian. Stability of retained austenite in high–Al, low–Si TRIP–assisted steels processed via continuous galvanizing heat treatments. *Metallurgical and Materials Transactions A*, 42:3627–3637, 2011.

[168] P. J. Jacques, E. Girault, Ph. Harlet, and F. Delannay. The developments of cold-rolled TRIP–assisted multiphase steels. low silicon TRIP–assisted multiphase steels. *ISIJ International*, 41:1061–1067, 2001.

[169] Y. Tomita and K. Morioka. Effect of microstructure on transformation–induced plasticity of silicon-containing low–alloy steel. *Materials Characterisation*, 38:243–250, 1997.

[170] P. J. Jacques, Q. Furnemont, A. Mertens, and F. Delannay. On the sources of work hardening in multiphase steels by transformation-aided plasticity. *Philosophical Magazine A*, 81:1789–1812, 2001.

[171] A. Itami, M. Takahashi, and K. Ushioda. Plastic stability of retained austenite in the cold-rolled 0.14C-1.9Si-1.7Mn sheet steel. *ISIJ International*, 35:1121–1127, 1995.

[172] K. Sugimoto, M. Kobayashi, A. Nagasaka, and S. Hashimoto. Warm stretch-formability of TRIP aided dual-phase sheet steels. *ISIJ International*, 35:1407–1414, 1995.

[173] H. K. D. H. Bhadeshia. Properties of fine–grained steels generated by displacive transformation. *Materials Science and Engineering A*, 481–482:36–39, 2008.

[174] D. J. Dyson and B. Holmes. Effect of alloying additions on the lattice parameter austenite. *Journal of the Iron and Steel Institute*, 208:469–474, 1970.

[175] N. Ridley, H. Stuart, and L. Zwell. Lattice parameters of Fe–C austenites at room temperature. *Transactions of the Metallurgical Society of AIME*, 245:1834–1836, 1969.

[176] G. Gao, H. Zhang, X. Gui, P. Luo, Z. Tan, and B. Bai. Enhanced ductility and toughness in an ultrahigh-strength Mn–Si–Cr–C steel: The great potential of ultrafine filmy retained austenite. *Acta Materialia*, 76:425–433, 2014.

[177] F. G. Caballero, H. K. D. H. Bhadeshia, K. J. A. Mawella, D. G. Jones, and P. Brown. Design of novel high strength bainitic steels: Part 2. *Materials Science and Technology*, 17:517–522, 2001.

[178] M. Sherif, C. Garcia-Mateo, T. Sourmail, and H. K. D. H. Bhadeshia. Stability of retained austenite in TRIP–assisted steels. *Materials Science and Technology*, 20:319–322, 2004.

[179] W. A. Dollase. Correction of intensities for preferred orientation in powder diffractometry: application of the March model. *Journal of Applied Crystallography*, 19:267–272, 1986.

[180] A. Zarei Hanzaki, P. D. Hodgson, and S. Yue. Hot deformation characteristics of Si–Mn TRIP steels with and without Nb microalloy additions. *ISIJ International*, 35:324–331, 1995.

[181] R. C. Ruhl. Splat quenching of iron-carbon alloys. *Transactions of the Metallurgical Society of AIME*, 245:241, 1969.

[182] N. H. Van Dijk, A. M. Butt, L. Zhao, J. Sietsma, S. E. Offerman, J. P. Wright, and S. Van der Zwaag. Thermal stability of retained austenite in TRIP steels studied by synchrotron X–ssray diffraction during cooling. *Acta Materialia*, 53:5439–5447, 2005.

[183] L. Cheng, A. Böttger, Th. H. De Keijser, and E. J. Mittemeijer. Lattice parameters of iron-carbon and iron-nitrogen martensites and austenites. *Scripta metallurgica et materialia*, 24:509–514, 1990.

[184] C. S. Roberts. Effect of carbon on the volume fractions and lattice parameters of retained austenite and martensite. *Transactions of the Metallurgical Society of AIME*, 197:203–204, 1953.

[185] E. Kozeschnik and B. Buchmayr. MATCALC–a simulation tool for multicomponent thermodynamics, diffusion and phase transformations. In *Fifth international seminar on the numerical analysis of weldability*, pages 349–361, 1999.

[186] M. Peet and H. K. D. H. Bhadeshia. Software for transformations in steels. http://www.msm.cam.ac.uk/map/steel/programs/mucg83.html, 1982.

[187] T. Okumura. Software for modelling of the thermodynamics and kinetics of solid-state transformations in steels. http://www.msm.cam.ac.uk/map/steel/programs/MTTTDATA.html, 2004.

[188] S. S. Babu, K. Hono, and T. Sakuri. APFIM studies on martensite tempering of Fe–C–Si–Mn steel. *Applied Surface Science*, 67:321–327, 1993.

[189] S. S. Babu, K. Hono, and T. Sakuri. APFIM study of partitioning of substitutional elements during tempering of low alloy steel martensite. *Metallurgical & Materials Transactions A*, 25:499–508, 1994.

[190] J. Fridberg, L.-E. Torndähl, and M. Hillert. Diffusion in iron. *Jernkontorets Annaler*, 153:263–276, 1969.

[191] J. Kučera and K. Stránský. Diffusion in iron, iron solid solutions and steels. *Materials Science and Engineering*, 52:1–38, 1982.

[192] H. S. Yang and H. K. D. H. Bhadeshia. Uncertainties in the dilatometric determination of the martensite–start temperature. *Materials Science and Technology*, 23:556–560, 2007.

[193] S. J. Jones and H. K. D. H. Bhadeshia. Software for TTT to CCT conversion using scheil's additivity. http://www.msm.cam.ac.uk/map/steel/subs/tttcct-b.html, 1982.

[194] J. W. Christian. *Theory of Transformations in Metals and Alloys, Part I*. Pergamon Press, Oxford, U. K., 2 edition, 1975.

[195] L.-E. Svensson, B. Gretoft, and H. K. D. H. Bhadeshia. Analysis of cooling curves from the fusion zone of weld deposits. *Scandanavian Journal of Metallurgy*, 15:97–103, 1986.

[196] H. K. D. H. Bhadeshia. *The theory and significance of retained austenite in steels*. PhD thesis, University of Cambridge, 1979.

[197] C. N. Hulme-Smith, M. J. Peet, I. Lonardelli, A. C. Dippel, and H. K. D. H. Bhadeshia. Further evidence of tetragonality in bainitic ferrite. *Materials Science and Technology*, 2014.

[198] S. S. Zhang, M. Q. Li, Y. G. Liu, J. Luo, and T. Q. Liu. The growth behavior of austenite grain in the heating process of 300M steel. *Materials Science and Engineering: A*, 528:4967–4972, 2011.

[199] H. K. D. H. Bhadeshia and A. R. Waugh. Bainite: An atom probe study of the incomplete reaction phenomenon. *Acta Metallurgica*, 30:775–784, 1982.

[200] S. Chatterjee and H. K. D. H. Bhadeshia. TRIP–assisted steels: cracking of high carbon martensite. *Materials Science and Technology*, 22:645–649, 2006.

[201] W. W. Mullins. The effect of thermal grooving on grain boundary motion. *Acta metallurgica*, 6:414–427, 1958.

[202] L. Guo, H. Roelofs, M. I. Lembke, and H. K. D. H. Bhadeshia. Modelling of size distribution of blocky retained austenite in Si-containing bainitic steels. *Materials Science and Technology*, 34:54–62, 2018.

[203] C. T. Rueden, J. Schindelin, M. C. Hiner, B. E. DeZonia, A. E. Walter, E. T. Arena, and K. W. Eliceiri. ImageJ2: ImageJ for the next generation of scientific image data. *BMC bioinformatics*, 18:529, 2017.

[204] H. K. D. H. Bhadeshia. Software for dilatometer data analysis. https://www.phase-trans.msm.cam.ac.uk/map/steel/programs/dilat2-b.html, 1982.

[205] J. Yang and S. K. Putatunda. Improvement in strength and toughness of austempered ductile cast iron by a novel two–step austempering process. *Materials & design*, 25:219–230, 2004.

[206] S. Chatterjee, H-S. Wang, J. R. Yang, and H. K. D. H. Bhadeshia. Mechanical stabilisation of austenite. *Materials Science and Technology*, 22:641–644, 2006.

[207] Q. Zhu, C. M. Sellars, and H. K. D. H. Bhadeshia. Quantitative metallography of deformed grains. *Materials Science and Technology*, 23:757–766, 2007.

[208] S. B. Singh and H. K. D. H. Bhadeshia. Topology of grain deformation. *Materials Science and Technology*, 14:832–834, 1998.

[209] G. R. Srinivasan and C. M. Wayman. The crystallography of the bainite transformation–I. *Acta Metallurgica*, 16:621–636, 1968.

[210] Y. Ohmori. Crystallography of the lower bainite transformation in a plain carbon steel. *Transactions of the Iron and Steel Institute of Japan*, 11:95–101, 1971.

[211] S. Hoekstra. A check of the IPS theory with the aid of an accurate determination of habit planes and orientation relationships in bainitic steels. *Acta Metallurgica*, 28:507–517, 1980.

[212] B. P. J. Sandvik. The bainite reaction in Fe–Si–C alloys: the primary stage. *Metallurgical Transactions A*, 13:777–787, 1982.

[213] C. P. Luo, G. C. Weatherly, and Zheng-Yi Liu. The crystallography of bainite in a medium-carbon steel containing Si, Mn, and Mo. *Metallurgical Transactions A*, 23:1403–1411, 1992.

[214] G. M. A. M. El Fallah and H. K. D. H. Bhadeshia. Tensile behaviour of thermally-stable nanocrystalline bainitic-steels. *Materials Science and Engineering: A*, 746:145–153, 2019.

[215] H. K. D. H. Bhadeshia and D. V. Edmonds. The bainite transformation in a silicon steel. *Metallurgical Transactions A*, 10A:895–907, 1979.

[216] G. Miyamoto, N. Iwata, N. Takayama, and T. Furuhara. Reconstruction of parent austenite grain structure based on crystal orientation map of bainite with and without ausforming. *ISIJ International*, 51:1174–1178, 2011.

[217] S. K. Giri, A. Durgaprasad, K. V. Manikrishna, C. R. Anoop, S. Kundu, and I. Samajdar. Exploring the origin of variant selection through martensite-austenite reconstruction. *Philosophical Magazine*, 99:699–717, 2019.

[218] T. Nyyssönen, M. Isakov, P. Peura, and V.-T. Kuokkala. Iterative determination of the orientation relationship between austenite and martensite from a large amount of grain pair misorientations. *Metallurgical and Materials Transactions A*, 47:2587–2590, Jun 2016.

[219] T. Nyyssönen. *Quenching and partitioning of high-aluminum steels*. PhD thesis, Tampere University of Technology, 2017.

[220] T. Nyyssönen, P. Peura, and V.-T. Kuokkala. Crystallography, morphology, and martensite transformation of prior austenite in intercritically annealed high-aluminum steel. *Metallurgical and Materials Transactions A*, 49:6426–6441, Dec 2018.

[221] S. Van Dongen. *Graph clustering by flow simulation*. PhD thesis, University of Utrecht, 2000.

[222] M. J. Peet and H. K. D. H. Bhadeshia. Surface relief due to bainite transformation at 473 K (200 °C). *Metallurgical and Materials Transactions A*, 42:3344, Jun 2011.

[223] M. J. Peet and H.K.D.H. Bhadeshia. Unpublished work. University of Cambridge, U.K., 2010.

[224] ISO 10447:0215. Resistance welding–testing of welds–peel and chisel testing of resistance spot and projection welds, 2015.